

High Temperature Salt Deposit-Assisted Corrosion of Silicon
Carbide-Based Ceramic Matrix Composites: Effects of Composite
Chemistry and Architecture

A Dissertation Presented to the Faculty of the
School of Engineering and Applied Science
University of Virginia

In Partial Fulfillment of the Requirements for the Degree of
Doctor of Philosophy

by

Joseph M. Hagan¹

Department of Materials Science and Engineering

May, 2015

¹ Funding Provided by ONR Grant N00014-11-1-0601

Approval Sheet

The dissertation is submitted in partial fulfillment of the requirements
for the degree of Doctor of Philosophy

Joseph M Hagan



Author

The dissertation has been read and approved by the examining committee:

Elizabeth Opila – MSE, Advisor

Robert Kelly – MSE, Chair

Haydn Wadley – MSE

Gary Koenig – ChE

Nathan Jacobson – NASA-Glenn Research Center

Accepted for the School of Engineering and Applied Science:



Dean, School of Engineering and Applied Science

May, 2015

Table of Contents

1	Abstract.....	1
2	Objectives.....	3
2.1	Task 1 – Hot Corrosion of Model Materials	3
2.2	Task 2 – Hot Corrosion of CMC Coupons	4
2.3	Task 3 – Solubility of Oxides in Sodium Sulfate.....	4
3	Introduction.....	5
4	Experimental Procedures	20
4.1	Task 1 – Hot Corrosion of Model Materials	20
4.2	Task 2 – Hot Corrosion of CMC Coupons	25
4.3	Task 3 – Solubility of Oxides in Sodium Sulfate.....	28
5	Task 1 – Hot Corrosion of Model Materials	38
5.1	Results	38
5.1.1	Model Materials Characterization.....	38
5.1.2	Time Dependence for SiC Hot Corrosion.....	40
5.1.3	Temperature Dependence for SiC Hot Corrosion.....	43
5.1.4	Substrate Dependence for SiC Hot Corrosion	46
5.1.5	Chemistry Dependence of SiC Hot Corrosion: C & BN.....	48
5.1.6	Chemistry Dependence of SiC Hot Corrosion: Si.....	54
5.1.7	SO ₂ Concentration Dependence of SiC Hot Corrosion	54
5.1.8	Pitting Results for Hot Corrosion of SiC.....	57
5.1.9	Microscopy Results.....	60

5.1.10	X-Ray Diffraction Results.....	70
5.2	Discussion	71
5.2.1	Hot Corrosion Mechanism	74
5.2.2	Chemistry Effects.....	75
5.3	Conclusions.....	77
5.4	Recommendations for Future Work.....	78
6	Task 2 – Hot Corrosion of CMC Materials	80
6.1	Results	80
6.1.1	Material Characterization	80
6.1.2	Furnace Exposed CMCs	87
6.1.3	Burner Rig Exposed CMCs	96
6.2	Discussion	105
6.2.1	Materials Characterization	105
6.2.2	Furnace-Exposed CMCs	105
6.2.3	Burner Rig-Exposed CMCs.....	107
6.3	Conclusions.....	111
6.4	Recommendations for Future Work.....	112
7	Task 3 – Solubility of Oxides in Sodium Sulfate.....	115
7.1	Results	115
7.1.1	NiO Solubility.....	115
7.1.2	SiO ₂ Solubility.....	120
7.1.3	B ₂ O ₃ Solubility.....	126
7.2	Discussion	133

7.2.1 NiO Solubility.....	133
7.2.2 SiO ₂ Solubility.....	133
7.2.3 B ₂ O ₃ Solubility.....	136
7.3 Conclusions.....	138
7.4 Recommendations for Future Work.....	139
8 Conclusions	142
9 Acknowledgements	143
Appendix A Electrochemical Potential Derivation	144
Appendix B Radar Plot Data	146
Appendix C Microscopy of CMC Coupons.....	147
Appendix D Electrochemical Measurement Data.....	181
10 Works Cited.....	183

List of Figures

Figure 1 – Phase stability diagram for Na ₂ O and SiO ₂ at 900°C with the basic end on the left and the acidic end on the right. All phases are predicted to be solid at 900°C.	8
Figure 2 – Phase stability diagram for Na ₂ O and SiO ₂ at 1000°C with the basic end on the left and the acidic end on the right. All phases are predicted to be solid at 1000°C.	9
Figure 3 – Phase stability diagram for Na ₂ O and B ₂ O ₃ at 900°C with the basic end on the left and the acidic end on the right. All phases are predicted to be liquid at 900°C.	11
Figure 4 – Phase stability diagram for Na ₂ O and B ₂ O ₃ at 1000°C with the basic end on the left and the acidic end on the right. All phases are predicted to be liquid at 1000°C.	12
Figure 5 – Compilation of measured solubilities for several oxides in fused pure Na ₂ SO ₄ at 1200 K, recreated from Rapp ²³	15
Figure 6 – Ellingham diagram showing relative thermodynamic stability of composite constituents toward oxidation.	17
Figure 7 – Image of a coupon loaded with approximately 2.5 mg/cm ² Na ₂ SO ₄	21
Figure 8 – Loaded sample carrier (with 4 samples) before being placed into furnace.	22
Figure 9 – CMC coupons for burner rig exposure. Top coupon is CVI-SiC and bottom is MI-SiC. Both coupons measure approximately 1.25 cm x 0.3 cm x 11 cm.	26

Figure 10 – SiC CMC coupon loaded into Mach 0.3 burner rig at 950°C with cut edge as leading edge. Orange color is due to the sodium from the injected 8ppm Na ₂ SO ₄ solution.....	27
Figure 11 – Schematic of the sectioning plan for the burner rig coupons.....	28
Figure 12 – Cutaway schematic of the end cap assembly on the left showing the location and configuration of electrodes and components. The right schematic is an isometric view of the whole end cap and furnace tube assembly.....	29
Figure 13 - Cutaway schematic of the closed end of the sodium electrode on the left and the top of the electrode on the right showing arrangement of the components.	30
Figure 14 – Cutaway schematic of the closed end of the oxygen electrode on the left and the top of the 4-bore alumina sheath on the right showing arrangement of the components.	32
Figure 15 – Cutaway schematic of the bottom of the furnace tube showing the alumina crucible, oxygen electrode, sodium electrode, and gas inlet.	33
Figure 16 – Schematics showing the approximate location and shape of the oxides used. From left to right: NiO powder, SiO ₂ pieces, and aluminoborate pellets.	36
Figure 17 – Al ₂ O ₃ -B ₂ O ₃ pseudo-binary phase diagram taken from Gielisse and Foster ⁶⁰ , with the two-phase field of interest shaded.....	37
Figure 18 – Electron micrograph of the top surface of a Hexoloy coupon, EDS map of B, and EDS map of C.	39

Figure 19 – Auger depth profiles of the deposited C and BN coatings, showing a coating thickness of around 700nm.....40

Figure 20 – Normalized mass loss (mg/cm²) after corrosion products removed as a function of exposure time (hr) for CVD SiC and Hexoloy coupons exposed at 1000°C.....42

Figure 21 – Total Si found in corrosion products (μg) using ICP-OES as a function of exposure time (hr) for CVD SiC and Hexoloy coupons exposed at 1000°C.....42

Figure 22 – Examples of non-uniform corrosion on CVD SiC coupons exposed at 1000°C for 6-hr.43

Figure 23 – Temperature dependence of sodium sulfate induced hot corrosion of SiC (Hexoloy) plotted as the log of total Si found in the corrosion products (μg) and log of mass loss after corrosion products are removed (mg) vs. inverse temperature (K). In the temperature range of 950-1100°C the apparent activation energy is 71.5 kJ/mol ±34 kJ/mol for linear mass loss and 80.8 kJ/mol ±40 kJ/mol (95% confidence intervals) for linear total Si in the corrosion products.44

Figure 24 - Temperature dependence of sodium sulfate induced hot corrosion of SiC (Hexoloy) plotted as the log of total Si found in the corrosion products squared (μg) and log of mass loss after corrosion products are removed squared (mg) vs. inverse temperature (K). In the temperature range of 950-1100°C the apparent activation energy is 143.0 kJ/mol ±68 kJ/mol for parabolic mass loss and 161.5 kJ/mol ±80 kJ/mol (95% confidence intervals) for parabolic total Si in the corrosion products.....45

Figure 25 – Radar plot comparing relative hot corrosion resistance of uncoated CVD SiC and Hexoloy coupons exposed for 24 hr at 1000°C.....47

Figure 26 – Radar plot comparing relative hot corrosion resistance of C coated CVD SiC and Hexoloy coupons exposed for 24 hr at 1000°C in 0.1% SO₂/O₂49

Figure 27 – Radar plot comparing relative hot corrosion resistance of BN coated CVD SiC and Hexoloy coupons exposed for 24 hr at 1000°C in 0.1% SO₂/O₂.50

Figure 28 – Radar plots showing Na and S found in each of the digestion steps as well as total Na and S for CVD SiC and Hexoloy coupons as a function of surface coating after hot corrosion for 24 hr at 1000°C in 0.1% SO₂/O₂.....51

Figure 29 – Radar plots showing B and Si found in each of the digestion steps as well as total B and Si for CVD SiC and Hexoloy coupons as a function of surface coating after hot corrosion for 24 hr at 1000°C in 0.1% SO₂/O₂.....52

Figure 30 – The image on the left shows the sample carrier loaded with 4 coupons after salt deposition and before exposure. The top two coupons are C-coated and the bottom two coupons are BN-coated, showing the increased wetting of the aqueous salt solution on the BN-coated coupons. The image on the right shows the same samples after exposure for 24-hours at 1000°C, where the corrosion products on the BN-coated sample are more evenly distributed.....53

Figure 31 –SEM micrograph of a coupon after exposure for 24 hours at 1000°C in 2.5 ppm SO₂/O₂.....55

Figure 32 – Plot showing the difference in normalized mass loss between the three Hexoloy coupon types exposed in 1000ppm SO ₂ /O ₂ and 2.5 ppm SO ₂ /O ₂	56
Figure 33 – Plot showing the difference in normalized mass loss between the three CVD coupon types exposed in 1000ppm SO ₂ /O ₂ and 2.5 ppm SO ₂ /O ₂	56
Figure 34 – Electron micrograph of a Hexoloy coupon exposed for 24 hr at 1000°C showing extensive pitting of the sample surface.	58
Figure 35 – Topographical maps of pits (inverted to become peaks) comparing the pitting behavior of Hexoloy and CVD-SiC exposed for 24 hr at 1000°C. Note the different height scales in each map.	59
Figure 36 – Pitting results for Hexoloy (mean depth, mean diameter, max depth, and pit density) plotted as a function of exposure time.....	59
Figure 37 - Pitting results for CVD-SiC (mean depth, mean diameter, max depth, and pit density) plotted as a function of exposure time.....	60
Figure 38 – Electron micrograph and corresponding Na EDS map of a Hexoloy coupon exposed for 24 hr at 1000°C.	61
Figure 39 – Backscattered electron micrograph of a cross-sectioned CVD-SiC coupon exposed for 24 hr at 1000°C showing a thick section of the scale.....	63
Figure 40 – EDS maps for (clockwise from top left) C, O, Na, and Si that correspond with the micrograph in Figure 39, showing a thick sodium-silicate layer which contains silica laths on top of a thin silica layer at the scale-substrate interface.....	64
Figure 41 – Electron micrograph of a cross-sectioned CVD-SiC coupon exposed for 24 hr at 1000°C showing a thin section of the scale.	65

Figure 42 – EDS maps for (clockwise from top left) C, O, Na, and Si that correspond with the micrograph in Figure 41, showing a thin sodium-silicate layer on top of a thin silica layer at the scale-substrate interface.	66
Figure 43 – Electron micrograph of a Hexoloy coupon before exposure.	67
Figure 44 – Electron micrograph of a Hexoloy coupon after corrosion for 24 hr at 1000°C.....	68
Figure 45 – Electron micrograph of a Hexoloy coupon after the water digestion step.....	68
Figure 46 – Electron micrograph of a Hexoloy coupon after the HCl digestion step.....	69
Figure 47 – Electron micrograph of a Hexoloy coupon after the HF digestion step.....	69
Figure 48 – X-Ray diffraction data for selected model material coupons.	71
Figure 49 – Schematic illustrating the hot-corrosion of SiC by Na ₂ SO ₄ resulting in a layered corrosion product consisting of a thin silica layer at the substrate-scale interface with a partially-porous mixed silicate on top as well as some residual sodium sulfate.	75
Figure 50 – SEM micrograph of the one of the CVI-F composites with the seal coat ground off before exposure in the furnace.....	81
Figure 51 – Two micrographs of the CVI-F composite, SE on top and BSE on bottom. The micrographs show the SiC fibers, BN interphase, dense CVD layer, PIP slurry with SiC particulates, and MI Si.....	83
Figure 52 – Micrograph of the MI-F coupon showing the Hi-Nicalon-S fibers, BN interphase, SiC matrix, and residual Si from the MI process.....	84
Figure 53 – SEM micrograph of one of the CVI-F coupons before exposure showing large voids present in the matrix between the Sylramic fiber tows.	84

Figure 54 – SEM micrographs of the burner rig composite cross sections taken near the end of the coupon. The MI-BR composite is on the top and the CVI-BR composite is on the bottom.85

Figure 55 – SEM micrograph of an MI-BR coupon showing the fairly dense matrix with some small pores/voids.....86

Figure 56 – SEM micrographs an MI-BR coupon showing the SiC particulates and residual Si in the matrix.86

Figure 57 – SEM micrographs a CVI-BR coupon showing the large voids on the left and the locally dense SiC matrix on the right.....87

Figure 58 – Two SEM micrographs of the CVI-F composites after exposure for 24 hours at 1000°C. The coupon on the left was exposed in 2.5 ppm SO₂/O₂ while the coupon on the right was exposed in 1000 ppm SO₂/O₂.....88

Figure 59 – Two SEM micrographs of the CVI-F composites after exposure for 24 hours at 1000°C. The coupon on the left was exposed in 2.5 ppm SO₂/O₂ and shows the crystalline laths while the coupon on the right was exposed in 1000 ppm SO₂/O₂ and shows the bubbly morphology.88

Figure 60 – Two SEM micrographs of the CVI-F composites after the water digestion step. The coupon on the left was exposed in 2.5 ppm SO₂/O₂ while the coupon on the right was exposed in 1000 ppm SO₂/O₂.89

Figure 61 – Two SEM micrographs of the CVI-F composites after the HCl digestion step. The coupon on the left was exposed in 2.5 ppm SO₂/O₂ while the coupon on the right was exposed in 1000 ppm SO₂/O₂.90

Figure 62 – Two micrographs of the CVI-F composites after the HF digestion step. The coupon on the left was exposed in 2.5 ppm SO₂/O₂ while the coupon on the right was exposed in 1000 ppm SO₂/O₂.....91

Figure 63 – Two SEM micrographs of the CVI-F composites after the HF digestion step showing the pitting and attack of the Sylramic fibers.....92

Figure 64 – Two SEM high magnification micrographs after the HF digestion step, a Sylramic fiber on the left and a Hi-Nicalon-S fiber on the right, showing rougher texture and etching on the Sylramic fiber as compared to the smooth surface of the Hi-Nicalon-S fiber.....92

Figure 65 – SEM micrograph of the CVI-F composite after HF digestion showing attack on the matrix. Note the dense CVD layers and distinct SiC particulates remaining from the PIP/MI process.93

Figure 66 – Top: An SEM micrograph showing a Sylramic fiber after HF digestion with residual BN and dense CVD SiC. Middle: EDS maps for B (left) and N (right). Bottom: EDS maps for C (left) and Si (right).94

Figure 67 – Radar plot comparing relative hot corrosion between the MI-F and CVI-F coupons exposed at low (2.5 ppm) and high (1000 ppm) SO₂ levels.....96

Figure 68 – Macro photos of the burner rig coupons after exposure. Note that the leading edge of each coupon is presented on top. From top to bottom: MI-BR-24, CVI-BR-24, MI-BR-45, CVI-BR-45. All coupons measure approximately 10.8 cm x 1.25 cm.97

Figure 69 – Radar plot comparing relative hot corrosion between the MI-BR and CVI-BR coupons exposed for 24 and 45 hours..... 104

Figure 70 – Schematics showing the selective attack of the MI silicon. Top: SiC particulates are surrounded by MI Si. Middle: Silica scale grows on top, consuming Si first. Bottom: After HF digestion, voids left where MI Si was oxidized and removed..... 108

Figure 71 – SEM micrographs showing the difference in hot corrosion attack on Sylramic, Hi-Nicalon, and Hi-Nicalon-S fibers after corrosion products are removed. 110

Figure 72 – Plot of all NiO data points from this study in black along with the NiO summarized results from Gupta and Rapp. 117

Figure 73 – Plot of NiO data points from this study in black along with the summarized NiO results from Gupta and Rapp. The open circles indicate data points that were removed due to visible contamination with NiO powder..... 118

Figure 74 – Plot of NiO data points from this study in black along with the summarized NiO results from Gupta and Rapp. The open circles indicate data points that were removed since they were the first three samples collected in that batch and had not equilibrated yet. 119

Figure 75 – Plot of NiO data points from this study in black along with the summarized NiO results from Gupta and Rapp and the raw data from Gupta and Rapp. The data collected in this study have the same general trend as the Gupta and Rapp data but have more scatter. 120

Figure 76 – SiO₂ solubility data plotted as a function of Na₂O activity..... 122

Figure 77 – SiO ₂ solubility data plotted as a function of Na ₂ O activity. Open diamonds indicate averaged solubilities for a given run.....	123
Figure 78 – SiO ₂ solubility data plotted as a function of Na ₂ O activity. Open diamonds indicate averaged solubilities for a given run and the black line is a trend line fitted to the averaged data. The vertical dashed grey line is the predicted stability boundary between Na ₂ Si ₂ O ₅ and SiO ₂ + Na ₂ SO ₄	124
Figure 79 – SiO ₂ solubility data plotted as a function of Na ₂ O activity. Open diamonds indicate averaged solubilities for a given run and the black line is a trend line fitted to the averaged data. The open triangles are the data from Shi and Rapp and the horizontal dashed line is the average of that data. The vertical dashed grey line is the predicted stability boundary.....	126
Figure 80 – XRD pattern for one of the aluminoborate samples. All peaks not labeled as alumina peaks correspond with the 2:1 aluminoborate phase.....	127
Figure 81 – B ₂ O ₃ solubility data plotted as a function of Na ₂ O activity.....	129
Figure 82 – B ₂ O ₃ solubility data plotted as a function of Na ₂ O activity. The open circles are data that were removed due to B depletion or improper sampling.....	130
Figure 83 – B ₂ O ₃ solubility data plotted as a function of Na ₂ O activity. The black line is the trend line calculated from Equation 18 and fitted to the data.....	132
Figure 84 – Summary plot of the solubility of several oxides in molten Na ₂ SO ₄ at 900°C, existing data from Rapp ²³	138

List of Tables

Table 1 – Partial pressures of SO ₂ , SO ₃ , and O ₂ , as well as Na ₂ O activity at each experimental condition.	10
Table 2 – Solubility of compounds in the digestion solutions.	24
Table 3 – Descriptions and abbreviations for the composite materials used in Task 2.....	25
Table 4 – Selected information about the SiC fibers studied ⁷ , including their manufacturers, compositions, and descriptions.	26
Table 5 – Chemical compounds used in the electrochemical analysis.....	30
Table 6 – Averaged pitting data for uncoated CVD-SiC, uncoated Hexoloy, C-coated Hexoloy, and BN-coated Hexoloy coupons exposed for 24-hr at 1000°C.....	58
Table 7 – Possible rate-limiting steps for SiC hot corrosion.	73
Table 8 – Mass change values for the burner rig coupons. Mass change includes deposition of Na ₂ SO ₄ and growth of silicates. Surface area was assumed to be 6.84 cm ² for all coupons.....	103

1 Abstract

Hot corrosion behavior of $\text{SiC}_{\text{fiber}}/\text{BN}_{\text{interphase}}/\text{SiC}_{\text{matrix}}$ Ceramic Matrix Composites (CMCs) was investigated to better understand molten Na_2SO_4 deposit-induced degradation of this class of composites proposed for use in turbine engines operating in marine environments. Model materials were studied to isolate the CMC chemistry from the composite architecture. Model materials included additive-containing sintered- α SiC (Hexoloy), Chemical Vapor Deposited (CVD) SiC, and Si coupons. SiC coupons were studied in the uncoated condition, or with a C- or BN-coating to simulate the fiber/matrix interphase material. Coupons were loaded with 2.5 mg/cm^2 Na_2SO_4 and exposed in a tube furnace at temperatures between 900 and 1100°C, for times between 0.75 and 96 hours, in gas atmospheres containing either 2.5 or 1000 ppm SO_2/O_2 . Additionally, CMC materials were tested in the tube furnace by the same procedure as model materials and in a Mach 0.3 burner rig with salt injection to determine their hot corrosion resistance. The solubility of SiO_2 and B_2O_3 in molten Na_2SO_4 was explored at 900°C as a function of Na_2O activity using an electrochemical cell.

Specimens were characterized after hot corrosion using mass change measurements, scanning electron microscopy, energy dispersive x-ray spectroscopy, profilometry, and x-ray diffraction analysis. The elemental composition of the corrosion products was analyzed using inductively coupled plasma optical emission spectrometry after removal from specimens by stepwise digestion in water, HCl, and HF.

The presence of boron was found to have a negative impact on the hot corrosion resistance of the model materials and CMC coupons. CMC coupons exposed in the tube

furnace and the burner rig showed that a dense SiC matrix (from CVD and chemical vapor infiltration) is more resistant to hot corrosion while any chemical inhomogeneities or interfaces (from matrix processing by polymer infiltration and pyrolysis or melt infiltration) result in increased hot corrosion attack. The solubility of SiO₂ and B₂O₃ in molten Na₂SO₄ was determined over a range of SO₃ partial pressures. As the SO₃ partial pressure decreases, the solubility of B₂O₃ and SiO₂ is predicted to increase, indicating that low sulfur contents in fuels will lead to increased dissolution of silica or borosilicate scales grown on SiC.

2 Objectives

Turbine engines operating in environments that contain salt (such as marine environments) can form molten deposits on components leading to accelerated deposit-induced corrosion, or hot corrosion. This phenomenon has been extensively studied in the context of metallic alloy systems, however there has been a recent push to replace hot-section turbine engine metallic alloys with ceramic-based materials, in this case silicon carbide (SiC) ceramic matrix composites (CMCs). SiC-based composites offer the potential for increased efficiency through lower density, higher operating temperatures, and reduced cooling loads, but their hot corrosion performance is not well understood and is therefore an important area worth investigating if these materials are to be used in turbine engines.

The objectives of this work were to characterize the hot corrosion of SiC-based CMCs, and this work was broken into 3 tasks. In the first task model materials were used to isolate composite chemistry (SiC, Si, BN, C) from architecture. In the second task CMC materials were used to incorporate the architecture complexity. In the final task the solubility of SiO_2 and B_2O_3 in Na_2SO_4 was determined over a range of SO_3 partial pressures to understand how these oxides would be affected by hot corrosion, and to determine sulfur content guidelines for fuels to minimize the hot corrosion. These three tasks are described in more detail below.

2.1 Task 1 – Hot Corrosion of Model Materials

The objectives of this task were to firstly confirm the time dependence of SiC hot corrosion previously reported¹⁻⁵ and provide new results on the temperature dependence and pitting behavior. Model systems have been used here to isolate the effects of chemical

additions to SiC on hot corrosion. Exploring hot corrosion of these model systems allowed for data collection without the obfuscation of the complex CMC architecture. These results provided a baseline for exploring effects of C, BN, and Si on hot corrosion of SiC-based CMCs, and a greater insight into the chemistry of CMC hot corrosion.

2.2 Task 2 – Hot Corrosion of CMC Coupons

The goal of this task was to investigate the effects of complex composite architecture, including variable corrosion resistance of SiC fibers, interphases, and matrices produced by different processing routes (Chemical Vapor Infiltration [CVI], Polymer Infiltration and Pyrolysis [PIP], and silicon Melt Infiltration [MI]) on the high-temperature Na₂SO₄-assisted corrosion of SiC-based CMCs. The information gathered in Task 1 was used to isolate the architecture effects from the chemistry effects.

2.3 Task 3 – Solubility of Oxides in Sodium Sulfate

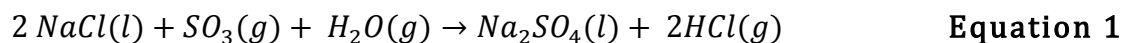
The goal of this task was to determine the solubility of SiO₂ and B₂O₃ in molten Na₂SO₄ over a range of Na₂O activities. These data were used to confirm the limited acidic solubility of SiO₂ as shown by Shi and Rapp⁶, to explore the basic dissolution of SiO₂ predicted by the equilibrium phase stability diagram, and to uncover the solubility behavior of B₂O₃ which had not yet been studied. The Na₂O activities where oxide dissolution occurs were then used to predict ranges of SO₃ partial pressures and S impurity levels found in combustion environments where hot corrosion of CMCs will occur.

3 Introduction

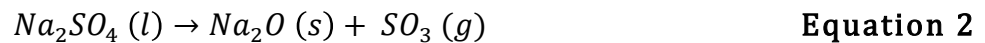
Molten salt deposits can form on turbine engine components when operated in marine environments leading to accelerated deposit-induced corrosion, or hot corrosion. This phenomenon has been extensively studied in the context of metallic alloy systems, however there has been a recent push to replace hot-section turbine engine metallic alloys with ceramic-based materials, such as silicon carbide (SiC) ceramic matrix composites (CMCs). SiC-based composites offer the potential for increased efficiency through lower density, higher operating temperatures, and reduced cooling loads, but their hot corrosion performance is not well studied. It is therefore critical to investigate the hot corrosion behavior of SiC-based materials if these materials are to be used in turbine engines.

In a SiC_{fiber}/SiC_{matrix} CMC there is a necessary interfacial layer between the fibers and the matrix that is applied as a coating on the fibers. The purpose of this coating is to prevent the fibers from bonding to the matrix and to allow fiber slip, or pullout, to lengthen crack propagation paths⁷. Graphite (or pyrocarbon) and boron nitride (BN) are the most commonly selected interphase materials due to their layered hexagonal crystal structures that allows for easy slip between the lattice planes⁸⁻¹⁰. Additionally, the matrix may contain B₄C added for oxidation protection or free silicon from the melt infiltration process⁹. All of these factors present a more complex chemistry for hot corrosion of SiC-based CMCs than SiC alone, and these chemistry effects will be investigated in this work.

In a turbine engine combustion environment, ingested NaCl combines with sulfur impurities in the fuel to create the stable salt Na₂SO₄ as shown in Equation 1.



Hot corrosion occurs at temperatures between the melting temperature of Na_2SO_4 (884°C) and the dew point of the salt, which is a function of $p\text{SO}_3$, Na concentration, and P_{atm} . The dew point of Na_2SO_4 increases with increasing pressure, so in a turbine engine salt deposition will occur at higher temperatures due to the higher pressures¹¹. The partial pressure of SO_3 in the gas atmosphere has a strong effect on $\text{Na}_2\text{SO}_4(l)$ induced hot corrosion as the activity of Na_2O is inversely proportional to the partial pressure of SO_3 as shown in Equation 2.



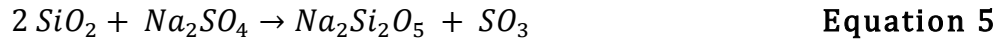
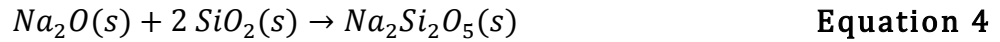
Using Lewis acid/base descriptions of oxides, a high activity of Na_2O is considered a basic melt, while a low Na_2O activity is considered acidic¹¹. This definition of acidic and basic melts is based on the acidity or basicity of the oxide species themselves. Flood and Förland¹² provide the following definition of basic and acidic oxides that is analogous to the definition of aqueous acids and bases:



From this definition Na_2O is a base and SO_3 is an acid as shown in Equation 2.

Previous work on the oxidation of monolithic SiC has shown that a protective silica (SiO_2) scale is formed at high temperatures in dry oxygen, but in atmospheres containing water-vapor (such as those found in a combustion environment) the volatile species $\text{Si}(\text{OH})_4$ is formed which leads to rapid degradation of the material under parabolic kinetics^{3, 13-15}. Additionally, it has been shown that SiC is susceptible to accelerated corrosion in the presence of molten salts^{1, 3, 11, 16} and salt vapor¹⁷⁻²⁰. In these environments the sodium-containing species Na_2O reacts with the silica scale to form a sodium silicate as

shown in Equation 4. Note that the reaction in Equation 4 can also be written in terms of Na_2SO_4 reacting and releasing SO_3 gas as shown in Equation 5.



This sodium silicate has a lower melting temperature (1088°C vs. 1723°C) and higher oxygen diffusivity^{21, 22} than silica, and is therefore expected to be less protective. The hot corrosion of SiC initiates very rapidly and begins to slow when a continuous silica layer forms at the substrate-scale interface¹. Under certain conditions, however, the silica scale can be attacked due to what is known as “fluxing”. Rapp^{23, 24} defines this fluxing as the dissolution of a protective oxide into a less protective species resulting in accelerated attack.

The dissolution of SiO_2 is predicted to occur when the Na_2O activity is high enough. A high SO_3 partial pressure prevents Equation 2 from going forward and makes dissolution of SiO_2 in Na_2SO_4 unfavorable²⁵. Figure 1 shows the calculated phase stability diagram for Na_2O and SiO_2 at 900°C with the basic end on the left (high Na_2O activity) and the acidic end (high SO_3 activity) on the right. This diagram predicts that SiO_2 will be insoluble in Na_2SO_4 at $a_{\text{Na}_2\text{O}} < 1 \times 10^{-11}$. At $a_{\text{Na}_2\text{O}} > 1 \times 10^{-11}$ sodium silicates are predicted to form. Therefore understanding the solubility of the protective silica layer over a range of Na_2O activities is important for determining the long-term stability of SiC CMCs in hot corrosion environments. The solubility of SiO_2 in molten Na_2SO_4 has been explored at 900°C by Shi and Rapp⁶ previously, however only at Na_2O activities between 1×10^{-11} and $1 \times 10^{-14.2}$. This leaves the basic side of the phase stability diagram (and the predicted dissolution of silica

as described in Equation 4) as yet uncharacterized. The phase stability diagram for Na_2O and SiO_2 at 1000°C is shown in Figure 2.

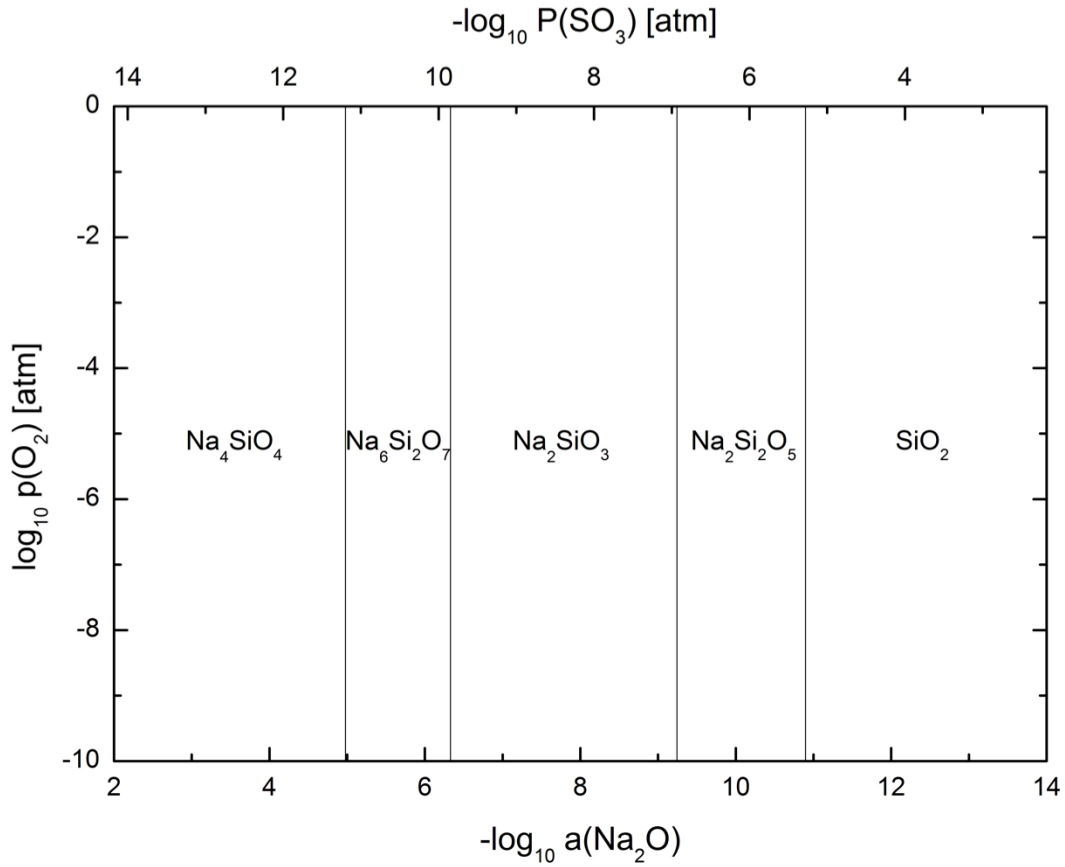


Figure 1 – Phase stability diagram for Na_2O and SiO_2 at 900°C with the basic end on the left and the acidic end on the right. All phases are predicted to be solid at 900°C .

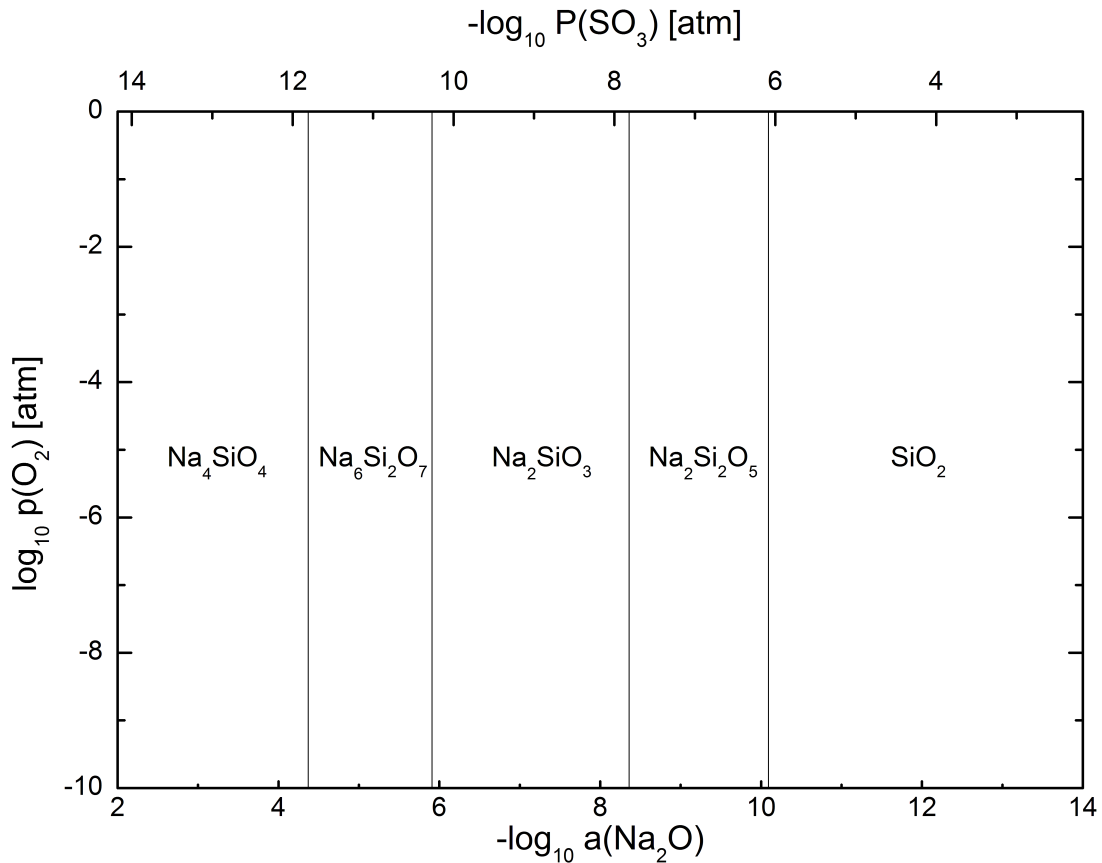
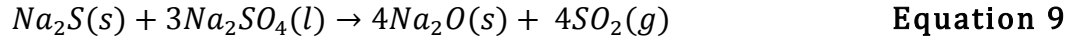


Figure 2 – Phase stability diagram for Na₂O and SiO₂ at 1000°C with the basic end on the left and the acidic end on the right. All phases are predicted to be solid at 1000°C.

Prior work on the effects of the carbon interphase on oxidation of SiC CMCs²⁶⁻²⁸ has shown that C is susceptible to rapid oxidation at temperatures as low as 500°C, leading to the formation of CO and CO₂ gas as shown in Equations 6 and 7 and the removal of the beneficial interphase.



When C interacts with a silica scale and the molten salt present in hot corrosion it raises the Na₂O activity in the melt^{2, 11, 14, 16} as shown in Equations 8 and 9, driving the reaction into a basic regime (according to Lewis acid/base concepts).



When carbon is located at the sample-scale interface (in the form of a carbon coating or carbon particulates in the material) a basic condition is created at the melt bottom (regardless of gas atmosphere) that can lead to the self-sustaining fluxing of the scale, as described by Jacobson¹¹.

Table 1 – Partial pressures of SO₂, SO₃, and O₂, as well as Na₂O activity at each experimental condition.

Exposure	Temperature	SO ₂ Concentration	P(SO ₂) [atm]	P(SO ₃) [atm]	P(O ₂) [atm]	a(Na ₂ O)
Furnace	900°C	1000 ppm	7.56x10 ⁻⁴	2.44x10 ⁻⁴	0.99	2.42x10 ⁻¹⁴
	950°C	1000 ppm	8.23x10 ⁻⁴	1.77x10 ⁻⁴	0.99	2.96x10 ⁻¹³
	1000°C	2.5 ppm	2.18x10 ⁻⁵	3.23x10 ⁻⁶	1.00	1.24x10 ⁻¹⁰
	1000°C	1000 ppm	8.71x10 ⁻⁴	1.29x10 ⁻⁴	0.99	3.10x10 ⁻¹²
	1050°C	1000 ppm	9.05x10 ⁻⁴	9.52x10 ⁻⁵	0.99	2.80x10 ⁻¹¹
	1100°C	1000 ppm	9.29x10 ⁻⁴	7.11x10 ⁻⁵	0.99	2.16x10 ⁻¹⁰
Solubility	900°C	1 ppm	7.56x10 ⁻⁷	2.44x10 ⁻⁷	1.00	2.42x10 ⁻¹¹
	900°C	2.5 ppm	1.89x10 ⁻⁶	6.11x10 ⁻⁷	1.00	9.68x10 ⁻¹²
	900°C	10 ppm	7.56x10 ⁻⁶	2.44x10 ⁻⁶	1.00	2.42x10 ⁻¹²
	900°C	25 ppm	1.89x10 ⁻⁵	6.11x10 ⁻⁶	1.00	9.68x10 ⁻¹³
	900°C	100 ppm	7.56x10 ⁻⁵	2.44x10 ⁻⁵	1.00	2.42x10 ⁻¹³
	900°C	250 ppm	1.89x10 ⁻⁴	6.11x10 ⁻⁵	1.00	9.68x10 ⁻¹⁴
	900°C	1000 ppm	7.56x10 ⁻⁴	2.44x10 ⁻⁴	0.99	2.42x10 ⁻¹⁴
	900°C	10,000 ppm	7.57x10 ⁻³	2.44x10 ⁻³	0.90	2.42x10 ⁻¹⁵
Burner Rig	950°C	15.6 ppm*	1.33x10 ⁻⁵	8.12x10 ⁻⁷	0.08	6.46x10 ⁻¹¹

*Measured S content in fuel

Previous work investigating the impact of BN on SiC CMC oxidation^{9, 10, 14, 29, 30} has shown that BN oxidizes to form boria (B₂O₃) which has a low melting temperature (450°C), is very unstable in water vapor (forming volatile oxy-hydroxides)²⁹, and mixes with the silica to form a borosilicate with a lower melting temperature and a greatly increased oxygen diffusivity^{31, 32}. The effects of BN on hot corrosion of SiC have not been studied.

The phase stability diagram for Na₂O and B₂O₃, shown in Figure 3, indicates that boria is predicted to be soluble in sodium sulfate under more acidic conditions (near an Na₂O activity of 1x10⁻¹⁵) than silica. Also, both boria and the predicted sodium borates are

liquid at 900°C, so their reactivity and rate of inward oxygen diffusion is likely to be higher. The phase stability diagram for Na₂O and B₂O₃ at 1000°C is shown in Figure 4. The dissolution of boria in Na₂O is shown in Equation 10. Note that the reaction in Equation 10 can also be written in terms of Na₂SO₄ reacting and releasing SO₃ gas as shown in Equation 11. As boron-containing compounds are present in SiC CMCs, it is of interest to explore the solubility of boria in molten sodium sulfate, however these data do not exist in the literature.

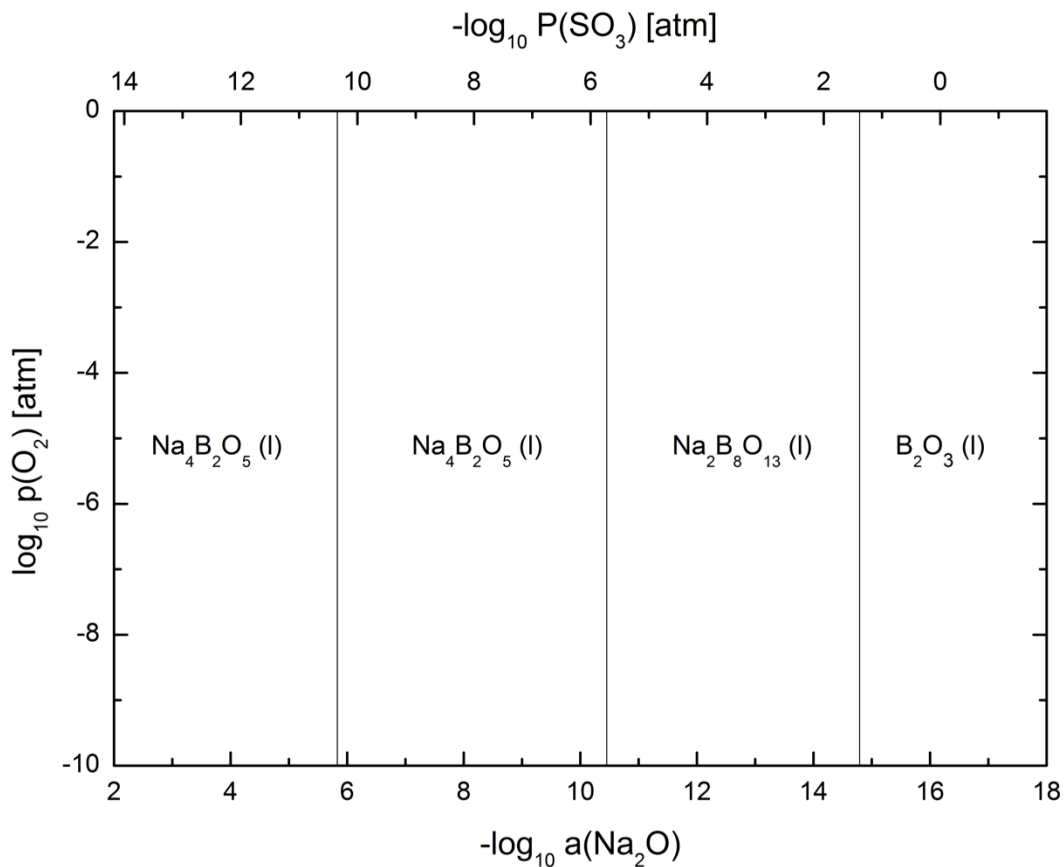
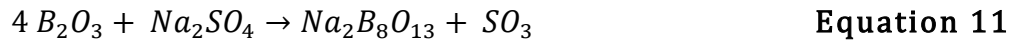
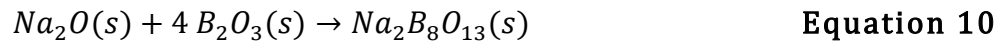


Figure 3 - Phase stability diagram for Na₂O and B₂O₃ at 900°C with the basic end on the left and the acidic end on the right. All phases are predicted to be liquid at 900°C.

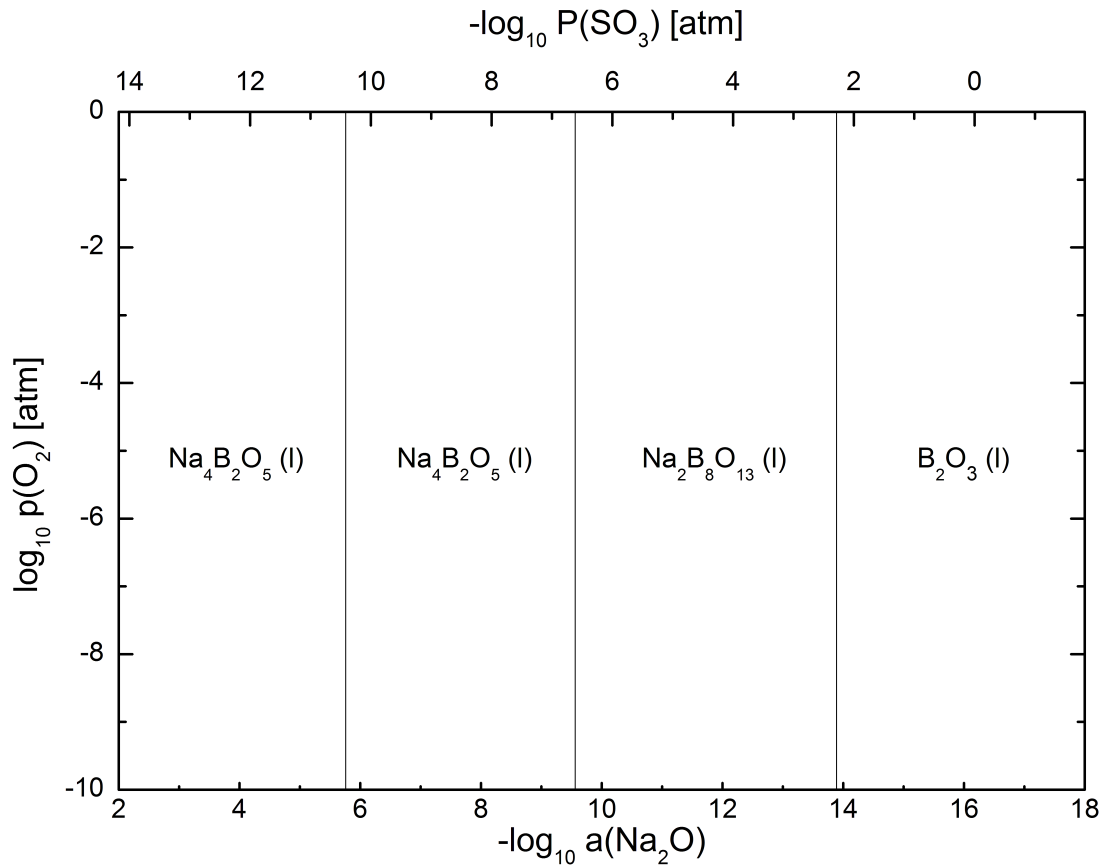


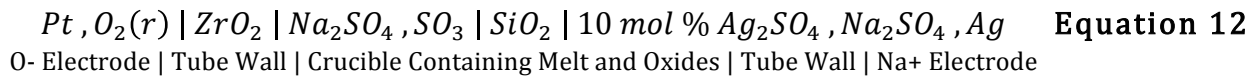
Figure 4 - Phase stability diagram for Na₂O and B₂O₃ at 1000°C with the basic end on the left and the acidic end on the right. All phases are predicted to be liquid at 1000°C.

It is worth noting that the stability diagrams shown are for equilibrium crystalline phases. In both systems, silicates and borates, the tendency is to form amorphous phases rather than crystalline ones. This is largely due to the sluggish kinetics associated with crystallizing the amorphous silicates³³ and borates³⁴. For this reason the stability diagrams are expected to act as a guideline for when dissolution is likely to begin, however rather than a crystalline phase with fixed stoichiometry there will likely be a compositional range of amorphous phases.

Molten Na₂SO₄ is an electrolyte, therefore, hot corrosion can be considered an electrochemical reaction, as suggested by Rapp²⁴. The Na₂O activity of a sodium sulfate

melt can be measured electrochemically using an appropriate cell. The Na₂O activity in the melt can be controlled by changing the pSO_3 in the gas atmosphere as described in Equation 2. The solubility of oxides in molten sodium sulfate can then be measured as a function of Na₂O activity in the melt. This technique allows quantification of oxide solubility as a function of Na₂O and SO₃ activities, which is important for predicting solubility of oxides experiencing hot corrosion.

Electrode cell considerations for measurement of Na₂O activity have been discussed by Watt, Andersen, and Rapp³⁵. The most useful cell arrangement for hot corrosion studies is shown in Equation 12. This cell arrangement is a modification of one proposed by Jacobson that substitutes fused quartz (SiO₂) for mullite³.



In this cell two reference electrodes are used, a ZrO₂ electrode and an Ag/Ag⁺ electrode. The ZrO₂ oxygen electrode consists of a closed-end stabilized zirconia tube which is platinized on the inside, a platinum lead wire which is kept in contact with the bottom of the sealed tube, and a type-R (Pt/Pt-10Rh) thermocouple for monitoring temperature. The oxygen partial pressure is controlled inside the electrode. The Ag/Ag⁺ Na⁺ electrode consists of a closed-end fused quartz tube which contains a solution of 10 mol-% Ag₂SO₄/Na₂SO₄ and a silver wire immersed in the solution. In the overall cell the zirconia tube acts as an oxygen ion conductor and the fused quartz tube acts as a sodium ion conductor. The potential between the electrodes, given by Equation 13, allows for measurement of the Na₂O activity in the melt. A derivation of Equation 13 is provided in Appendix A.

$$E_a = 1.498 + 0.116 \log a_{Na_2O} \quad \text{Equation 13}$$

The electrodes are submerged into a crucible containing molten sodium sulfate as well as a powder or pellets of the metal oxide to be dissolved. After an equilibration period the melt is sampled and analyzed using a chemical analysis technique to determine the concentration of metal dissolved in the salt. Several samples are taken over a range of Na_2O activities (as controlled by changing the partial pressure of SO_3 in the gas atmosphere). Previous work by Rapp et al.²³ has determined the solubility for several oxide species over a range of basicities relevant to hot corrosion of turbine alloys. Notably absent from these results are the previously mentioned basic dissolution of SiO_2 and any data on the solubility of B_2O_3 . A summary plot of these results from Rapp²³ is shown in Figure 5. On this plot the silica solubility line is independent of Na_2O activity over the acidic range studied by Rapp as silica forms no known sulfate species and therefore has no acidic dissolution leg. This behavior is expected for boria as well as it has no known sulfate species.

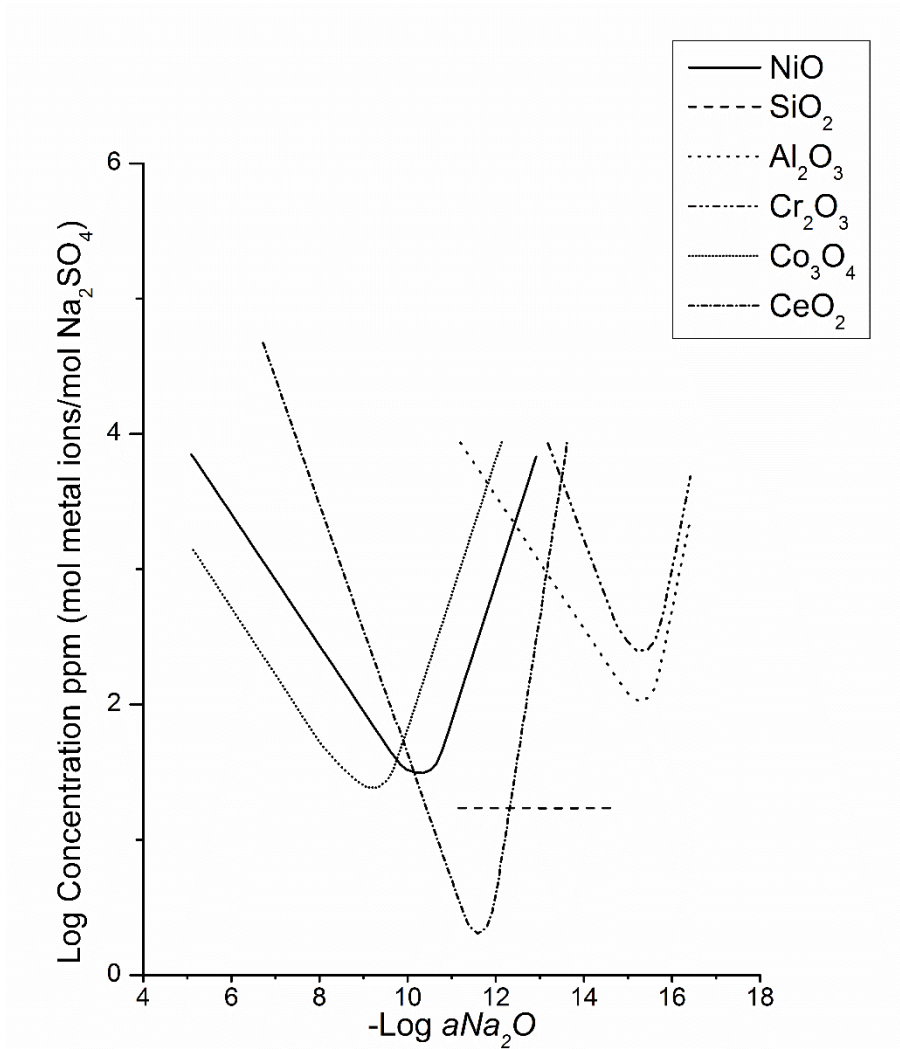


Figure 5 – Compilation of measured solubilities for several oxides in fused pure Na_2SO_4 at 1200 K, recreated from Rapp²³.

Oxidation and hot corrosion behavior of CMCs cannot easily be predicted by considering only effects of the constituent chemistries as the overall architecture of the composite plays a role as well. The oxidation performance of SiC/SiC as well as carbon fiber reinforced SiC CMCs^{26–28, 36–40} has been characterized. It has been shown that in the case of oxidation in dry air or oxygen the presence of B-bearing species can be beneficial since the B generates a low melting point, low viscosity B_2O_3 -containing glass that seals the composite and protects it from further oxidation⁹. Additionally, some work has

characterized the degradation of CMCs in combustion environments^{28, 39, 41}, while other studies have explored the effects of interphase thickness as it relates to oxidation performance^{26, 27, 42}.

The relative stability of oxidation products can be predicted based on the Ellingham diagram provided in Figure 6, which was calculated using FactSage⁴³. This diagram predicts that at temperatures between 900 and 1100°C chemical species such as Si, B, B₄C, and TiB₂ will oxidize before SiC, and that BN and C should remain stable when located near SiC which will act as an oxygen getter. This work will relate phase assemblages experimentally observed after hot corrosion to the relative stability of composite constituents depicted in the Ellingham Diagram.

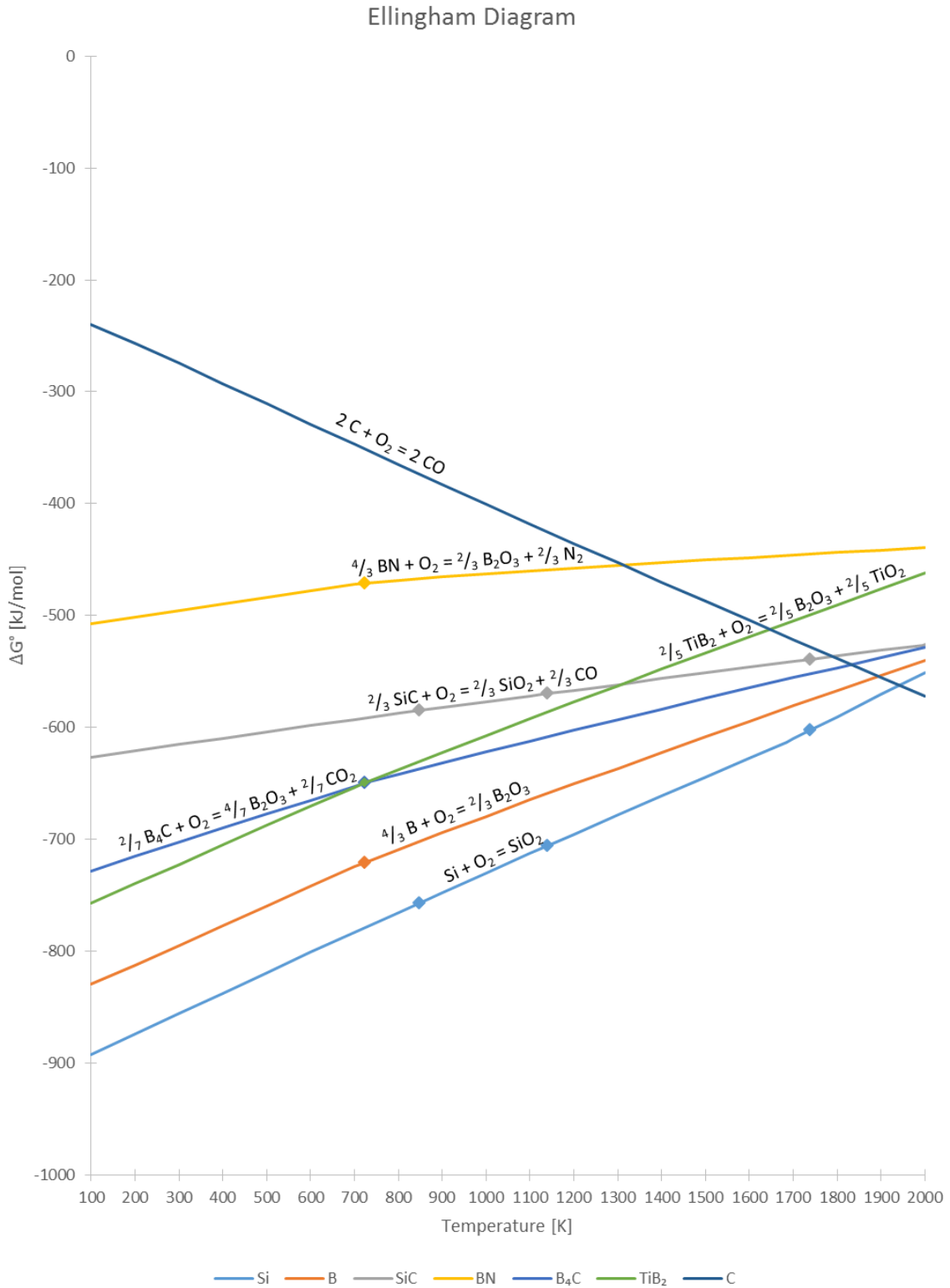


Figure 6 - Ellingham diagram showing relative thermodynamic stability of composite constituents toward oxidation.

Very little work on the hot corrosion of SiC/SiC CMCs was found. The most relevant SiC/SiC CMC hot corrosion studies available in the literature have evaluated changes in composite properties after exposure to sodium sulfate and Calcium-Magnesium-Alumino-Silicate (CMAS)^{17, 44, 45}. Work by Faucett and Choi⁴⁴ characterized SiC/SiC CMCs based on Sylramic and Hi-Nicalon fibers with melt infiltrated (MI) matrices exposed at 1200°C. Their work showed that irrespective of fiber type there was greater strength degradation when the CMCs were exposed to CMAS and molten Na₂SO₄ rather than just CMAS. Wu et. al.¹⁷ investigated the hot corrosion of SiC/SiC CMCs based on Hi-Nicalon fibers with Chemical Vapor Infiltrated (CVI) matrices at temperatures between 1000 and 1500°C. Rather than using a molten salt deposit Wu et. al. used Na₂SO₄ vapor that was evaporated from a crucible upstream and carried to the samples in a combined oxygen, argon, water vapor gas stream. Their results showed that below 1200°C the presence of water vapor dominated the corrosion and mass loss of the composites. Lowden and James⁴⁵ studied SiC/SiC composites based on Nicalon fibers with carbon interphase coatings and CVI matrices exposed for 100-hr at 1000°C in a burner rig. The combustion environment contained both a sulfur-bearing gas (H₂S) and a sodium source (Na₂CO₃ salt in a boat upstream), creating the most accurate hot corrosion environment of the studies found. Lowden and James observed that when a protective seal coat was not present, Na was found at the fiber-matrix interface throughout the composite, S was found in localized regions of the fiber-matrix interface, and corrosion rates were much more severe with either Na or S present. A detailed mechanistic understanding of the role of both composite chemistry and architecture on CMC hot corrosion is lacking, however.

In operation, CMCs will require the use of an environmental barrier coating (EBC) for protection from water vapor in a combustion environment^{14, 46, 47}. EBCs are typically refractory oxides, including silicates^{14, 46, 47}. Interactions between molten Na₂SO₄ and EBCs are important as the EBC will be the first material to come into contact with the molten salt, however, these interactions are outside the scope of this work. Instead this work focuses on understanding the hot corrosion mechanisms of the underlying composite that must be understood in the case of a coating failure.

4 Experimental Procedures

4.1 Task 1 – Hot Corrosion of Model Materials

Two varieties of silicon carbide were used as substrate materials: pure SiC (>99.9995%) made via Chemical Vapor Deposition (CVD) (Pure SiC LR, CoorsTek, Golden, CO) and a commercial sintered- α SiC product, Hexoloy (Hexoloy SA, Saint-Gobain, Niagara Falls, NY). Pure CVD-SiC was chosen as it is the best material for a model system looking at ideal conditions (corrosion of SiC) and is representative of CVI-SiC present in CMCs as protective layers on coated fibers, CVI matrix, and the seal coat on some CMCs. The Hexoloy material was chosen because it has sintering aids (B- and C-based) and its compositional inhomogeneity is more representative of the matrix material chemistry found in some CMCs^{48, 49}. Si substrates (10x10mm diced wafer, Ted Pella, Redding, CA) were used as a model material for the residual silicon from the melt-infiltration process.

SiC materials were cut into coupons measuring 12.5mm (0.5") x 12.5mm (0.5") x 3.2mm (0.125") and were used with the as-received (machined) surface finish. A selection of coupons was coated with either C or BN at a thickness of approximately 700nm. Coatings were prepared using PVD techniques by Laurie Dudek at Case Western Reserve University, and coating thicknesses and chemistry were quantified using Auger depth profiling (Evans Analytical Group, East Windsor, NJ).

Samples were weighed on an analytical balance (MS105DU, Mettler Toledo, Columbus, OH) with 0.01mg resolution. Na₂SO₄ was dissolved in de-ionized water (18.2 M Ω) and dropped onto the top face of the sample. Samples were placed into a convection oven at 120°C until the water had evaporated (\approx 5 min). Samples were weighed again to

ensure sufficient loading, and additional salt was added if needed. Samples were loaded with approximately 2.5 mg/cm² Na₂SO₄. An image of a salt-loaded coupon is shown in Figure 7.

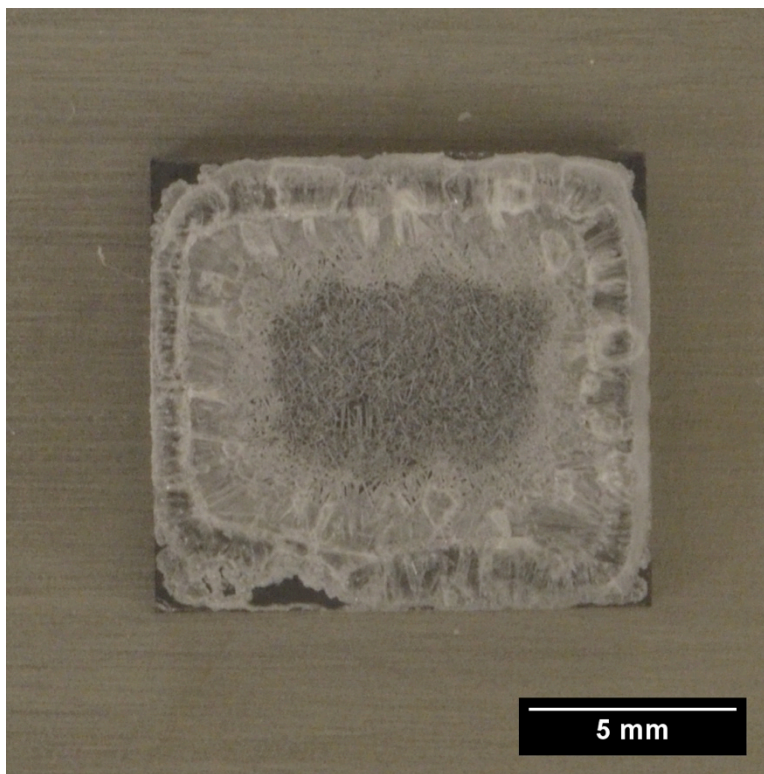


Figure 7 – Image of a coupon loaded with approximately 2.5 mg/cm² Na₂SO₄.

Hot corrosion exposures were performed in a single-zone horizontal tube furnace (GSL-1100X, MTI Corporation, Richmond, CA) with a 50mm OD fused quartz tube (Quartz Scientific, Harbor, OH). Temperatures were calibrated and monitored during exposure using an in-tube type-R thermocouple connected to an external reader. The furnace tube ends were terminated with stainless steel end-caps containing gas fittings and a sealed port for thermocouple access. Exhaust gas flowed through a gas wash bottle containing water. Samples were loaded onto a custom sample carrier constructed of Pt-Rh wire wrapped around an alumina boat to suspend the coupons in the gas flow and off the bottom of the boat. The loaded sample carrier, shown in Figure 8, was placed into the furnace prior to

Experimental Procedures – Task 1 – Hot Corrosion of Model Materials 21

heating, and samples were present in the hot zone of the furnace during heating and cooling.

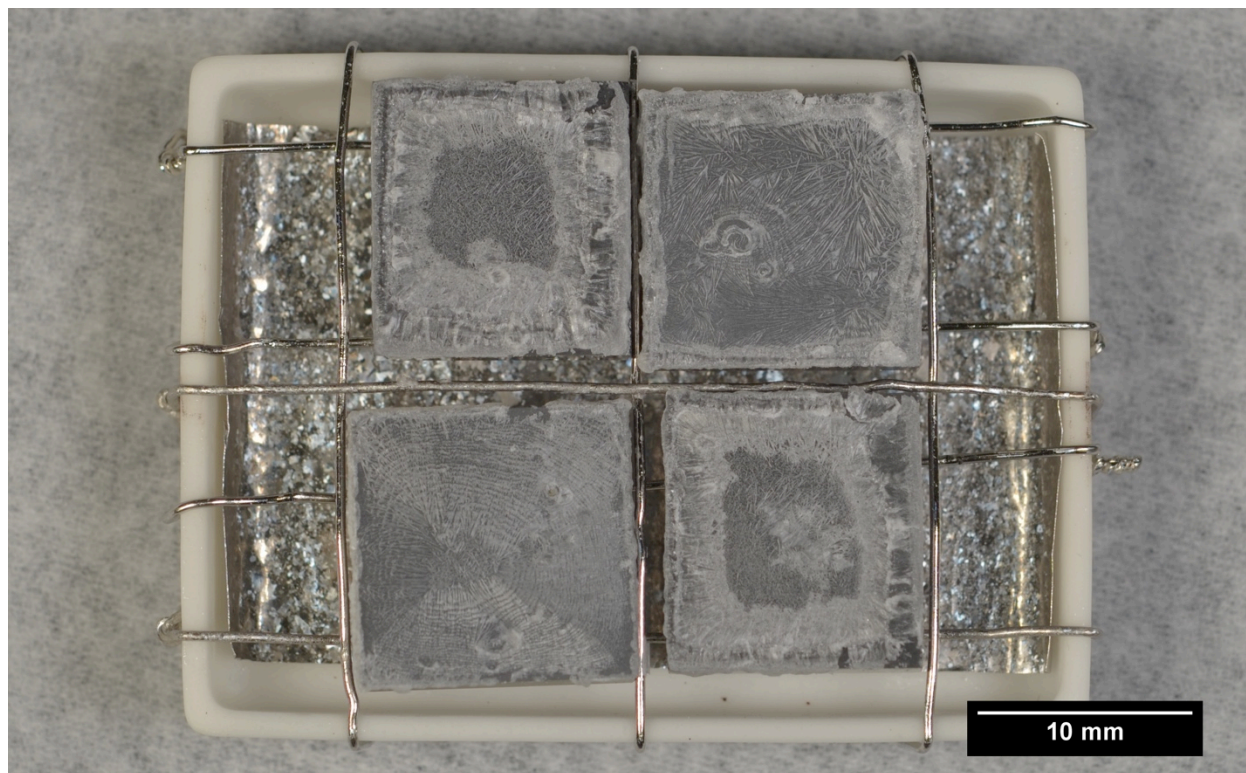


Figure 8 - Loaded sample carrier (with 4 samples) before being placed into furnace.

During heating and cooling at approximately 50°C/min the samples were exposed to a 100 sccm dry oxygen atmosphere (Model 1179 Mass Flow Controller, MKS Instruments, Andover, MA). Once samples were within 90% of the final isothermal temperature the gas was switched to the experimental gas (either 1000 ppm SO₂/O₂ or 2.5 ppm SO₂/O₂), also at 100 sccm. Gas was switched 4 min early to allow time for the gas to make its way through the system and to the samples. All gasses were run through a bed of anhydrous calcium sulfate to remove moisture. A platinized alumina catalyst was used initially to help ensure equilibrium between SO₂ and SO₃, however it was found that there was no difference in corrosion results without the catalyst (likely due to the rapid kinetics of SO₂/SO₃ equilibrium at such temperatures) so its use was discontinued.

Samples were exposed to temperatures of 900, 950, 1000, 1050, and 1100°C. 900°C was chosen as a low-end temperature as the melting point of Na₂SO₄ is 884°C. 1100°C was chosen as an upper limit since the dew point of Na₂SO₄ at 1 atm is around 1150°C (though it depends on the both partial pressure of SO₃ and the concentration of Na^{25, 50}) as well as to reduce load on the tube furnace.

Samples were exposed for times of 45 min, 3 hours, 6 hours, 24 hours, 48 hours, and 96 hours. Volatility of Na₂SO₄ was a concern so a set of samples was also exposed for 48 hours with cooling and re-application of salt followed by an additional 48 hour exposure for comparison to the 96 hour exposure.

The chemistry of the corrosion products formed on the sample surface was characterized using a step-wise digestion for Inductively Coupled Plasma Optical Emission Spectrometer (ICP-OES) analysis similar to the technique reported by Jacobson¹. Samples were first placed into 10ml of water for a minimum of 48 hours in a heated water bath at 35°C as sodium sulfate and sodium-rich silicates are soluble in water^{1, 51, 52}. After H₂O digestion, samples were removed, dried, weighed, and photographed. The digestion solution was retained for analysis. The digestion process was repeated using HCl and then HF for a total of three digestion steps. As shown in Table 2, HF removes silica and silicates from SiC¹, but the intermediate HCl step was added to try to selectively dissolve sodium silicates that are insoluble in water. Analysis was performed on the digestion solutions using an ICP-OES (iCAP 6200, Thermo Scientific, Waltham, MA) where a minimum of two peaks were used for each element (B, Na, S, Si) and three replicates of each sample were collected and averaged. Samples were weighed at each step in the digestion process (after exposure and after each ICP-OES digestion step).

Table 2 – Solubility of compounds in the digestion solutions.

Compound	H ₂ O	HCl	HF
Na ₂ SO ₄	Soluble	Soluble	Soluble
Na-Rich Silicates	Partially Soluble	Soluble	Soluble
Na-Lean Silicates	Insoluble	Partially Soluble	Soluble
SiO ₂	Insoluble	Insoluble	Soluble
B ₂ O ₃	Soluble	Soluble	Soluble
SiC	Insoluble	Insoluble	Insoluble

Sample microstructures were characterized using an SEM (Quanta 650, FEI Company, Hillsboro, OR) with a silicon-drift EDS detector (X-Max 150, Oxford Instruments, Abingdon, England). For large samples, multiple SEM micrographs were stitched together using the stitching plugin⁵³ contained within FIJI⁵⁴. Cross-sections were mounted in epoxy and diamond polished to a 1- μ m finish. Ethylene glycol was used as the polishing lubricant and 200-proof ethyl alcohol was used as the cleaning agent to minimize loss of water-soluble products.

Sample pitting data were collected using an optical profilometer (NewView 7300, Zygo Corporation, Middlefield, CT) at four locations on each sample. The data were then edited using MountainsMap (Digital Surf, Besançon, France) to generate topographical maps and calculate pitting statistics. Pits had to be wider than 5 microns to be analyzed. The pit depth was calculated by creating an averaged plane across the top of the sample, and only pits deeper than 2.5 microns past this plane (or about 5 microns deeper than the highest point) were measured. This software was also used to calculate surface roughness values from the profilometry data.

X-ray diffraction data was collected on selected specimens using a diffractometer (X'pert, PANalytical, Almelo, The Netherlands) with Cu K α radiation over a 2 θ range of 10-100°. Pattern analysis was done using HighScore Plus (PANalytical).

4.2 Task 2 – Hot Corrosion of CMC Coupons

Two varieties of ceramic matrix composite were used for the furnace exposures in this task, however due to proprietary restrictions relating to one of the materials only one CMC variety will be shown and described in detail. One composite used Sylramic fibers and the other used Hi-Nicalon Type S fiber. The CMC materials have been given abbreviated names based on their matrix and the type of exposure they were subjected to in this work, and those are provided in Table 3. Table 4 shows the composition of the fibers used in these composites^{55, 56}. Both CMCs had a BN interphase and a SiC matrix. Processing information was not available for either of the composites, so the materials were characterized to provide baseline microstructures and establish likely matrix processing routes. The Sylramic composite was made by weaving SiC fiber tows in a 2x2 twill pattern. The matrix was likely processed by Chemical Vapor Infiltration (CVI), followed by Polymer Infiltration and Pyrolysis (PIP) with SiC particulates, and finally silicon Melt Infiltration (MI). The CMC materials were cut into coupons measuring approximately 10mm x 10mm x 3mm. Samples were then ground using diamond polishing supplies to remove the protective SiC seal coat for exposure of both fibers and matrix to hot corrosion.

Table 3 – Descriptions and abbreviations for the composite materials used in Task 2.

Abbreviation	Fiber Type	Matrix Processing Route	Exposure Type	Vintage
CVI-F	Sylramic	CVI/PIP/MI	Furnace	2001
MI-F	Hi-Nicalon-S	MI	Furnace	2011
CVI-BR	Hi-Nicalon-S	CVI	Burner Rig	Unknown
MI-BR	Hi-Nicalon	MI	Burner Rig	Unknown

Table 4 – Selected information about the SiC fibers studied⁷, including their manufacturers, compositions, and descriptions.

Fiber	Manufacturer	Elemental Composition [wt %]	Description
Hi-Nicalon	Nippon-Carbon	62 Si + 37 C + 0.5 O	Low Oxygen
Hi-Nicalon S	Nippon-Carbon	69 Si + 31 C + 0.2 O	Low Oxygen, Stoichiometric
Sylramic	COI Ceramics	67 Si + 29 C + 2.3 B + 2.1 Ti + 0.8 O + 0.4 N	Low Oxygen, Stoichiometric

Samples were exposed in a tube furnace using the same experimental procedure as in Task 1, however the coupons were only exposed at 1000°C for 24 hours.

In addition to the furnace exposures two other varieties of SiC/SiC CMC were exposed in the Mach 0.3 burner rig at NASA-Glenn Research Center⁵⁷. One CMC contained Hi-Nicalon Type S fibers in a SiC matrix processed primarily by CVI and the other contained Hi-Nicalon fibers in a matrix processed primarily by MI. As with the other CMC materials in this study, detailed processing information was not available, so the baseline microstructure and likely processing routes were determined from microscopy of the composites. As can be seen in Figure 9 the CVI-SiC coupons have a matte, dark grey appearance while the MI-SiC coupons have a shiny silver appearance.



Figure 9 – CMC coupons for burner rig exposure. Top coupon is CVI-SiC and bottom is MI-SiC. Both coupons measure approximately 1.25 cm x 0.3 cm x 11 cm.

The burner rig coupons were cut from larger samples to a final dimension of approximately 1.25 cm x 0.5 cm x 11 cm. This machining step left one edge of each coupon as-cut without any protective seal-coat. The coupons were placed into the burner rig with the cut edge as the leading edge, as shown in Figure 10, to accelerate hot corrosion rates

with the goal of establishing the hot corrosion mechanism. Burner rig exposures were conducted at approximately 950°C (as monitored by a pyrometer). The fuel burned was JP-8 with approximately 15.6ppm sulfur content according to chemical analysis carried out at NASA. Water containing 8ppm Na₂SO₄ was injected into the burner rig at 22 cc/hr.

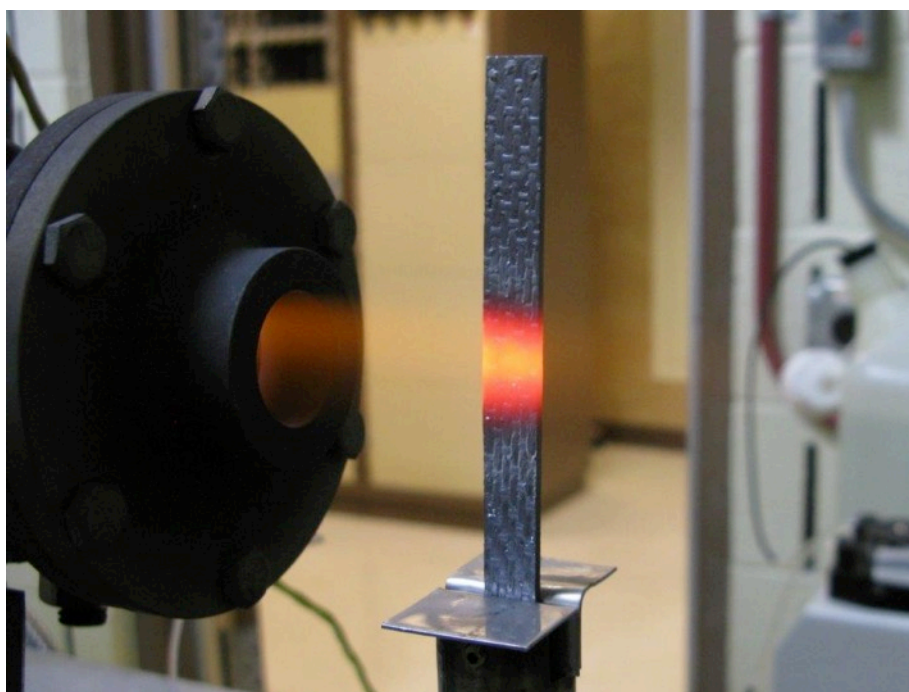


Figure 10 – SiC CMC coupon loaded into Mach 0.3 burner rig at 950°C with cut edge as leading edge. Orange color is due to the sodium from the injected 8ppm Na₂SO₄ solution.

Burner rig coupons were imaged in the SEM after corrosion to characterize the corrosion products formed on the sample. After this analysis the coupons were each cut in half on a low-speed diamond saw without lubrication to preserve as much corrosion product as possible and avoid saturating the CMCs with any cutting fluid. One half of each coupon was mounted in epoxy for cross sectioning. Samples were cut to produce two cross-sections near the original mid-point of the coupons and one section from the end of the samples outside the impingement area from the burner rig for comparison, as shown in Figure 11.

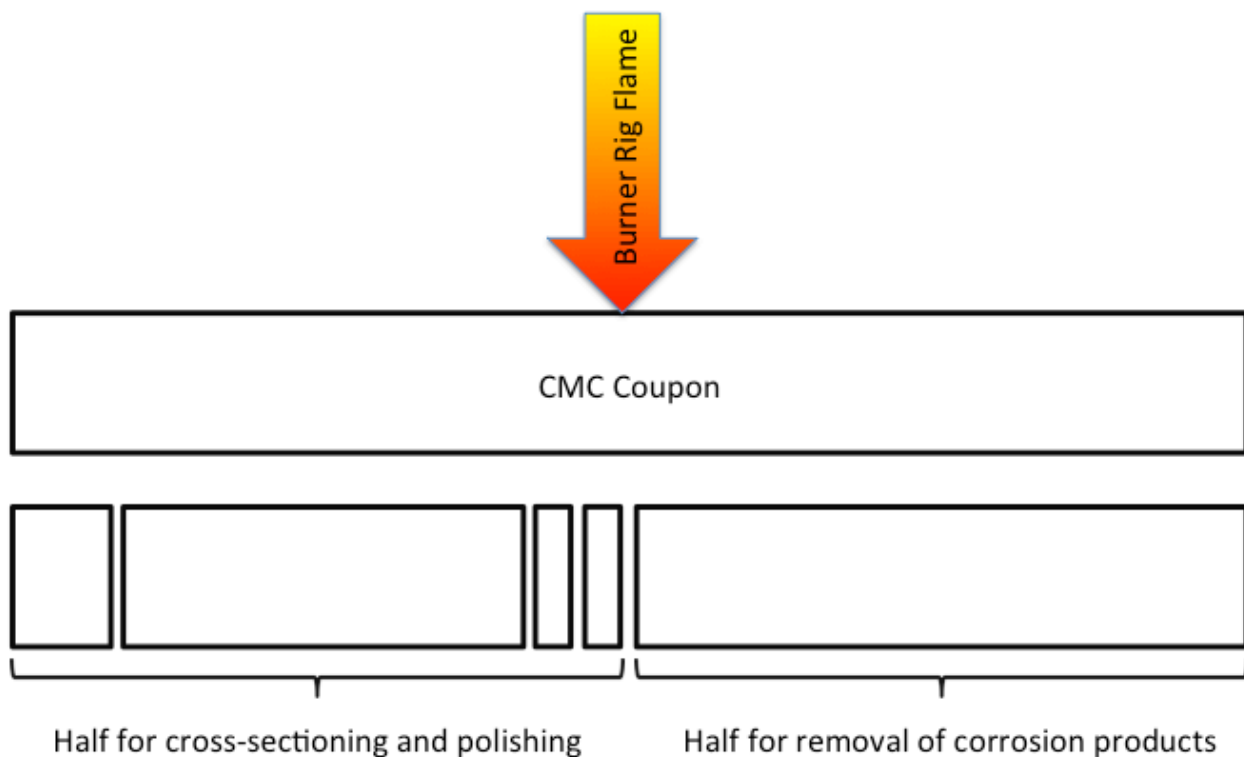


Figure 11 – Schematic of the sectioning plan for the burner rig coupons.

These cross-sections were re-mounted in epoxy and polished to a 1 μm finish using diamond supplies, ethylene glycol, and 200-proof ethanol as before. The other half of each coupon was subjected to a stepwise water and HF digestion similar to before (excluding the HCl step) with SEM characterization after each solution.

4.3 Task 3 – Solubility of Oxides in Sodium Sulfate

A single-zone vertical tube furnace (GSL-1100X, MTI Corporation, Richmond, CA) was used for the oxide solubility experiments. A 2" mullite tube (CoorsTek, Golden, CO) with one rounded closed bottom end was used as the primary furnace tube to contain the electrochemical setup. The tube was terminated and sealed at the top with a stainless steel end-cap. As shown in Figure 12, the end cap contained a $\frac{1}{4}$ " gas fitting to allow inlet and exhaust of gas, two $\frac{1}{4}$ " vacuum fittings for the sodium electrode and sampling/addition

tube, and one 3/8" vacuum fitting for the oxygen electrode. The gas flow was established by a concentric tee fitting inlet/outlet setup constructed using Ni-alloy tubing (alloy 600 selected for high-temperature corrosion resistance) within the furnace tube. The sampling/addition tube (to be inserted in the empty vacuum fitting in the isometric view in Figure 12) was a 1/4" diameter single bore alumina tube (CoorsTek, Golden, CO) which was terminated outside the furnace with a removable closed-end vacuum fitting.

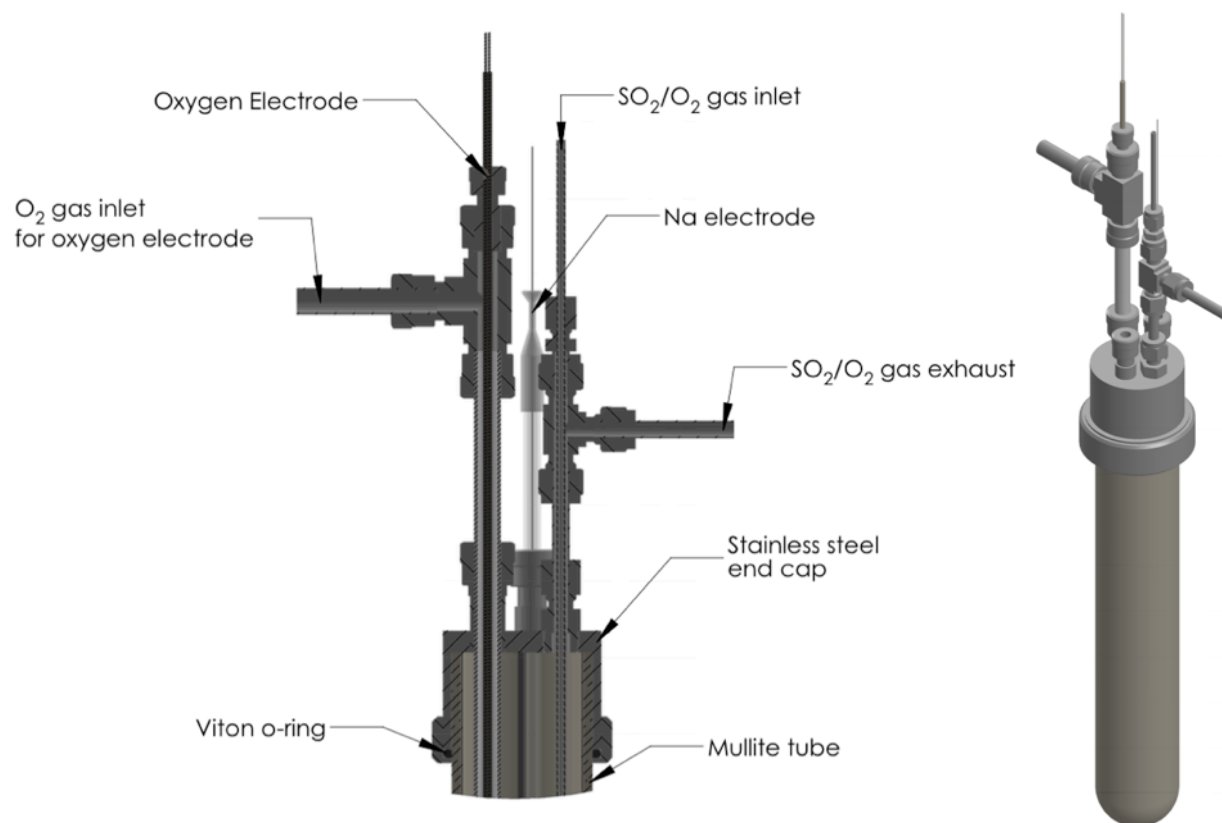


Figure 12 – Cutaway schematic of the end cap assembly on the left showing the location and configuration of electrodes and components. The right schematic is an isometric view of the whole end cap and furnace tube assembly.

The sodium electrode, shown in Figure 13, was constructed out of a 1/4" fused quartz tube (Arklay S. Richards, Newton Highlands, MA) with one rounded closed bottom end. Inside the sodium electrode a short (5-7 cm) silver wire (1 mm diameter) was attached (via spot welding or folding/crimping) to a long (45 cm) platinum wire lead that exited the top

Experimental Procedures – Task 3 – Solubility of Oxides in Sodium Sulfate 29

of the fused quartz tube, leaving the silver wire suspended at the bottom of the tube. The electrode was filled with approximately 300 mg of a mixture of 90 mole % Na_2SO_4 and 10 mole % Ag_2SO_4 . The chemicals used in the sodium electrode, as well as the rest of the chemicals used in Task 3, are described in Table 5. The top of the fused quartz tube was sealed with a short section of Tygon tubing and a tube clamp, which allowed the platinum lead wire to exit while sealing the fused quartz tube, limiting volatility of sodium sulfate.

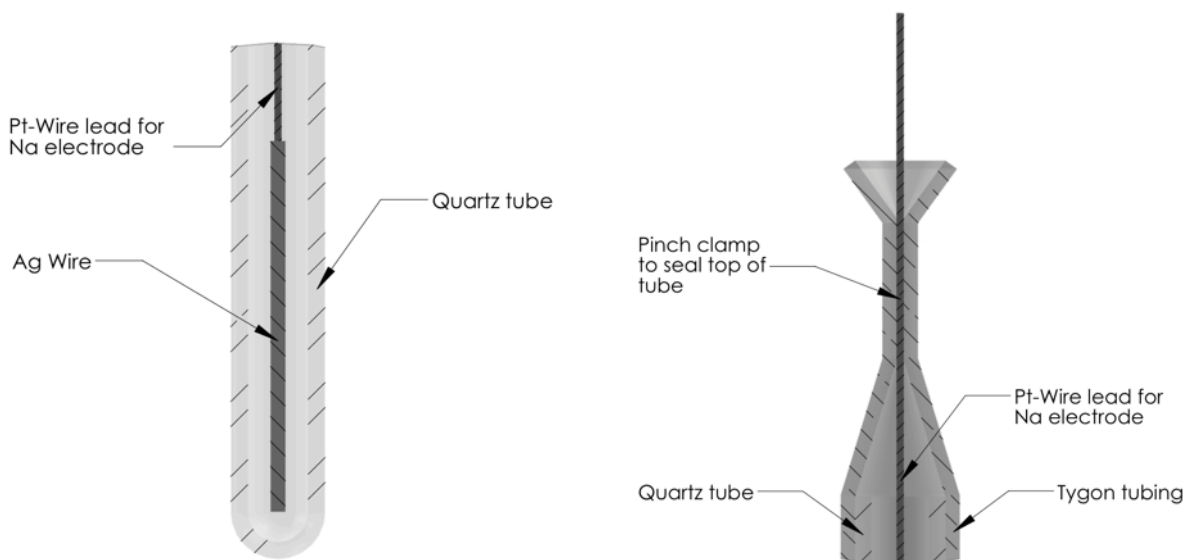


Figure 13 - Cutaway schematic of the closed end of the sodium electrode on the left and the top of the electrode on the right showing arrangement of the components.

Table 5 - Chemical compounds used in the electrochemical analysis.

Compound	Purity	Description	Vendor
Ag_2SO_4	99.99%	Fine powder	Sigma Aldrich
Al_2O_3	99.9%	1 μm APS powder, α -phase	Alfa-Aesar
B_2O_3	99.98%	Boric Anhydride, fine powder	Sigma Aldrich
Na_2SO_4	99.0%	Anhydrous, granular	Sigma Aldrich
NiO	99.999%	Fine powder	Sigma Aldrich
SiO_2	99.9%	Granular, 4-20 mesh, fused quartz	Sigma Aldrich
Na_2O_2	97%	Granular, +140 mesh	Sigma Aldrich

The oxygen electrode, shown in Figure 14, was constructed of a 3/8" OD (1/4" ID) yttria-stabilized zirconia (YSZ) tube (McDanel Ceramics, Beaver Falls, PA) with one

rounded closed bottom end. The interior of the closed end of the oxygen electrode was painted with platinum paint (CL11-5349, Heraeus, West Conshohocken, PA) then heat treated according to the manufacturers recommendations to cure the coating. This heat treatment involved a drying step at 100°C for 1 hour followed by a firing step at 950°C for 2 hours. A 4-bore alumina tube measuring 1/8" in diameter was placed inside the zirconia tube to carry both legs of a type-R thermocouple as well as a platinum wire lead that was placed in contact with the platinized area inside the end of the zirconia tube. The gas atmosphere inside the oxygen electrode was fixed by flowing 25 sccm (Model 1179 Mass Flow Controller, MKS Instruments, Andover, MA) of pure O₂ through a concentric tee fitting that exhausted through the 4-bore alumina tube.

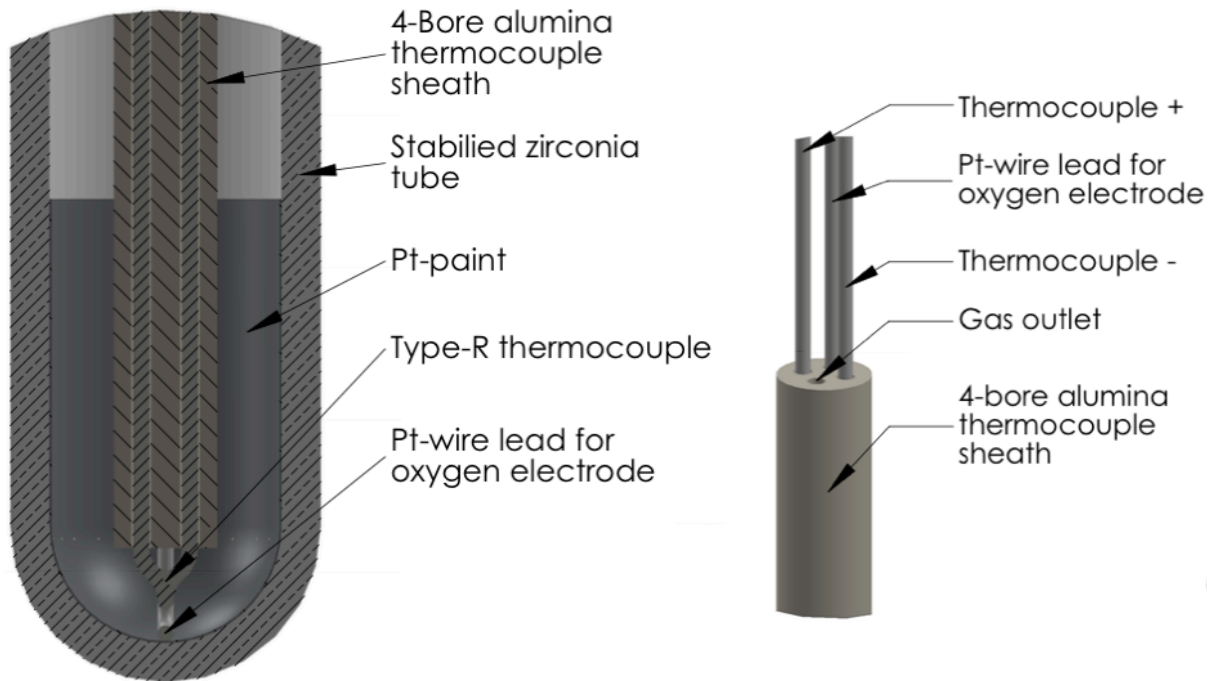


Figure 14 – Cutaway schematic of the closed end of the oxygen electrode on the left and the top of the 4-bore alumina sheath on the right showing arrangement of the components.

The sample melt was contained inside a cylindrical 40 mm OD (approximately 36 mm ID) flat-end alumina crucible measuring 165 mm tall (CoorsTek, Golden, CO). The crucible was initially supported by a cage structure attached to the end cap and constructed of nickel alloy as shown in Figure 15. This support cage was abandoned as it was found that the combination of small dimensions needed to fit inside the furnace tube and corrosive environment led to rapid failure of the alloy. Instead, the crucible was supported by filling the closed end of the furnace tube with alumina polishing powder (Buehler, Lake Bluff, IL). The volume of powder was chosen so that the melt within the crucible would be positioned within the hot zone of the furnace (3 cm length within 1° C). A 4-legged section of platinum wire was used to facilitate insertion and removal of the crucible. The crucible was filled with approximately 20 grams of Na₂SO₄ and

approximately 5 grams of the relevant oxide of interest. Once the crucible was inserted and the furnace was assembled the sample was heated to 200°C for 120 minutes while flowing dry argon through the furnace to drive off moisture. After this drying step the furnace was heated to 900°C and the gas was switched to the relevant SO₂/O₂ mixture. 900°C is a practical upper limit for this electrochemical cell as the melting point of the silver wire is 962°C. Temperatures were calibrated and monitored during exposure using the type-R thermocouple inside the oxygen sensor that was connected to an external reader.

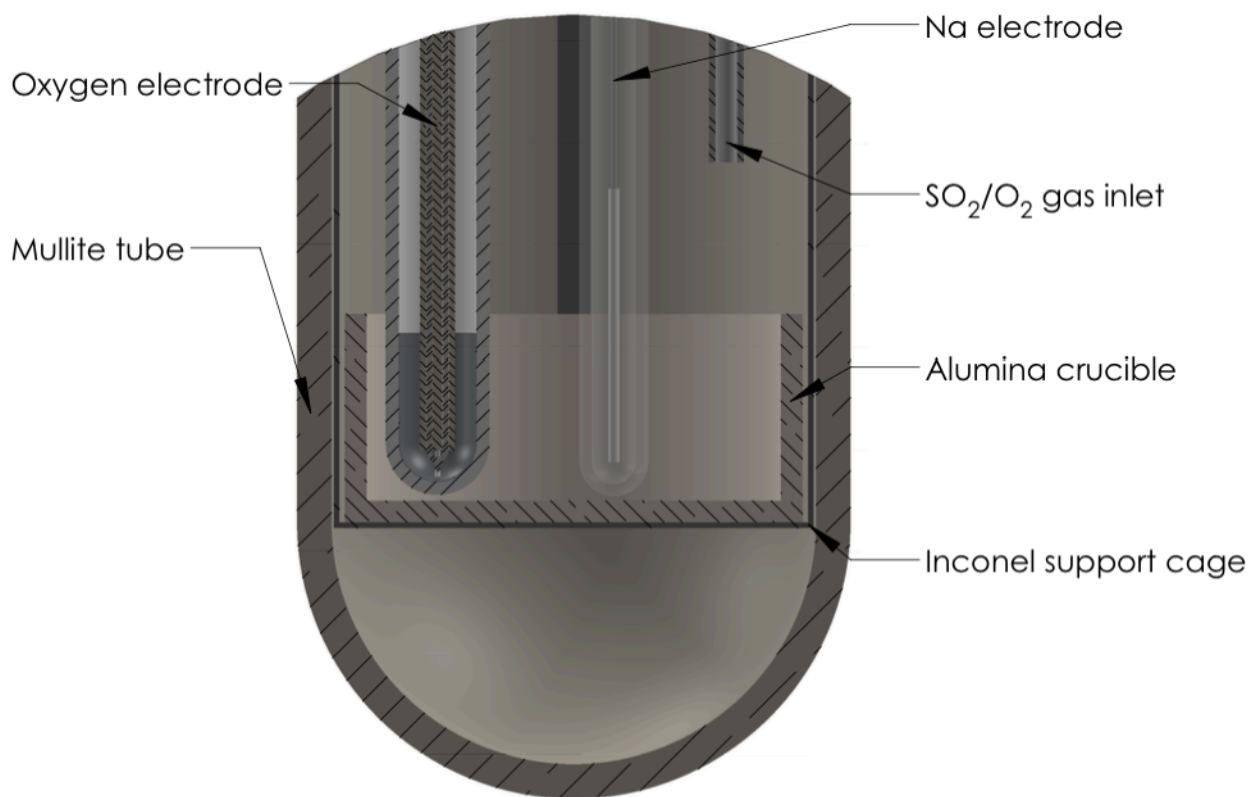


Figure 15 – Cutaway schematic of the bottom of the furnace tube showing the alumina crucible, oxygen electrode, sodium electrode, and gas inlet.

The electrodes were submerged in the melt and the potential between the platinum leads in the oxygen and sodium electrodes was monitored on a 6.5 digit digital multimeter (Model 34461A, Agilent Technologies, Santa Clara, CA). This potential was monitored over

Experimental Procedures – Task 3 – Solubility of Oxides in Sodium Sulfate 33

the course of several hours to determine when the potential had stabilized and equilibrated. Once stable (usually in 24-48 hours) samples of the melt were taken for chemical analysis (ICP-OES). The potential was recorded immediately prior to sampling to determine the steady-state Na_2O activity in the melt at the time of sampling. The Na_2O activity was varied run-to-run by changing the SO_2 concentration in the gas stream. Na_2O_2 was added in conjunction with the low SO_2 gas to raise the Na_2O activity higher than could be achieved with the gas alone.

Sampling was accomplished by inserting a 1/8" diameter alumina rod (CoorsTek, Golden, CO) through the sampling/addition tube so that it made contact with the top surface of the melt within the crucible. The sampling rod was left in contact with the melt until it heated up enough to slightly penetrate the melt (typically around 5 minutes). The rod was marked approximately 2 mm above the length needed to reach the top of the melt. A movable plastic zip-tie was placed on this mark to keep the rod from penetrating too deeply in the melt. The sampling tube was open during this process so the potentials measured during sampling were not indicative of the chemistry in the melt but were influenced by the short-term changes in temperature and gas atmosphere. The sampling rod was removed from the furnace and the furnace was re-sealed to re-equilibrate before sampling again. When possible, a minimum of 4 samples were taken at each experimental condition (oxide and gas combination) with several hours in between samples to allow the melt to re-equilibrate. When fewer samples were collected it was typically due to experimental difficulties resulting from furnace failure or lost signals due to electrode failures.

The sampling rod was weighed before and after sampling to determine the mass of sample removed from the furnace, which was typically between 5-15mg. After weighing, the sampling rod was inserted into a 15 mL centrifuge tube and broken above the highest point of visible salt so that both the frozen salt/oxide melt and the end of the alumina sampling rod were within the tube. The salt sample was then dissolved with water in this tube for ICP analysis.

Nickel oxide (NiO) was used in preliminary experiments to validate the technique by comparison to the literature^{23,58}. NiO ($\rho=6.67 \text{ g/cm}^3$) is denser than molten sodium sulfate ($\rho=2.06 \text{ g/cm}^3$)⁵⁹ so the NiO powder was added to the sample crucible before Na_2SO_4 and remained at the bottom of the crucible allowing sampling from the top of the melt without sampling undissolved NiO. After these initial nickel oxide experiments, SiO_2 solubility was studied. The density of silica ($\rho=2.68 \text{ g/cm}^3$) is very similar to that of molten sodium sulfate, so the silica was added as coarse granules before the Na_2SO_4 rather than as a powder to limit the possibility of sampling un-dissolved silica. Boria, however, has a melting temperature below that of sodium sulfate and the liquid has a lower density (about 1.51 g/cm^3)⁵⁹ than molten sodium sulfate, meaning that at 900°C , liquid boria would be floating on top of the sodium sulfate making it impossible to insert and remove the sampling rod without sampling un-dissolved boria as well. For this reason a compound within the $\text{Al}_2\text{O}_3\text{-B}_2\text{O}_3$ system was used to study boria solubility in Na_2SO_4 . Schematics of each of these oxides, their form, and relative location in the Na_2SO_4 melt are shown in Figure 16.

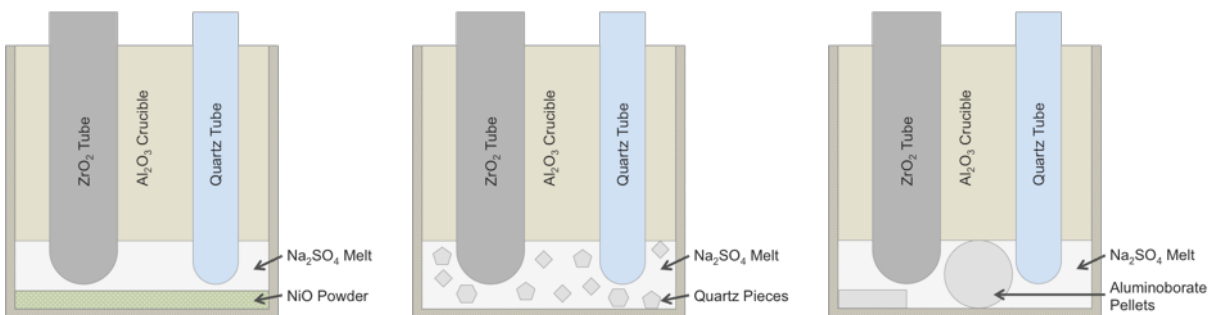


Figure 16 – Schematics showing the approximate location and shape of the oxides used. From left to right: NiO powder, SiO₂ pieces, and aluminoborate pellets.

The Al₂O₃-B₂O₃ system was chosen as a source of B₂O₃ because it has a two-phase field where both intermediate compounds melt above 900°C. This field is shown in Figure 17 and is between the line compounds with stoichiometries of 9:2 and 2:1 Al₂O₃:B₂O₃. FactSage⁴³ calculations show that within this field the activity of B₂O₃ is 0.56, so dissolving significant boria into the sodium sulfate melt was achievable. The density of the 9:2 phase is ≈2.6 g/cm³ and the density of the 2:1 phase is ≈2.9 g/cm³, so both are expected to be denser than Na₂SO₄. Additionally, while boria is the oxide species of interest the alumina crucible is already in direct contact with the melt so using the aluminoborates does not introduce any new chemistry other than the B₂O₃.

Aluminoborates were prepared by mixing alumina and boria powders at a stoichiometry of 2:1. These powder mixtures were reacted in a covered Pt-10Au crucible at 900°C for 3 hours in air within a box furnace (CM Furnaces, Bloomfield, NJ). The powders were mixed at a ratio of 2:1 with the understanding that some of the boria was likely to volatilize and the final product should fall within the two-phase field shown in Figure 17. X-ray diffraction was used to verify the presence of the aluminoborate phases. The powders were then cold-pressed into cylindrical pellets measuring 0.5" diameter and

0.25-0.75" tall. The pellets were placed into the crucible before the Na_2SO_4 , however they were so relatively large that they often stuck out above the top surface of the melt.

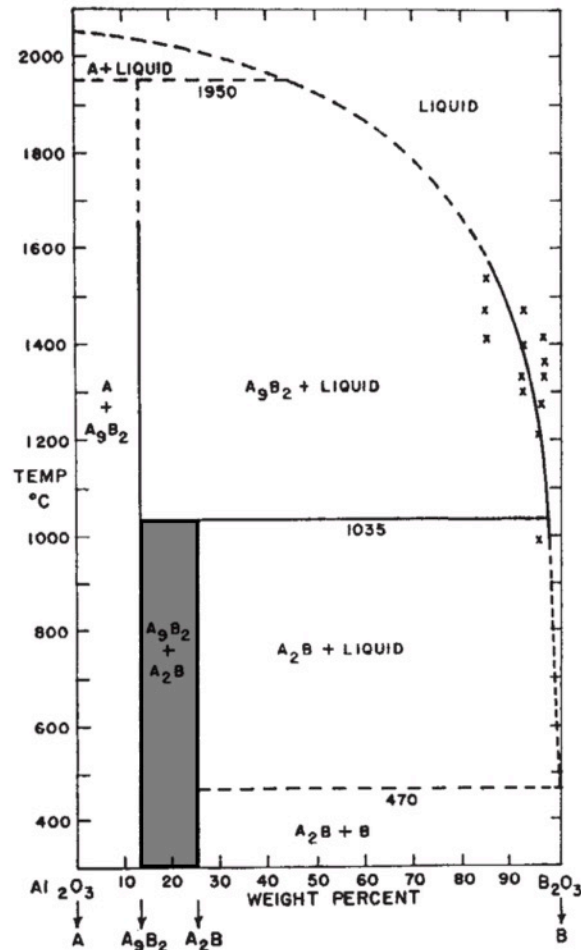


Figure 17 - Al_2O_3 - B_2O_3 pseudo-binary phase diagram taken from Gielisse and Foster⁶⁰, with the two-phase field of interest shaded.

5 Task 1 – Hot Corrosion of Model Materials

5.1 Results

5.1.1 Model Materials Characterization

A Hexoloy coupon was characterized using SEM and EDS to determine the relative area fraction of sintering additives and their compositions. Semi-quantitative EDS point analysis found two additives were present: C (~95%), or B (~64%) plus C (~34%), consistent with prior work⁶¹. The Hexoloy was found to have an average area fraction of 6.3% C-based impurities, and 0.4% B-based impurities as shown in Figure 18.

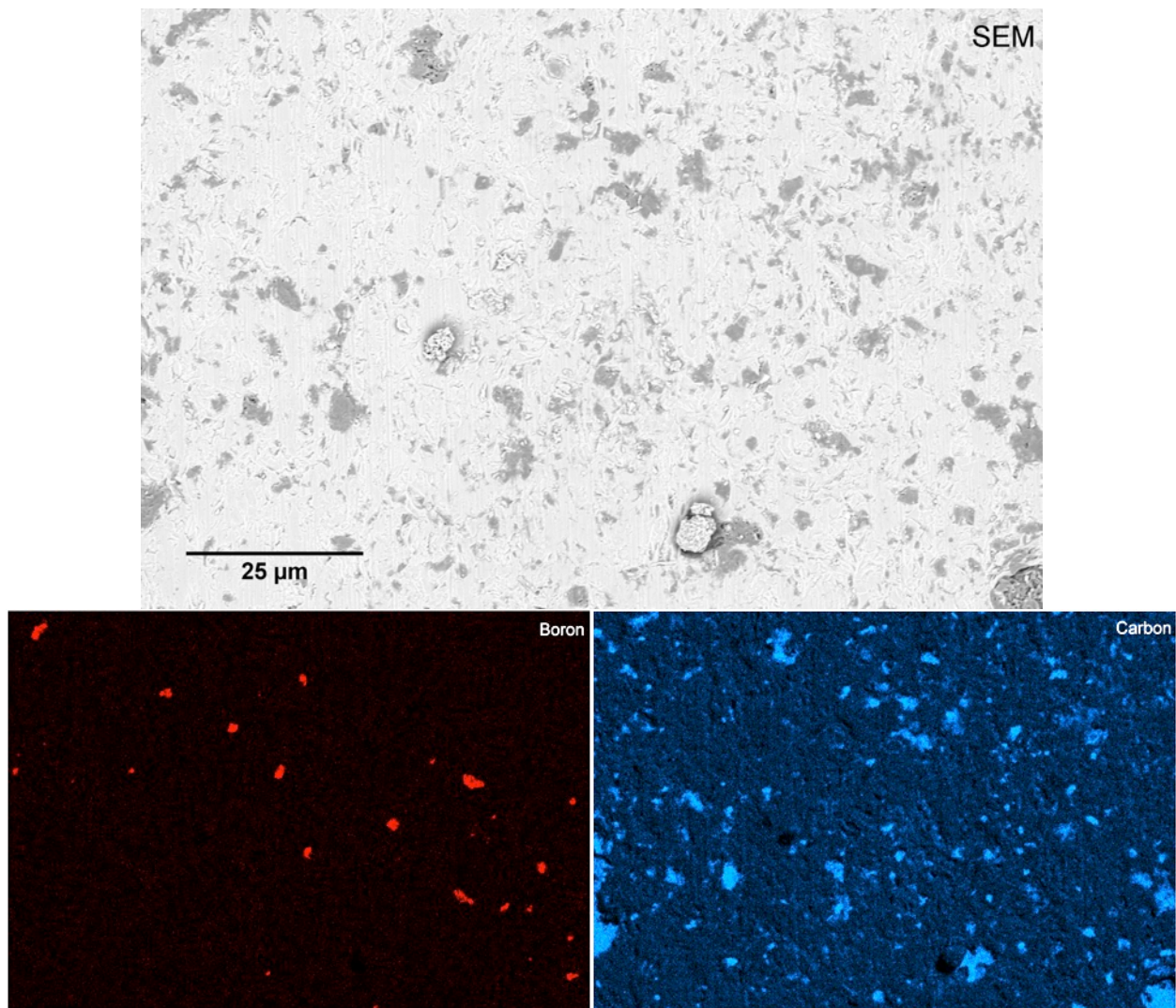


Figure 18 – Electron micrograph of the top surface of a Hexoloy coupon, EDS map of B, and EDS map of C.

Baseline ICP analysis was performed using the 3-step digestion process on an as-received Hexoloy coupon. The combined total amount of B and Si found in all three digestion steps was $0.35\mu\text{g}/\text{cm}^2$ and $5.2\mu\text{g}/\text{cm}^2$ respectively. These values are 2-3 orders of magnitude lower than the values found in corroded samples, indicating that the digestion process is removing the corrosion products and not dissolving the substrate.

The thickness and composition of the C and BN coatings was verified using scanning Auger depth profiling. Figure 19 shows the Auger depth profiles that were collected on the C and BN coated substrates. These results show that both coatings are around 700nm thick. The C coating was high purity within the resolution of AES, however there are C, Si, and O impurities in the BN coating which is a reasonable model for the dopants and impurities in BN fiber coatings^{62, 63}.

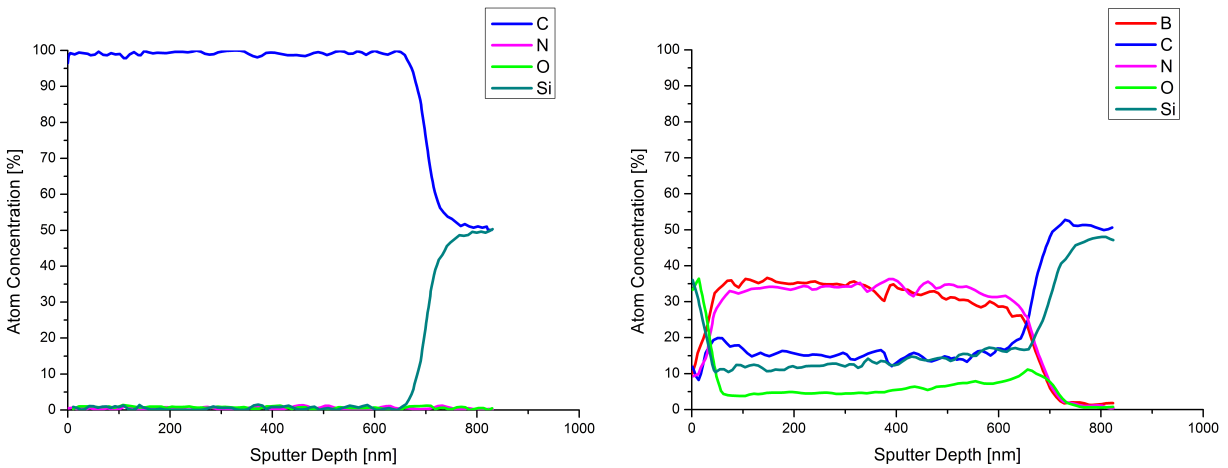


Figure 19 – Auger depth profiles of the deposited C and BN coatings, showing a coating thickness of around 700nm.

5.1.2 Time Dependence for SiC Hot Corrosion

The time dependence of the hot corrosion reaction was determined for coupons of both sintered Hexoloy as well as CVD-SiC for exposures between 0.75 and 96 hours at 1000°C, as shown in Figures 20 and 21. The large amount of scatter in the data is likely due to the non-uniformity of corrosion on the macro-scale as seen in Figure 22. A rapid onset of corrosion is observed in mass loss values, total Si found in the corrosion products, and pitting data collected (as will be described in a later section). The rapid corrosion occurred in 0.75 hours for Hexoloy and in 6 hours for CVD-SiC. After this initial rapid corrosion

period the mass loss plateaus, which has been seen previously^{4,5}, and is consistent with formation of a continuous, protective silica on the sample as observed by Jacobson¹⁻³.

The effect of salt depletion due to volatility was probed. Several samples were exposed for 48-hr, removed from the furnace for application of additional salt, then re-inserted into the furnace for an additional 48-hr exposure (a total of 96-hr). These data are represented by the open symbols in Figures 20 and 21. The corrosion results when salt was re-applied are not statistically different from results for a single loading and 96-hr exposure. A 24 hour exposure time was used for the remainder of the exposures to determine the temperature dependence of hot corrosion since at 24 hours the bulk of the corrosion had already occurred, yet Na₂SO₄ volatility was minimized.

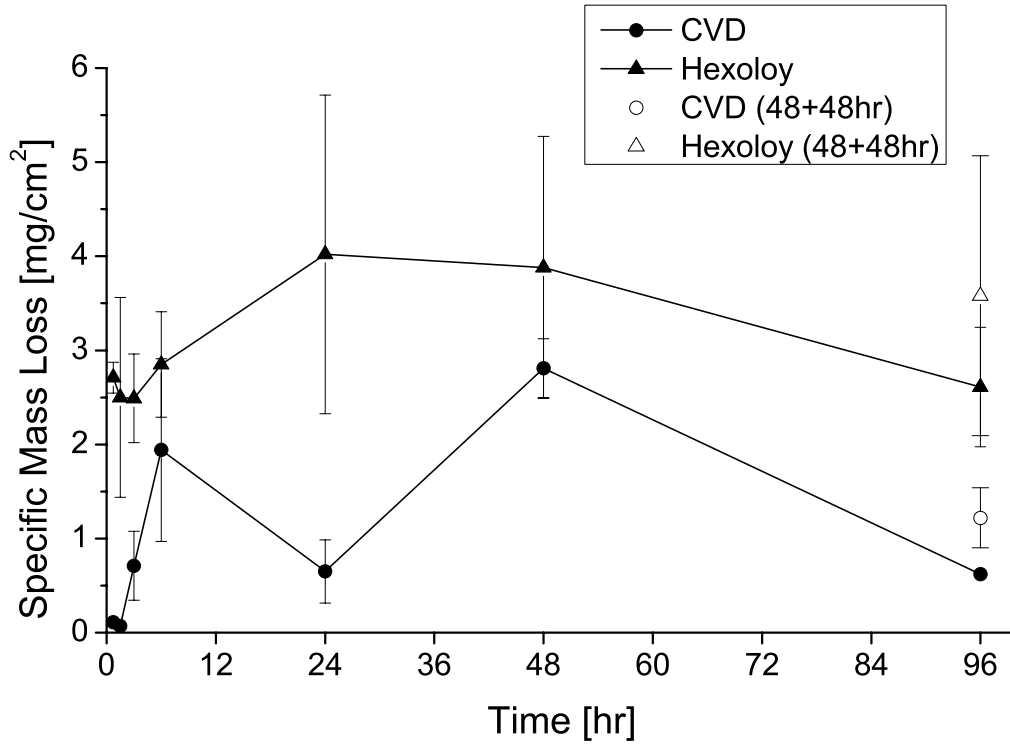


Figure 20 - Normalized mass loss (mg/cm²) after corrosion products removed as a function of exposure time (hr) for CVD SiC and Hexoloy coupons exposed at 1000°C.

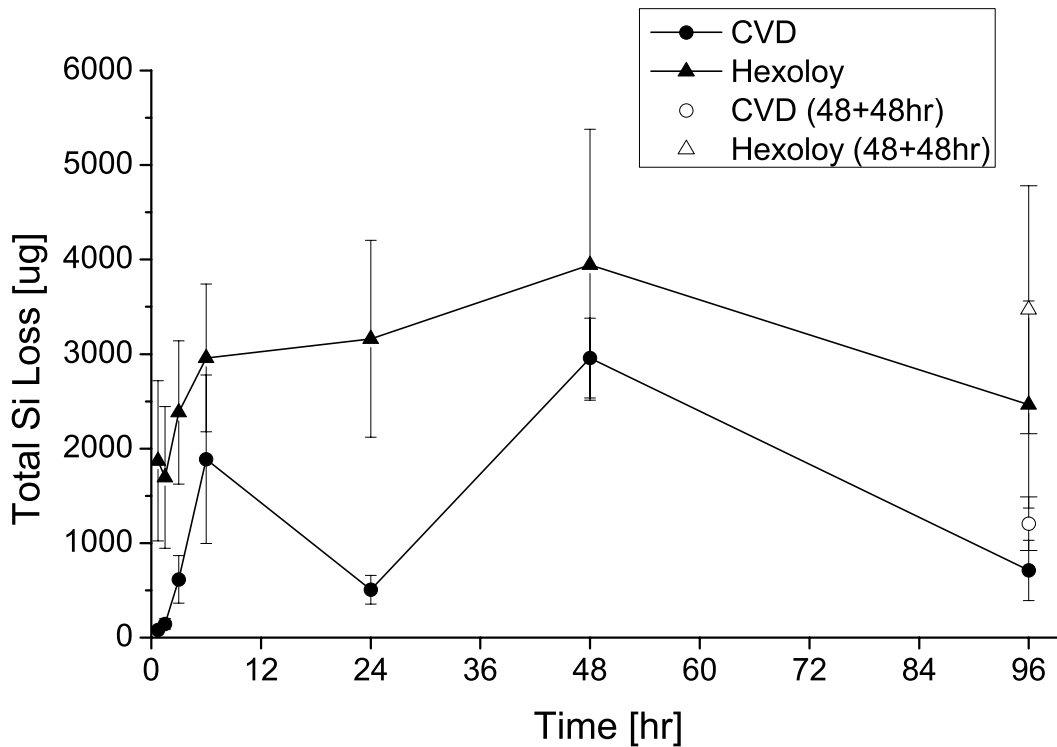


Figure 21 - Total Si found in corrosion products (µg) using ICP-OES as a function of exposure time (hr) for CVD SiC and Hexoloy coupons exposed at 1000°C.

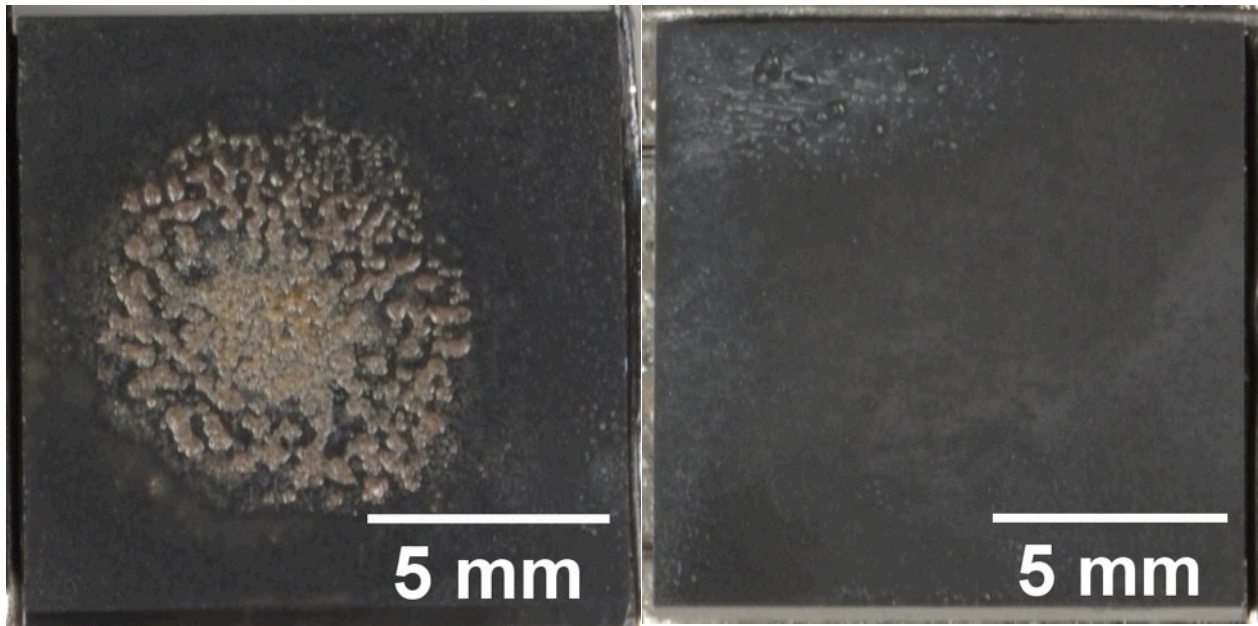


Figure 22 – Examples of non-uniform corrosion on CVD SiC coupons exposed at 1000°C for 6-hr.

5.1.3 Temperature Dependence for SiC Hot Corrosion

The temperature dependence for hot corrosion was examined only for Hexoloy samples after hot corrosion for 24 hours. Because a definitive rate law was not identified for the temperature dependence of hot corrosion, bounding cases of linear kinetics (reaction controlled) and parabolic kinetics (diffusion controlled) were considered. Figure 23 presents the log of mass loss (after all corrosion products are removed) and total mass of Si found in corrosion products (through ICP-OES analysis) for Hexoloy specimens corroded for 24 hr plotted against reciprocal temperature which assumes a linear (reaction controlled) rate process. Figure 24 shows the same data plotted as log of mass loss squared and log of total mass of Si squared versus reciprocal temperature which assumes a parabolic (diffusion controlled) rate process.

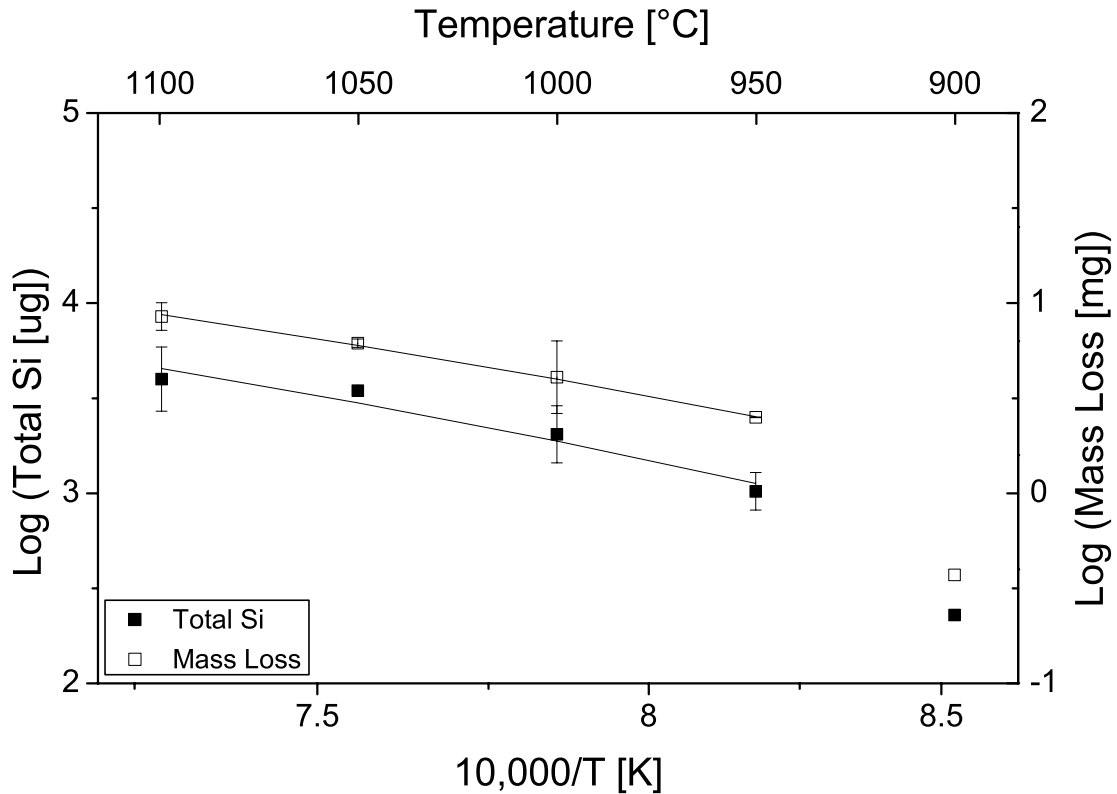


Figure 23 – Temperature dependence of sodium sulfate induced hot corrosion of SiC (Hexoloy) plotted as the log of total Si found in the corrosion products (μg) and log of mass loss after corrosion products are removed (mg) vs. inverse temperature (K). In the temperature range of 950-1100°C the apparent activation energy is 71.5 kJ/mol \pm 34 kJ/mol for linear mass loss and 80.8 kJ/mol \pm 40 kJ/mol (95% confidence intervals) for linear total Si in the corrosion products.

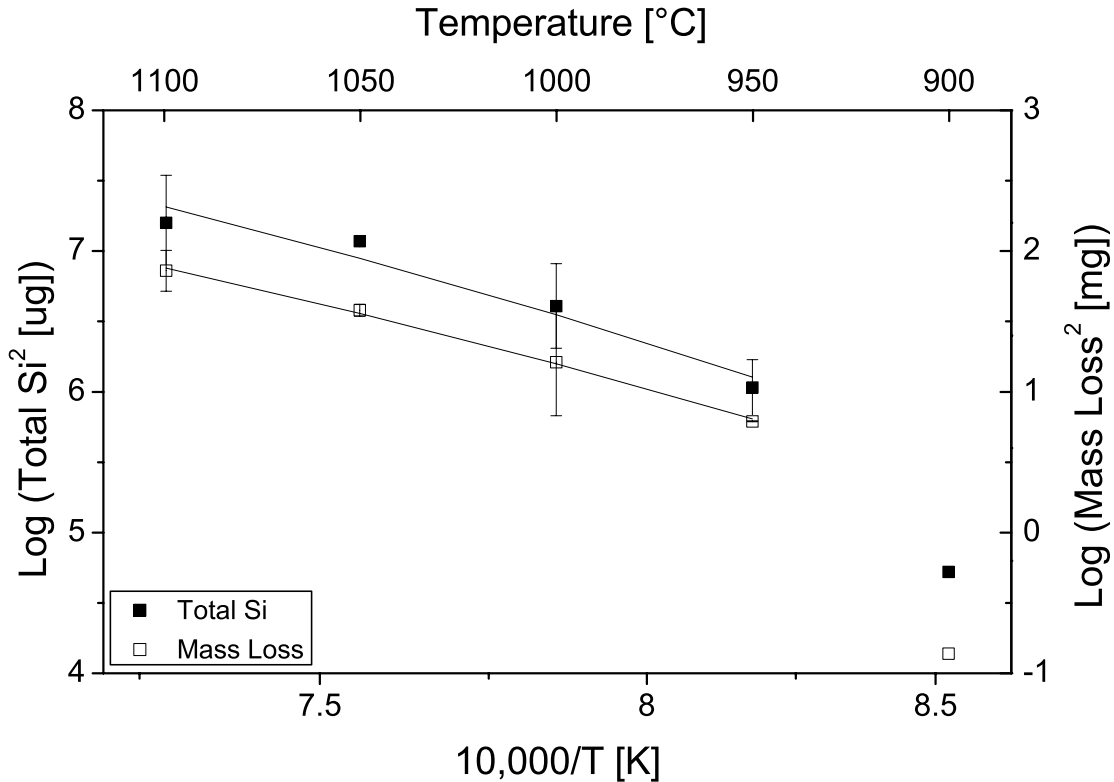


Figure 24 - Temperature dependence of sodium sulfate induced hot corrosion of SiC (Hexoloy) plotted as the log of total Si found in the corrosion products squared (μg) and log of mass loss after corrosion products are removed squared (mg) vs. inverse temperature (K). In the temperature range of 950-1100°C the apparent activation energy is 143.0 kJ/mol \pm 68 kJ/mol for parabolic mass loss and 161.5 kJ/mol \pm 80 kJ/mol (95% confidence intervals) for parabolic total Si in the corrosion products.

In the temperature range of 950-1100°C the apparent activation energy is 71.5 kJ/mol \pm 34 kJ/mol for linear mass loss and 80.8 kJ/mol \pm 40 kJ/mol (95% confidence intervals) for linear total Si in the corrosion products. The apparent activation energy is 143.0 kJ/mol \pm 68 kJ/mol for parabolic mass loss and 161.5 kJ/mol \pm 80 kJ/mol (95% confidence intervals) for parabolic total Si in the corrosion products. This doubling of the apparent activation energies is a direct result of squaring the weight change values. These bounding cases will be evaluated in the discussion section.

Little mass loss was observed at 900°C, even though it is above the melting temperature of Na_2SO_4 (884°C), however this is consistent with previous work⁴.

Additionally, there was little pitting of the sample surface at 900°C, and little Si present in the solutions analyzed by ICP-OES as described below. 1000°C was chosen as the temperature at which to conduct the remainder of the experiments. This temperature falls within a range of temperatures with constant apparent activation energy, there are some existing data that has been collected at 1000°C^{1, 2, 11, 16, 17} for comparison, and the load on the furnace at 1000°C is lower than would be needed to run the exposures at a higher temperature.

5.1.4 Substrate Dependence for SiC Hot Corrosion

The extent of corrosion and identification of corrosion products was determined by mass gain after exposure, mass loss after successive H₂O, HCl, and HF digestion steps, and amounts of reactant and corrosion products (Si, B, Na, S) found in each digestion solution. Comparing all of these data (25 values) is difficult, therefore a radar plot, or spider chart, was used to present all of these factors and to compare the relative hot corrosion resistance of SiC-based materials as shown in Figure 25.

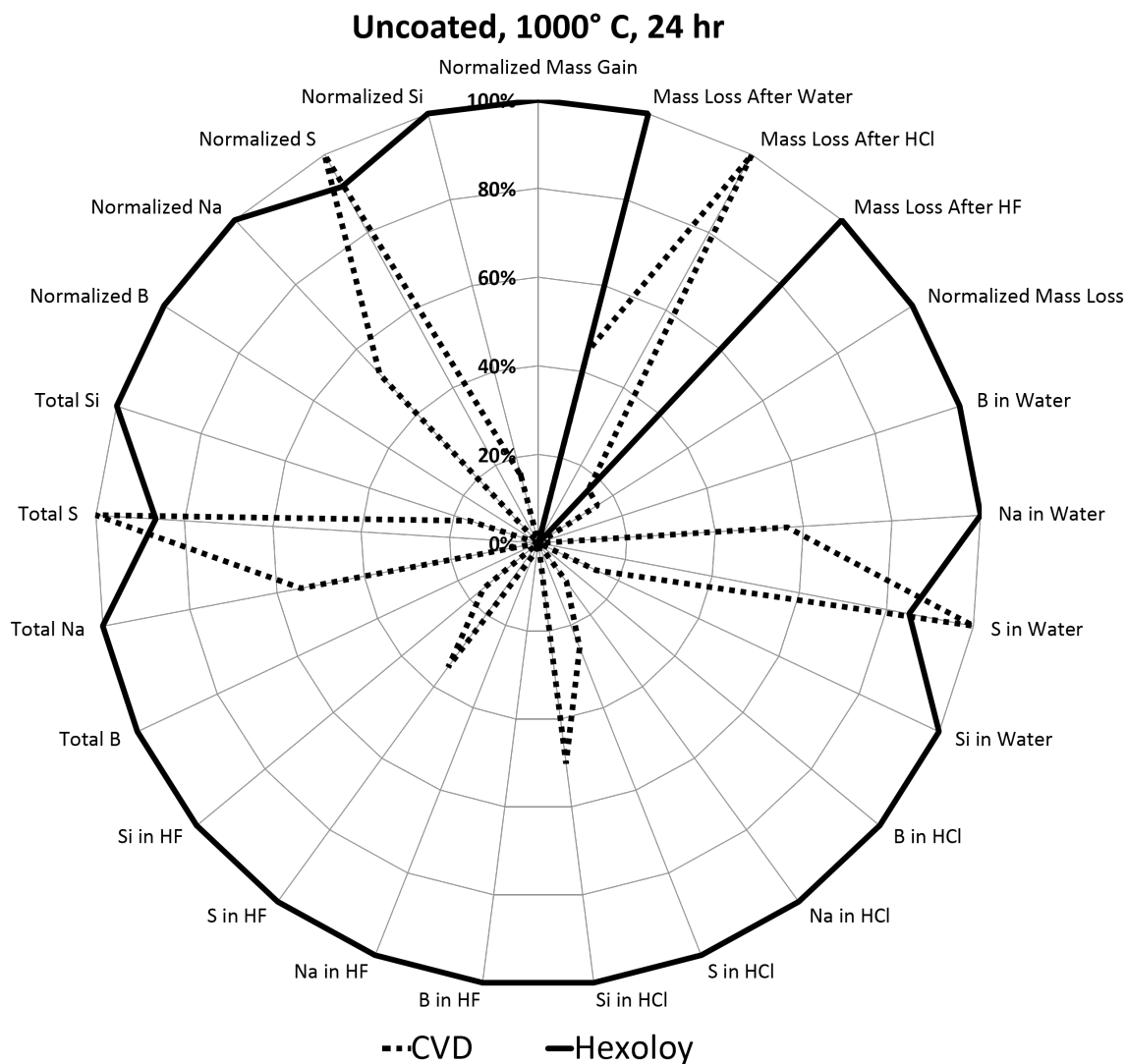


Figure 25 – Radar plot comparing relative hot corrosion resistance of uncoated CVD SiC and Hexoloy coupons exposed for 24 hr at 1000°C.

This plotting method allows for viewing large amounts of data at once and is well suited for making comparisons. The results within each category are averaged, normalized to the largest value in that category, and plotted as a percentage of the largest value to allow for comparison between samples. For example, in Figure 25 the average mass loss of CVD and Hexoloy are compared. The average mass losses for CVD SiC and Hexoloy were 0.64 mg/cm² and 4.05 mg/cm² respectively, so in this figure the value for Hexoloy was

plotted at 100% and the value for CVD was plotted at 15.9%. Table B-1 in Appendix B lists all of the averaged values shown in Figure 25 for each series including their standard deviations.

Hexoloy exhibited more corrosion than CVD SiC as seen in Figure 25 by comparing mass loss after corrosion products are removed, as well as more Si found in all of the ICP-OES digestion steps. It is also observed that more S is retained on the CVD-SiC substrate as compared to Hexoloy indicating less Na_2SO_4 reactant consumed.

The amount of corrosion products found was compared to the oxidation of SiC under similar conditions (dry O_2 , 1000°C , 24 hr). Ramberg et al.⁶⁴ found an oxide thickness of $0.3\ \mu\text{m}$ for oxidation of CVD SiC and a baseline oxide thickness of $0.86\ \mu\text{m}$ for oxidation of Hexoloy was found in this study. For hot corrosion the calculated oxide thickness (found from the mass-loss values after all corrosion products were removed) was $8.56\ \mu\text{m}$ for CVD SiC and $53.51\ \mu\text{m}$ for Hexoloy, or 1-2 orders of magnitude greater than oxidation.

The general reaction kinetics of the hot corrosion and scale formation agreed well with the literature^{1, 2, 11, 16}, though the values for total corrosion product formed were slightly lower ($\approx 5\ \text{mg}/\text{cm}^2$ vs. $\approx 10\ \text{mg}/\text{cm}^2$) than found previously.

5.1.5 Chemistry Dependence of SiC Hot Corrosion: C & BN

The effect of C and BN coatings on the hot corrosion of both CVD and sintered- α SiC are shown in the radar plots in Figures 26 and 27 respectively. As described previously the results within each category are averaged, normalized to the largest value in that category, and plotted as a percentage of the largest value to allow for comparison between samples⁴⁸. These results show that the corrosion is more severe for C- or BN-coated Hexoloy than it is for the same coatings on CVD, which follows the trend for uncoated materials.

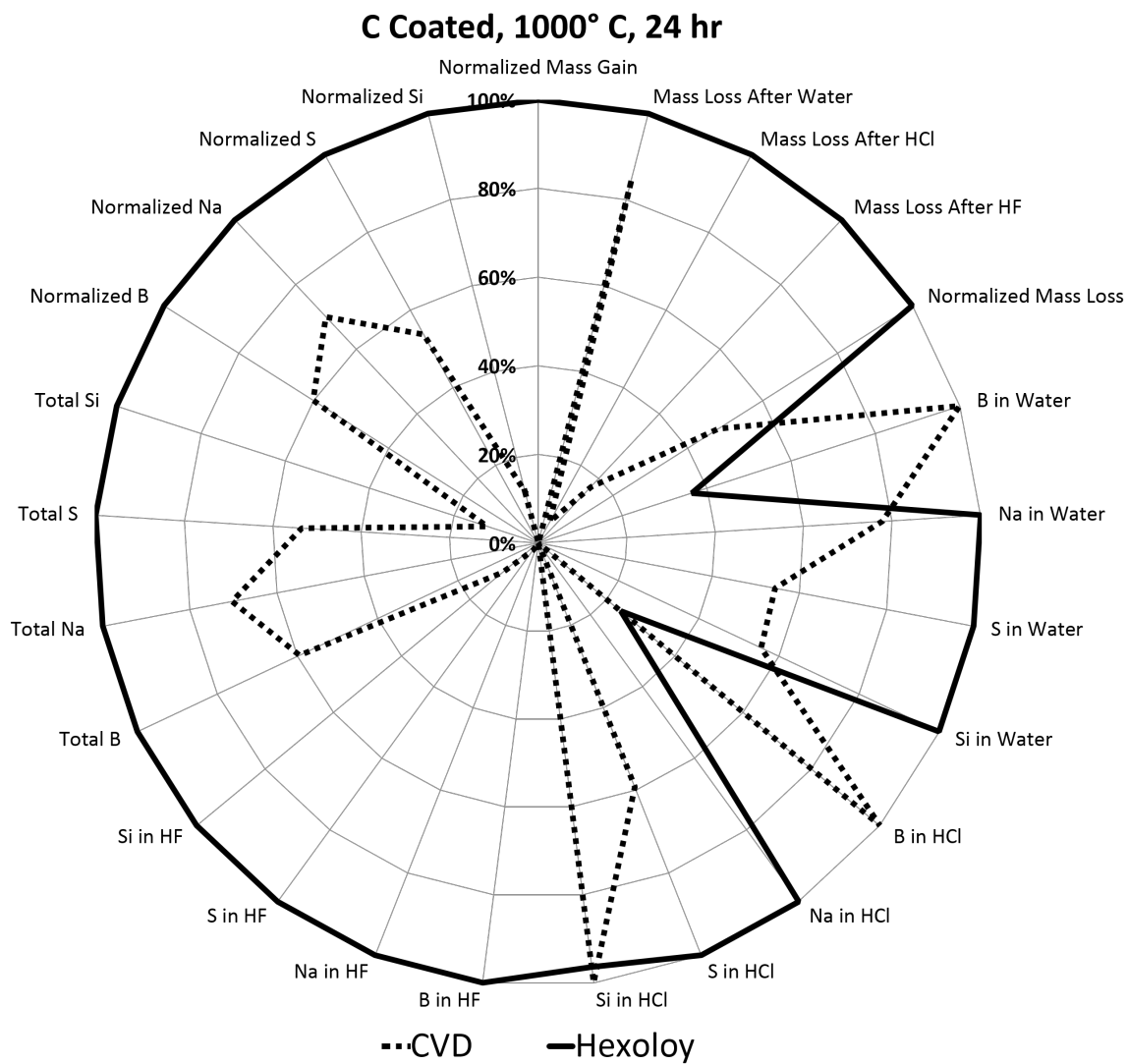


Figure 26 – Radar plot comparing relative hot corrosion resistance of C coated CVD SiC and Hexoloy coupons exposed for 24 hr at 1000°C in 0.1% SO₂/O₂ .

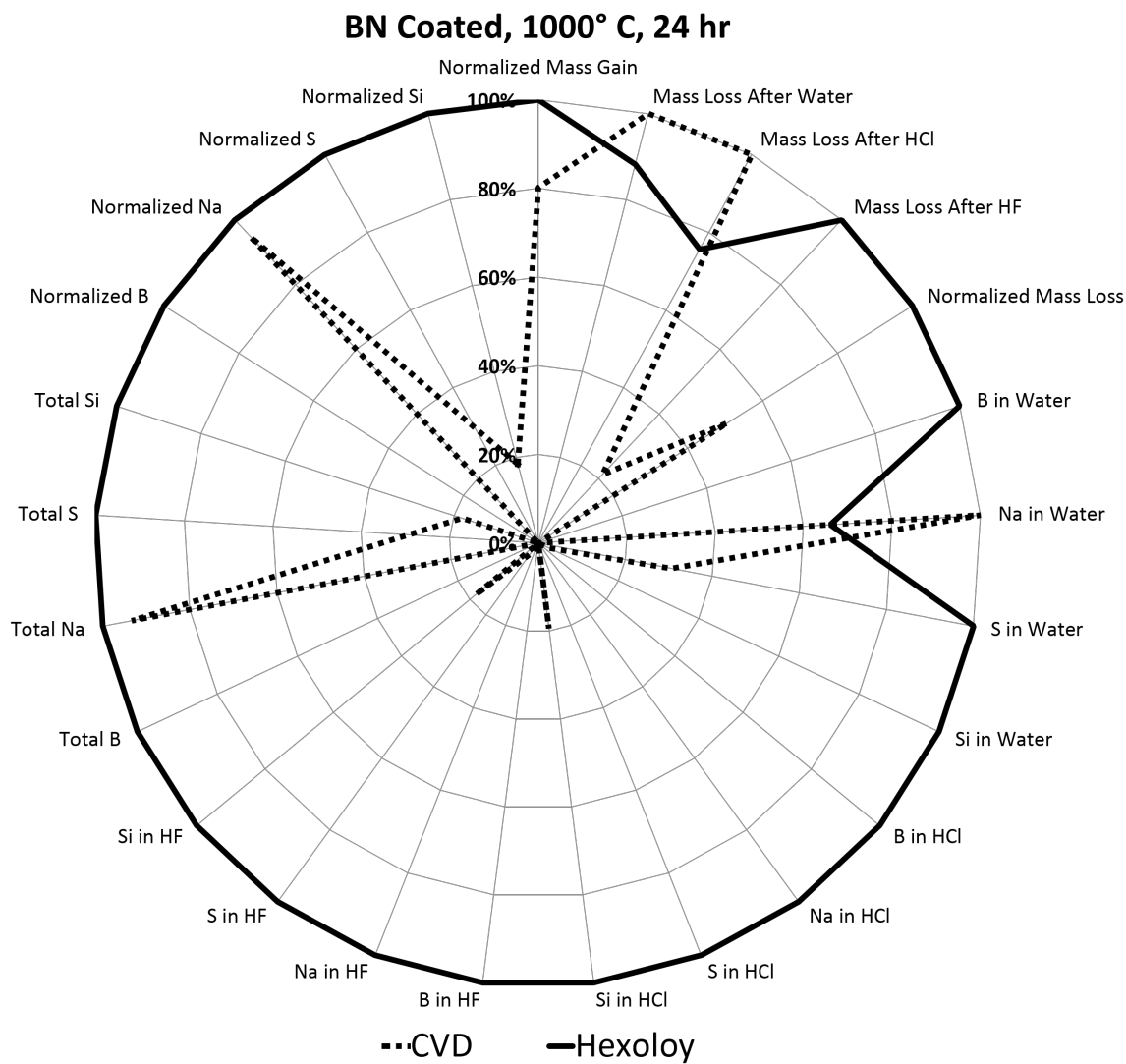


Figure 27 – Radar plot comparing relative hot corrosion resistance of BN coated CVD SiC and Hexoloy coupons exposed for 24 hr at 1000°C in 0.1% SO₂/O₂.

Figures 28 and 29 compare effects of coating composition for CVD-SiC and Hexoloy substrates by examining Na, S, B, and Si found in the ICP solution analysis. Key results are highlighted in the following summary.

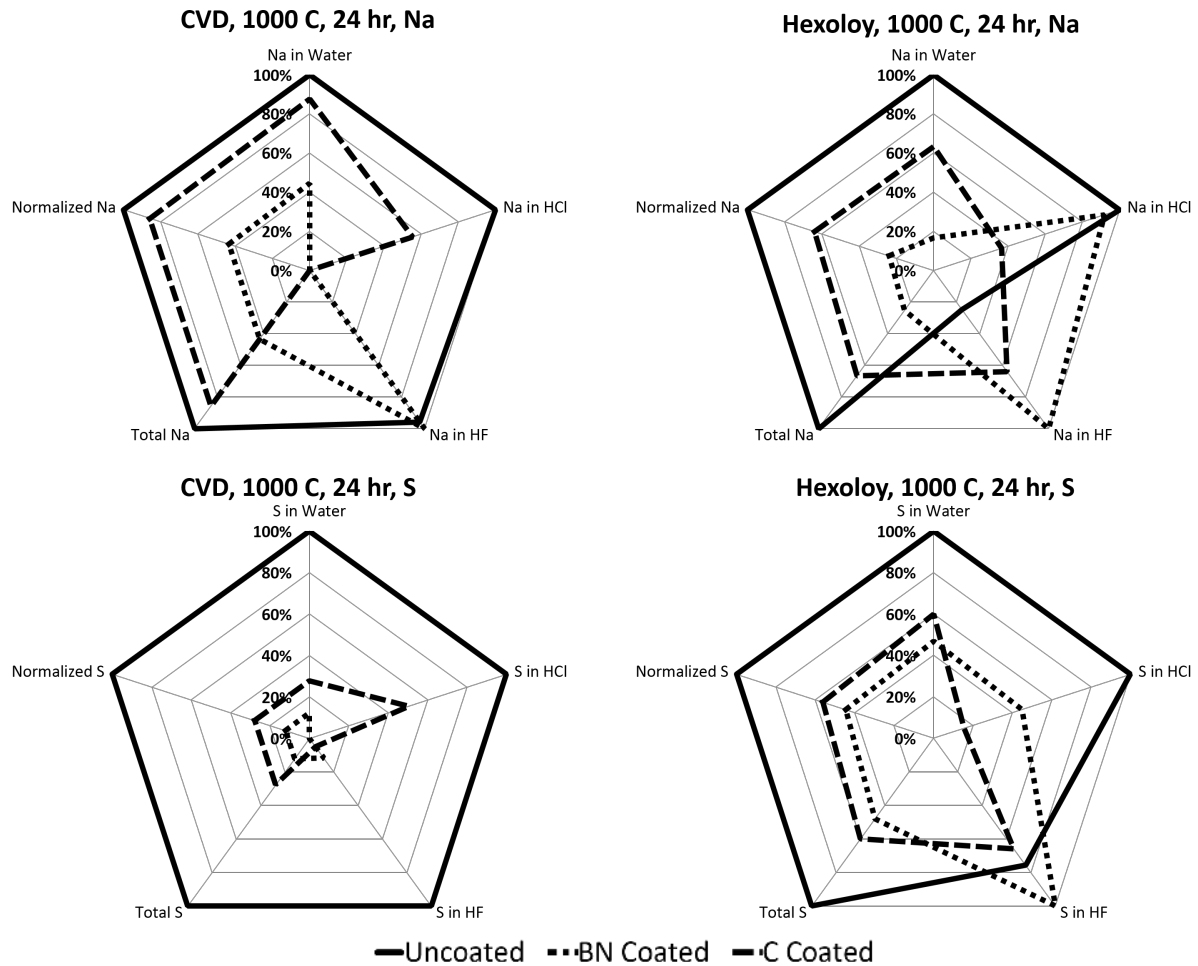


Figure 28 – Radar plots showing Na and S found in each of the digestion steps as well as total Na and S for CVD SiC and Hexoloy coupons as a function of surface coating after hot corrosion for 24 hr at 1000°C in 0.1% SO₂/O₂.

Figure 28 shows that there is more water soluble Na and S, as well as total Na and S left on both types of coupons when they are uncoated (solid line on the outside). Residual Na and S in water is a measure of unreacted Na₂SO₄ and higher S indicates less reaction as seen for example in Equations 2 and 4. This shows that the uncoated coupons experience the least interaction between Na₂SO₄ and SiO₂.

The C coating on CVD coupons reduces the Na removed in the HF dissolution step as compared to uncoated which indicates that there was less reaction between Na₂SO₄ and SiO₂. The BN coating on CVD reduces the Na found in every dissolution step except for HF

which indicates that the sodium was tied up in non-water soluble silicates which are only formed by corrosion of the SiC substrate (and thus a sign of degradation). In the Hexoloy system, a C coating increases the Na found in HF as compared to uncoated coupons again indicating sodium incorporation into relatively insoluble silicates. The BN coating results in the greatest amount of Na and S removed in HF which corresponds with the largest amount of reaction between Na_2SO_4 and SiO_2 .

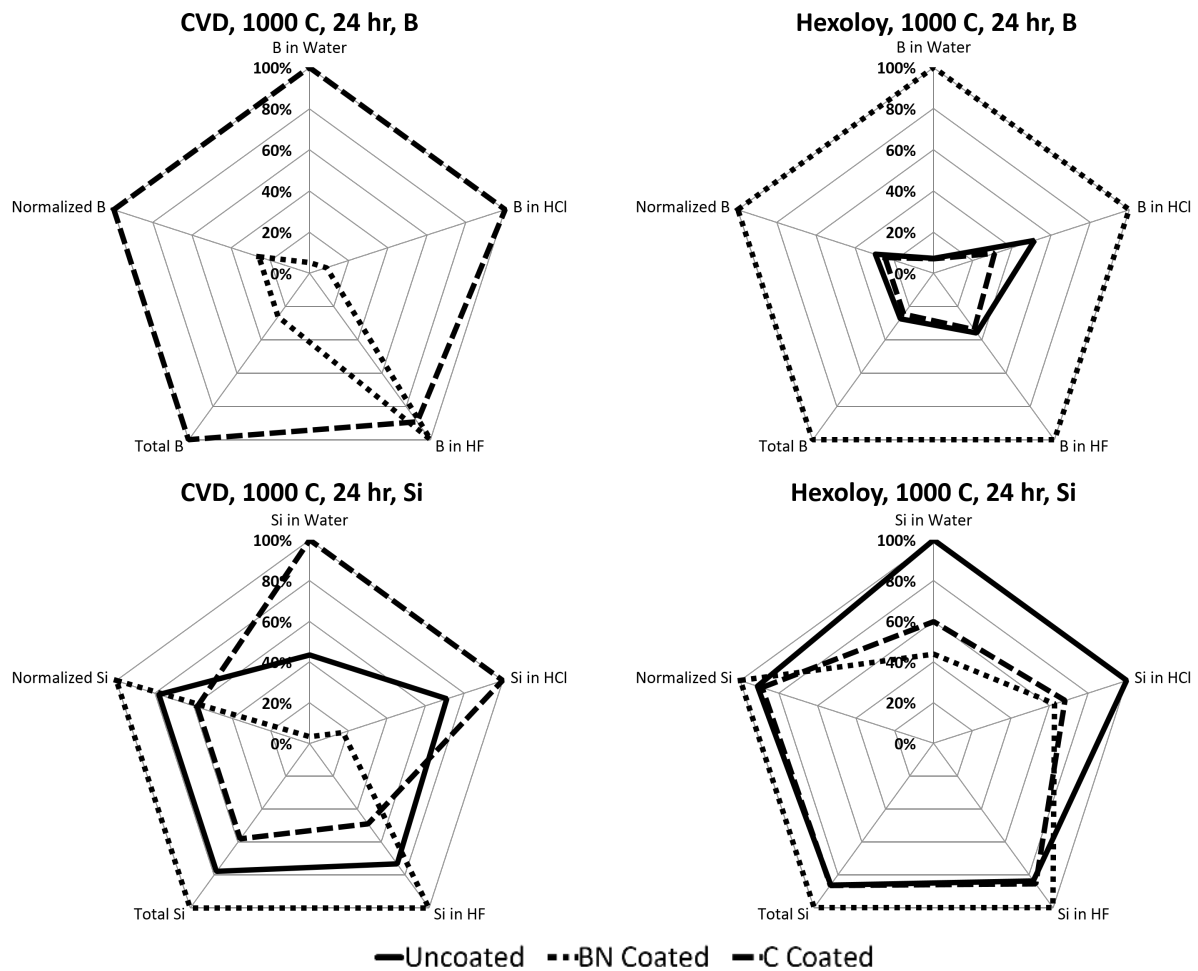


Figure 29 – Radar plots showing B and Si found in each of the digestion steps as well as total B and Si for CVD SiC and Hexoloy coupons as a function of surface coating after hot corrosion for 24 hr at 1000°C in 0.1% SO_2/O_2 .

From Figure 29 it is seen that no B is found on the uncoated CVD samples (which is to be expected), but there is a greater amount of B found on the C-coated samples. The B

was found at a very low level (3 μg) and could come from impurities in the coating or contamination in the hot corrosion exposure. The total Si removed from the CVD coupons (and Si in HF) is greatest for the BN-coated coupons, second greatest for the uncoated coupons, and least for the C-coated coupons. Total Si removed is a measure of total corrosion.

The B in corrosion products was greatest on the BN-coated Hexoloy coupons as expected. Total Si removed (and Si in HF) is greatest for BN-coated Hexoloy but only by a small margin over the uncoated and C-coated samples which are nearly identical.

During sample preparation it was observed that aqueous sodium sulfate solution beaded up on uncoated and C-coated coupons but wetted the surface of BN-coated coupons. BN-coated coupons were found to have more even coverage of corrosion products after exposure, so improved wetting of the molten salt is suspected as well. This behavior is shown in the images in Figure 30.

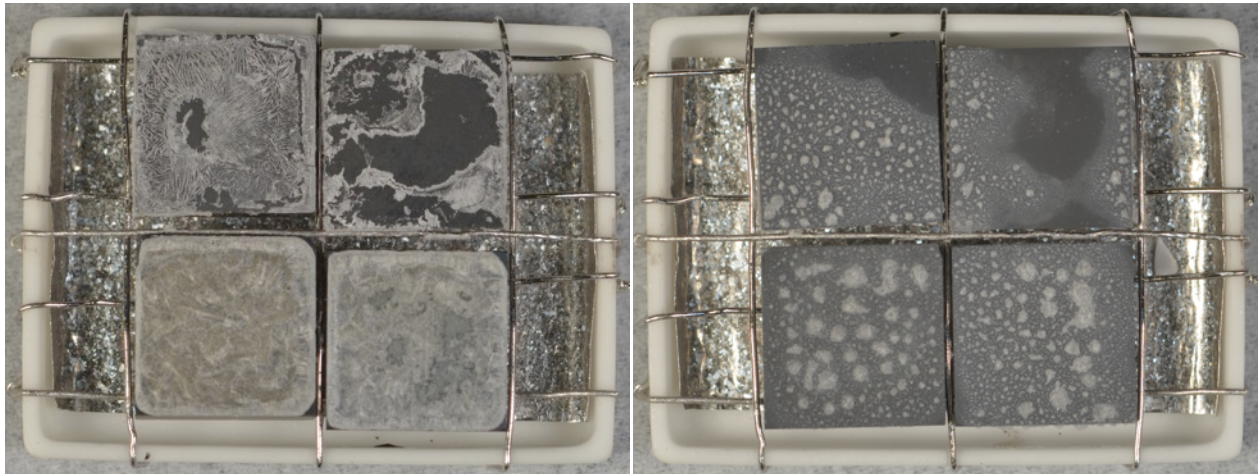


Figure 30 – The image on the left shows the sample carrier loaded with 4 coupons after salt deposition and before exposure. The top two coupons are C-coated and the bottom two coupons are BN-coated, showing the increased wetting of the aqueous salt solution on the BN-coated coupons. The image on the right shows the same samples after exposure for 24-hours at 1000°C, where the corrosion products on the BN-coated sample are more evenly distributed.

5.1.6 Chemistry Dependence of SiC Hot Corrosion: Si

The hot corrosion of the silicon coupons showed little attack overall. The samples did not pit and appeared only slightly etched (the shiny surface became matte) after exposure for 24 hours at 1000°C. The oxide thickness or surface recession was calculated from the normalized mass loss found after removing corrosion products in HF (baseline digestion of an as-received coupon showed no measurable mass loss in HF) The oxide thickness was found to be 3.15 μm for hot corrosion of Si, which is higher than the 0.46 μm calculated for oxidation of Si⁶⁵. This value is, however, lower than the oxide thickness values for hot corrosion of Hexoloy (53.51 μm) and CVD-SiC (8.56 μm) described earlier.

5.1.7 SO₂ Concentration Dependence of SiC Hot Corrosion

A small selection of coupons were exposed for 24 hours at 1000°C under a 2.5ppm SO₂/O₂ gas atmosphere in order to determine the dependence on SO₂ concentration. Coupons exposed at this gas condition exhibited a characteristic scale morphology that contained evidence of crystalline laths in the silicate as shown in Figure 31. The scale was also generally smoother, more uniform in thickness, and less bubbly than the scale generated under a 1000ppm SO₂/O₂ atmosphere (results presented in Section 5.1.9).

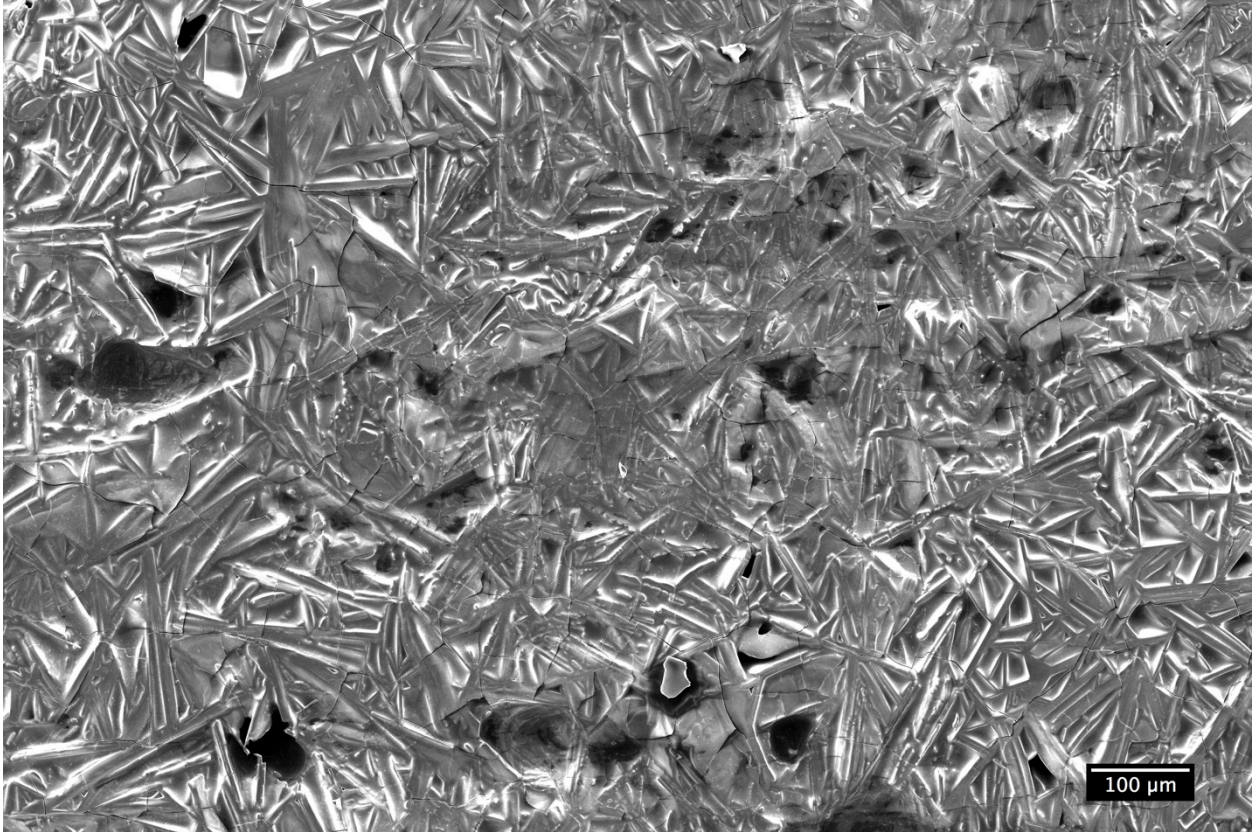


Figure 31 -SEM micrograph of a coupon after exposure for 24 hours at 1000°C in 2.5 ppm SO₂/O₂.

The compared normalized mass loss between the model material coupons exposed under a 1000 ppm SO₂/O₂ environment and those exposed under a 2.5 ppm SO₂/O₂ environment are shown in Figures 32 and 33. The Hexoloy coupons appear to have a normalized mass loss that is fairly similar in both gasses, while the CVD coupons have increased hot corrosion attack under the low SO₂ gas.

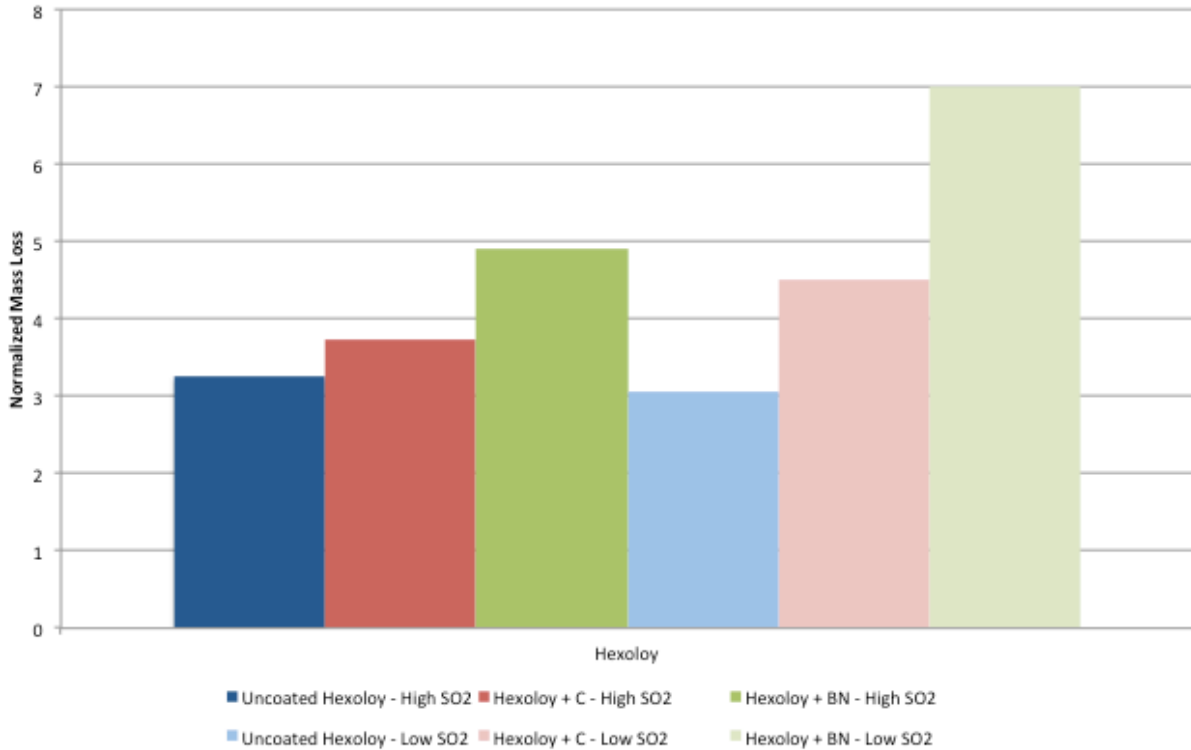


Figure 32 – Plot showing the difference in normalized mass loss between the three Hexoloy coupon types exposed in 1000ppm SO₂/O₂ and 2.5 ppm SO₂/O₂.

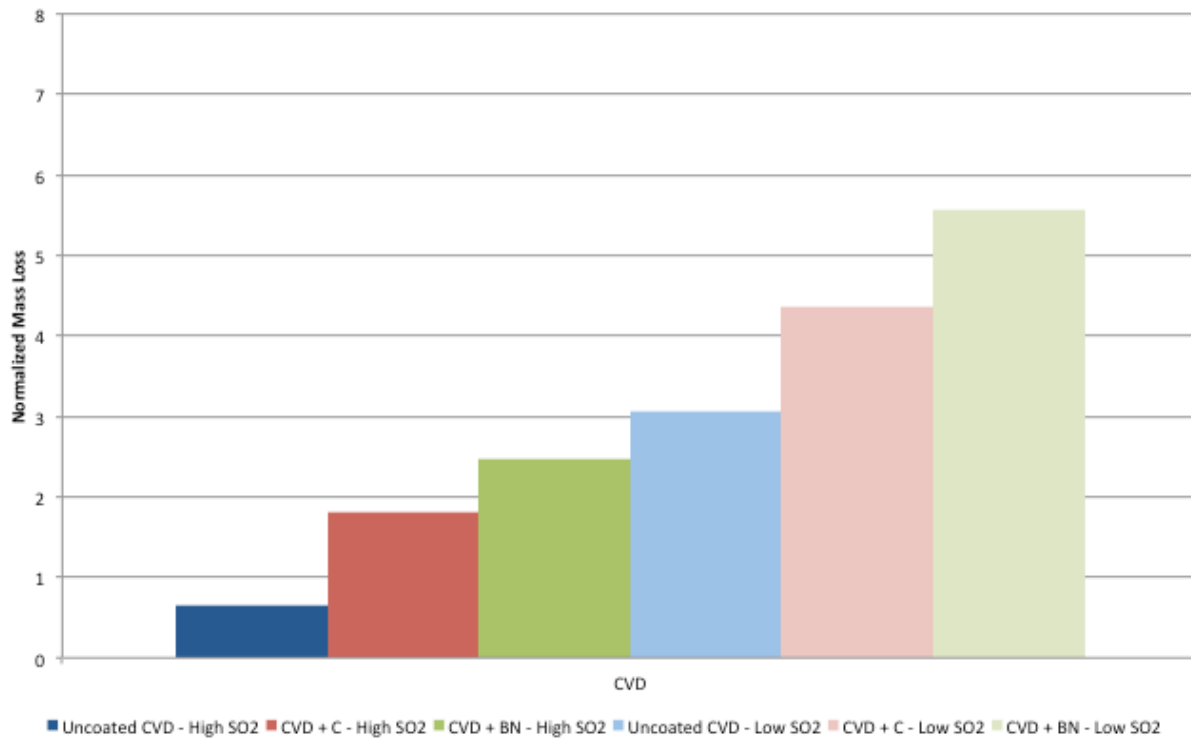


Figure 33 – Plot showing the difference in normalized mass loss between the three CVD coupon types exposed in 1000ppm SO₂/O₂ and 2.5 ppm SO₂/O₂.

5.1.8 Pitting Results for Hot Corrosion of SiC

Figure 34 contains an electron micrograph of a Hexoloy coupon with corrosion products removed after a 24 hr exposure at 1000°C showing severe pitting. The pitting data collected using optical profilometry are presented in Table 6 and Figure 35. The pits are inverted to become peaks to aid in visualization as well as data analysis. Table 6 shows the averaged values for six different sample types all exposed under the same conditions (24-hr, 1000°C) after corrosion products were removed in the ICP digestion. The data in Table 6 indicate that the Hexoloy coupons pit much more severely than the CVD-SiC coupons. The mean pit depth, max pit depth, and mean pit diameters are all much greater for Hexoloy, which contains B₄C and C particles in the material. This is consistent with previous work by Jacobson² showing that the presence of carbon leads to pitting of SiC. The maps in Figure 35 indicate that the attack for CVD is more uniform and reflects the as-fabricated surface roughness on the coupons (found to be 0.021 μm Ra).

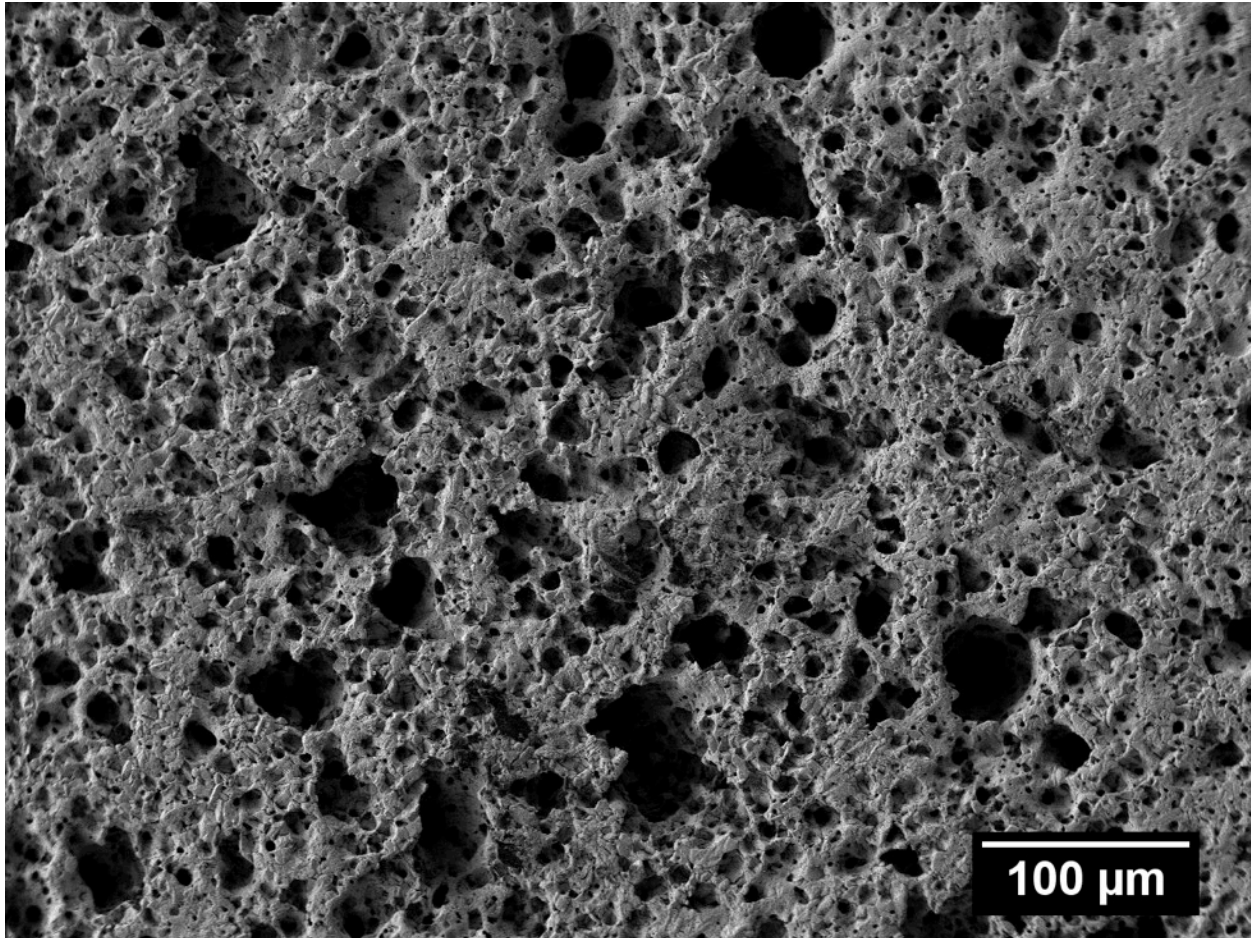


Figure 34 – Electron micrograph of a Hexoloy coupon exposed for 24 hr at 1000°C showing extensive pitting of the sample surface.

Table 6 – Averaged pitting data for uncoated CVD-SiC, uncoated Hexoloy, C-coated Hexoloy, and BN-coated Hexoloy coupons exposed for 24-hr at 1000°C.

Sample	Mean Pit Depth [μm]	Pit Density [$\#/\text{mm}^2$]	Mean Pit Diameter [μm]	Max Pit Depth [μm]
Uncoated CVD-SiC	0.2 ± 0.04	31.9 ± 10.0	7.0 ± 1.2	5.0 ± 1.7
Uncoated Hexoloy	9.6 ± 2.1	33.1 ± 11.8	19.9 ± 1.5	57.2 ± 7.0
C-Coated CVD-SiC	1.1 ± 0.5	279.4 ± 44.8	15.0 ± 1.4	19.9 ± 4.5
C-Coated Hexoloy	2.7 ± 2.4	40.3 ± 9.9	9.7 ± 4.8	48.1 ± 19.0
BN-Coated CVD-SiC	2.3 ± 0.4	202.6 ± 47.4	16.9 ± 0.9	14.6 ± 1.7
BN-Coated Hexoloy	7.2 ± 0.5	46.4 ± 4.5	20.8 ± 3.7	32.4 ± 3.1

The pitting results are plotted as a function of time for Hexoloy in Figure 36 and for CVD-SiC in Figure 37. In the case of CVD-SiC there is a strong correlation between all of the pitting parameters (mean pit depth, mean pit diameter, max pit depth, and pit density) and the observed mass change measurements and total Si removed as seen in Figures 20 and

21. For the Hexoloy material the results for mean pit depth and mean pit diameter agree well with the time dependence found for the mass change and total Si found, while the maximum pit depth appears to be somewhat more variable (while still following a similar trend).

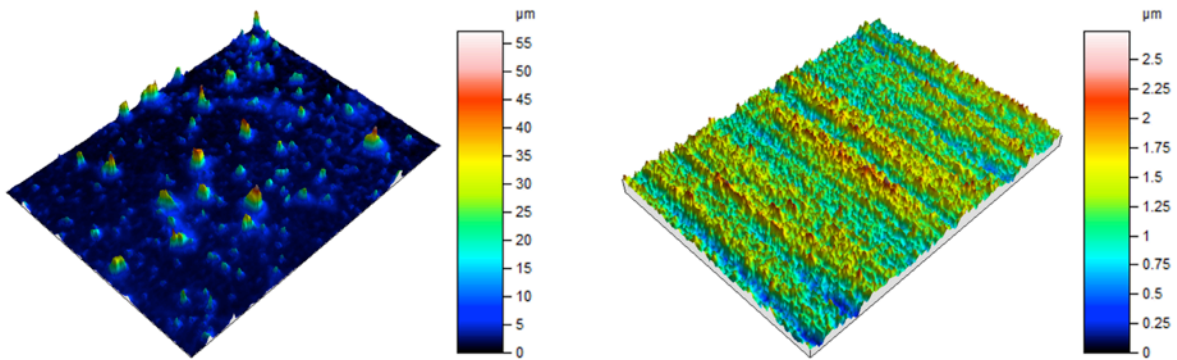


Figure 35 - Topographical maps of pits (inverted to become peaks) comparing the pitting behavior of Hexoloy and CVD-SiC exposed for 24 hr at 1000°C. Note the different height scales in each map.

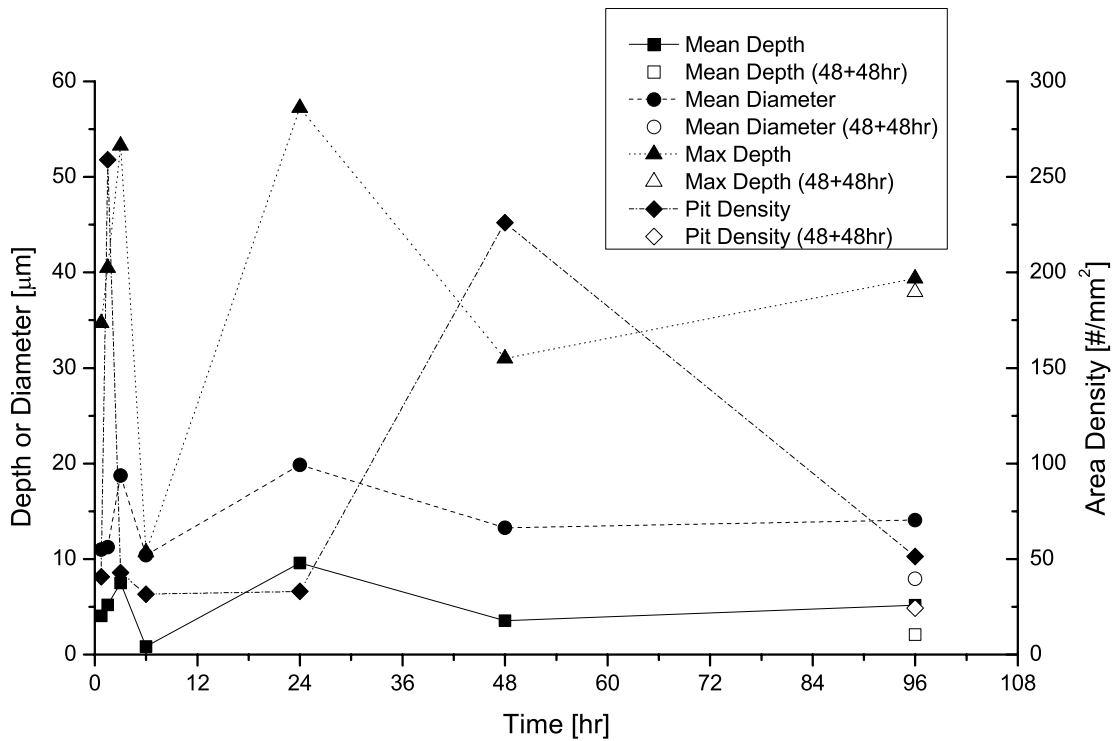


Figure 36 - Pitting results for Hexoloy (mean depth, mean diameter, max depth, and pit density) plotted as a function of exposure time.

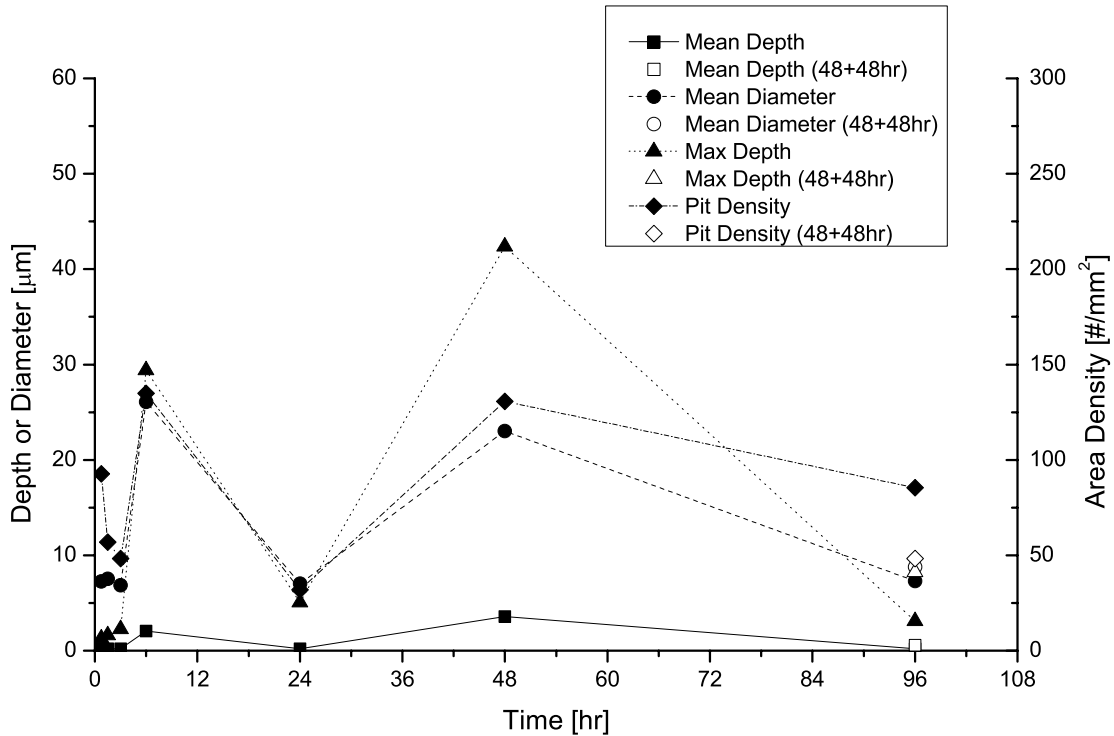


Figure 37 - Pitting results for CVD-SiC (mean depth, mean diameter, max depth, and pit density) plotted as a function of exposure time.

5.1.9 Microscopy Results

SEM and EDS were used to investigate the morphology and distribution of phases within the corrosion products from a plan view as well as a cross-section. Figure 38 shows an electron micrograph of the plan view of a Hexoloy coupon that had been corroded for 24 hr at 1000°C which contains corrosion product morphology that is representative of most of the samples. EDS analysis has shown that the surfaces are composed primarily of rough/pebbly silica with pools of smooth sodium sulfate and occasional protrusions of silica. The Na EDS map below the micrograph shows some of the pools of Na₂SO₄ that remain on the sample surface after 24 hours, which are surrounded by silica features (the S map is not shown but the S is concentrated with the Na).

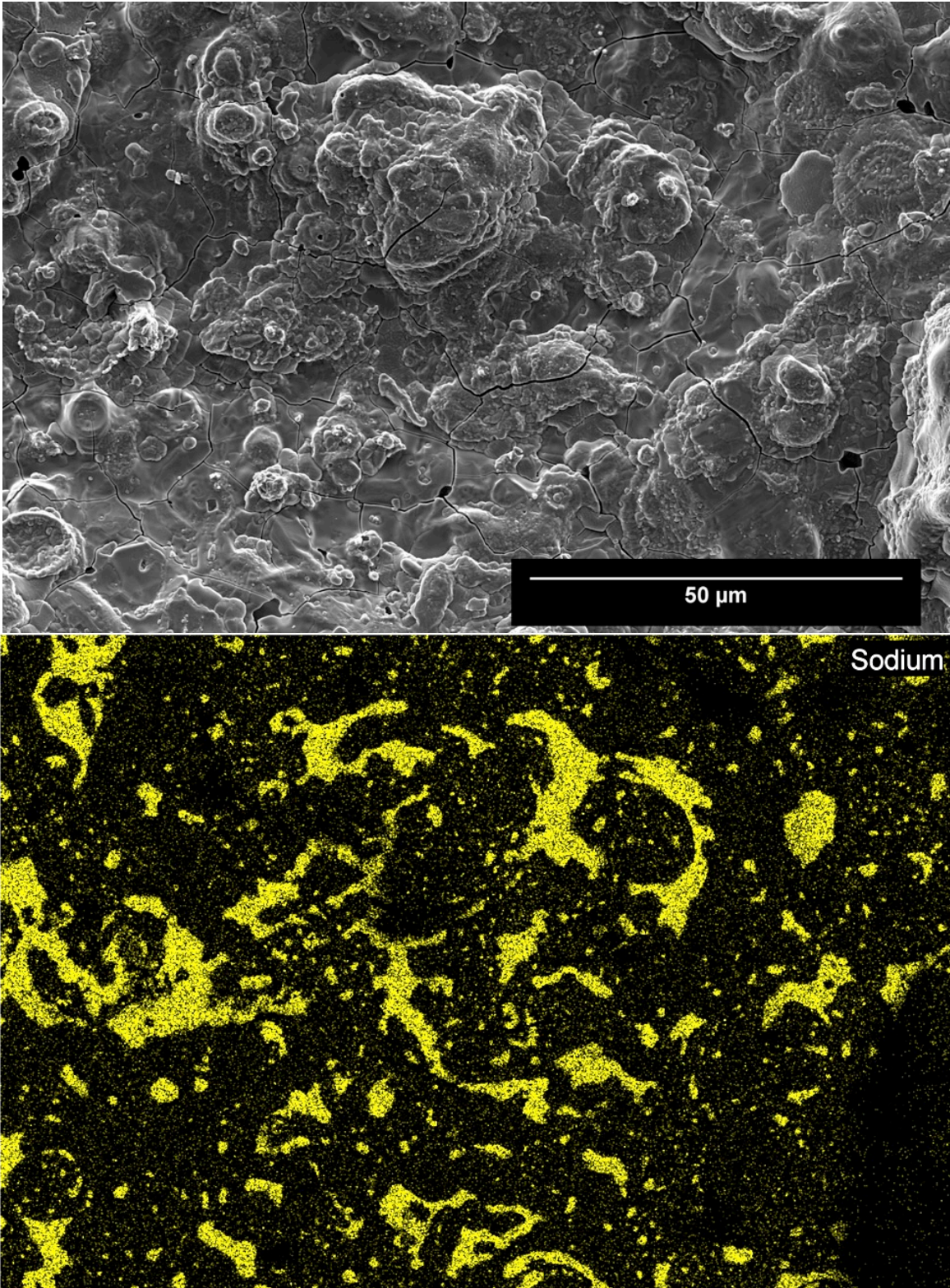


Figure 38 - Electron micrograph and corresponding Na EDS map of a Hexoloy coupon exposed for 24 hr at 1000°C.

Cross-sectional analysis was performed on each of the SiC coupon varieties exposed for 24 hours at 1000°C under 1000ppm SO₂/O₂. This analysis was not statistical or used to calculate averaged scale thicknesses (the ICP results provide this average scale data and the scales were found to be non-uniform across the sample surface) however it was used to look for differences in scale morphology between the various coupons. Cross-sectional analysis showed that there was not a significant difference in the scale appearance and composition between the various coupon types. The most noticeable difference was the presence of clear pitting in the Hexoloy coupons that corresponds with the pitting results mentioned earlier. One observed trend was that the thickness of the scale appeared to correlate with the fraction of sodium silicate in the scale. In areas with a thin corrosion product there was a continuous layer of silica at the scale-substrate interface with a thin layer of sodium silicate on top. In areas with thick corrosion products and large bubbles there still appeared to be a thin silica layer at the scale-substrate interface but the bulk of the corrosion product was sodium silicate.

Figure 39 is an electron micrograph of a CVD-SiC coupon cross-sectioned after exposure for 24 hr at 1000°C showing corrosion product morphology that is representative of the thick scale sections found on most of the samples. The SiC substrate is visible on the bottom of the micrograph and can be identified by its slightly rougher texture. The scale is visible on top of the substrate and has a varying thickness and a large fraction of pores or bubbles, some of which are now filled with epoxy. Figure 40 contains EDS maps that correspond to the micrograph in Figure 39. From these EDS maps the scale composition is found to be a mixed silica/sodium silicate, however there does not appear to be a sodium gradient. Note that boron and sulfur maps were not included as there was no evidence of

boron or sulfur in the scale. The sodium appears to be present in the top layer of silicate (which contains some lath-like silica features), and there is little evidence of sodium in the silica at the scale-substrate interface.

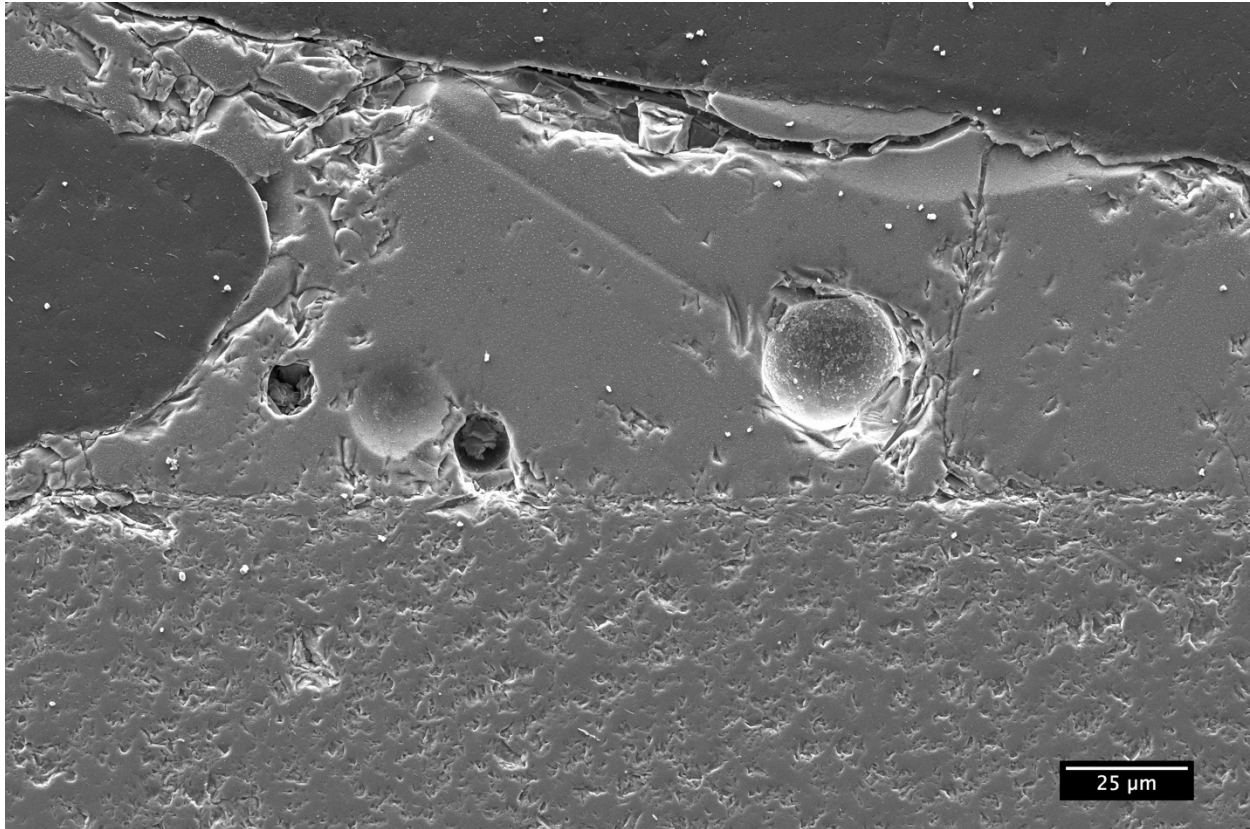


Figure 39 – Backscattered electron micrograph of a cross-sectioned CVD-SiC coupon exposed for 24 hr at 1000°C showing a thick section of the scale.

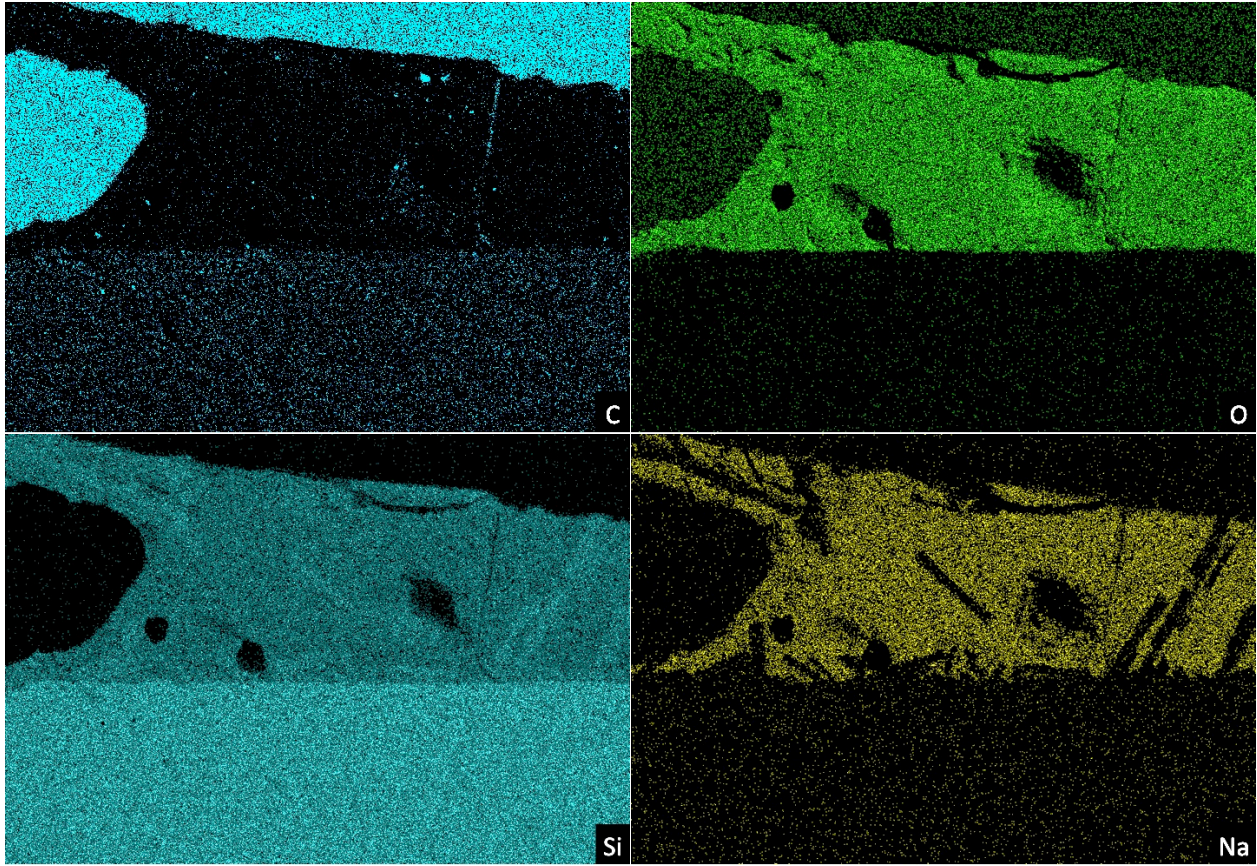


Figure 40 – EDS maps for (clockwise from top left) C, O, Na, and Si that correspond with the micrograph in Figure 39, showing a thick sodium-silicate layer which contains silica laths on top of a thin silica layer at the scale-substrate interface.

Figure 41 is an electron micrograph of a CVD-SiC coupon cross-sectioned after exposure for 24 hr at 1000°C showing corrosion product morphology that is representative of the thin scale sections found on most of the samples. Figure 42 contains EDS maps that correspond to the micrograph in Figure 41. Note that the magnification and image scale is different for these figures than for those corresponding to the thick scale. From these EDS maps the scale composition is found to be a thin sodium silicate on top of a thin silica layer at the scale-substrate interface.

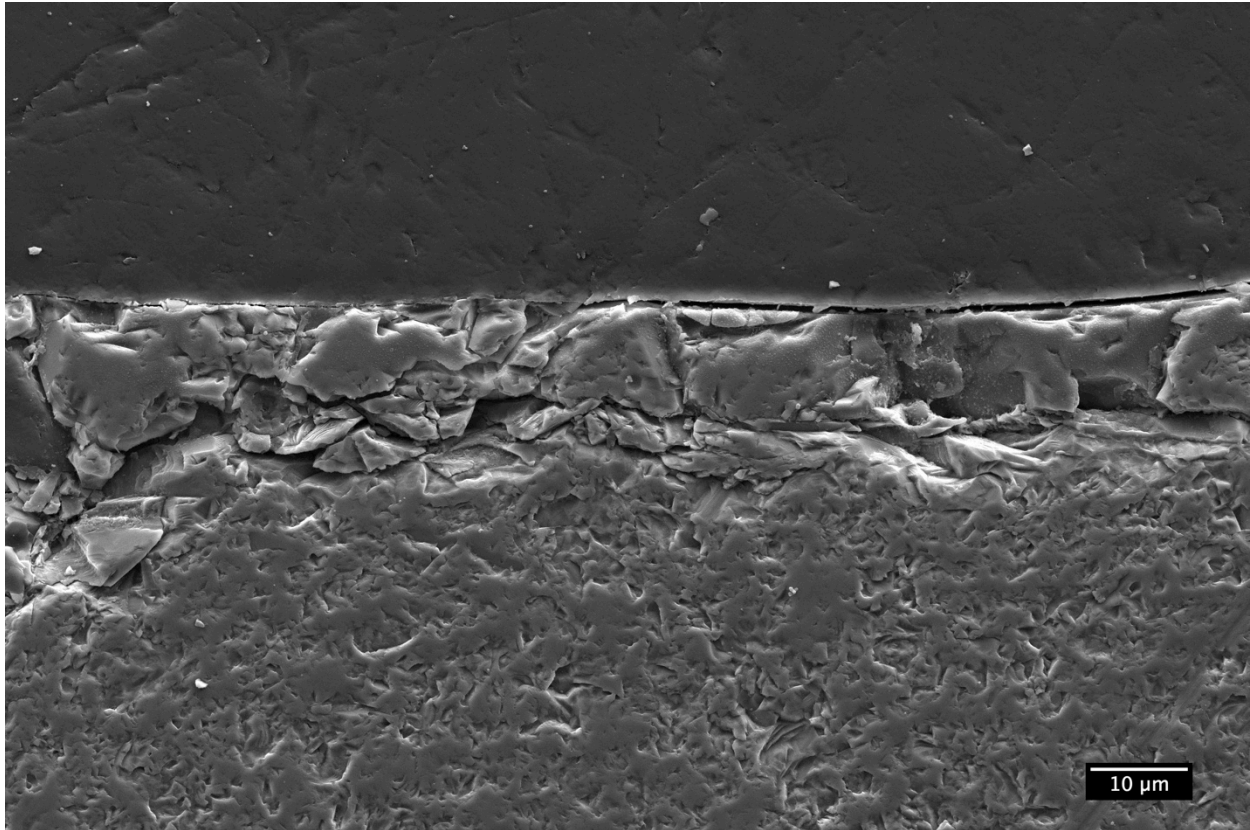


Figure 41 - Electron micrograph of a cross-sectioned CVD-SiC coupon exposed for 24 hr at 1000°C showing a thin section of the scale.

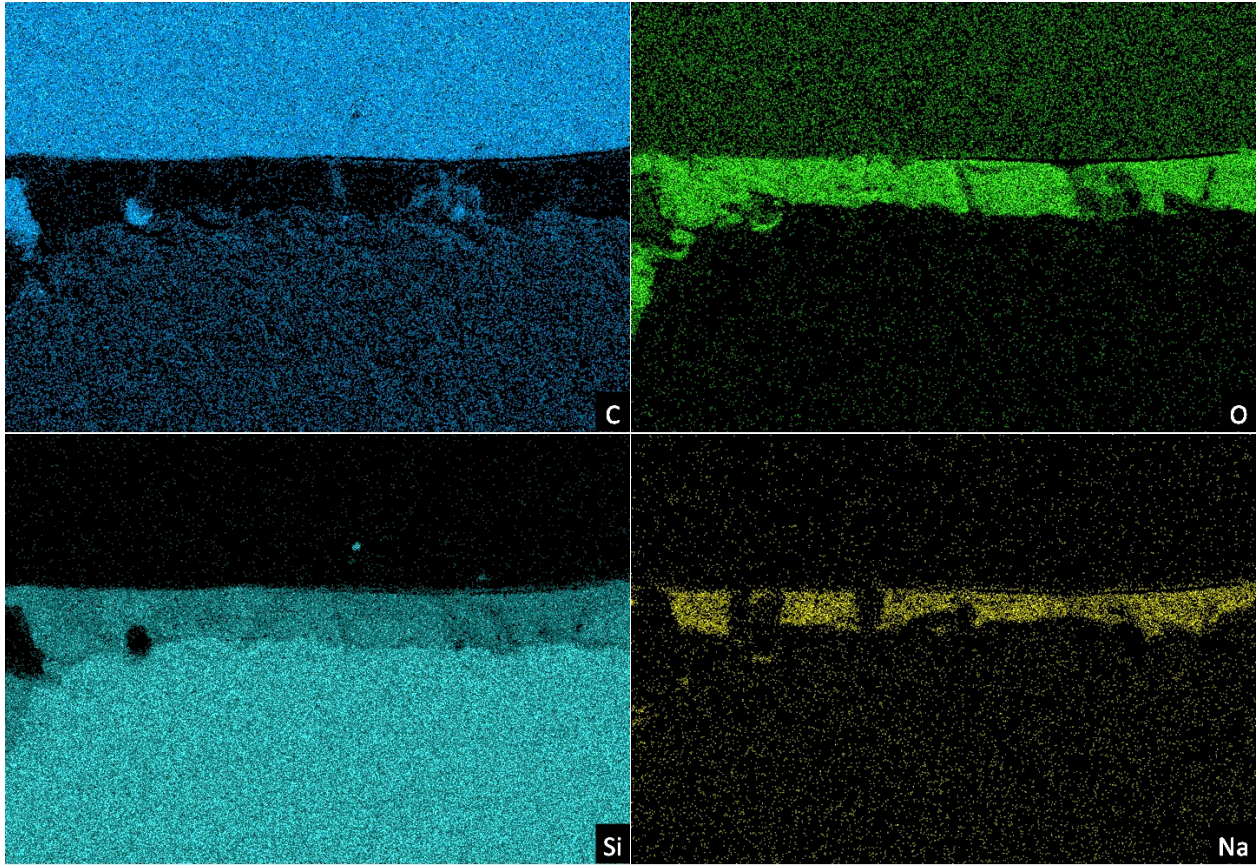


Figure 42 – EDS maps for (clockwise from top left) C, O, Na, and Si that correspond with the micrograph in Figure 41, showing a thin sodium-silicate layer on top of a thin silica layer at the scale-substrate interface.

Cross-sectional analysis also confirmed that both CVD-SiC and Hexoloy coupons exposed for 6 hours at 1000°C had already formed a continuous, protective, silica layer. This result is in agreement with the mass change and ICP values shown earlier indicating that after an initially rapid period of corrosion the formation of a silica layer slows further hot corrosion.

Electron micrographs of a Hexoloy coupon after corrosion and in between each of the ICP-OES digestion steps were taken to characterize the corrosion products formed and how they layer as well as correlation with any underlying features in the substrate, if possible. One corner of the Hexoloy coupon was chamfered and micrographs were taken at

this corner and stitched together. The area near the chamfered corner was imaged before exposure in the furnace to characterize the distribution of sintering aids. This micrograph is shown in Figure 43. The following Figures 44, 45, 46, and 47 show the same coupon at the same location after exposure in the furnace for 24 hr at 1000°C, after the water digestion step, after the HCl digestion step, and after the HF digestion step, respectively.

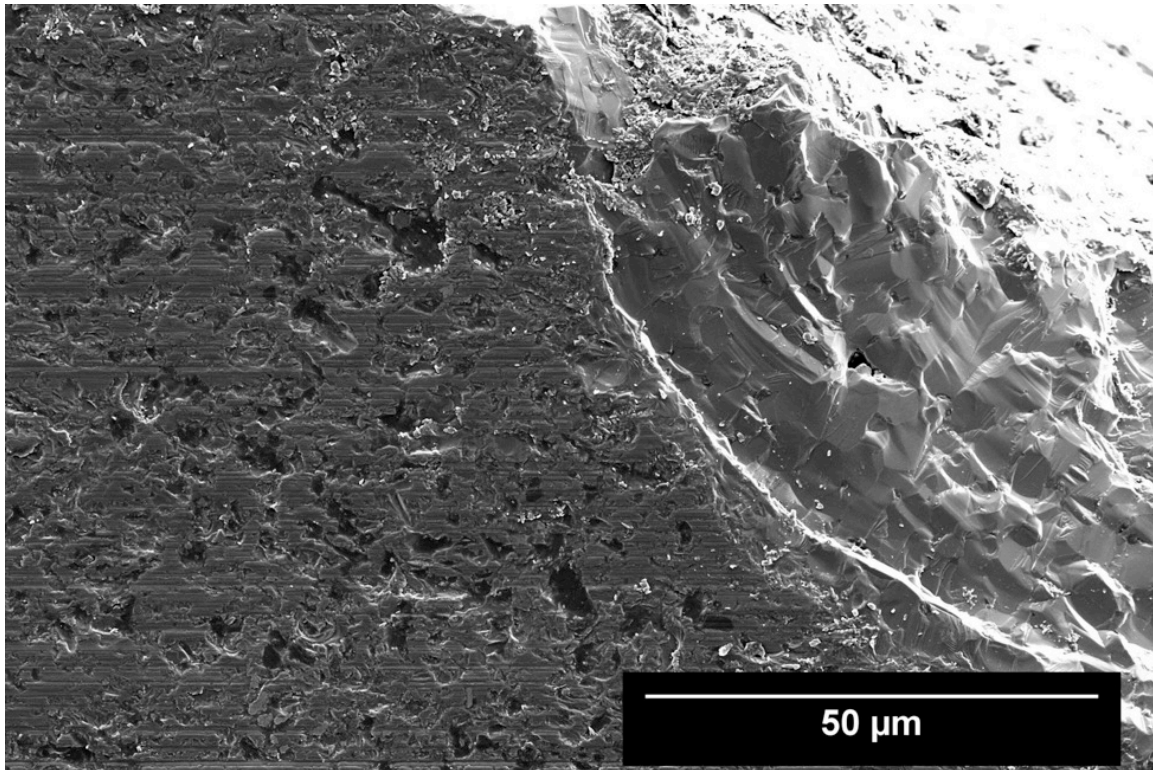


Figure 43 – Electron micrograph of a Hexoloy coupon before exposure.

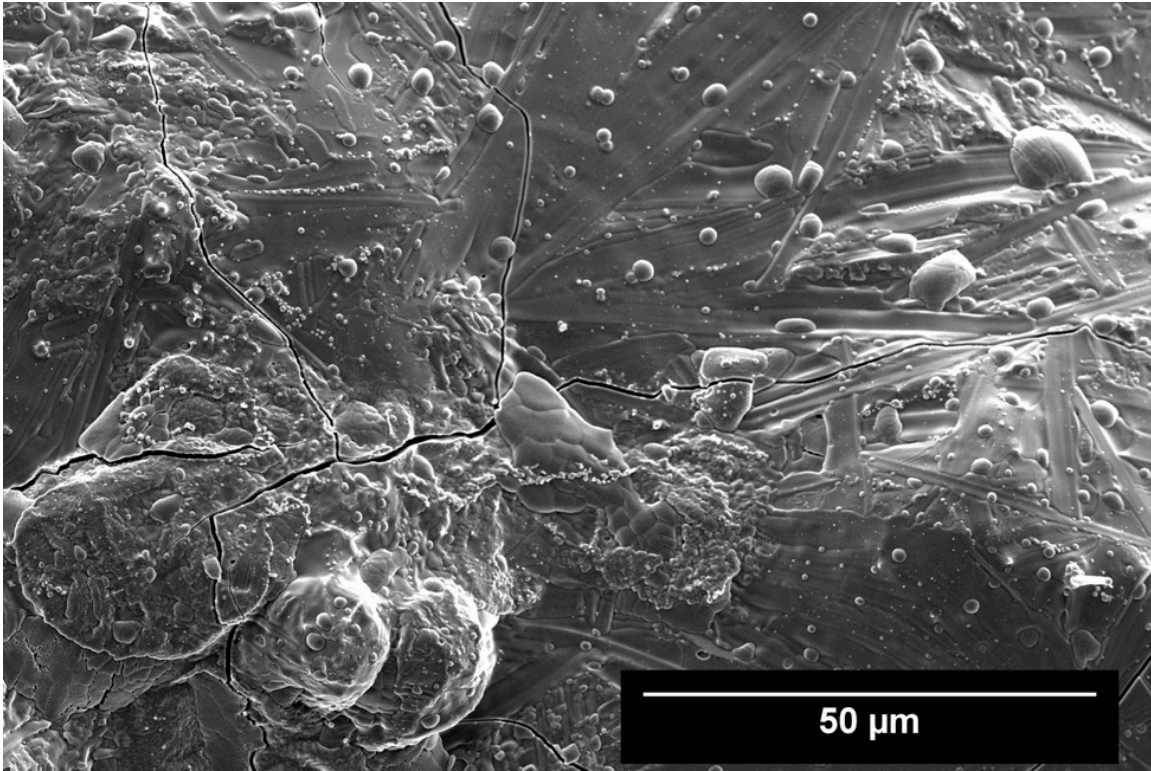


Figure 44 - Electron micrograph of a Hexoloy coupon after corrosion for 24 hr at 1000°C.

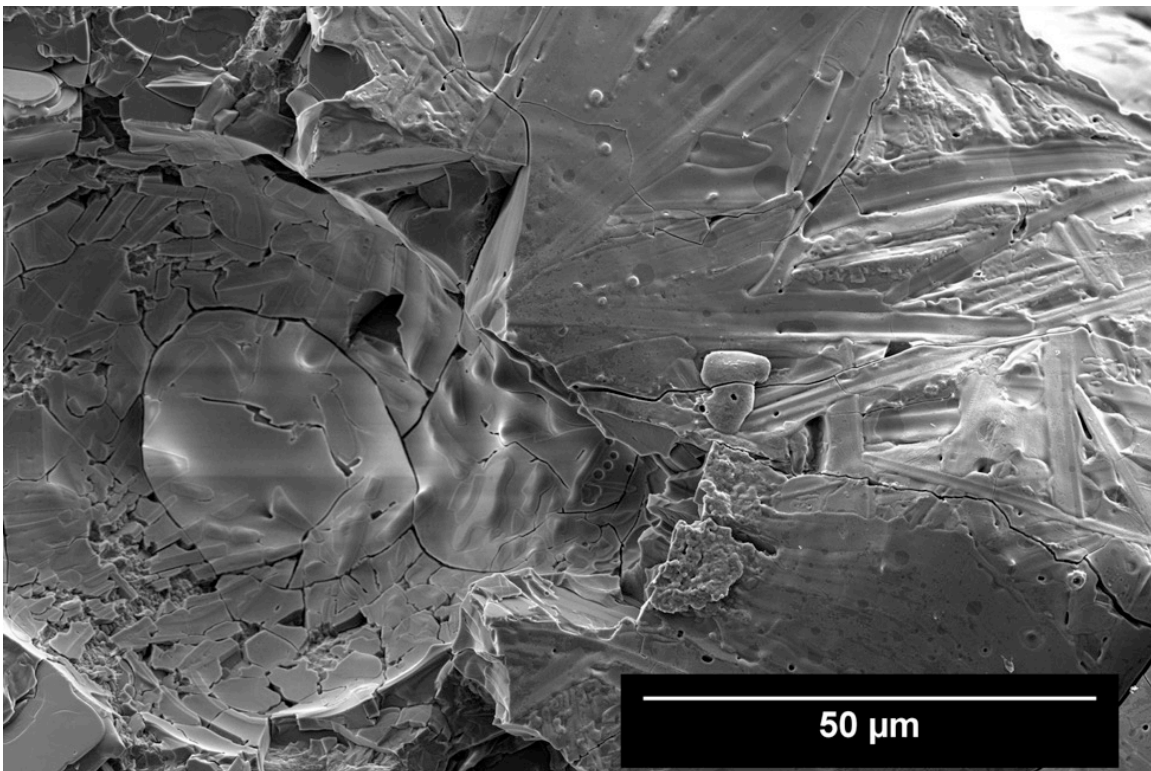


Figure 45 - Electron micrograph of a Hexoloy coupon after the water digestion step.

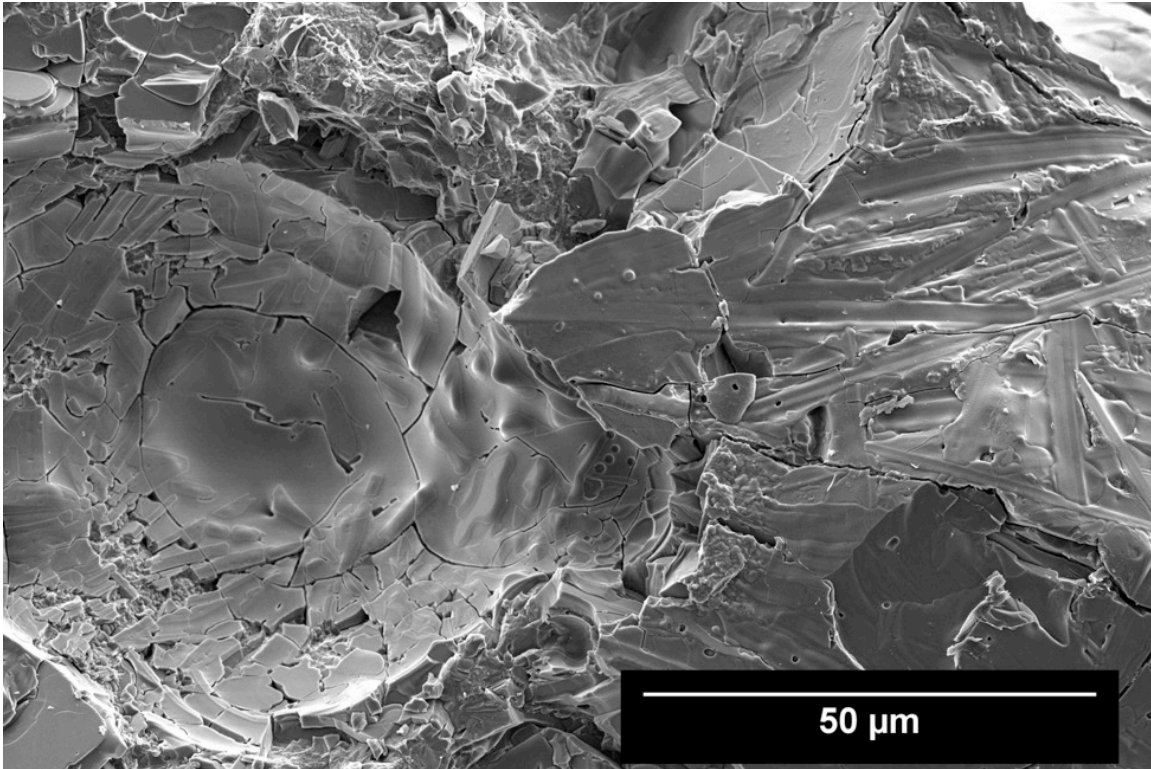


Figure 46 - Electron micrograph of a Hexoloy coupon after the HCl digestion step.

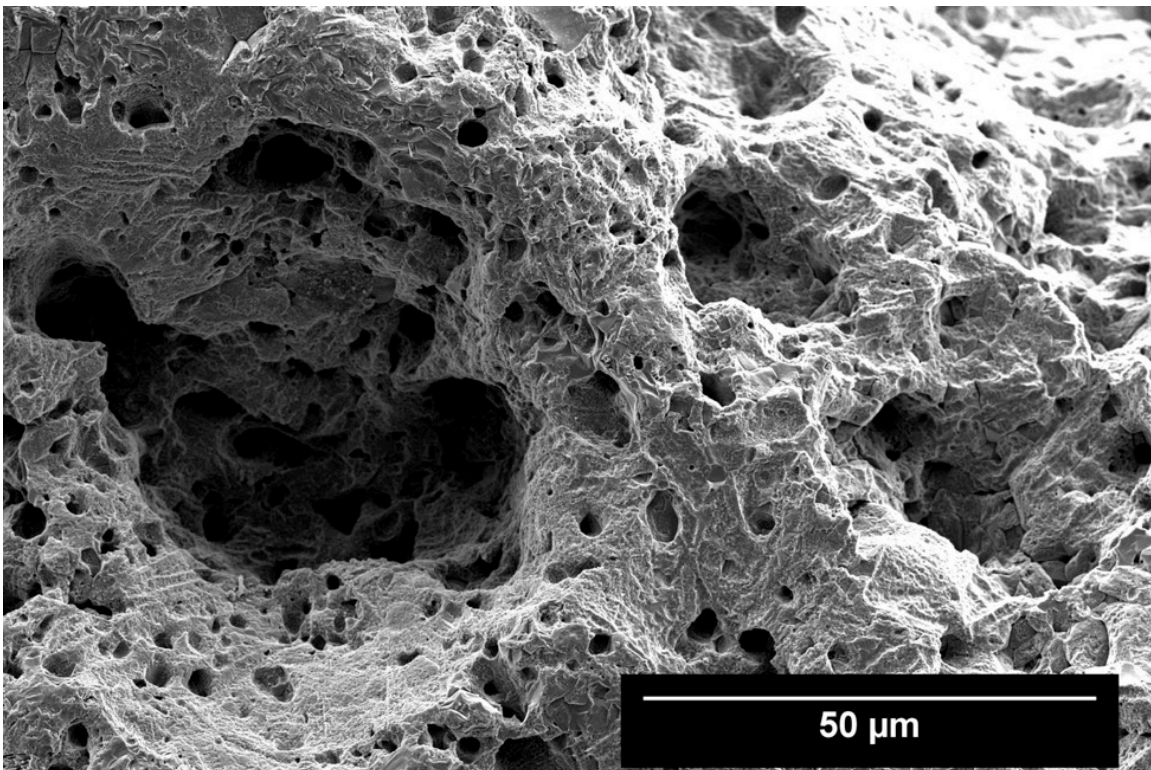


Figure 47 - Electron micrograph of a Hexoloy coupon after the HF digestion step.

These micrographs show a few corresponding features which help to explain the morphology and evolution of the scale. For example, the raised area on the left of Figure 44 is likely a silicate bubble based on the cross-sections that have been examined previously. In Figure 45 this bubble is no longer on the sample, and beneath the bubble is a pit that is filled with silica. There is little loss of this silica after the HCl digestion, although Figure 46 does show a few regions that change indicating a small loss of corrosion product. After all of the products are removed, in Figure 47, the large silica-filled pit corresponds well with a deep pit left in the Hexoloy substrate. With the exception of some of the very large pits the distribution of pit size and density is similar to that of the sintering aids but direct correlation to the features found in Figure 43 was not possible due to the surface recession.

5.1.10 X-Ray Diffraction Results

X-ray diffraction was performed on a selection of exposed coupons and the results are presented in Figure 48. These results confirmed that the Hexoloy coupons were hexagonal α -phase, while the CVD-SiC coupons were cubic β -phase. All coupons showed evidence of the silica phase Tridymite, which is known to be stabilized by the presence of impurities^{21, 31, 66}. The presence of Cristobalite was not found, however many of the Cristobalite peaks overlap with peaks for Tridymite and SiC making identification difficult. There were a few un-identified peaks on several of the spectra, including a peak found on all samples at a 2θ value of 40° . None of the samples showed evidence of crystalline sodium silicates. The diffraction patterns contained well-defined SiO_2 peaks indicating high crystallinity with little evidence of amorphous phases.

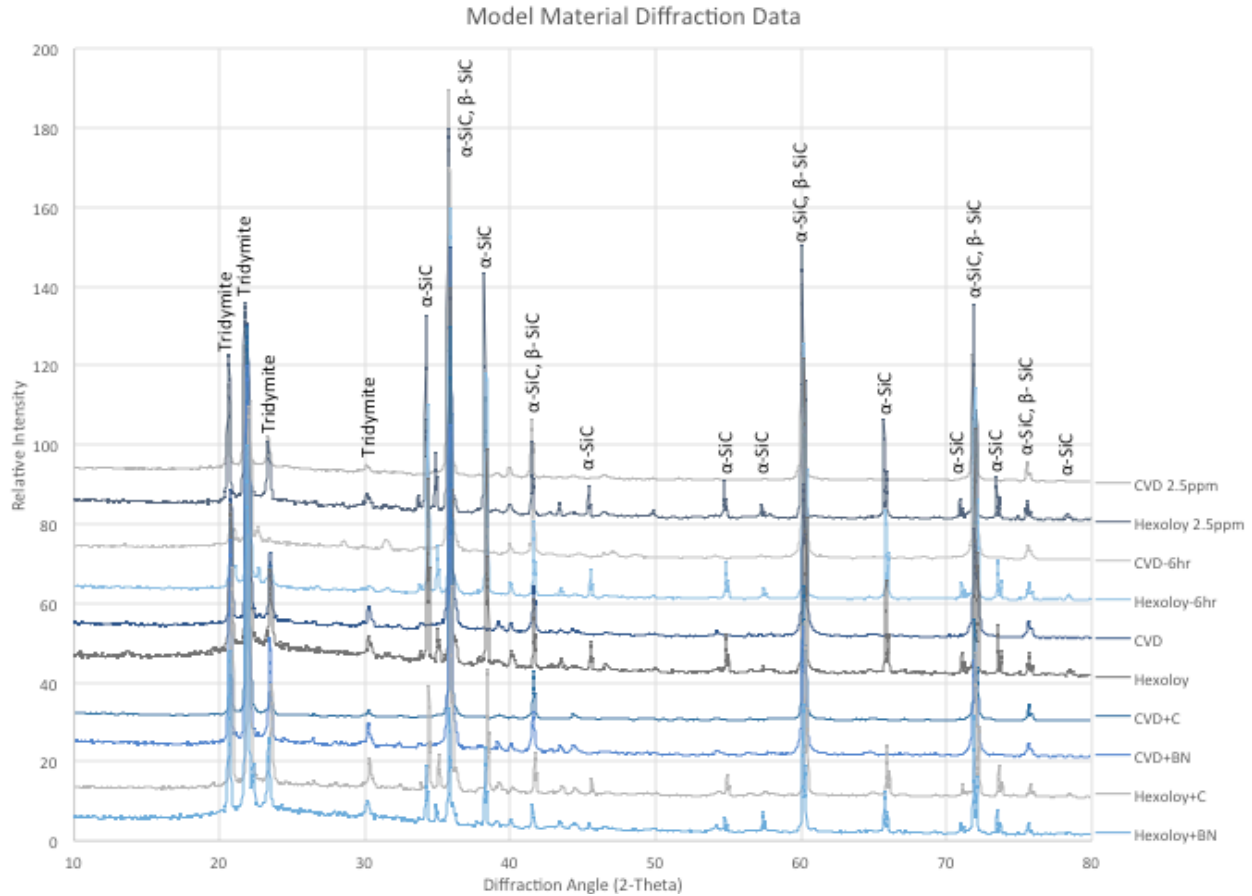
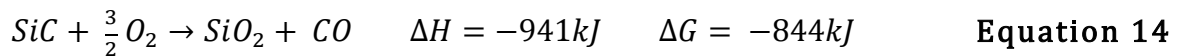


Figure 48 – X-Ray diffraction data for selected model material coupons.

5.2 Discussion

The time dependence of hot corrosion of SiC was found to depend on substrate material, but in general a rapid attack was observed with corrosion reaching a plateau. This plateau observed agrees with results obtained under similar conditions by Jacobson^{1, 2}, and is consistent with the formation of a protective silica layer. The more rapid attack of uncoated Hexoloy compared to uncoated CVD-SiC is likely due to the large fraction of carbon- and boron-based inclusions in the Hexoloy material. These results indicate that the presence of C- and B-containing phases in CMC matrix materials are likely to result in more severe hot corrosion, which is agreement with previous literature^{2, 16}.

A common mechanism was found to be responsible for the hot corrosion of SiC at temperatures between 950 and 1100°C with little to no observed corrosion at 900°C. Because a definitive rate law could not be determined, data were plotted with both linear (reaction controlled) and parabolic (diffusion controlled) fits (Figures 23 and 24). The values generated with a linear fit are between 70-80 kJ/mol. Possible reactions include the oxidation of SiC as shown in Equation 14, and the reaction between SiO₂ and Na₂SO₄ as shown in Equation 15, both of which have ΔH values that are inconsistent with these data.



If the mass changes are plotted as Log(Δm²) vs. 1/T then a parabolic rate law is assumed, which would be consistent with a diffusion controlled process. The values generated this way are between 140-160 kJ/mol. These apparent activation energy values for assumed parabolic mass loss (SiC consumed to form SiO₂) are in the same range as experimental values for the oxidation of Si and SiC (120-220 kJ/mol^{3, 21, 65, 67}), and are consistent with a rate controlled by diffusion of oxygen through an impure silica layer^{18, 21, 67-71}. Table 7 lists possible rate limiting steps for the hot corrosion of SiC, and whether the observations in this work support each of those options. Based on these observations we can say that our reaction is likely limited by the diffusion of oxygen through a silica layer at 24 hours (once a protective layer has formed), although there is a combination of oxidation of SiC and dissolution of SiO₂ by Na₂SO₄.

Table 7 – Possible rate-limiting steps for SiC hot corrosion.

Step	Activation Energy [kJ/mol]	Observations	
		Microstructure	Temperature Dependence
Oxygen Diffusion Inward	120-220	✓	✓
CO ₂ Diffusion Outward	340-460 ⁷²		
SiO ₂ Dissolution Reaction	295		
Gas Phase Diffusion	Unknown		
SiC Oxidation Reaction	-941		

By using a modification of a previously defined liquid digestion process¹ to remove the corrosion products for ICP-OES analysis the relative stability of corrosion products was explored. The microscopy that was done in between each of the digestion steps showed that the majority of the sodium silicate layer is removed by the water step which is consistent with the literature^{1, 51, 52}. A small amount of sodium silicate is removed by the HCl step leaving a thin, nearly continuous, silica layer that is removed in the HF step. The mass change after the HCl digestion step and the ICP-OES analysis of the HCl solution indicated that there were very little HCl soluble products that remained after the water digestion step (two orders of magnitude less than the amount removed in HF), so the presence of a large intermediate layer is not suspected. The ratio of Na to Si in the HCl solution indicates that the product removed is likely a sodium-silicate, however, it has been shown that HCl can leach Na₂O from sodium silicates leaving an insoluble silicate layer⁷³. EDS analysis of cross-sections showed a large incorporation of sodium into the silicate scale on top of a thin silica layer at the scale-substrate interface that is consistent with the ICP-OES results.

The silica layer that remains after HCl digestion is likely still Na-doped. This result is confirmed by the ICP-OES analysis of the HF digestion solution. The doping of silica with sodium ions will modify the silica network and allow for faster diffusion through the doped

silica²¹. This is expected to result in a less protective silica layer when Na is present in the corrosion products.

The SO₂ partial pressure dependence was found to have a minor impact on the amount of hot corrosion of SiC. The impact was most noticeable with the CVD-SiC coupons that generally had less corrosion than the Hexoloy coupons to begin with, so it appears that the chemistry of the Hexoloy coupons had a greater impact than the gas composition. As will be discussed in more detail in Task 3, the SO₂ partial pressures used in this study were very likely not low enough to move the melt chemistry into a region on the phase stability diagram where sodium silicates are predicted to form, and this agrees with the minor impact on amount of corrosion shown here.

The morphology of the scale changed with SO₂ partial pressure, with low SO₂ exposures containing a less bubbly scale and a larger fraction of crystalline laths. The XRD results indicate that the scale formation is predominantly crystalline tridymite, with no other crystalline silica or silicate phases present, so these laths are most likely the tridymite detected in XRD. This result agrees with the literature as tridymite has been shown to form in lath-like crystals⁷⁴, and is known to be impurity-stabilized^{21, 31, 66}. The stabilizing impurity in this case is suspected to be Na₂O, which should exist in higher quantities in the low SO₂ environments, leading to the larger fraction of laths in the low SO₂ coupons.

5.2.1 Hot Corrosion Mechanism

The proposed hot corrosion mechanism is shown schematically in Figure 49. This figure shows the progression of Na₂SO₄-induced hot corrosion for a SiC substrate. The corrosion begins with the rapid diffusion of oxygen through the molten salt layer leading to

formation of SiO_2 , $\text{CO}_2(\text{g})$, and $\text{SO}_3(\text{g})$ bubbles in the molten layer. As SiC continues to oxidize the reaction between silica and sodium sulfate leads to the formation of an increasingly thick sodium silicate layer which does little to hinder oxygen diffusion to the substrate. Once the silica layer is sufficiently thick and continuous the rapid corrosion of SiC slows and further corrosion is limited by the diffusion of oxygen through the silica layer. This mechanism is consistent with those proposed previously by Berthold⁵¹ and Jacobson¹.

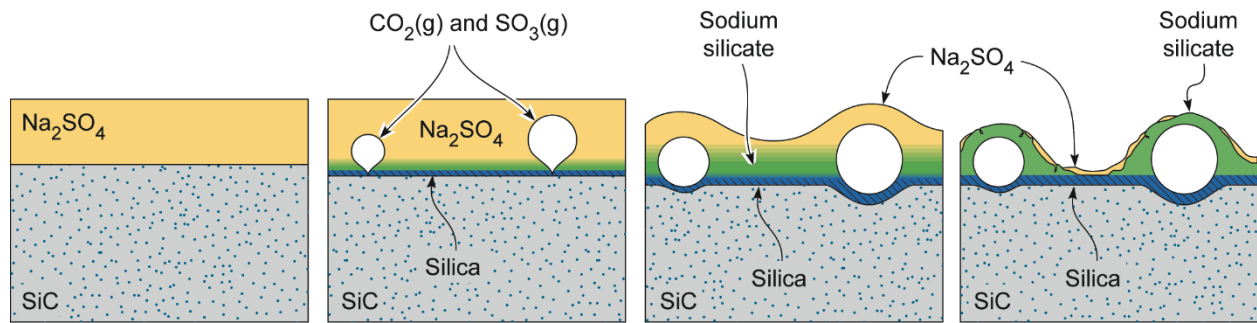


Figure 49 – Schematic illustrating the hot-corrosion of SiC by Na_2SO_4 resulting in a layered corrosion product consisting of a thin silica layer at the substrate-scale interface with a partially-porous mixed silicate on top as well as some residual sodium sulfate.

5.2.2 Chemistry Effects

The presence of a carbon layer did not appear to make the hot corrosion more severe for either substrate type. The mass change and total Si found in the corrosion products both show that the presence of a carbon layer either has no effect or has the effect of making corrosion slightly less severe. It is worth noting, that due to the wide distribution of the hot corrosion results the apparent protective nature of a C coating could be statistically insignificant. These results appear to be at odds with previous results demonstrating that carbon raised the Na_2O activity, creating a more basic corrosion

environment which induces more hot corrosion¹¹, however the total amount of carbon present in the 700 nm thick coatings may not be enough to affect the Na₂O activity of the molten salt. If the carbon coating is indeed providing some protective benefit this is most likely an artifact of the specimen geometry that would not occur in a CMC. The protective nature of the C films are proposed to come from one of two sources: (1) the presence of a continuous carbon layer effectively blocks contact between Na₂SO₄ and SiC and acts as a physical barrier to the oxidation of silicon carbide; and (2) the small amount of carbon raises the Na₂O activity temporarily which causes rapid corrosion and scale formation, the carbon is consumed and the basic conditions become acidic, allowing the thick layer of protective silica to shut off further oxidation.

The presence of a BN coating made the corrosion worse. This result was confirmed by the mass change results, total Si found in the corrosion products, and the pitting results. It was observed that the presence of a BN layer increased the wetting of both aqueous sodium sulfate as well as the molten corrosion products and this likely lead to increased attack (or attack over a greater area of the coupon), however the main factors leading to the increased attack where likely chemistry related. BN oxidizes to form B₂O₃ which reacts with SiO₂ to form a borosilicate glass. Borosilicate glasses have a lower melting temperature, a lower viscosity, and a higher oxygen diffusivity³² than SiO₂ and are therefore less protective than pure silica. The phase stability diagrams shown in Figures 1 and 3 illustrate the Na₂O activity range over which B₂O₃ or SiO₂ are expected to be soluble in Na₂SO₄ at 900°C. The Na₂O activity under 1000ppm SO₂/O₂ is predicted to be 1x10^{-13.6}, which indicates that SiO₂ is not expected to be soluble in Na₂SO₄ while B₂O₃ is soluble in Na₂SO₄. This is consistent with work by Poerschke showing a significant reaction between

B_2O_3 and Na_2SO_4 relative to that observed for SiO_2 and Na_2SO_4 in thermogravimetric studies under argon⁷⁵. This predicted solubility also corresponds with the high concentration of Na found in HF-soluble corrosion products on BN-coated coupons which is indicative of a greater reaction between the salt and the oxides as shown in Equation 4 for SiO_2 and Equation 10 for B_2O_3 .

The hot corrosion of Si coupons was found to be much lower than that of SiC. This indicates that the presence of residual Si in CMCs processed via melt infiltration should not degrade the hot corrosion resistance of those composites. Furthermore, the residual Si may act as a Si reservoir aiding in the formation of a protective silica layer as Si will preferentially oxidize before any of the other components of the CMC (SiC, BN, etc.) according to the Ellingham diagram in Figure 6.

5.3 Conclusions

Hot corrosion was found to initiate rapidly and reach a plateau by 24 hours. The initiation was quicker in the case of sintered- α (Hexoloy) SiC which contained C- and B-based sintering aids while the pure CVD-SiC had a slower initiation. The rapid onset was confirmed by mass change data, pitting results, and ICP-OES analysis of the removed corrosion products. It was found that C- and B-based sintering aids in the matrix materials have a negative effect on the hot corrosion performance of SiC leading to increased corrosion of Hexoloy as compared to the corrosion found for CVD-SiC.

The temperature dependence of the salt-deposit-assisted corrosion of SiC was found to be consistent with the diffusion of oxygen through a continuous silica layer formed after

24 hours, with an apparent activation energy in the range of 140-160 kJ/mol at temperatures between 950 and 1100°C. Minimal corrosion was observed at 900°C.

Hot corrosion of pure Si was found to be much slower and less severe than that of SiC, indicating that residual Si may be beneficial in CMC matrices. The presence of a carbon layer on SiC did not worsen hot corrosion, and in fact may have provided some measure of protection to the substrate. A BN layer on SiC, on the other hand, did result in more severe corrosion attack on both types of SiC substrate.

The step-wise dissolution of SiC hot corrosion products resulted in a combination of residual salt and sodium silicate scale removal in the water solution and silica removal in an HF solution. Negligible sodium silicates were removed in an intermediate HCl digestion step. These results are consistent with the two-layer assemblage of corrosion-products observed by EDS.

5.4 Recommendations for Future Work

It would be valuable to explore the effects of time and temperature on the hot corrosion behavior of the BN-coated model materials. Varying temperature between 900 and 1100°C would allow for exploring whether the presence of boron affects the kinetics of oxide layer growth by altering the silicate scale properties. Additionally, since BN is known to oxidize and form boria (which has a low melting point) it would be interesting to see if that liquid scale allows for additional corrosion at lower temperatures than was observed here.

Further exploration of hot corrosion at short times would be valuable not only for the BN-coated model materials but also for the uncoated materials. Conducting exposures

between 15 minutes and 6 hours followed by detailed microscopy of cross-sections should allow for characterization of initial scale formation. The presence of a continuous silica layer is shown at longer times, but based on the results shown in Figure 20 and Figure 21 the scale is expected to form at much shorter times.

Exploration of higher temperatures, up to 1200°C would be valuable as well, however the furnace used in this study was limited to 1100°C. Exposures using a higher temperature furnace would not only allow for a greater kinetic exploration but a closer simulation of the extreme temperatures inside a combustion environment.

6 Task 2 – Hot Corrosion of CMC Materials

6.1 Results

6.1.1 Material Characterization

The composite materials used in this task were referred to by their abbreviated names as described in Table 3, to simplify discussion. The CVI-F and MI-F coupons were exposed to an HF solution to determine the stability of the coupons in the most aggressive of the ICP digestion steps. The coupons were exposed to the solution with the seal-coat ground off of one face as with the coupons exposed in the furnace. The MI-F coupon experienced a relatively large mass loss in HF of 5.1 mg/cm², while the CVI-F coupon experienced a comparatively low mass loss of 0.05 mg/cm². For reference the mass loss experienced by the baseline Hexoloy coupon exposed to the complete ICP digestion process in Task 1 was 0.23 mg/cm². As mentioned in the experimental details, the MI-F coupon will not be discussed or shown in as much detail as the CVI-F coupon due to proprietary restrictions.

Coupons for furnace exposure were imaged in the SEM with the seal coat ground off to characterize the microstructural features found in the composites before corrosion. The micrograph in Figure 50 shows the CVI-F composite with its woven architecture before exposure in the furnace.

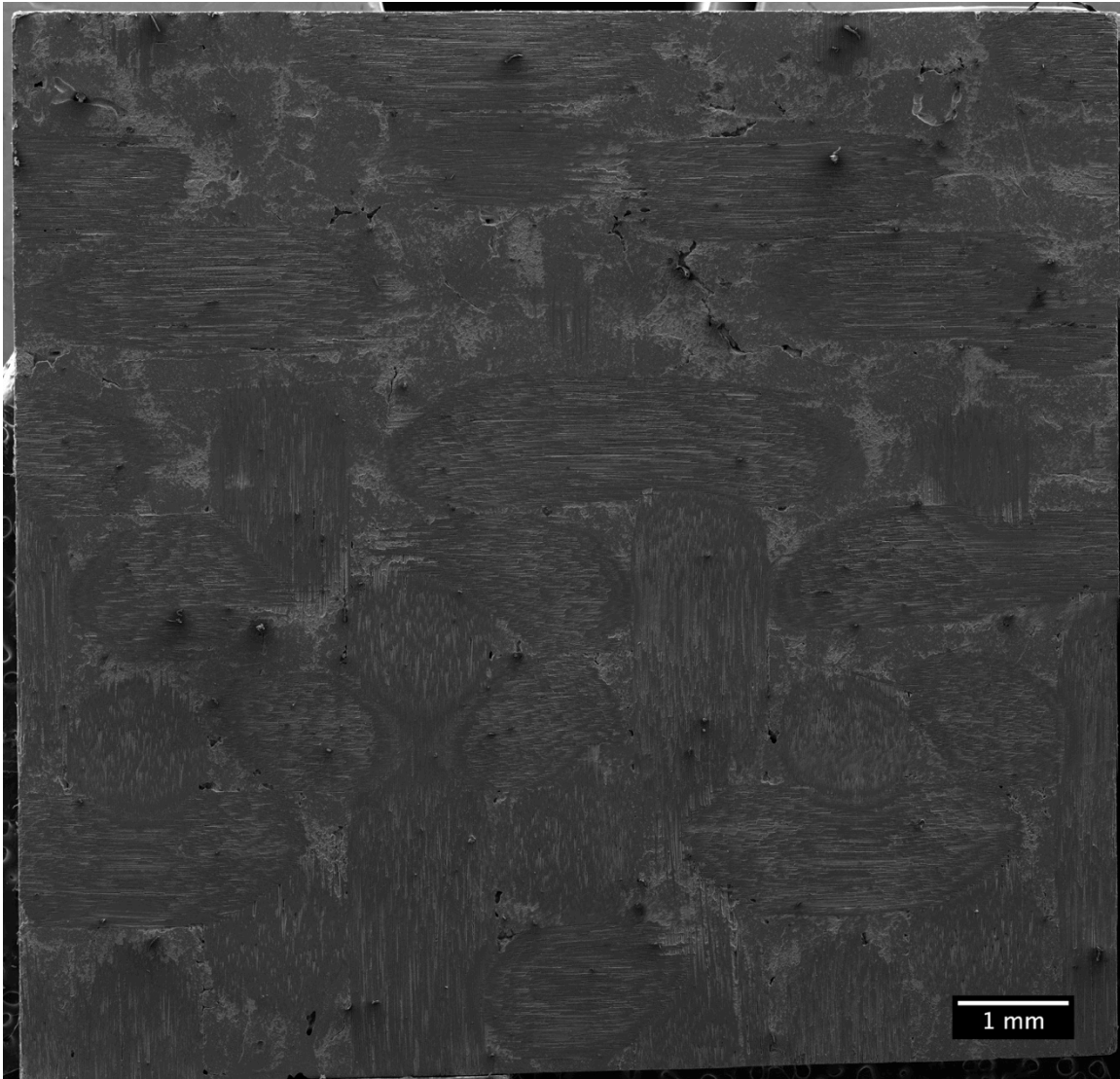


Figure 50 – SEM micrograph of the one of the CVI-F composites with the seal coat ground off before exposure in the furnace.

Based on SEM characterization the microstructure and likely processing steps of the CVI-F composites were elucidated as described in the following paragraph. The CVI-F coupons are comprised of woven tows of BN-coated Sylramic fibers. These woven tows are then initially coated with a dense CVD-SiC layer to protect the interphase during subsequent matrix processing. Following this process, a slurry containing SiC particles is infiltrated and pyrolyzed to fill many of the voids. Finally silicon is melt-infiltrated to fill any remaining porosity. Each of these features are shown in the micrographs in Figure 51

where electron back-scatter imaging is used to reveal the phase contrast. This process used to create the matrix leaves some very large voids, most often where fiber tows overlap, which are shown in the micrograph in Figure 53. Additionally, on a shorter length scale there are small voids and porosity as shown in Figure 51 as well as compositional inhomogeneities between boron-rich particles (which show up as black spots), SiC particles, and MI Si. It was found that the Hi-Nicalon-S fibers had a smoother finish upon polishing (and the fibers were less likely to exhibit chipping) than the Sylramic fibers, shown in Figure 52.

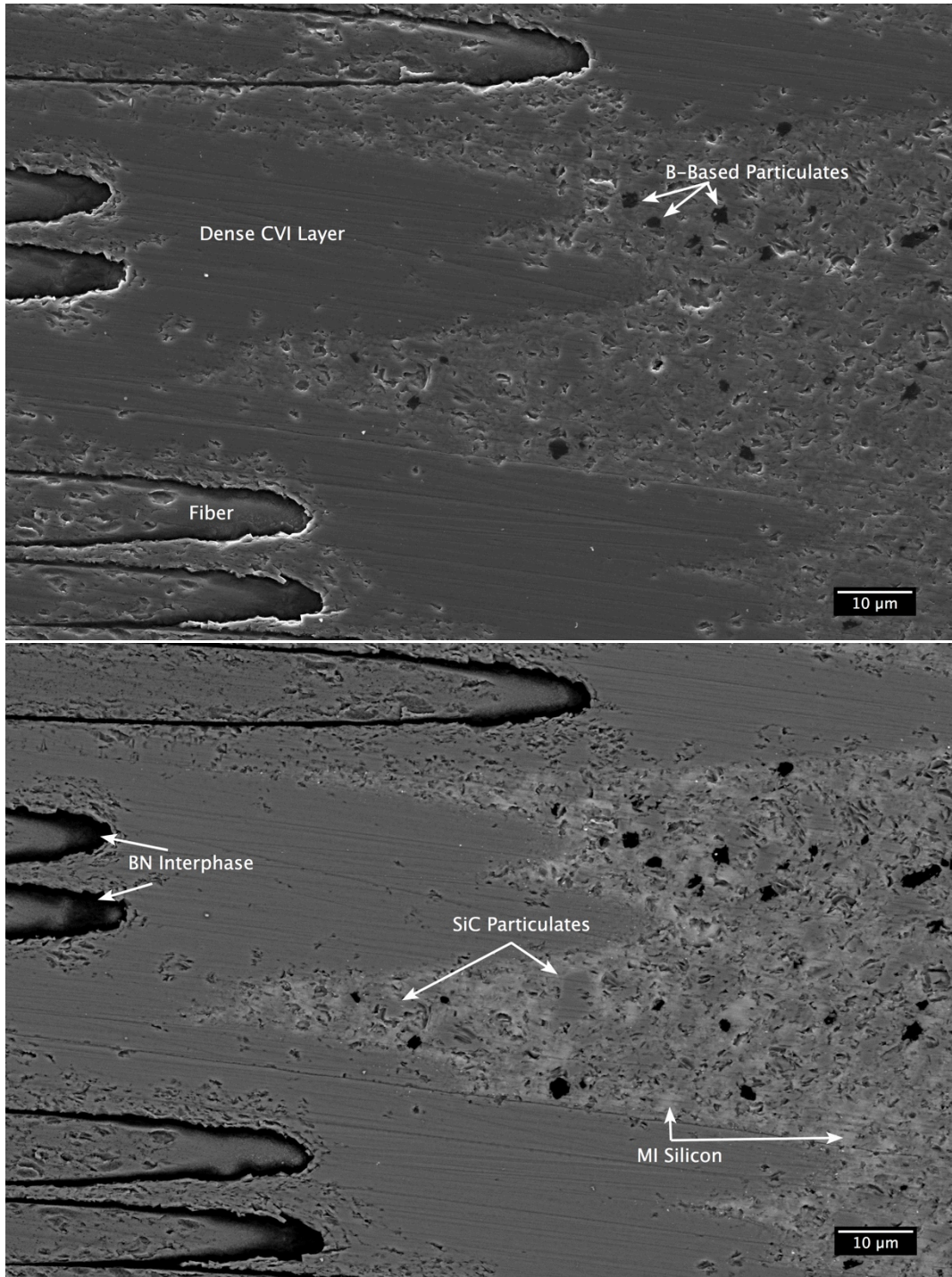


Figure 51 - Two micrographs of the CVI-F composite, SE on top and BSE on bottom. The micrographs show the SiC fibers, BN interphase, dense CVD layer, PIP slurry with SiC particulates, and MI Si.

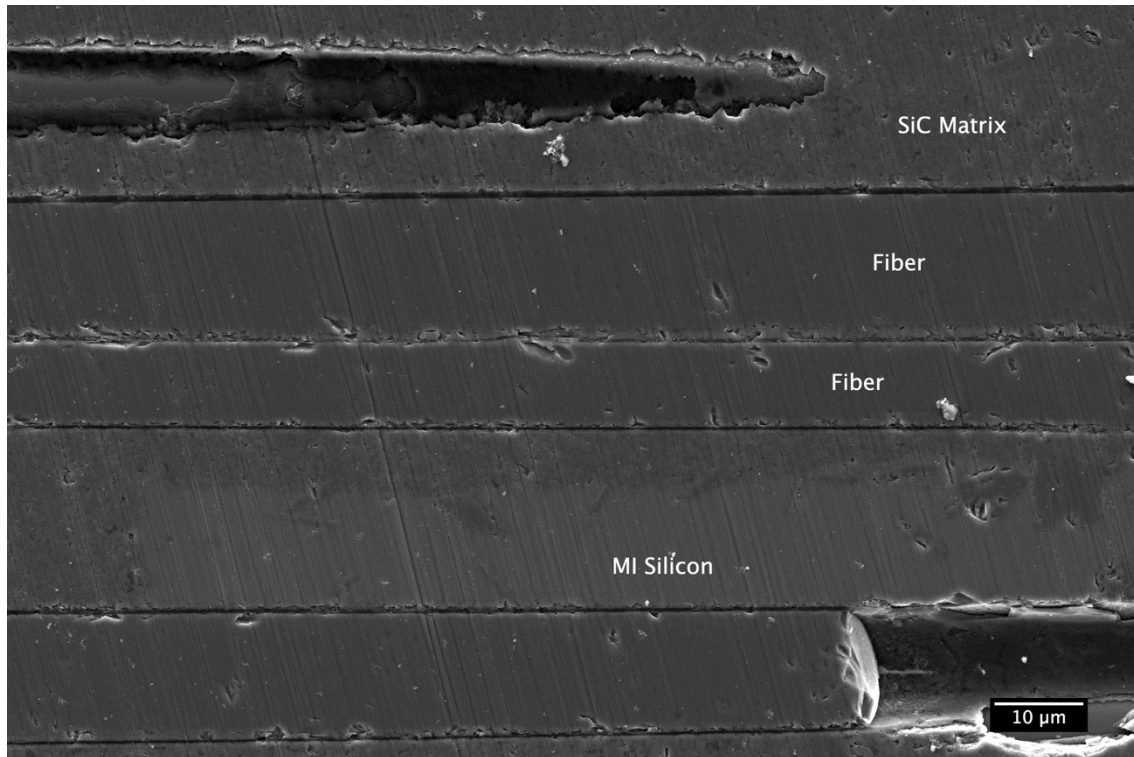


Figure 52 – Micrograph of the MI-F coupon showing the Hi-Nicalon-S fibers, BN interphase, SiC matrix, and residual Si from the MI process.

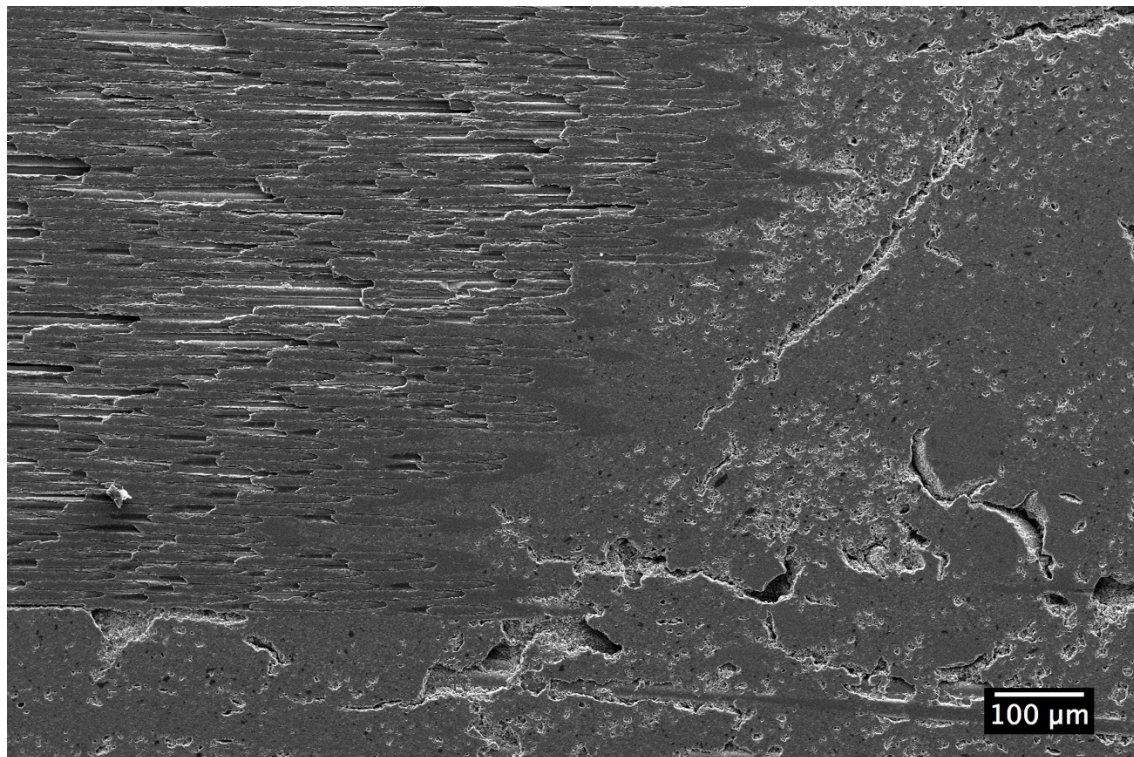


Figure 53 – SEM micrograph of one of the CVI-F coupons before exposure showing large voids present in the matrix between the Sylramic fiber tows.

The burner rig coupons were sectioned far from the hot zone (as described in Figure 11) to characterize the microstructural features found in the composites. Micrographs of one of each type of coupon are shown in Figure 54. The MI-BR coupons were found to be fairly dense, with some small porosity and voids, as shown in Figure 55. Figure 56 shows that in between the Hi-Nicalon fiber tows there are SiC particles surrounded by residual Si from the MI process.

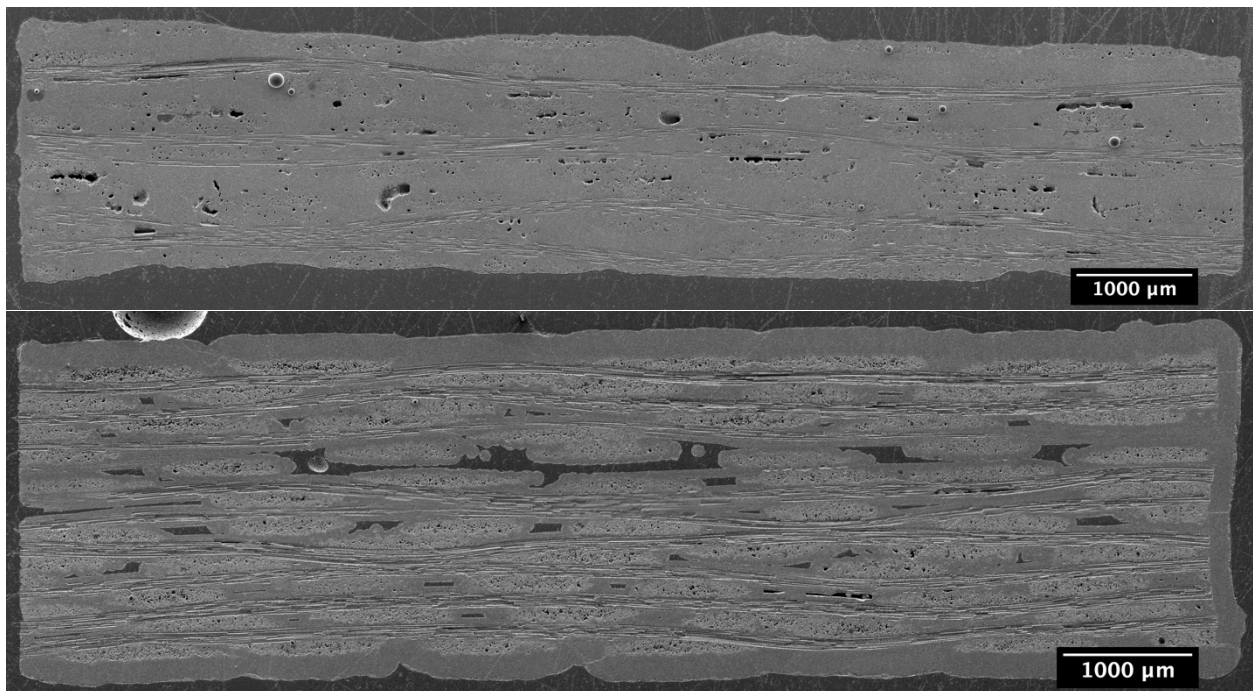


Figure 54 – SEM micrographs of the burner rig composite cross sections taken near the end of the coupon. The MI-BR composite is on the top and the CVI-BR composite is on the bottom.

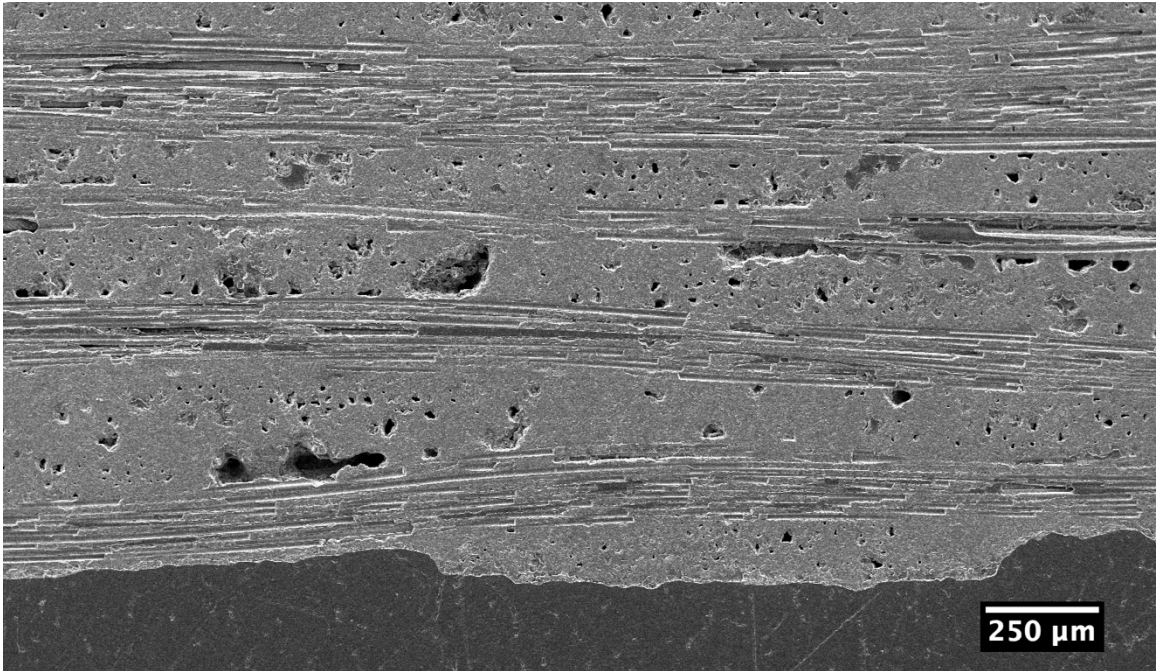


Figure 55 – SEM micrograph of an MI-BR coupon showing the fairly dense matrix with some small pores/voids.

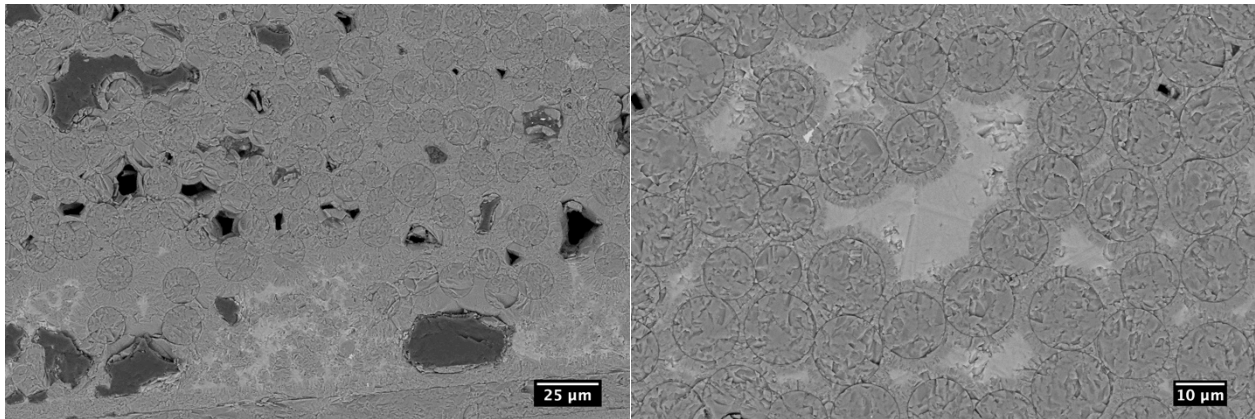


Figure 56 – SEM micrographs an MI-BR coupon showing the SiC particulates and residual Si in the matrix.

Figure 57 shows micrographs of the structure in the CVI-BR coupons. The CVI matrix is very locally dense (no small-scale porosity) but has very large voids in the matrix where pathways closed prohibiting further CVI deposition.

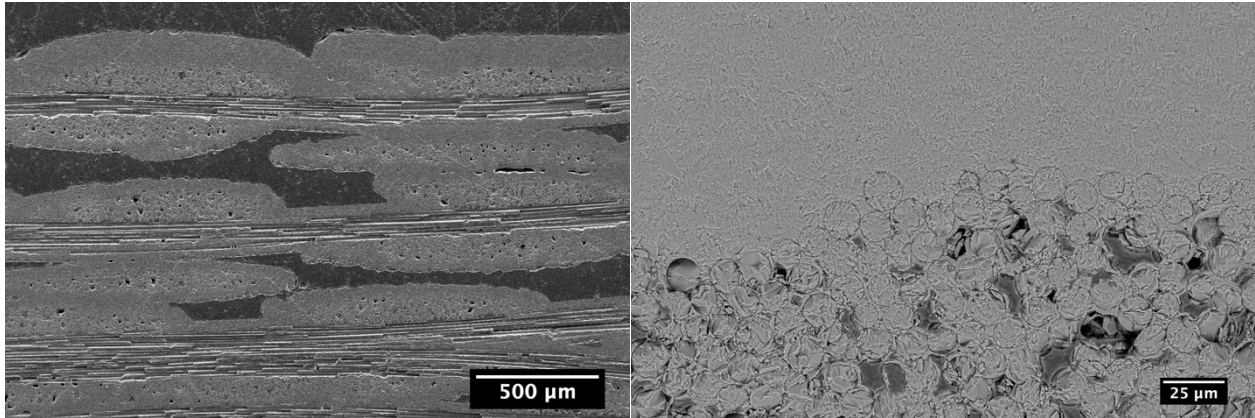


Figure 57 – SEM micrographs a CVI-BR coupon showing the large voids on the left and the locally dense SiC matrix on the right.

6.1.2 Furnace Exposed CMCs

CVI-F and MI-F coupons were exposed to two different gas atmospheres (both for 24 hours at 1000°C), either 1000 ppm SO₂/O₂ or 2.5 ppm SO₂/O₂. The coupons exhibited different corrosion product morphologies at each SO₂ level as shown in Figures 58 and 59. The coupon exposed in a low SO₂ environment had corrosion products that contained a large volume of crystalline laths, while the coupon exposed in the high SO₂ environment had corrosion products that were comprised of large bubbly structures.

All furnace-exposed CMC coupons were used for the stepwise digestion, imaging in between each step, and ICP analysis. This means that due to time and material constraints no CVI-F or MI-F coupons were examined in cross-section with the corrosion products intact.

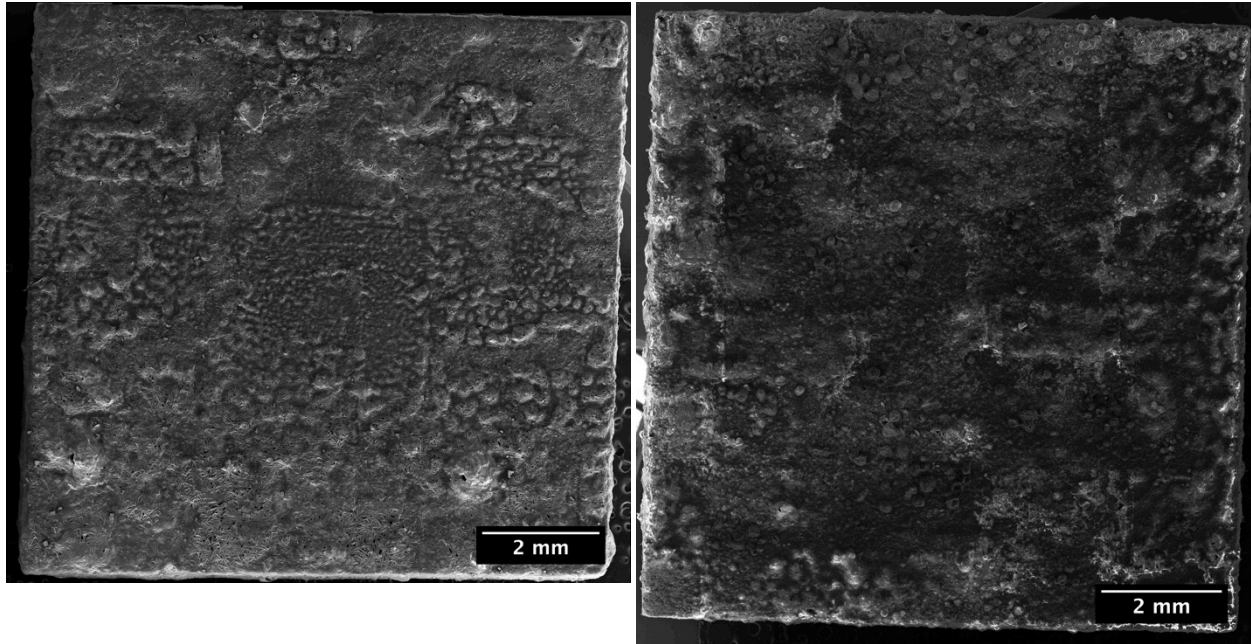


Figure 58 – Two SEM micrographs of the CVI-F composites after exposure for 24 hours at 1000°C. The coupon on the left was exposed in 2.5 ppm SO₂/O₂ while the coupon on the right was exposed in 1000 ppm SO₂/O₂.

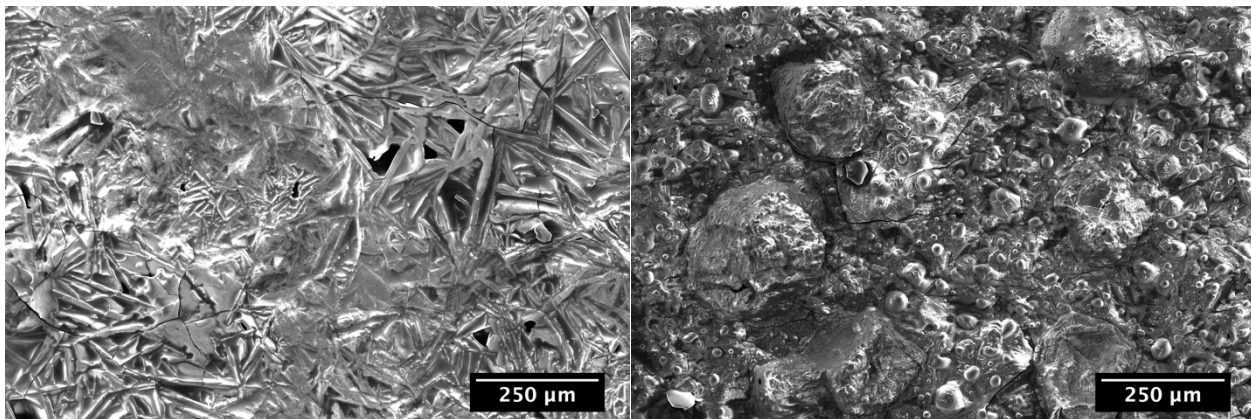


Figure 59 – Two SEM micrographs of the CVI-F composites after exposure for 24 hours at 1000°C. The coupon on the left was exposed in 2.5 ppm SO₂/O₂ and shows the crystalline laths while the coupon on the right was exposed in 1000 ppm SO₂/O₂ and shows the bubbly morphology.

The micrographs in Figure 60 show the coupons after the 48-hr water digestion step to remove the residual Na₂SO₄ and some of the corrosion products. As with the model materials in Task 1, the water digestion step removed the residual sodium sulfate as well as some amount of silicate.

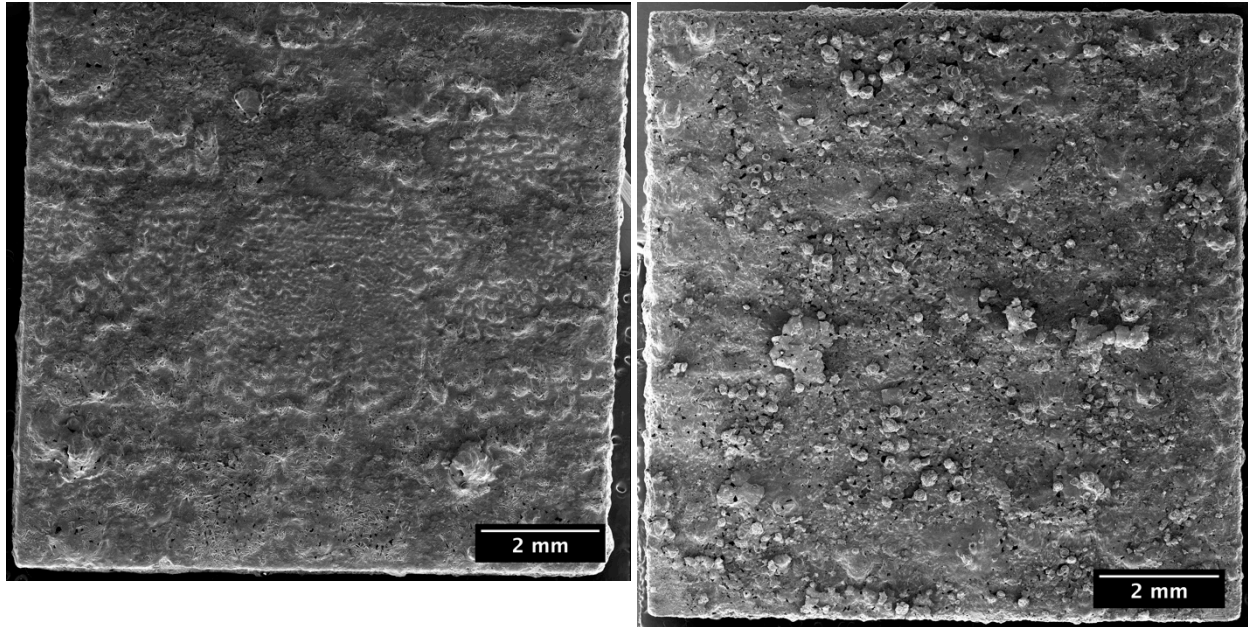


Figure 60 – Two SEM micrographs of the CVI-F composites after the water digestion step. The coupon on the left was exposed in 2.5 ppm SO₂/O₂ while the coupon on the right was exposed in 1000 ppm SO₂/O₂.

The micrographs in Figure 61 show the coupons after the HCl digestion step to remove some of the corrosion products. There is visually little change to the coupons, however unlike in Task 1 the HCl digestion step appears to have removed a fairly large fraction of borosilicate corrosion product as found in the ICP analysis.

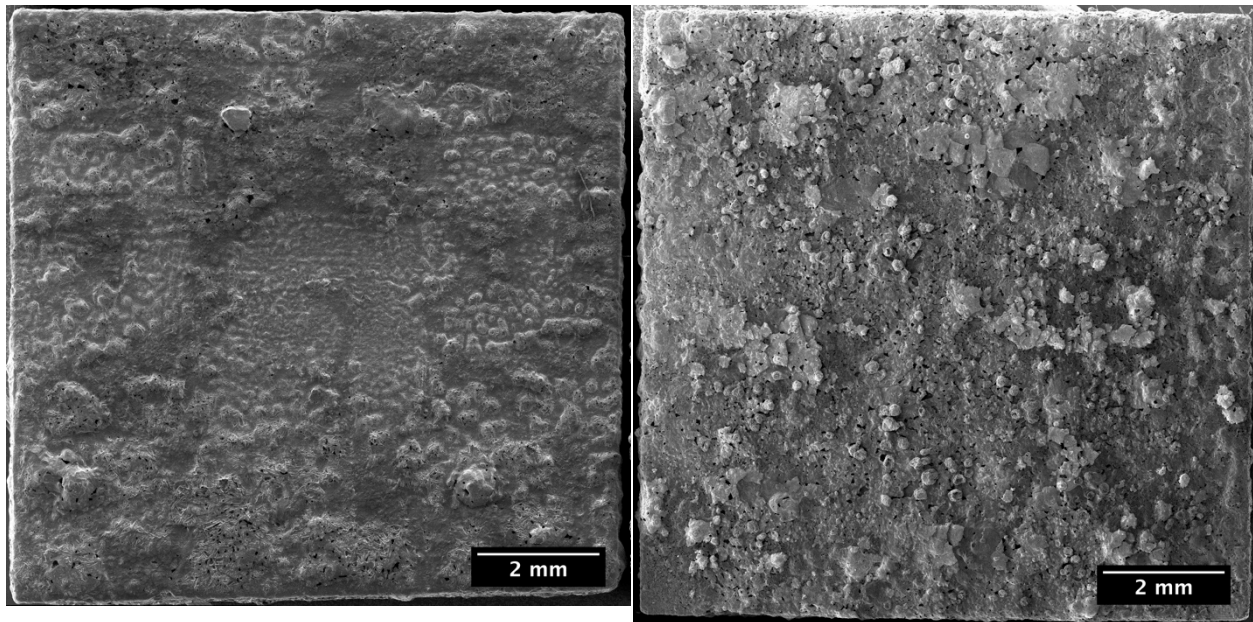


Figure 61 - Two SEM micrographs of the CVI-F composites after the HCl digestion step. The coupon on the left was exposed in 2.5 ppm SO₂/O₂ while the coupon on the right was exposed in 1000 ppm SO₂/O₂.

The micrographs in Figure 62 show the coupons after the HF digestion step. As with the model materials in Task 1 the HF digestion step removed the entire remaining silicate corrosion product and revealed an etched/pitted sample surface. These micrographs show significant attack of the matrix material in these coupons, particularly in regions containing large volumes of matrix material, such as the spaces between fiber tows. Figure 63 shows that there is significant pitting and attack of the Sylramic fibers on both the macro-scale as well as the micro-scale. The Hi-Nicalon-S fibers remained much smoother and less pitted after hot corrosion than the Sylramic fibers, as shown in Figure 64. Figure 65 shows some of the microstructural attack of the matrix where the dense CVI layers hold up reasonably well but the less homogeneous PIP/MI matrix appear to have larger attack. The model materials indicated that this might be the case when the Hexoloy coupons showed greater attack and corrosion rates due to both their boron content as well as the inhomogeneities in the material.

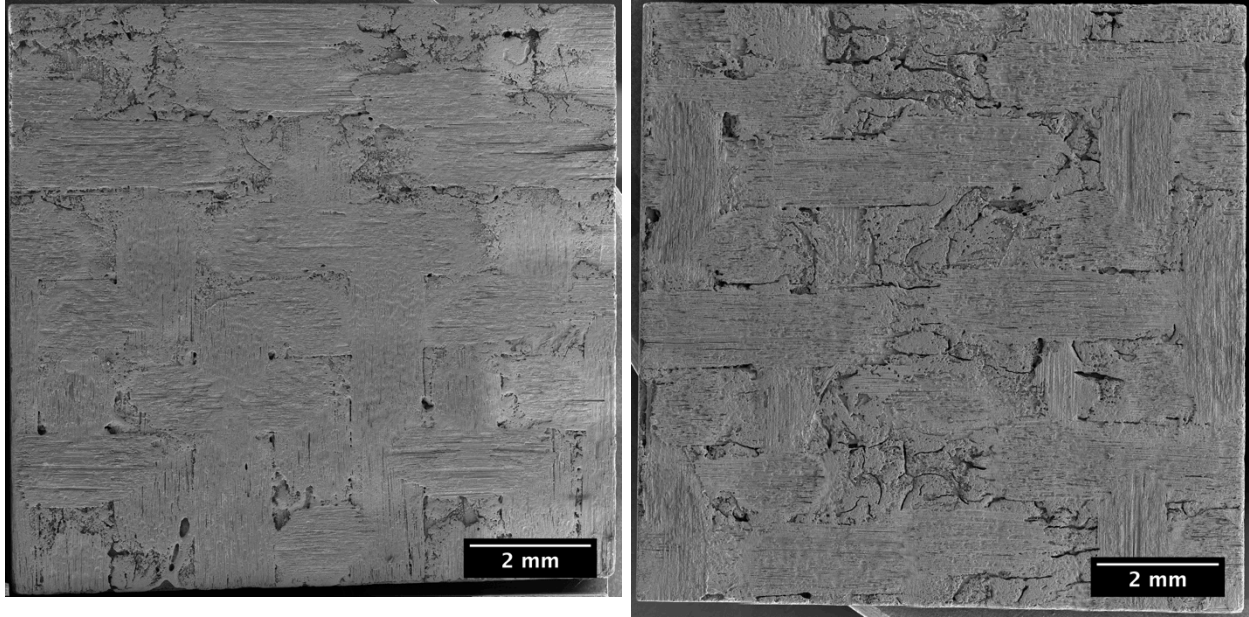


Figure 62 – Two micrographs of the CVI-F composites after the HF digestion step. The coupon on the left was exposed in 2.5 ppm SO₂/O₂ while the coupon on the right was exposed in 1000 ppm SO₂/O₂.

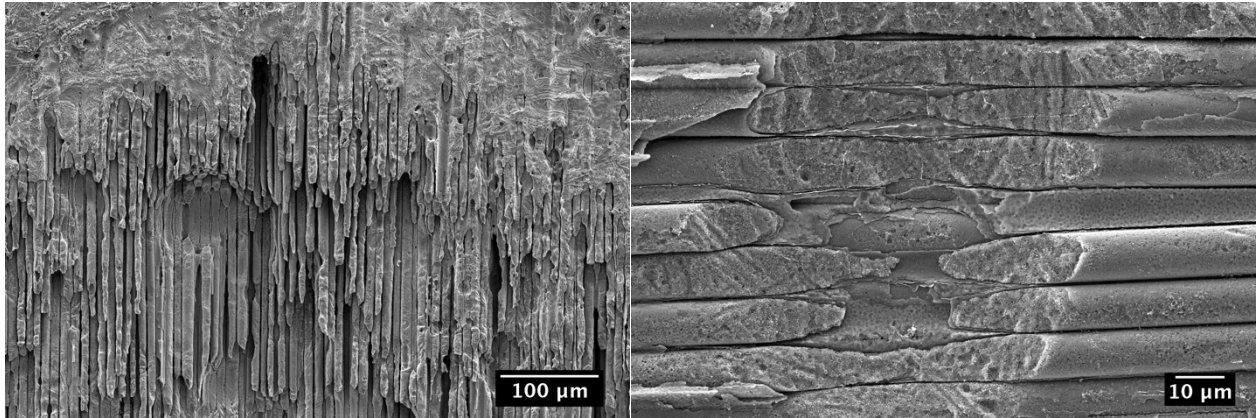


Figure 63 - Two SEM micrographs of the CVI-F composites after the HF digestion step showing the pitting and attack of the Sylramic fibers.

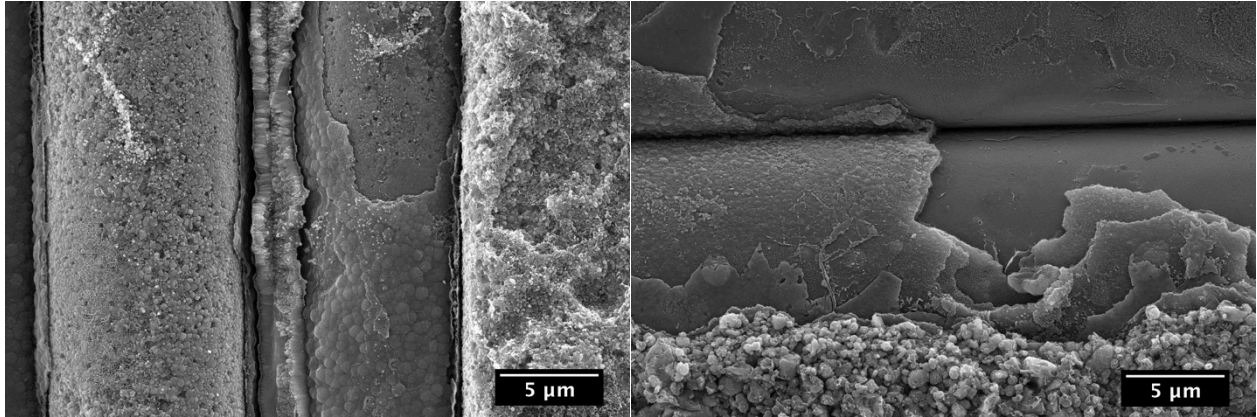


Figure 64 - Two SEM high magnification micrographs after the HF digestion step, a Sylramic fiber on the left and a Hi-Nicalon-S fiber on the right, showing rougher texture and etching on the Sylramic fiber as compared to the smooth surface of the Hi-Nicalon-S fiber.

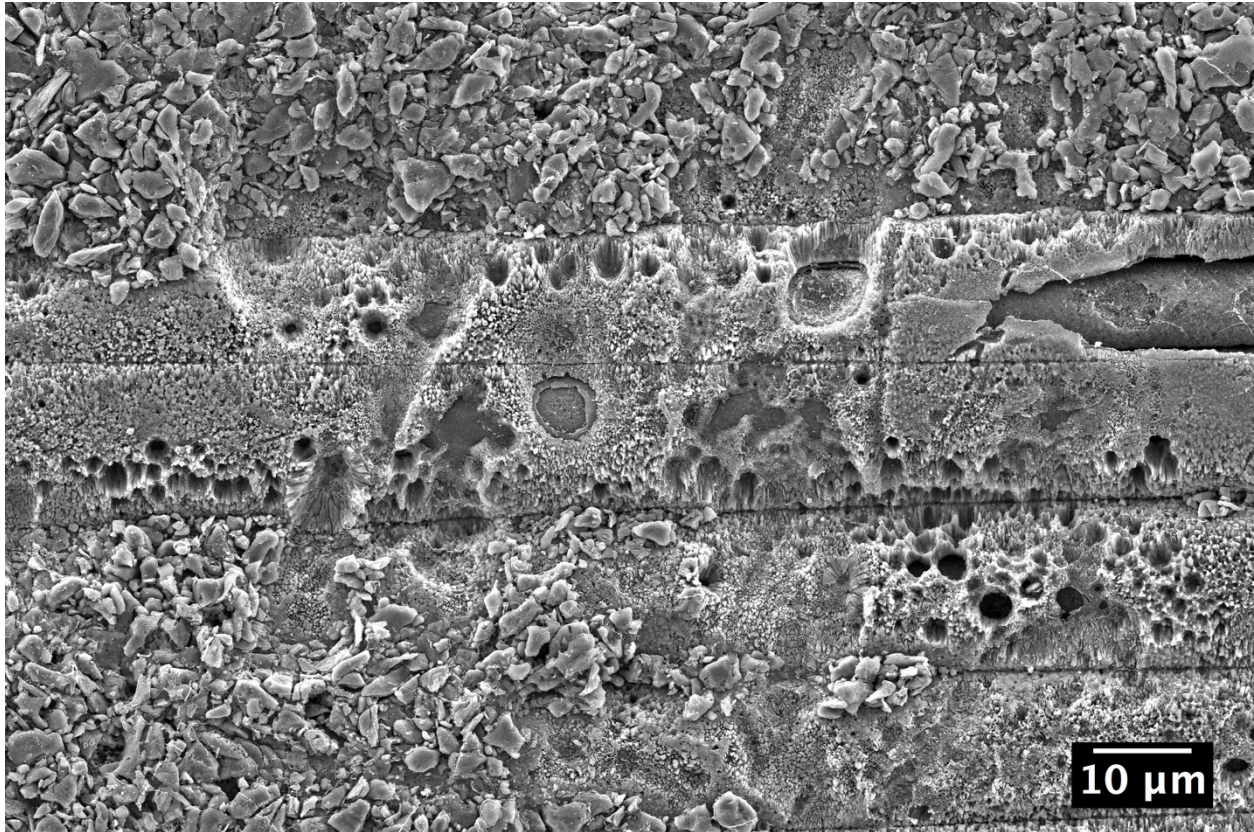


Figure 65 – SEM micrograph of the CVI-F composite after HF digestion showing attack on the matrix. Note the dense CVD layers and distinct SiC particulates remaining from the PIP/MI process.

After the corrosion products had been removed in HF some of the BN interphase was still present, as shown in Figure 66. The BN was primarily found in regions that were fairly protected (away from edges and high points) and where the fibers had just begun to be oxidized.

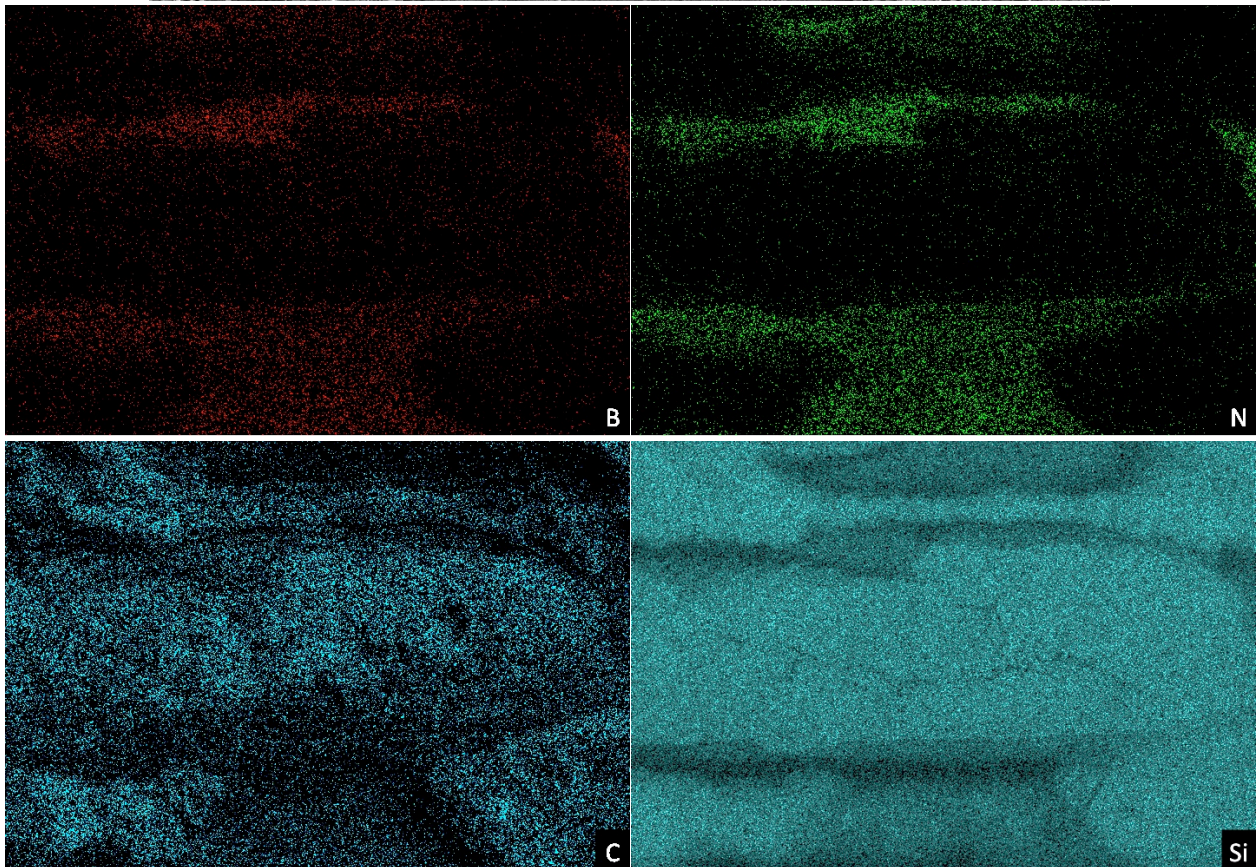
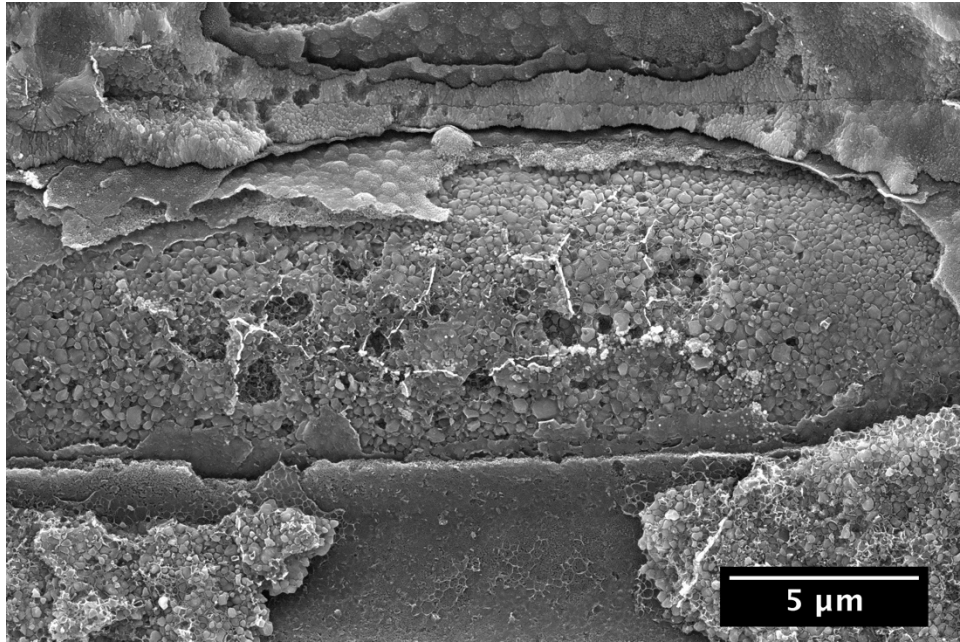


Figure 66 – Top: An SEM micrograph showing a Sylramic fiber after HF digestion with residual BN and dense CVD SiC. Middle: EDS maps for B (left) and N (right). Bottom: EDS maps for C (left) and Si (right).

A summary of the parameters explored quantitatively for the furnace-exposed CMCs is presented in the radar plot in Figure 67. A few trends become apparent from this plot:

1. The coupons exposed in the low SO_2 atmosphere have a lower amount of S in the corrosion products than the coupons exposed in a high SO_2 atmosphere. The low SO_2 gas is predicted to create a higher Na_2O activity in the melt, resulting in less Na_2SO_4 according to Equation 2, which is consistent with this observation.
2. Overall the CVI-F coupons showed a higher concentration of both B and Si in the corrosion products as compared to the MI-F coupons. This makes sense as the CVI-F composites were shown to have a high area fraction of residual MI as well as B-bearing particulates in the matrix. The CVI-F coupons also showed a large amount of B in the water-soluble corrosion products, indicating that perhaps the B-bearing particulates are not very stable in water.
3. The CVI-F coupons also had a higher amount of HF-soluble corrosion products than the MI-F composites. This observation also agrees with the microscopy results that show greater attack (and generation of silica) on the CVI-F composites.
4. Within the MI-F coupons, the low SO_2 exposure had more Si in the corrosion products than the high SO_2 exposure. This agrees with the concept of greater attack at higher Na_2O activities. The CVI-F coupons displayed the opposite trend, however, and no satisfactory explanation was determined for this result, other than perhaps differences from coupon to coupon.

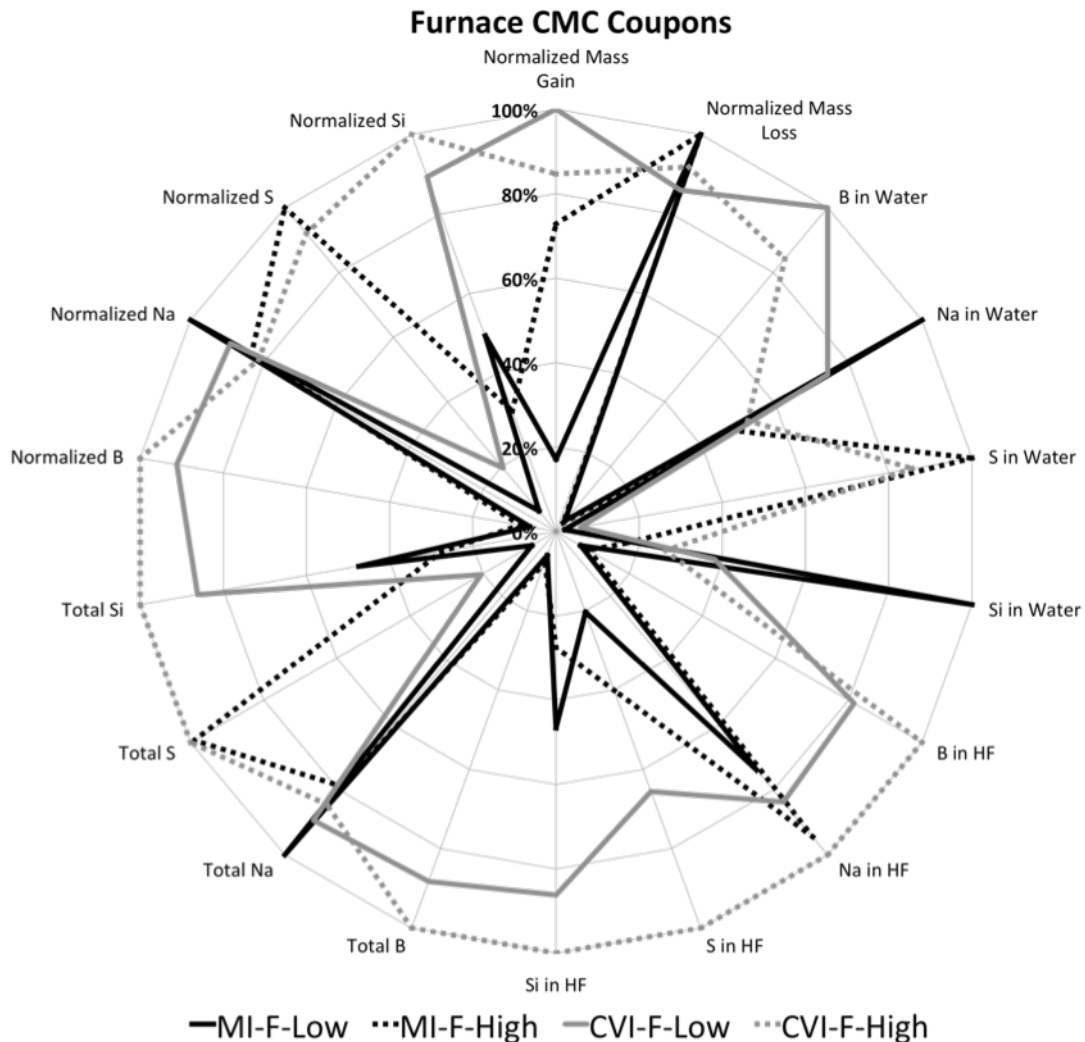


Figure 67 – Radar plot comparing relative hot corrosion between the MI-F and CVI-F coupons exposed at low (2.5 ppm) and high (1000 ppm) SO₂ levels.

6.1.3 Burner Rig Exposed CMCs

The burner rig coupons will be referred to using abbreviations provided in Table 3 and their exposure time (in hours) to simplify discussion. For instance, the MI-BR coupon exposed in the burner rig for 45-hours will be described as MI-BR-45. Additionally, as there are so many micrographs that need to be reproduced in high-resolution almost all of the micrographs are shown in Appendix C rather than in this chapter. The results will be

described here and the figures in the appendix will be referenced throughout. For ease of reading Appendix C should be viewed as a separate document.

The burner rig coupons have a significant amount of glassy product on their surfaces as shown in the macro photographs in Figure 68.



Figure 68 – Macro photos of the burner rig coupons after exposure. Note that the leading edge of each coupon is presented on top. From top to bottom: MI-BR-24, CVI-BR-24, MI-BR-45, CVI-BR-45. All coupons measure approximately 10.8 cm x 1.25 cm.

SEM micrographs of the burner rig coupons after exposure are shown in Figures C-1, C-2, C-3, and C-4. These figures show the faces of the coupons and are oriented to show the same face shown in the macro photos in Figure 68. These micrographs show evidence of recession in the impingement site that will be quantified later. EDS analysis confirms that the majority of the smooth product found on the sample faces is sodium sulfate, though there are some glassy silicates as well.

Figures C-5, C-6, C-7, and C-8 show SEM micrographs of the leading edges of the burner rig coupons after exposure. In these micrographs the silicate scale and the sodium sulfate on the samples obscure most of the corrosion that has taken place, however there is evidence of attack. The surface morphology shows that there was differential attack (which will be described in more detail later) of the fiber tows oriented end-on, the fiber tows oriented lengthwise, and the matrix.

Figures C-9, C-10, C-11, and C-12 show SEM micrographs of the faces of the coupons after sectioning and water digestion. Note that the regions shown in these micrographs might not correspond to the micrographs in Figures C-1, C-2, C-3, and C-4 or the macro photos in Figure 68, but that all following micrographs will be of the same view as shown here. These micrographs show that after submerging in water the majority of the surface products (sodium sulfate and sodium-rich silicates) were removed. What was left behind was primarily silica.

Figures C-13, C-14, C-15, and C-16 show SEM micrographs of the leading edges of the burner rig coupons after sectioning and water digestion. As with the face views the edges show the removal of the sodium sulfate and some of the silicates with a greater amount of silica remaining. The attack on the CMC coupons is still becoming more visible, however.

Figures C-17, C-18, C-19, and C-20 show SEM micrographs of the faces of the coupons after sectioning and HF digestion. As with previous materials the HF digestion step removed all of the remaining corrosion product, exposing the attacked CMC material. The MI-BR-45 and MI-BR-24 coupons show significant pitting and attack on the faces. Near the leading edges the matrix has been attacked so much the fiber tows within the coupon

can be seen. The CVI-BR-45 and CVI-BR-24 coupons, however, show little or no attack on the faces, with some degradation near the leading edge.

Figures C-21, C-22, C-23, and C-24 show SEM micrographs of the leading edges of the burner rig coupons after sectioning and HF digestion. As with previous materials the HF digestion step removed all of the remaining corrosion products, exposing the attacked CMC material. As with the face views the leading edges of the MI-BR-45 and MI-BR-24 coupons show significant attack to fibers and matrix. The leading edge views make it apparent that in the MI-BR coupons the fiber tows that are exposed end-on (perpendicular to leading edge) are attacked the most aggressively leading to the deepest recession in those regions as corrosion proceeds down the length of the fibers. The fiber tows that are exposed lengthwise (parallel to leading edge) are slightly more resistant to attack, and the matrix material is the most resistant to attack. The CVI-BR coupons show significant attack as well, however in this case there is a more uniform attack of the fiber tows and matrix, resulting in less scalloping of the leading edge.

The Hi-Nicalon fibers in the MI-BR coupons experienced fairly uniform attack which is shown in Figures C-25, C-26, C-27, C-28, and C-29. Some Hi-Nicalon fibers did show more aggressive attack, however, such as those shown in Figure C-30. The Hi-Nicalon-S fibers in the CVI-BR coupons generally showed a more aggressive pitting attack as shown in Figures C-31, C-32, C-33, and C-34. Some Hi-Nicalon-S fibers showed less pitting attack, such as those in Figure C-35.

The matrix in the MI-BR coupons appeared to be more resistant to hot corrosion attack than the Hi-Nicalon fiber tows in those composites. Figure C-28 shows this behavior where the fiber tows exposed end-on experienced the greatest recession, followed by the

fiber tows exposed lengthwise, with the matrix showing the least recession. This is also evident in Figure C-36, which shows the fibers disappearing as they are corroded. This depletion of the MI Si was evident on the face of the coupons as well, as shown in Figure C-37. The dense CVI SiC layer in the MI-BR composites remained fairly resistant to hot corrosion attack, as shown on the leading edges in Figure C-26 and Figure C-38, and on the sample face in Figure C-39.

The matrix in the CVI-BR composites was fairly resistant to hot corrosion, and corroded at a uniform rate with the Hi-Nicalon-S fibers as shown in Figure C-33. The CVI matrix was more susceptible to attack at what appears to be an interface resulting from a multi-step CVI coating process. This selective attack of the coating layer interfaces is shown in Figure C-35.

Figure C-40 shows the first cross-section of the MI-BR-24 coupon after corrosion and Figure C-41 shows the second cross-section of the same coupon. The cross sections illustrate the non-uniform attack of the fiber tows and the matrix in the MI-BR composites. This behavior leads to the leading edges of the MI-BR coupons taking on a scalloped appearance. The scale can be seen wrapping around the full exterior of the coupon, indicating that either the faces of the coupons are not especially resistant to hot corrosion, or there is simply enough oxide generated that the shear forces of the burner rig cause it to flow along the whole coupon. Figure C-42 shows an SEM micrograph and corresponding EDS maps that further illustrate the differential hot corrosion of the fiber tows with the deepest scale penetration occurring when the fiber tows are exposed end-on.

Figure C-43 shows the first cross-section of the CVI-BR-24 coupon after corrosion and Figure C-44 shows the second cross-section of the same coupon. This CVI-BR coupon

has the seal coat protecting the trailing edge as well as the two faces, and the scale on this coupon does not wrap around the trailing edge of the coupon. This indicates that either the seal coat on the faces provided enough resistance to hot corrosion, or the total oxide formed was too little to allow it to coat the whole surface as in the MI-BR-24 coupon. The leading edge recession is fairly uniform, with slightly more attack occurring down the length of the fibers, as shown in Figure C-45.

Figure C-46 shows the first cross-section of the MI-BR-45 coupon after corrosion and Figure C-47 shows the second cross-section of the same coupon. As with the MI-BR-24 coupon the non-uniform attack of fiber tows and matrix is evident, and now with longer exposure times leads to further scalloping of the leading edge. The scale can be seen wrapping around the full exterior of the coupon once again, indicating that either the faces of the coupons are not especially resistant to hot corrosion, or there is simply enough oxide generated that the shear forces of the burner rig cause it to flow along the whole coupon. Figure C-48 illustrates the differential hot corrosion attack not only between the fiber tows and the matrix, but also between fiber tows exposed end-on and tows exposed lengthwise.

The corrosion spreads in between the fibers oriented lengthwise, resulting in greater recession than the matrix, but less overall recession than the fiber tows exposed end-on.

Figure C-49 shows the first cross-section of the CVI-BR-45 coupon after corrosion and Figure C-50 shows the second cross-section of the same coupon. The CVI-BR-45 coupon only had a dense seal-coat on the two faces of the coupon, not on the leading or trailing edges. Even at longer exposure times, though, the scale on the CVI-BR coupons did not wrap around to the trailing edge. The large voids in the CVI matrix show easy ingress paths for hot corrosion, however, and this is illustrated in the SEM micrograph and EDS

maps in Figure C-51. There is also some scale penetration down the fiber tows but overall the leading edge experiences uniform recession of both fibers and matrix.

Micrographs were arranged as shown schematically in Figure C-52 to determine the recession of the burner rig coupons. Using this arrangement the micrographs were scaled to the same size, made parallel, and lined up along their trailing edges. A horizontal line is used to visualize the recession. Figure C-53 shows the recession in the MI-BR-24 coupon, which was found to be approximately 1mm. Figure C-54 shows the recession in the CVI-BR-24 coupon, which was found to be approximately 2mm. Figure C-55 shows the recession in the MI-BR-45 coupon, which was found to be approximately 8mm. Due to the scalloping in the leading edge the recession was estimated at a distance half way between the most and least attacked parts of the leading edge. Figure C-56 shows the recession in the CVI-BR-45 coupon, which was found to be approximately 5mm.

All of the burner rig coupons experienced a mass gain after exposure. This is largely due to the deposition of Na_2SO_4 and the growth of a silicate scale. The mass changes are summarized in Table 8. The largest difference in mass change was due to the exposure time, and mass changes were similar for both materials at either exposure time. A direct comparison cannot be made between these values and the mass change values for the CMC materials exposed in the furnace, as sodium sulfate is continuously deposited in the burner rig. To make a rough comparison, though, the overall normalized mass gain (including corrosion and the deposited salt) for the model materials was between 1.45 and 3.76 mg/cm^2 and for the furnace-exposed CMC coupons it was between 3.83 and 5.53 mg/cm^2 .

Table 8 – Mass change values for the burner rig coupons. Mass change includes deposition of Na₂SO₄ and growth of silicates. Surface area was assumed to be 6.84 cm² for all coupons.

Coupon	Initial Mass [mg]	Final Mass [mg]	Normalized Mass Gain [mg/cm ²]
MI-BR-24	7445.6	7506.9	8.96
CVI-BR-24	6155.3	6214.7	8.68
MI-BR-45	8308.8	8430.3	17.76
CVI-BR-45	6250.6	6411.6	23.54

A summary of the parameters explored quantitatively for the burner rig-exposed CMCs is presented in the radar plot in Figure 69. A few trends become apparent from this plot:

1. The coupons exposed at 45 hours have the greatest mass change, which is to be expected.
2. The 45 hour exposures also have the greatest amount of sodium and sulfur, which is indicative of both the longer salt deposition time, and a greater amount of residual (unreacted) sodium sulfate on the sample surface.
3. The CVI-BR-45 coupon has a greater amount of S in the corrosion products than the MI-BR-45 coupon, which is indicative of less reaction between SiO₂ or B₂O₃ and Na₂SO₄ as shown in Equations 5 and 11. The trend is reversed for the 24 hour exposures, and in that case the higher surface area of the CVI-BR-24 coupon (with its voids) likely accounts for the difference.
4. The MI-BR coupons have a high fraction of water-soluble B, while the CVI-BR coupons have a high fraction of HF-soluble B. This likely indicates the formation of a B-rich (water soluble) silicate in the MI-BR coupons, and the formation of a large amount of B-lean (water insoluble) silicate in the CVI-BR coupons (which have a higher internal surface area).

- The MI-BR coupons both have a much higher amount of silicon in the corrosion products than the CVI-BR coupons, indicating a higher volume of scale formed and perhaps slight attack of the remaining MI Si in the matrix (though pure Si is shown to be stable in HF).

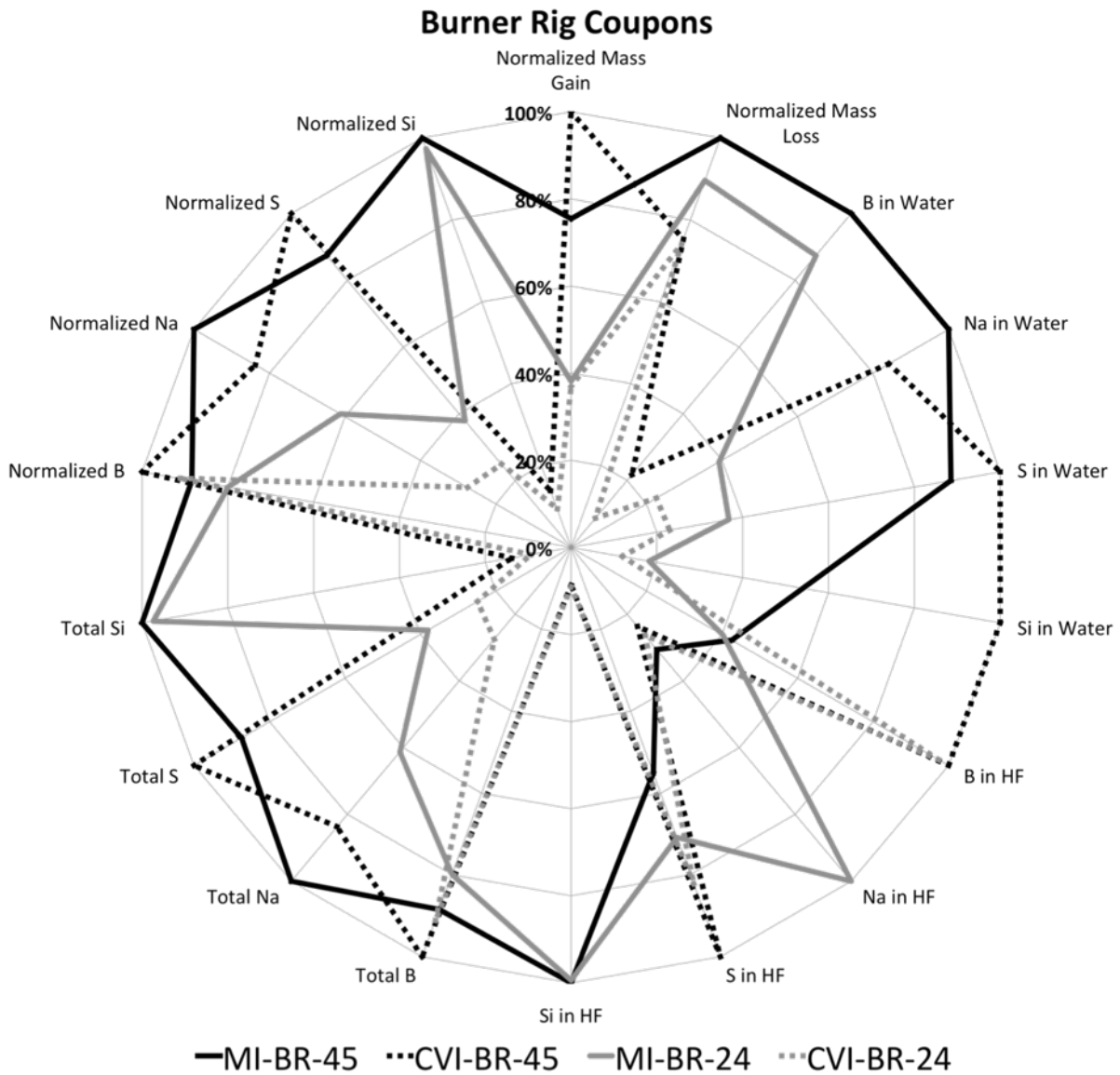


Figure 69 – Radar plot comparing relative hot corrosion between the MI-BR and CVI-BR coupons exposed for 24 and 45 hours.

6.2 Discussion

6.2.1 Materials Characterization

The material characterization revealed that the matrices found in the CMC varieties studied either contained fairly locally dense, uniform SiC (CVI-BR) or a less homogeneous matrix containing SiC particulates, Si-rich regions, and sometimes C- and B-based inclusions (CVI-F, MI-F, and MI-BR). The hot corrosion of model material substrates in the first task provides useful comparison to the CMC matrix material where CVD SiC simulates CVI SiC, Hexoloy simulates PIP/MI matrix, and pure Si simulates residual Si from the MI process, so long as the Si is not doped or otherwise chemically altered.

6.2.2 Furnace-Exposed CMCs

The overall nature of the corrosion product formed on the furnace-exposed CMC coupons was quite similar to what was found on the model materials. The lower SO₂ concentration in the gas (higher Na₂O activity in the scale) resulted in a less bubbly corrosion product and the formation of crystalline laths in the scale. The laths are predicted to be tridymite stabilized by Na₂O according to the XRD analysis in Task 1. The corrosion product solubility was similar as well, with sodium sulfate and a large fraction of silicate removed in water. The furnace exposed CMCs had an increased amount of borosilicate removed in the HCl step as compared to the model materials. This is likely due to either the increased volume of BN found in the CMC coupons or the distribution of BN throughout the coupon rather than the thin surface layer present on the model materials that likely reacted first. The SiC fibers and matrix materials were found to be severely attacked and pitted after 24 hours at 1000°C, with greater attack of the PIP/MI matrix than

the CVI matrix consistent with the increased rate of attack of the Hexoloy vs. CVD model materials.

The furnace-exposed CMC coupons showed evidence of remaining BN interphase after the corrosion products had been removed by HF. At first this seemed counter-intuitive since BN is known to oxidize readily. However, the oxygen partial pressure at the SiO₂ scale-SiC substrate interface is calculated to be 2.4×10^{-21} atm at 1000°C, preventing the oxidation of BN. SiC thus acts as an oxygen getter as demonstrated by Sheldon³⁰ and Jacobson²⁹ or as can be seen by looking at the Ellingham diagram in Figure 6. What is still surprising, however, is that this BN remained even after soaking in HF for upwards of 48 hours, as a baseline ICP analysis of a BN-coated CVD-SiC coupon showed that the water digestion removed all of the boron nitride. BN remaining after the HF digestion step was not observed in the BN-coated model materials, however the BN was present as a thin surface film on the SiC model materials, so it was likely the first to react. In the composites, SiC had already oxidized/corroded to form the silicate scale that protected the BN located deeper in the sample. In this aspect, the BN-coated model materials from Task 1 were not an accurate representation of the corrosion behavior of a CMC material.

The Sylramic fibers in the CV-F coupons showed a greater level of pitting and etching attack than the Hi-Nicalon-S fibers in the MI-F coupons. This increased attack may be caused by the presence of TiB₂ particulates in the fibers^{7,76}. The Ellingham diagram in Figure 6 shows that TiB₂ is expected to oxidize preferentially to SiC, leading to the formation of liquid boria. As in the rest of the study has shown so far, the presence of B or a boria scale generally contributes to increased hot corrosion and attack of SiC.

6.2.3 Burner Rig-Exposed CMCs

The burner rig exposures provided useful insight into limitations of the furnace exposures as representative of a turbine engine. The largest differences between the burner rig and the furnace exposures are the constant re-deposition of Na_2SO_4 in the burner rig and the velocity of the flame, which can lead to a shear force on the liquid corrosion products. It was found that in the furnace exposures the volume of salt loading used was sufficient for a 96 hour exposure, but at longer times depletion of the salt is likely to occur. In the burner rig the shearing force of the flame limited the build-up of a thick, protective silica layer at the leading edge. Thus, due to a lack of shear forces at longer times the furnace-exposed coupons will build up a thicker oxide layer and will become a less-accurate representation of the corrosion environment within a turbine engine.

In comparing the two different matrices in the burner rig coupons it was clear that the dense CVI SiC was generally more resistant to hot corrosion attack than the MI matrix. This result speaks to the anticipated efficacy of a dense CVD SiC seal coat on CMC components to limit hot corrosion attack, but that in the event of a coating failure the composition of the matrix will play an important role in CMC hot corrosion resistance. The MI Si in the matrix was selectively attacked leaving the SiC particulates remaining in the MI matrix. This preferential oxidation/corrosion of Si is explained by the Ellingham diagram in Figure 6, where Si is predicted to oxidize before SiC. This effect is shown schematically in Figure 70.

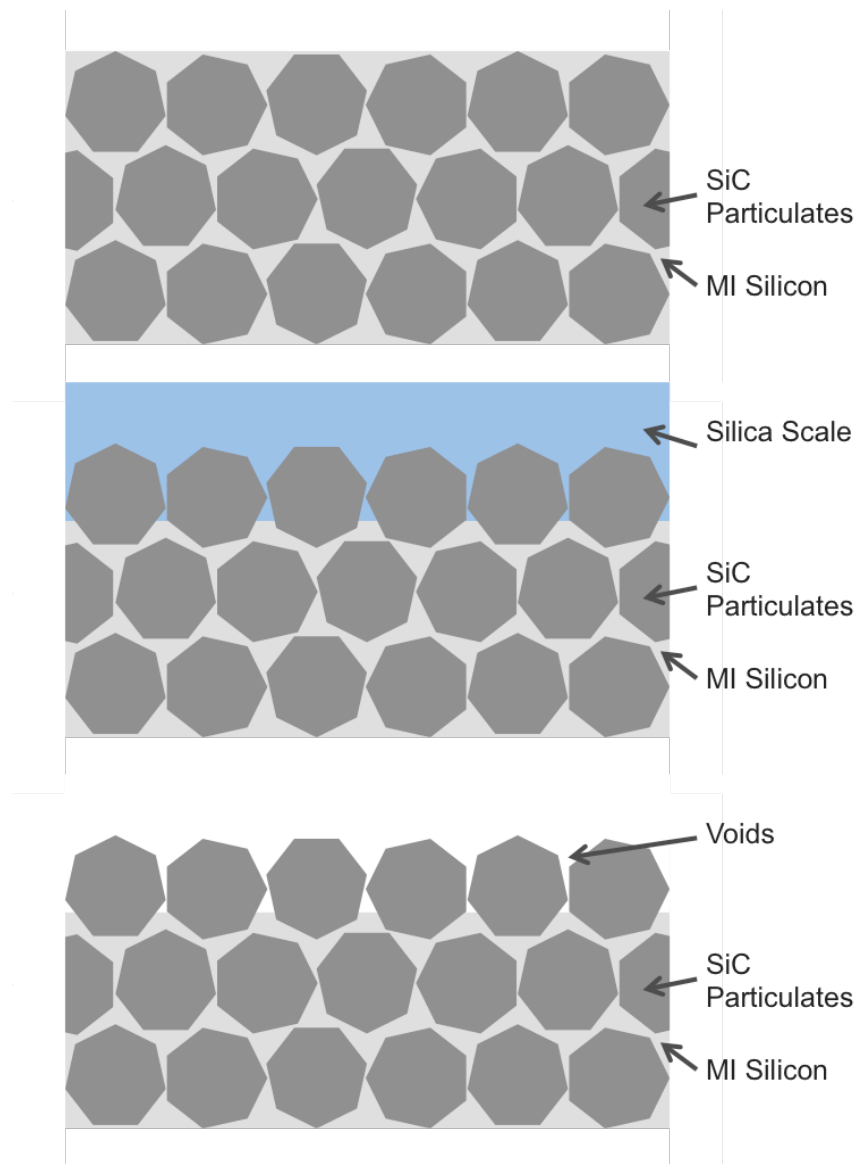


Figure 70 – Schematics showing the selective attack of the MI silicon. Top: SiC particulates are surrounded by MI Si. Middle: Silica scale grows on top, consuming Si first. Bottom: After HF digestion, voids left where MI Si was oxidized and removed.

The CVI matrix was also selectively attacked at interfaces between the CVI layers, indicating that boundaries between phases and coating layers may have a lower barrier to corrosion and can act as transport pathways for inward oxidation and corrosion. One other potential reason for the selective oxidation and attack seen in the MI Si would be if the Si

was not pure, and was doped for improved infiltration or oxidation properties. Doped Si might be expected to have a different hot corrosion resistance than pure Si.

The Hi-Nicalon fibers in the MI-BR coupons appeared to be slightly more resistant to hot corrosion attack than the Hi-Nicalon-S fibers in the CVI-BR matrix based on the pitting and attack found on the fibers in the SEM. Looking at the recession information, however, the Hi-Nicalon-S fibers in the CVI-BR coupons appeared to share a similar attack/recession rate with the dense CVI matrix while the Hi-Nicalon fibers in the MI-BR coupons showed a greater attack/recession than the MI matrix. These results conflict somewhat, and are obfuscated by the fact that the matrix in each composite is different. The Hi-Nicalon-S fibers might be expected to have better performance since they are a newer-generation material and achieve closer SiC stoichiometry than the Hi-Nicalon fibers. As with the lack of information available on the matrix processing, the fiber identifications should be confirmed as the CVI-BR coupons are a much older vintage than the MI-BR coupons and yet are identified as using a newer fiber. Overall, though, both Hi-Nicalon and Hi-Nicalon-S fibers show less localized pitting and attack than the Sylramic fibers in the composites studied, as shown in Figure 71.

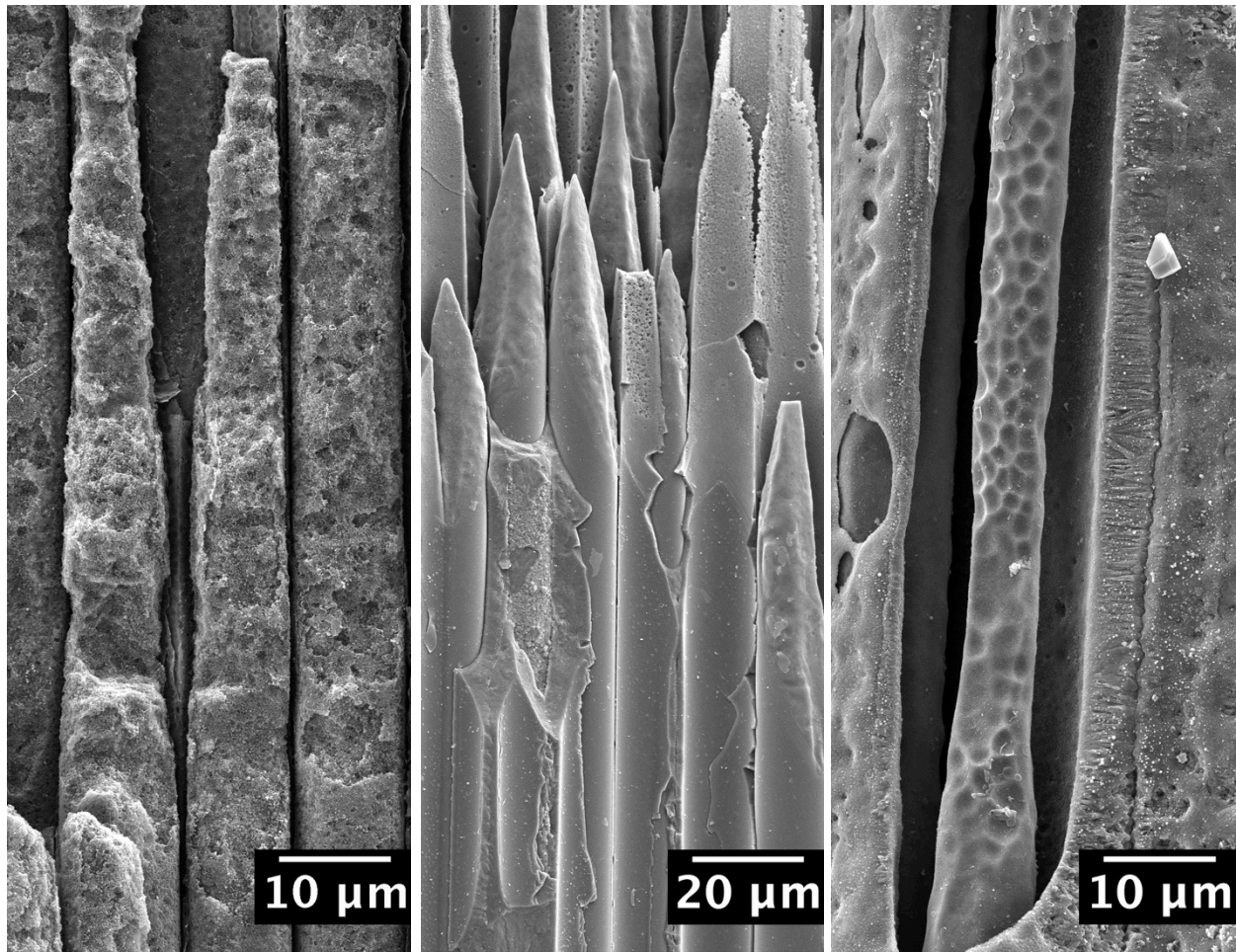


Figure 71 – SEM micrographs showing the difference in hot corrosion attack on Syllramic, Hi-Nicalon, and Hi-Nicalon-S fibers after corrosion products are removed.

The recession rates observed for the burner rig coupons exposed for 45 hours at 950°C were between 111 and 177 μm/hr for the CVI-BR and MI-BR coupons respectively. This is much greater than the recession rate observed for Hexoloy coupons exposed at 1000°C for 24 hours (0.52 μm/hr) in the tube furnace as those coupons formed an oxide that remained on the coupon. This recession rate is also much higher than the recession rates due to volatility in water vapor at 1316°C reported by Opila⁷⁷, which were between 2×10^{-4} and 4×10^{-2} μm/hr for furnace and Mach 0.3 burner rig exposures. Golden⁷⁸ has shown recession rates of between 3.23 and 5.16 μm/hr for SiC in a 1300°C steam jet furnace environment. The steam jet furnace provides a close approximation of the

Task 2 – Hot Corrosion of CMC Materials – Discussion 110

recession rates found in a turbine engine^{78,79}, and those rates are still nearly 2 orders of magnitude lower than what was observed in this work, indicating that hot corrosion attack of SiC CMCs is expected to contribute significantly to the degradation and failure of these materials in the event of an EBC coating defect or failure.

6.3 Conclusions

Hot corrosion resistance of the composites is a complex combination of relative stability of the phase assemblage. The following factors contribute to hot corrosion resistance in order of importance:

1. The matrix, and how it was processed, had the greatest effect on the overall material loss in the composites. The ability to create a dense, continuous, homogeneous SiC matrix appears to offer the greatest protection from hot corrosion, while any voids, particulates, interfaces, or chemical inhomogeneities appear to result in increased attack.
2. The orientation of the fiber tows had a great effect on hot corrosion resistance, and fiber tows always corroded/receded more than the surrounding matrix.
3. The Hi-Nicalon and Hi-Nicalon-S fibers are more resistant to localized hot corrosion attack than Sylramic fibers, and this is likely due to the TiB₂ particles found in the Sylramic fibers. While the fibers did show a difference in their hot corrosion resistance, the differences did not correlate with the overall degradation of the composites.

The hot corrosion of the model materials in Task 1 compare to the hot corrosion experienced in CMCs in the following ways:

1. The CVD-SiC coupons were more resistant to hot corrosion attack than the Hexoloy coupons, which indicated that dense homogeneous SiC is more resistant to attack than SiC with second phases (particularly those containing B).
2. Lower rates of hot corrosion in model materials relative to CMC materials are attributed to the BN surface thin films (700 nm thick) on SiC substrates acting as an imperfect model of the BN distribution in a CMC. Valuable insight into the effect of BN was gained from those materials, however.
3. The exposures in a tube furnace do not allow for the continuous re-deposition of Na_2SO_4 .
4. The low gas velocities in a tube furnace relative to a burner rig or turbine engine do not allow for the shear-induced redistribution of corrosion products.
5. The Si wafer is an incomplete model for the behavior of MI Si in a SiC matrix, where the relative stability of composite constituents dominates corrosion behavior.

The hot corrosion of SiC-based CMCs in the burner rig resulted in large recession of the composites. The recession observed was significantly higher than what would be expected from volatility in a water vapor environment alone, indicating that hot corrosion will be an important degradation mechanism in CMCs with EBC cracks or defects.

6.4 Recommendations for Future Work

Due to the cost, availability, and intellectual property issues with SiC CMC materials the scope of this task was necessarily limited. Having a larger variety of CMC materials to evaluate, particularly current-generation materials, would allow for a better understanding

of how the state-of-the-art materials will hold up in service. Access to a larger number of coupons to test would also allow for probing a greater number of experimental variables such as exposure time, temperature, and gas composition.

Additional microscopy on the two CMC varieties exposed in the furnace, particularly cross-sections after corrosion, would be valuable in comparing the hot corrosion resistance of the fibers and matrices in those materials. In the burner rig composites, cross-sections were analyzed, particularly to look for evidence of silica selectively growing from MI Si (as described in Figure 70), however this was not observed in the cross-sections shown here. Further microscopy to look for this effect is recommended.

It would be interesting to explore the shorter exposure times and compare with model materials, particularly times around 3-6 hours. The increased surface area and chemistry (reservoirs of C, BN, and Si) found in the CMC materials would likely lead to an increased rate of attack.

No hot corrosion was observed in the model materials at 900°C. It would be interesting to see if the additional complex chemistry in a CMC allows for hot corrosion at this lower temperature. The temperature dependence of CMC hot corrosion kinetics would be worth exploring to probe differences between the complex CMC materials relative to the model materials.

It will be shown in Task 3 that the equilibrium phase stability predictions made earlier rely heavily on the gas composition, and that reaching the predicted Na₂O activity is difficult. For this reason it would be interesting to expose CMC materials with gas mixtures that will raise the Na₂O activity and encourage further dissolution of silica in the molten sodium sulfate.

As the load-bearing capability of CMCs is largely dependent on the fiber properties, and the hot corrosion behavior of the fibers gathered here was obfuscated by the matrix behavior, it would be extremely valuable to determine the hot corrosion resistance of the different fibers outside of a CMC matrix.

Exposures of composites with an intact seal-coat would provide some insight into the durability of the seal coat (which might be modeled by CVD SiC coupons). Additionally, as the seal coat fails the rate of hot corrosion ingress through that coating failure could be evaluated as well.

As EBCs are necessary on SiC CMCs for protection from volatility in a combustion environment, the hot corrosion resistance of these EBCs should be evaluated as well. Hot corrosion of free-standing EBC materials should be explored, as should hot corrosion of EBC-coated CMC coupons.

7 Task 3 – Solubility of Oxides in Sodium Sulfate

7.1 Results

7.1.1 NiO Solubility

NiO solubility in molten Na_2SO_4 was determined to validate the experimental electrochemical cell setup and compare the results with the existing literature, in this case the work of Gupta and Rapp⁵⁸. It was found that the measured Na_2O activities did not correspond with the values predicted according to Equation 2 and that changing the SO_2 concentration in the gas did not vary the Na_2O activity as much as desired. The discrepancy between predicted and measured activities will be explained in the discussion, however for the analysis of the results the measured, rather than calculated, Na_2O activity was used. Sodium peroxide was used to increase the Na_2O concentration in the melt and reach higher Na_2O activities, however activities as high as those reported by Gupta and Rapp were not attained. A list of predicted and measured Na_2O activity values as well as corresponding voltages is provided in Table D-1 in Appendix D.

The ratio of Na:Ni as determined by the ICP analysis of the samples was used to calculate the concentration of dissolved NiO in Na_2SO_4 . The results of Gupta and Rapp were plotted as log of molar concentration (moles of NiO per moles of Na_2SO_4) in ppm vs. $-\log$ Na_2O activity. The ICP results in this study were determined in weight units, so conversion to molar values was performed. An example calculation is presented in Equation 16 where square brackets $[X]$ indicate the concentration, in weight, of species X as determined in the ICP, and M_X is the molar mass of species X .

$$Solubility_{NiO} = \log \left(2 * \frac{[Ni]/M_{Ni}}{[Na]/M_{Na}} * 1000000 \right) \quad \text{Equation 16}$$

The results of the NiO solubility study are shown in Figures 72, 73, 74, and 75. Figure 72 shows all of the data points generated in this study plotted as black dots over the black line, which is the summary curve from the Gupta and Rapp paper. Some of the data points were removed, however, as the samples clearly contained visible green powder indicating contamination due to un-dissolved NiO powder. Though NiO solubility in water is negligible^{80,81}, the powder itself was fine enough that these data points were removed in case the NiO powder was in suspension in the solutions for the ICP where it would create false intensity. Figure 73 shows the updated data set with the removed points indicated by the open circles. Furthermore it was found that in one of the runs the first three samples had steadily increasing concentrations, indicating that equilibrium had not yet been achieved, so those data points were removed as well. The updated plot is shown in Figure 74 with open circles indicating the removed points. This final data set is plotted in Figure 75 over the curve from the Gupta and Rapp paper as well as the data points from that paper (including excerpted data from private communications with Liang and Elliot). The data in this study follow the general trend demonstrated by Gupta and Rapp, however this new data set has more scatter.

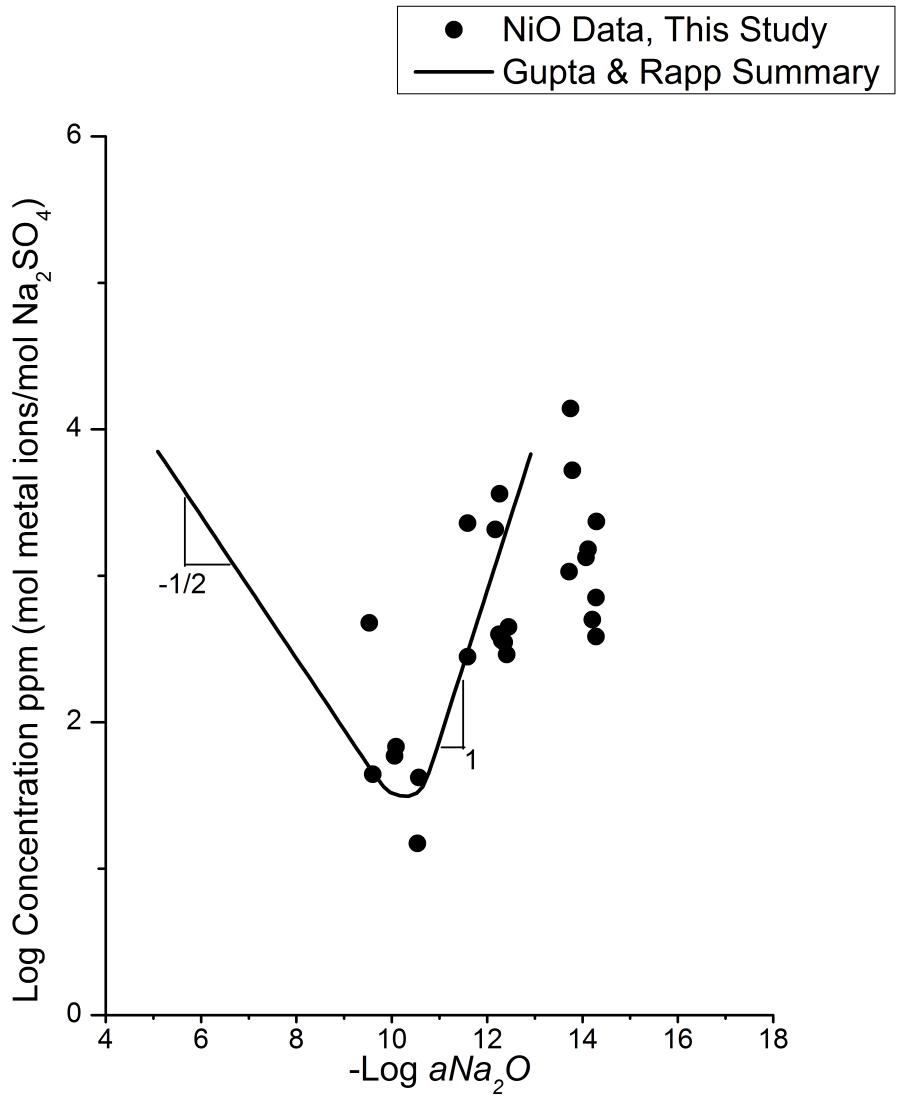


Figure 72 - Plot of all NiO data points from this study in black along with the NiO summarized results from Gupta and Rapp.

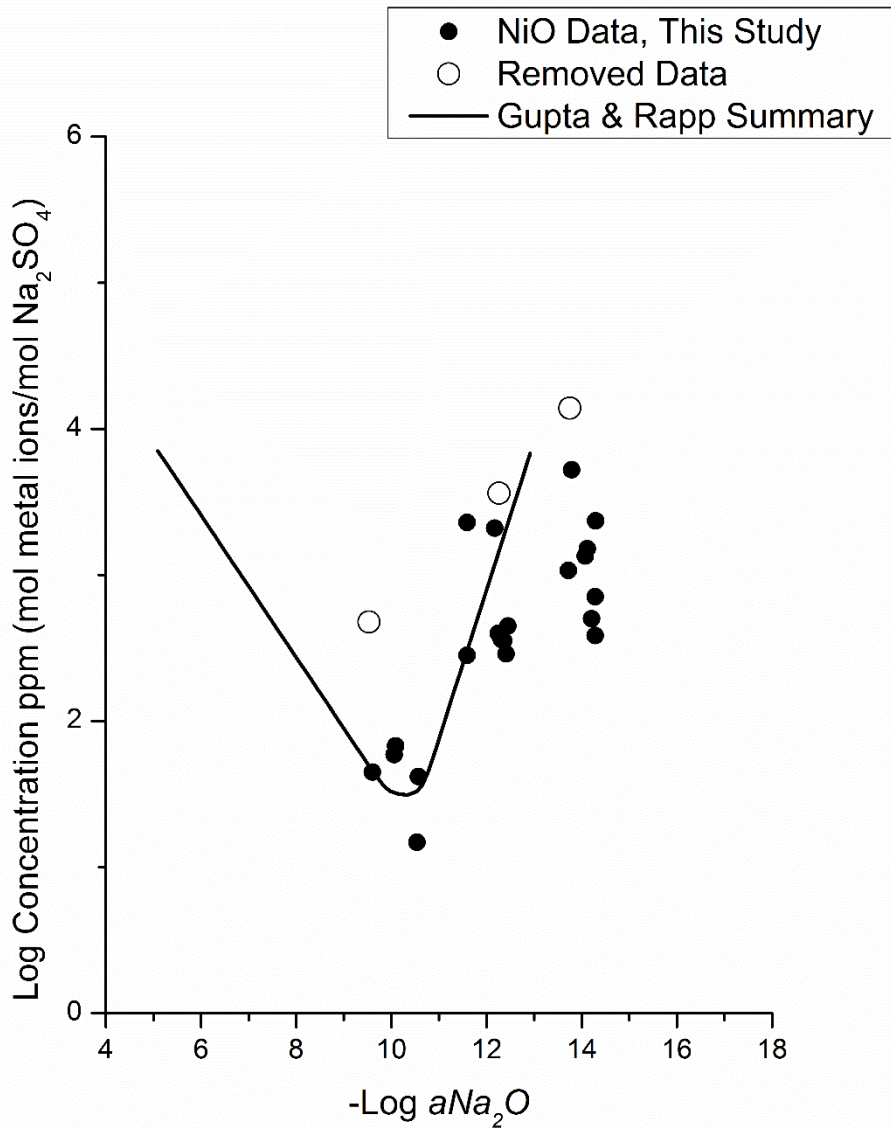


Figure 73 – Plot of NiO data points from this study in black along with the summarized NiO results from Gupta and Rapp. The open circles indicate data points that were removed due to visible contamination with NiO powder.

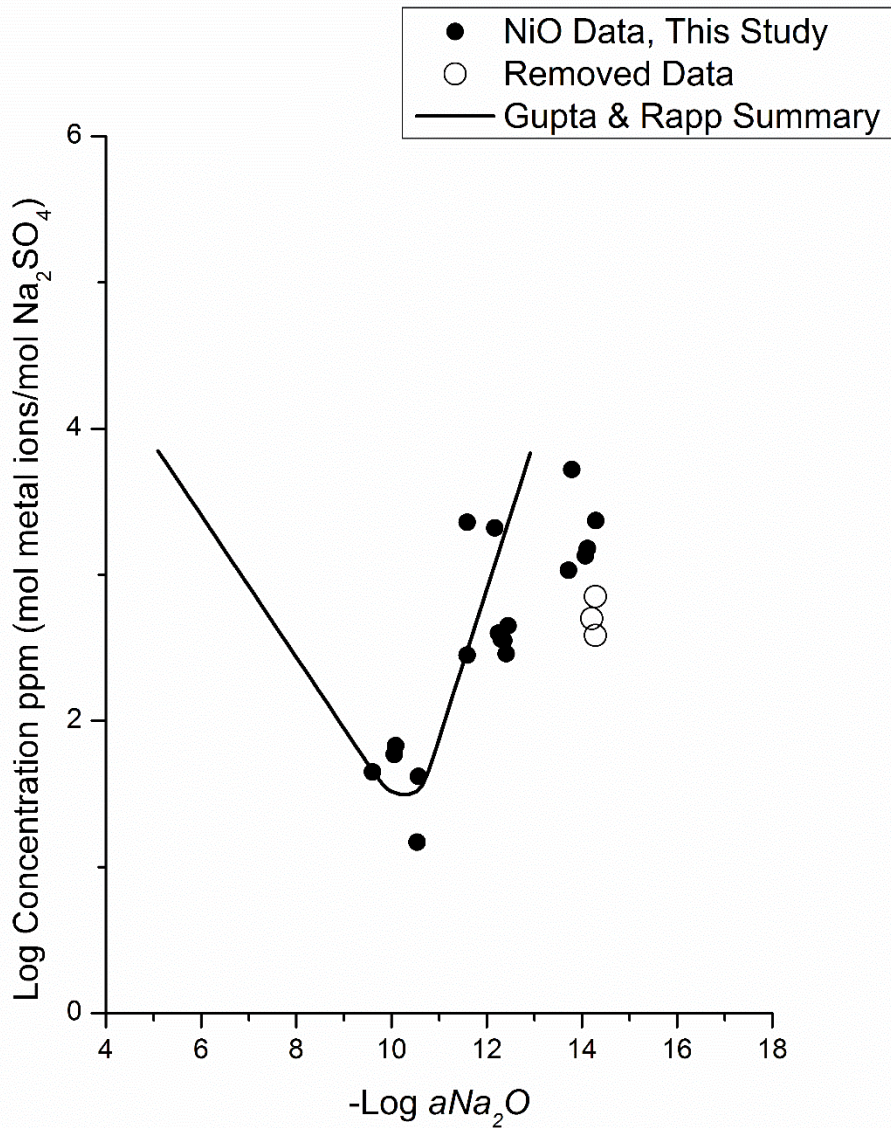


Figure 74 - Plot of NiO data points from this study in black along with the summarized NiO results from Gupta and Rapp. The open circles indicate data points that were removed since they were the first three samples collected in that batch and had not equilibrated yet.

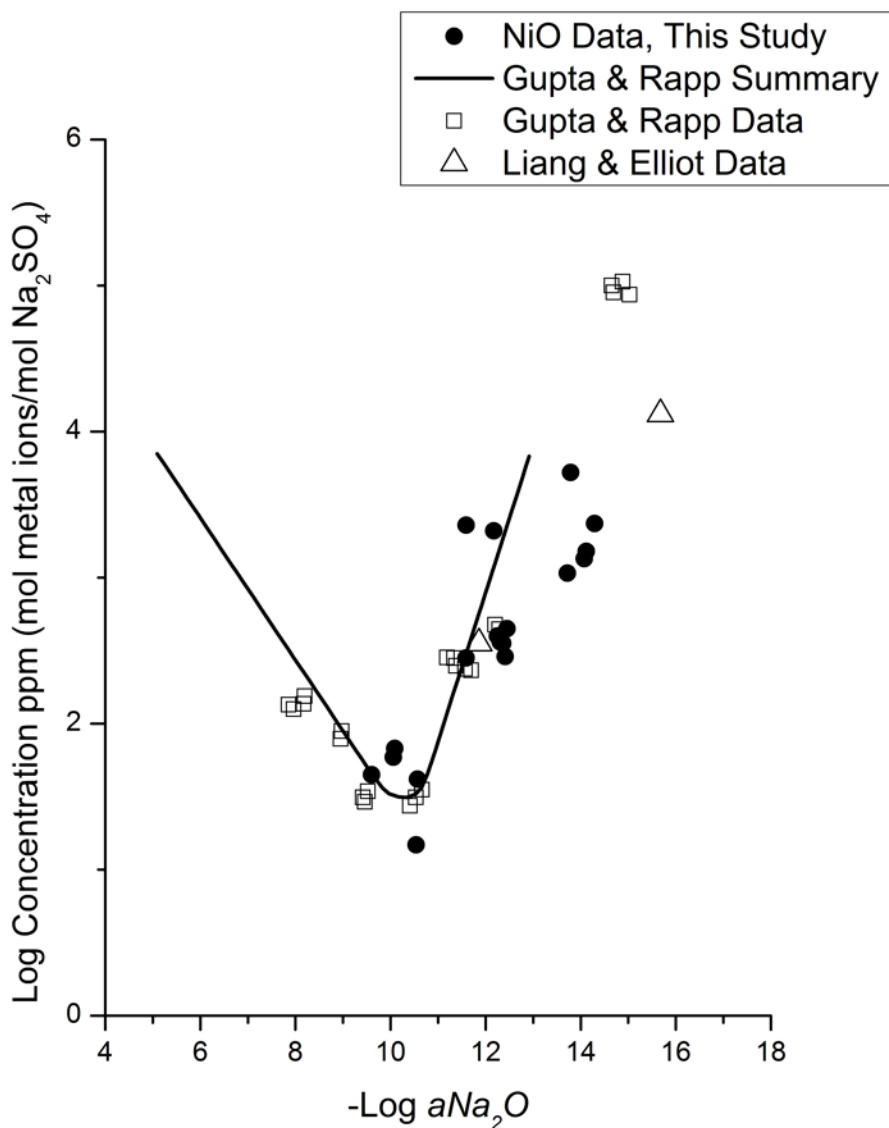


Figure 75 – Plot of NiO data points from this study in black along with the summarized NiO results from Gupta and Rapp and the raw data from Gupta and Rapp. The data collected in this study have the same general trend as the Gupta and Rapp data but have more scatter.

7.1.2 SiO₂ Solubility

The same method of plotting the data was used for the SiO₂ solubility study so the results could be compared with the rest of the solubility data generated by Rapp’s group. Longer equilibration times were used for the SiO₂ samples so as to avoid one of the

observed sources of error that ended up invalidating three of the NiO data points. Due to the fact that SiO₂ is colorless, unlike NiO, the oxide was added as granular crystals rather than a powder to aid in detecting the presence of un-dissolved silica in the sampled melt. A few samples clearly contained a crystalline piece of silica within the smooth glassy melt, however due to the insolubility of SiO₂ in water the concentration was not significantly different from the rest of the samples, so these data points were included in the plot in Figure 76.

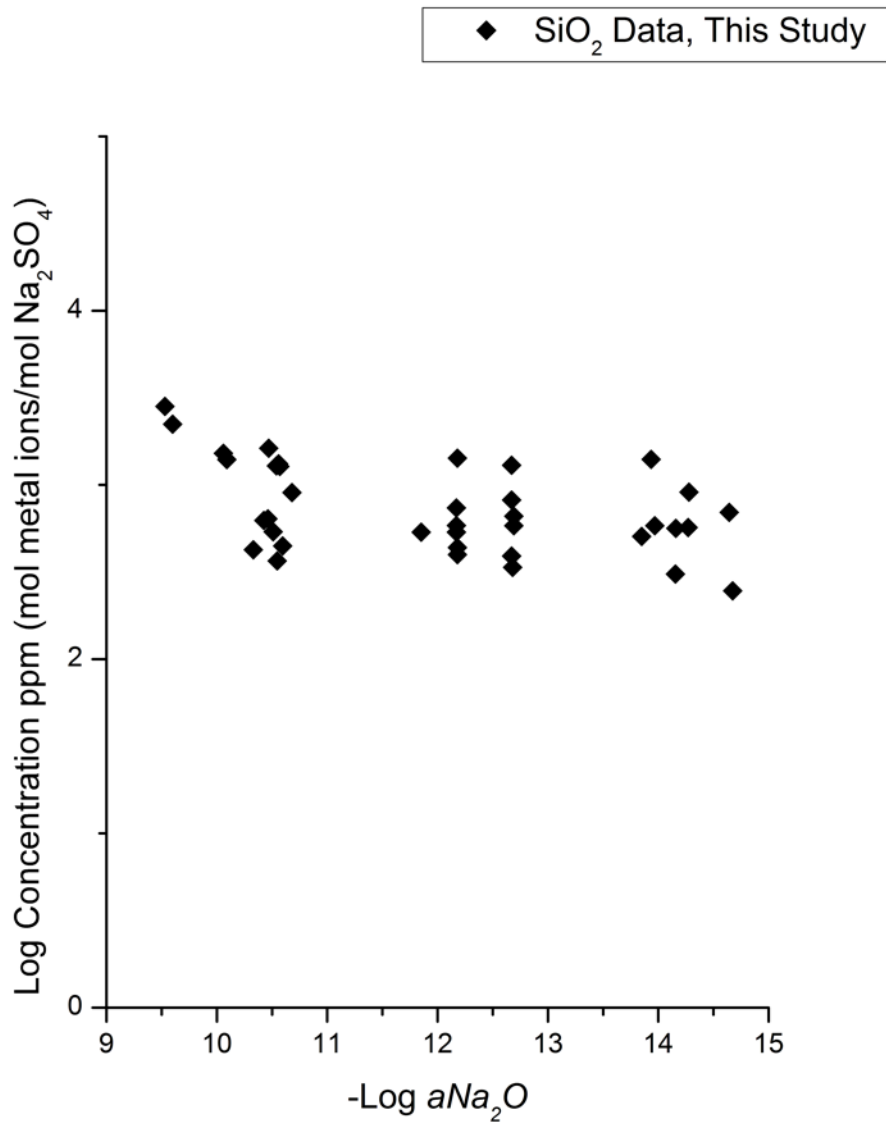


Figure 76 – SiO₂ solubility data plotted as a function of Na₂O activity.

The data from each run (a single loading of the furnace under a common gas) were then averaged to provide an average solubility at a given Na₂O activity. These averaged values are shown in Figure 77 as the open diamonds. Note that since SiO₂ was present in the melt environment during the NiO exposures in the form of the fused quartz tube used for the Na⁺ electrode, when measurable Si values were detected in those NiO runs the data are presented below as well.

slope of this trend line was found to be -0.46 , which has been simplified to $-1/2$. This averaged trend shows that the solubility of SiO_2 in Na_2SO_4 may begin to increase once passing into the sodium silicate phase field on the stability diagram in Figure 1, whose boundary is shown as a dashed vertical line in Figure 78.

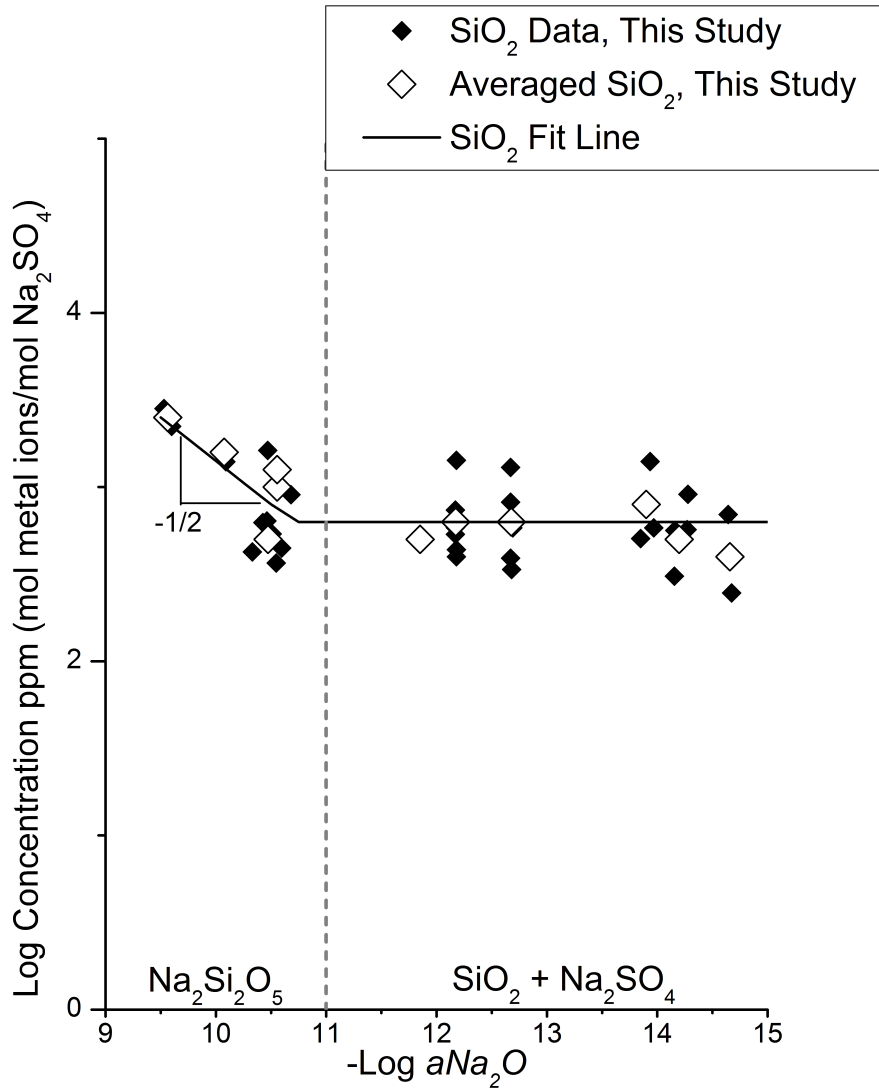
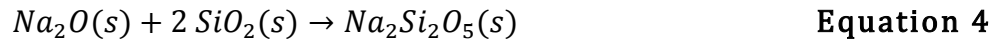


Figure 78 – SiO_2 solubility data plotted as a function of Na_2O activity. Open diamonds indicate averaged solubilities for a given run and the black line is a trend line fitted to the averaged data. The vertical dashed grey line is the predicted stability boundary between $\text{Na}_2\text{Si}_2\text{O}_5$ and $\text{SiO}_2 + \text{Na}_2\text{SO}_4$.

The slope predicted can be calculated theoretically from the solubility formula in Equation 4, and this calculation is shown in Equation 17. The slope of the manual fit, -0.5, does not agree with the predicted value of -1. Additionally, applying a slope such as this with so few data points very heavily weights the data at high Na₂O activity. If the same scatter found at lower Na₂O activities was found at the high Na₂O activities there would be no up-turn, and the entire trend line would be flat.



$$\left\{ \frac{\partial(\log a_{Na_2Si_2O_5})}{\partial(-\log a_{Na_2O})} \right\}_{O_2} = -1 \quad \text{Equation 17}$$

Figure 79 shows the same summary data from this work along with the data points from Shi and Rapp as well as a summary line for the Shi and Rapp data. The trend of no Na₂O dependence below an Na₂O activity of 1x10⁻¹¹ is shown in both data sets, however there is a large discrepancy (an order of magnitude) between the solubility found in this work and what was found by Shi and Rapp.

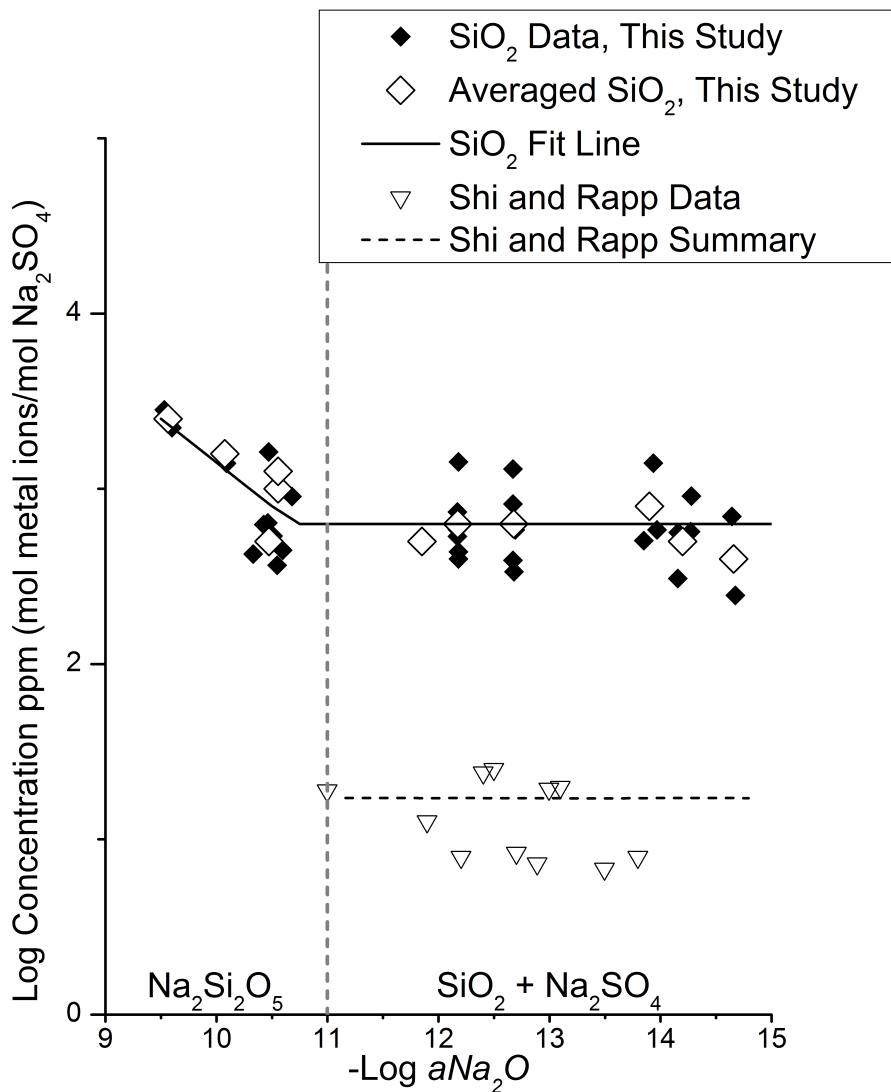


Figure 79 – SiO₂ solubility data plotted as a function of Na₂O activity. Open diamonds indicate averaged solubilities for a given run and the black line is a trend line fitted to the averaged data. The open triangles are the data from Shi and Rapp and the horizontal dashed line is the average of that data. The vertical dashed grey line is the predicted stability boundary.

7.1.3 B₂O₃ Solubility

The solubility of B₂O₃ in sodium sulfate was determined using the aluminoborate pellets described in the experimental section. Composition of the aluminoborate powders

was verified using XRD. The results of the XRD analysis showed the presence of at least one aluminoborate phase predicted in Figure 17 as well as additional un-reacted alumina. All samples showed evidence of the phase with a 2:1 ratio of alumina to boria, while only a few samples showed evidence of the 9:2 phase. As the 9:2 phase falls between the 2:1 phase and alumina, it was assumed that all compositions fell within the two-phase field highlighted in Figure 17. A sample diffraction pattern is provided in Figure 80.

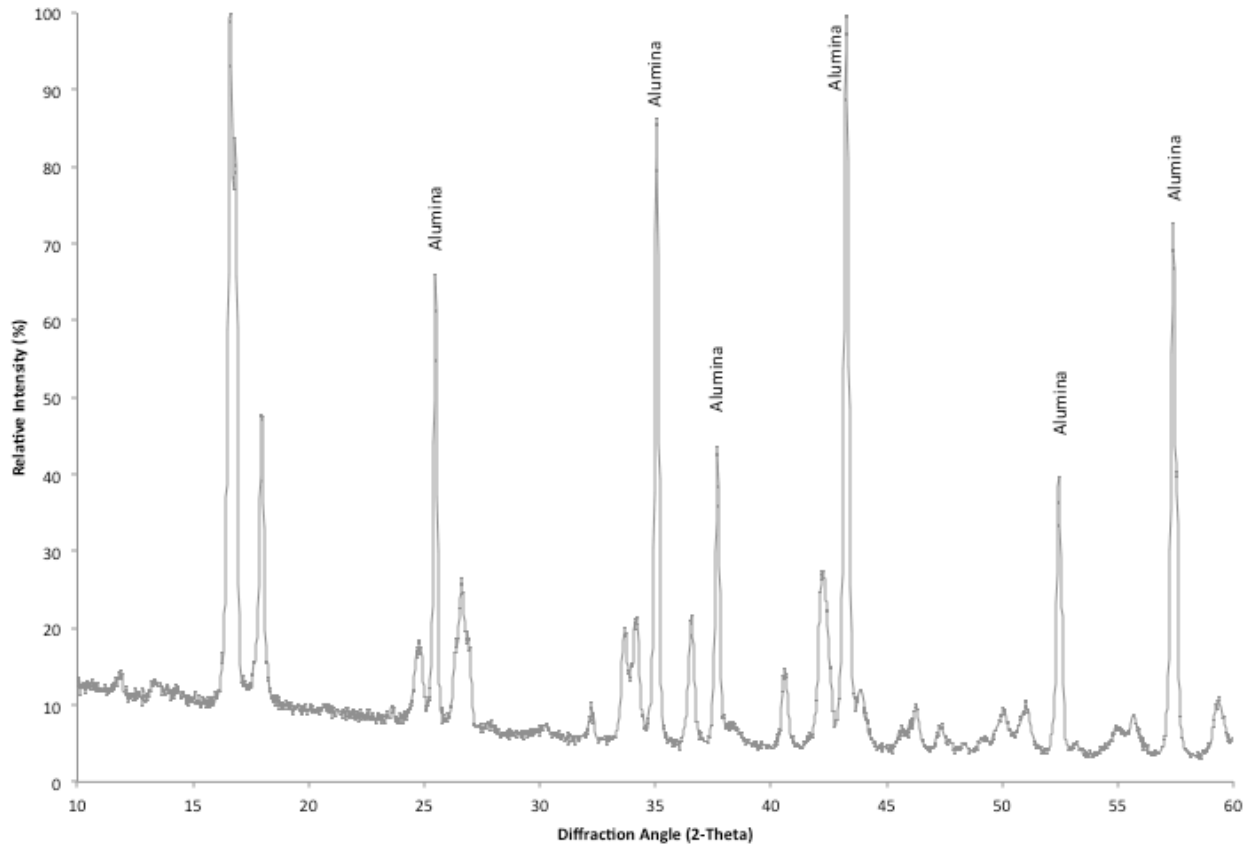


Figure 80 – XRD pattern for one of the aluminoborate samples. All peaks not labeled as alumina peaks correspond with the 2:1 aluminoborate phase.

The aluminoborate powders caused rapid deterioration of the pellet press die set due to the abrasive nature and small particle size of alumina ($<1\mu\text{m}$). This difficulty combined with time constraints resulted in acquisition of fewer data points for the B_2O_3 solubility study. The deviation between predicted Na_2O activity for a given gas atmosphere

and what was measured in the melt was much greater for the B_2O_3 samples than for the SiO_2 or NiO samples and these values are provided in Table D-1. Due to this deviation an even narrower range of Na_2O activities was explored for B_2O_3 than for NiO or SiO_2 .

As the aluminoborate pellets contained Al_2O_3 in addition to the alumina crucible the solubility of Al_2O_3 in Na_2SO_4 was analyzed as well to act as another comparison with the existing literature⁸². The solubility values were found to be much too high for Al_2O_3 , and it was determined that this was due to sub-micron alumina particles in the sample. These un-dissolved alumina particles were small enough that they were in suspension in the water digestion solution and were ionized in the ICP. For this reason no data are shown or compared for the Al_2O_3 solubility.

Figure 81 shows the B_2O_3 solubility data plotted as a function of Na_2O activity. As with previous data sets some of the data points were removed, and the updated data is provided in Figure 82. Two data points were removed as they were the last two data points collected at the end of a long run and the boron level was sharply declining, indicating possible depletion of boron in the melt. One other data point was removed as it was the lone data point collected on a run that was ended early due to a broken zirconia tube (which may have affected the potential).

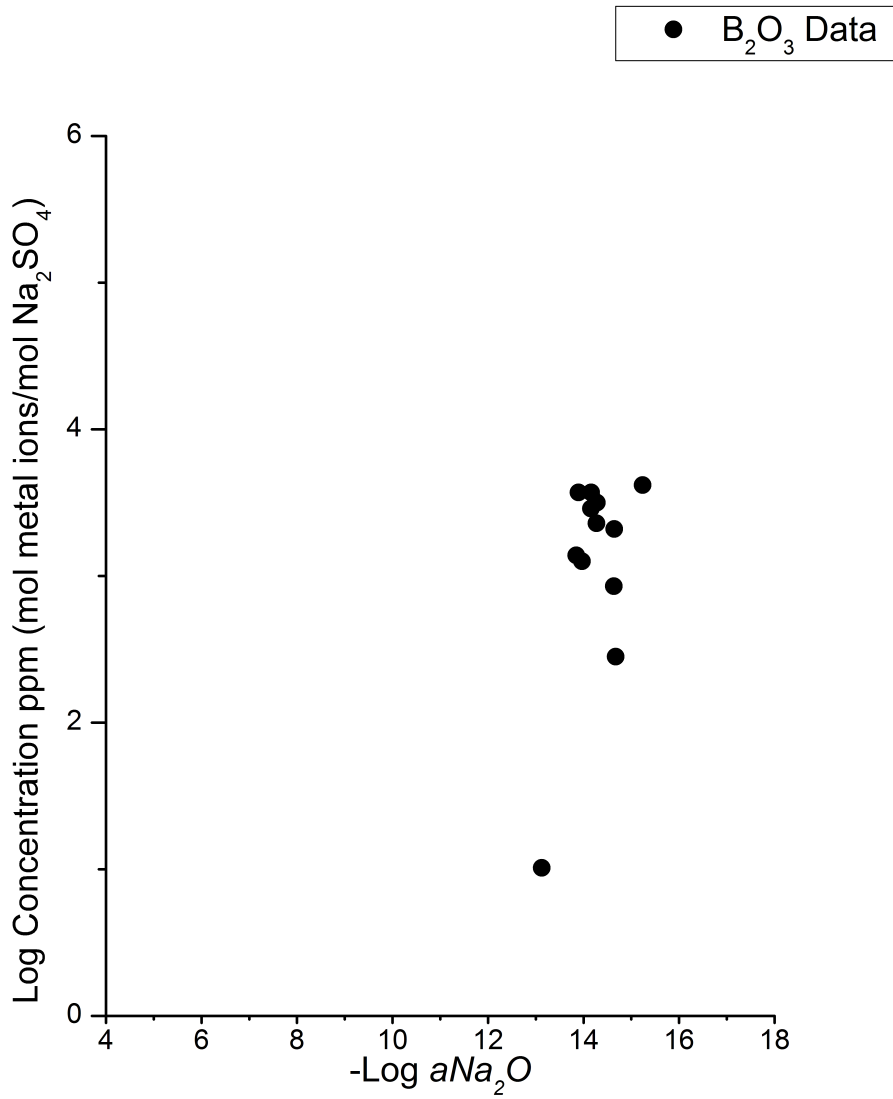


Figure 81 - B₂O₃ solubility data plotted as a function of Na₂O activity.

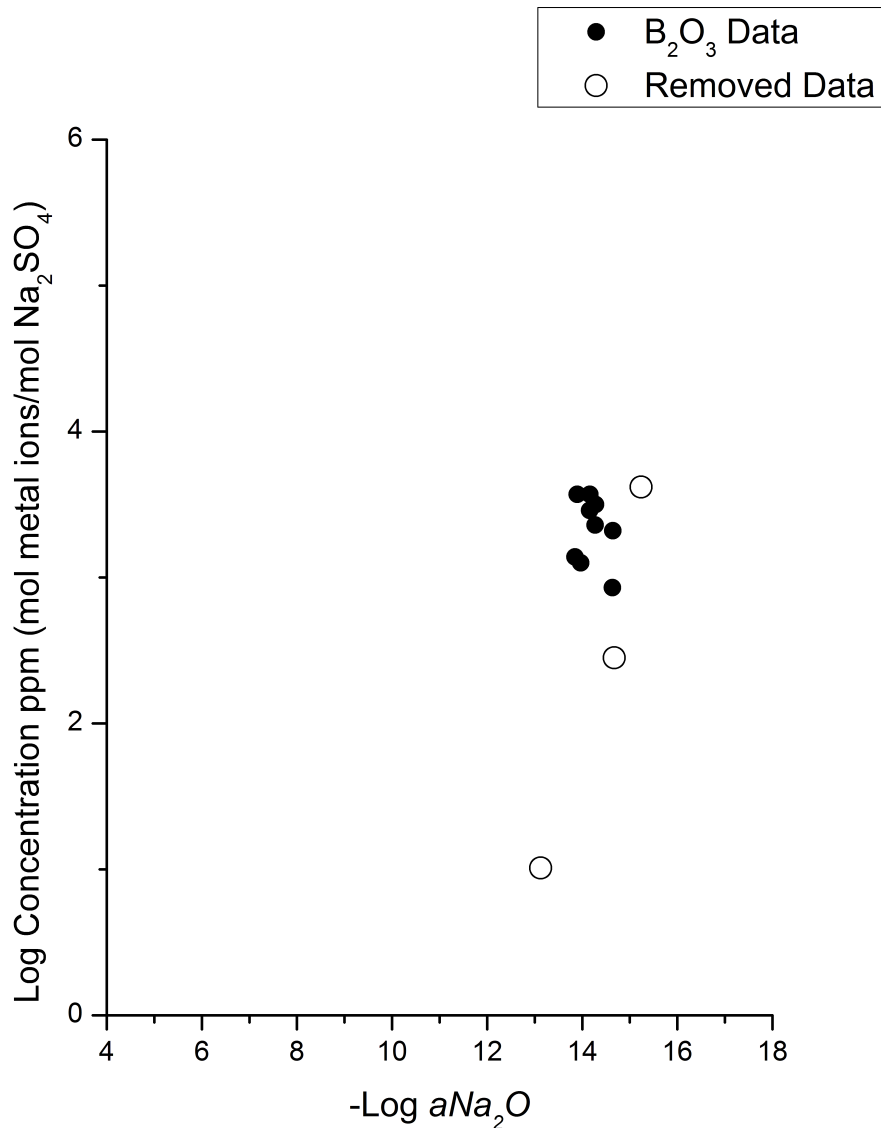
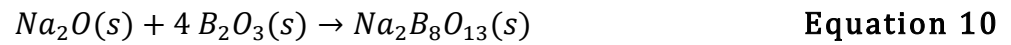


Figure 82 - B₂O₃ solubility data plotted as a function of Na₂O activity. The open circles are data that were removed due to B depletion or improper sampling.

As with silica, boria is not predicted to form sulfates, so the solubility of B₂O₃ is expected to be independent of Na₂O activity at Na₂O activities below $1 \times 10^{-14.8}$. Above $a_{Na_2O} = 1 \times 10^{-14.8}$ the slope solubility is expected to rise with a slope of -1 as shown in the calculation in Equation 18 which is based on the solubility reaction in Equation 10. A trend

line was generated that fit this formula and passed through the data, and that line is shown in Figure 83. The boundary between the boria and sodium borate phase fields shown in Figure 3 is indicated on this figure as a vertical dashed line.

$$\left\{ \frac{\partial(\log a_{Na_2B_8O_{13}})}{\partial(-\log a_{Na_2O})} \right\}_{O_2} = -1 \quad \text{Equation 18}$$



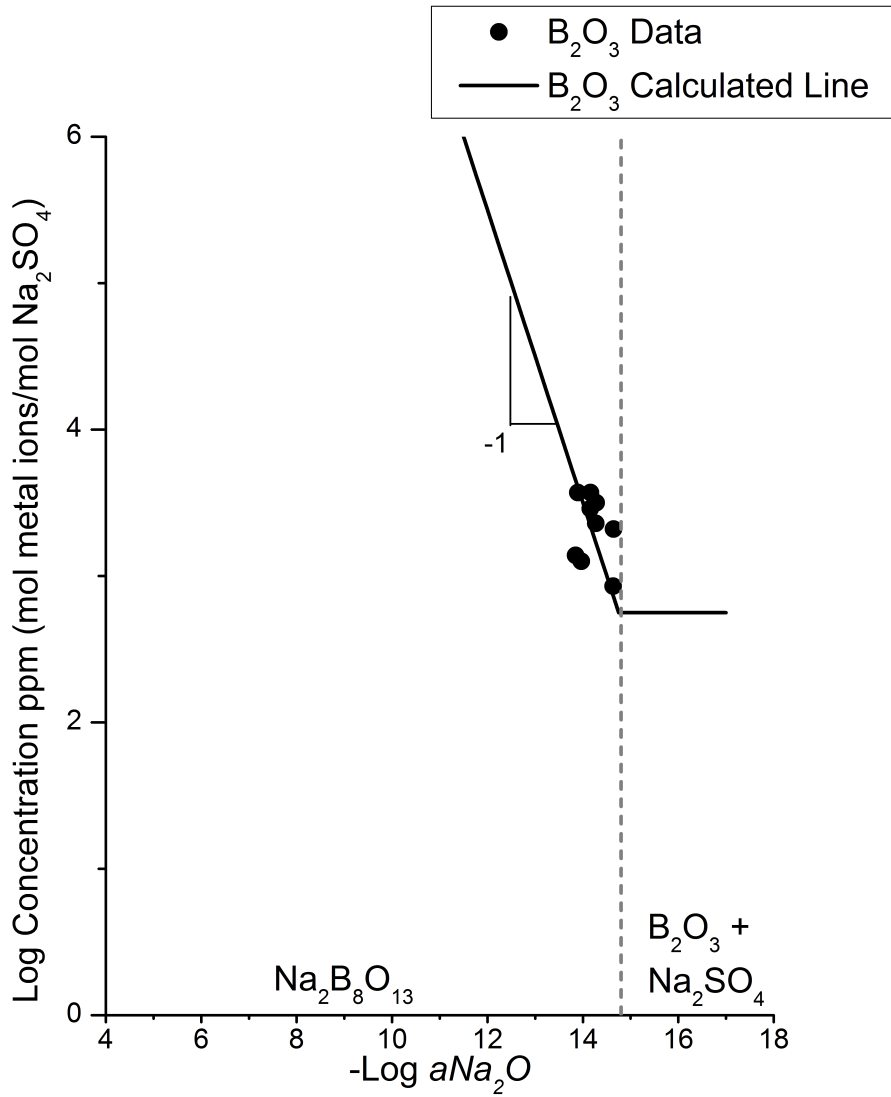
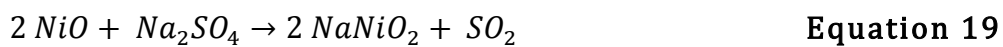


Figure 83 - B₂O₃ solubility data plotted as a function of Na₂O activity. The black line is the trend line calculated from Equation 18 and fitted to the data.

7.2 Discussion

7.2.1 NiO Solubility

The experimental setup created in this work was validated and compared against the literature by replicating the NiO solubility study of Gupta and Rapp. While the data generated here showed more scatter than that previous study the trends and magnitudes were very similar. The present study was not able to probe the extremely high Na₂O activities that Gupta and Rapp explored, however. Later work by the Rapp group switched from using Na₂O₂ additions to using a separate set of electrodes to act as an Na⁺ ion pump to create higher Na₂O activities in the melt. The Na⁺ ion pump method appears to generate a more stable condition in the melt, whereas this work found that the addition of Na₂O₂ led to temporary changes in Na₂O activity without long-term stability, as reported by Watt and Rapp³⁵. The discrepancy between the predicted Na₂O activities and those measured for a given gas were attributed to the SO₂/SO₃ gas generated as the oxide reacted with sodium sulfate by the reactions shown in Equations 5, 11, and 19.



7.2.2 SiO₂ Solubility

The SiO₂ solubility study was performed in an attempt to cover the same range that Shi and Rapp explored while also extending to higher Na₂O activities. The new data extend the data of Shi and Rapp by 1.5 orders of magnitude to Na₂O activities higher than and slightly past the boundary predicted by the phase stability diagram in Figure 1 as shown in Figure 79. The scatter in the data made it difficult to confidently extract a trend at Na₂O activities above 1x10⁻¹¹. When averages were used to visually reduce the scatter (in a

Task 3 – Solubility of Oxides in Sodium Sulfate – Discussion

manner similar to that used by Shi and Rapp) a general trend became visible. The confidence in this trend is low, however it is consistent with increased solubility of SiO_2 in molten Na_2SO_4 at higher Na_2O activities.

The large vertical scatter in the data reflects to different Si concentrations found in samples at a similar Na_2O activity. The difference in measured concentration did not correlate with the size of the sample or the order in which samples were taken (except for issues described previously with samples taken before equilibrium). The sample concentrations measured were at least an order of magnitude above the detection limit of the ICP-OES instrument, and within each sample the measured concentrations were repeatable. There is some variation in the location and depth of the alumina sampling rod, and there is expected to be a gradient in Na_2O activity through the depth of the melt as the Na_2O activity is only fixed at the melt surface where it meets with the gas. This discrepancy in sampling is likely the explanation for the scatter observed.

The slope of the SiO_2 solubility line at Na_2O activities above 1×10^{-11} is -0.5, which does not correlate with theoretical predictions from Equation 17. This slope, however, was fitted to relatively few data points, and there is low statistical confidence in its calculation. The slope might be expected to transition gradually from horizontal to a slope of -1 as the compound is formed. In addition the sodium silicate compound formed is amorphous (presumably with a compositional range) rather than crystalline (with a fixed stoichiometry).

The SiO_2 solubility results generated in this work differ from the results of Shi and Rapp by an order of magnitude. Several possible explanations were evaluated to account for this discrepancy:

1. Shi and Rapp used a quartz crucible (presumably fused quartz, though it is not specified) rather than the alumina crucible used in the study. The presence of additional silica in contact with the melt does not explain why their solubility values are lower, however.
2. Shi and Rapp used a mullite tube for their Na⁺ electrode, while this study used a fused quartz tube. This does result in additional SiO₂ available from the electrodes in this study, however it is unlikely this SiO₂ source would counteract the additional SiO₂ contact from the quartz crucible used by Shi and Rapp.
3. Shi and Rapp used quartz powder, though they do not specify the particle size. It is also unclear whether the quartz was actually crystalline or fused quartz. Fused quartz is known to be more soluble than crystalline quartz in water^{83, 84}, so the trend might be the same in Na₂SO₄ as well. In this study large pieces (≈1-2 mm) of fused quartz were used to reduce the chance of sampling undissolved silica. Even when silica particles were observed in the sample it did not appear to affect the results as the pieces of silica were large and the solubility of silica in water is negligible at these times⁸⁵. As with the quartz crucible, the use of a potentially fine quartz powder should only have resulted in Shi and Rapp measuring a silica solubility that is higher, rather than lower than the results obtained here, however if the solubility of amorphous and crystalline quartz is different, this may account for the difference.
4. Shi and Rapp used colorimetric absorption (or UV-Vis) spectrophotometry, unlike most of the rest of the papers on oxide solubility in molten sodium sulfate by Rapp and co-workers^{58, 82, 86, 87}, in which atomic absorption (AA)

spectrophotometry was used to determine the solubility. AA is an analytical technique much like ICP-OES where sample atoms are exposed to energizing source (typically a furnace or a flame) in order to dissociate molecules into atoms. In AA a carefully controlled light source is passed through the flame, and the sample atoms absorb some of the radiation. The modified radiation beam is then analyzed by a spectrometer and elemental concentrations are determined by comparison with calibration standards. UV-Vis uses a polychromatic light source and measures absorption, as in AA, but it does not excite or atomize the analyte during analysis. UV-Vis, therefore, analyzes the compounds and their bonding rather than analyzing the atoms themselves.

5. Finally, Shi and Rapp controlled the Na_2O activity in the sample melts by using a second set of electrodes to act as a sodium pump and fix the Na_2O activity electrochemically rather than chemically as in this study. If the additional effects of the Na_2O_2 additions were responsible for the increased solubility observed in this study, however, it wouldn't explain why the samples taken at the lowest Na_2O activities (without Na_2O_2) were also high.

In summary, no definitive explanation for the discrepancy between the work of Shi and Rapp and this study is identified.

7.2.3 B_2O_3 Solubility

The solubility of B_2O_3 was found to be of the same magnitude as the solubility of SiO_2 , though at much lower Na_2O activities. The fit line shown in Figure 83 indicates that the solubility of B_2O_3 is expected to increase as Na_2O activity increases. The magnitude of the B_2O_3 solubility (vertical positioning of the fit line) is not well defined by the data

collected in this work, however if the solubility trend is followed than B_2O_3 will be several orders of magnitude higher than that of SiO_2 over a very large range of SO_3 partial pressures.

The difference between the predicted and measured Na_2O activities were much larger for B_2O_3 than for SiO_2 or NiO at SO_2 concentrations below 1000ppm. Poerschke⁷⁵ has shown that B_2O_3 and Na_2SO_4 react more vigorously than SiO_2 and Na_2SO_4 at $900^\circ C$ in argon. Equation 11 shows that when Na_2SO_4 and B_2O_3 react SO_3 gas is evolved. If sufficient SO_3 gas is being generated by the reaction between boria and sodium sulfate, then the SO_3 partial pressure in the gas could be raised enough to affect the Na_2O activity within the melt. To determine if this was the case, at the end of one of the tests containing aluminoborate pellets (and using a 1 ppm SO_2/O_2 gas), the flow rate was increased from 100 sccm to 250 sccm to flush out excess SO_3 . When the flow rate was increased the measured potential rose steadily indicating an increase in the Na_2O activity in the melt.

Figure 84 is a revised version of Figure 5 with the newly generated data for SiO_2 and B_2O_3 . Also included on this figure are the fit line for SiO_2 and the theoretical line for B_2O_3 .

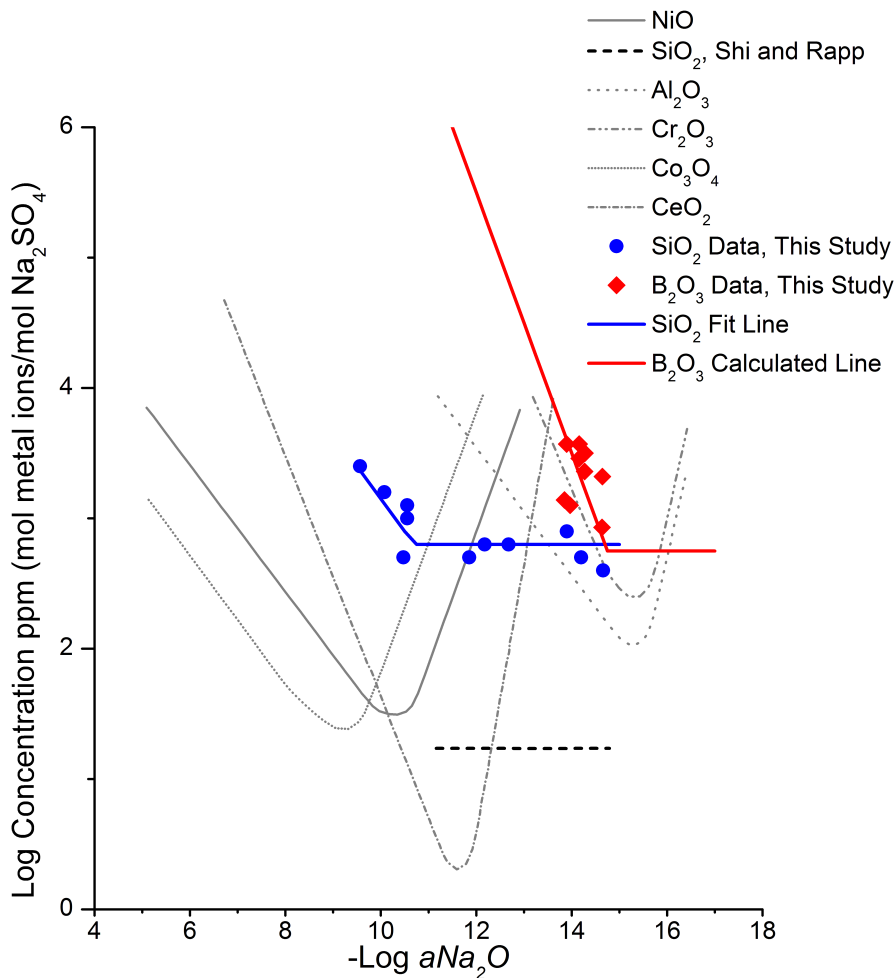


Figure 84 – Summary plot of the solubility of several oxides in molten Na₂SO₄ at 900°C, existing data from Rapp²³.

7.3 Conclusions

The electrochemical setup used in this task was validated by comparison to the literature data for the solubility of NiO. The solubility of SiO₂ in molten Na₂SO₄ was found to be higher than values found by Shi and Rapp, but the trend as a function of Na₂O activity was consistent. This work extended measured SiO₂ solubility by 1.5 orders of magnitude towards higher Na₂O activities and found that SiO₂ solubility likely increases as sodium

silicates are predicted to form above $aNa_2O = 1 \times 10^{-11}$. The solubility of B_2O_3 was found to be similar to that of silica, though at a lower Na_2O activity. B_2O_3 solubility is predicted to increase at $aNa_2O = 1 \times 10^{-14.8}$ with a slope of -1, making the predicted solubility much higher than that of SiO_2 at any given Na_2O activity above $1 \times 10^{-14.8}$.

The solubility results indicate that lowering sulfur contents in fuels is expected to result in increased hot corrosion attack of SiC/SiC CMCs. Silica remains stable at sulfur contents corresponding to SO_3 partial pressures above 1×10^{-5} atm. SO_3 partial pressures below $1 \times 10^{-1.5}$ (0.032 atm) are expected to result in B_2O_3 dissolution into Na_2SO_4 resulting in corrosion products with decreased viscosity and increased corrosive properties consistent with results from Tasks 1 and 2.

Combustion conditions were simulated using CEARUN^{88, 89}, and these results were analyzed in FactSage⁴³ to determine the SO_2 and SO_3 partial pressures as a function of sulfur content in fuel. It was found that the combined SO_2/SO_3 partial pressures are directly related to the sulfur content in the fuel. Therefore, for the JP-8 with 15.6 ppm S (as used in this study), the total pressure of S-bearing gas would be 1.56×10^{-5} atm. This indicates that having fuels with ppm level S content is expected to result in dissolution of B_2O_3 and SiO_2 scales in hot corrosion conditions.

7.4 Recommendations for Future Work

Future work on the solubility of SiO_2 and B_2O_3 will be extremely valuable as SiC/BN/SiC CMCs see widespread adoption in marine-based turbine engine environments. The most limiting factor in this study was the inability to accurately control the Na_2O activity in the melt at a specified value. The use of a furnace that allows for larger furnace

tube diameters ($\geq 3''$) and thus an additional set of electrodes to act as a sodium pump would be of great value in pushing the Na_2O activities higher in a controlled fashion.

The solubility of SiO_2 should be explored to higher Na_2O activities, and exploring the potential differences in solubility between crystalline and amorphous silica would be worth exploring.

Solubility of B_2O_3 should be explored further at both higher and lower Na_2O activities using aluminoborate materials with more well-defined and characterized phases (and coarser starting powders).

The composition of the Na^+ electrode should be characterized after an exposure to analyze the ratio of Na_2SO_4 to Ag_2SO_4 and see if it has changed from the start of the test. This ratio is an important factor in relating the measured potential to the Na_2O activity, so large changes in the ratio (due to Na^+ diffusing inward or Ag^+ diffusing outward) could affect the readings.

Solubility studies should also be carried out at higher temperatures. Higher temperatures are not only more similar to the environments found inside a turbine engine but also may result in very different solubilities as more of the oxide species become molten. The limiting factor right now is the need to use a silver wire in the Na^+ electrode. A silver alloy that contains a higher melting temperature, such as a gold-silver alloy with a known silver activity^{90, 91}, should allow for measurements at temperatures of 950 or 1000°C.

As EBCs are largely silicate-based, the solubility of the EBC materials in Na_2SO_4 should be evaluated. The EBCs often contain rare-earth elements such as Yb or Y, and the solubility of those elements and their oxides in Na_2SO_4 would be valuable information.

Pieces of complete coating material could be exposed as well, and the combined solubility of the coating can be determined (and un-dissolved coating pieces can be characterized to determine what elements have been selectively leached out).

8 Conclusions

Hot corrosion of SiC model materials indicated that hot corrosion initiates rapidly, and then plateaus. The temperature dependence kinetics are consistent with a rate limited by the diffusion of oxygen through a silica layer at the scale-substrate interface, once that layer has time to form (within a few hours). The presence of B, whether as a thin BN layer or as B-bearing additives in the SiC, resulted in increased hot corrosion attack of the SiC.

The hot corrosion of SiC CMCs was more rapid than that of the model materials, though the model materials were effective at predicting the hot corrosion resistance of various parts of the composite. The complex architecture of the CMCs introduces additional surface area, and selective attack of different phases leads to more severe recession. The high velocity of the burner rig leads to shearing of the corrosion products and increased attack. The recession rates observed indicate that hot corrosion of SiC CMCs will likely be at least as important as the volatility observed in a combustion environment with water vapor.

The solubility of SiO_2 and B_2O_3 was determined in Na_2SO_4 as a function of $p\text{SO}_3$. These results indicate that with low sulfur fuels the hot corrosion of SiC CMCs is expected to be more severe than with higher sulfur fuels due to increased dissolution of the oxides by Na_2SO_4 .

9 Acknowledgements

Beth Opila, for her guidance and patience as an advisor

Nathan Jacobson, for his assistance and insight into the electrochemical cell

My committee for their helpful comments

Dennis Fox and Michael Cuy, for running the burner rig samples

Elise Poerschke, for her assistance in preparing samples

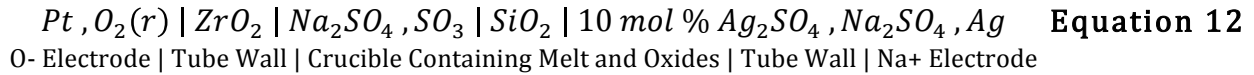
Siyang Liu, for her assistance in collecting pitting data

The rest of my lab mates for their help

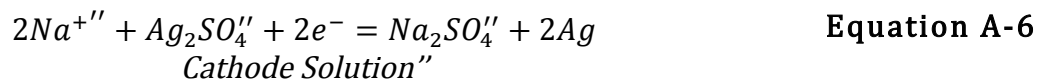
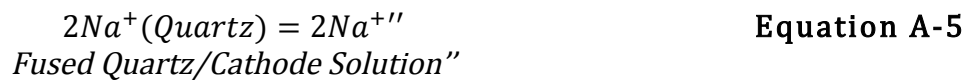
Joelle and Franklin

Appendix A Electrochemical Potential Derivation

To derive the measured potential and how it relates to the Na₂O activity in the melt we follow the derivation described by Watt, Andersen, and Rapp³⁵ and the derivation provided by Gupta and Rapp⁵⁸, and start with the overall cell reaction provided in Equation 12:



From this equation the individual reactions are as follows:



This yields the overall chemical reaction:



From the overall reaction involving two electrons one obtains:

$$E_A = E_A^o - \frac{2.303 \cdot R \cdot T}{2 \cdot F} \cdot \log \frac{P_{O_2}^{\frac{1}{2}}(r) \cdot a_{Na_2SO_4''}}{a_{Na_2O'} \cdot a_{Ag_2SO_4''}} \quad \text{Equation A-8}$$

where R is the gas constant, T is the temperature, and F is Faraday's constant. The activity of silver is excluded as $a_{Ag}=1$ for pure silver. By combining the activities of the sodium sulfate in the Ag/Ag^+ electrode and the P_{O_2} term Equation A-8 simplifies to:

$$E_A = E_A^{o'} - \frac{2.303 \cdot R \cdot T}{2 \cdot F} \cdot \log a_{Na_2O'} \quad \text{Equation A-9}$$

where:

$$E_A^{o'} = E_A^o - \frac{2.303 \cdot R \cdot T}{2 \cdot F} \cdot \log \frac{a_{Na_2SO_4''}}{a_{Ag_2SO_4''}} - \frac{2.303 \cdot R \cdot T}{4 \cdot F} \cdot \log P_{O_2}(r) \quad \text{Equation A-10}$$

and E_A^o can be calculated as follows:

$$E_A^o = \frac{-1}{2 \cdot F} \cdot [\Delta G_f^o(Na_2SO_4) - \Delta G_f^o(Na_2O) - \Delta G_f^o(Ag_2SO_4)] \quad \text{Equation A-11}$$

Using the thermodynamic data provided in Table A-1 the value of E_A^o is found to be 1.643 V.

Table A-1 - Thermodynamic data taken from FactSage⁴³.

Compound	ΔG_f^o [cal/mol]
Na ₂ SO ₄	-221358
Na ₂ O	-61492
Ag ₂ SO ₄	-84138

The value of Equation A-10 can be determined by using the activity coefficient ratio of 3.17 for $\gamma_{Na_2SO_4}/\gamma_{Ag_2SO_4}$ from Shores and John⁹². From this the $E_A^{o'}$ is found to be 1.474 V when the partial pressure of oxygen in the ZrO₂ tube is 1 atm.

Finally the potential measured in the cell as a function of Na₂O activity at 900°C is:

$$E_A = 1.474 + 0.119 \cdot \log a_{Na_2O'} \quad \text{Equation A-12}$$

Appendix B Radar Plot Data

Table B-1 – Maximum values and units for each category in Figures 25, 26, and 27

Category	Figure 25		Figure 26		Figure 27	
	CVD-SiC	Hexoloy	CVD+C	Hexoloy+C	CVD+BN	Hexoloy+BN
Normalized Mass Change (mg/cm ²)	-0.795 ± 0.51	1.37 ± 0.72	-1.28 ± 0.5	0.817 ± 0.5	0.895 ± 0.5	1.12 ± 0.5
Mass Loss After Water (mg)	2.21 ± 0.56	4.96 ± 1.3	2.94 ± 0.5	3.46 ± 0.5	5.83 ± 0.5	5.14 ± 0.5
Mass Loss After HCl (mg)	0.005 ± 0.015	0.590 ± 0.81	0.030 ± 0.5	0.547 ± 0.5	1.15 ± 0.5	0.870 ± 0.5
Mass Loss After HF (mg)	1.24 ± 0.035	7.48 ± 2.6	1.12 ± 0.5	6.41 ± 0.5	1.74 ± 0.5	8.24 ± 0.5
Normalized Mass Loss (mg/cm ²)	0.643 ± 0.32	4.05 ± 1.7	1.80 ± 0.5	3.74 ± 0.5	2.48 ± 0.5	4.90 ± 0.5
B in Water (µg)	-0.397 ± 1.5	1.21 ± 0.80	3.20 ± 0.5	1.17 ± 0.5	-0.211 ± 0.5	16.7 ± 0.5
Na in Water (µg)	666 ± 230	1180 ± 320	583 ± 0.5	749 ± 0.5	297 ± 0.5	196 ± 0.5
S in Water (µg)	1430 ± 1300	1210 ± 750	396 ± 0.5	727 ± 0.5	174 ± 0.5	568 ± 0.5
Si in Water (µg)	15.9 ± 35	110 ± 160	36.5 ± 0.5	65.7 ± 0.5	1.21 ± 0.5	48.1 ± 0.5
B in HCl (µg)	-0.457 ± 0.73	1.73 ± 3.8	4.34 ± 0.5	1.05 ± 0.5	-0.0330 ± 0.5	3.36 ± 0.5
Na in HCl (µg)	2.31 ± 2.4	21.4 ± 18	-2.30 ± 0.5	7.85 ± 0.5	-8.00 ± 0.5	19.7 ± 0.5
S in HCl (µg)	2.09 ± 1.9	8.19 ± 13	0.749 ± 0.5	1.27 ± 0.5	-0.610 ± 0.5	3.68 ± 0.5
Si in HCl (µg)	18.0 ± 15	35.9 ± 37	25.3 ± 0.5	24.4 ± 0.5	4.37 ± 0.5	22.5 ± 0.5
B in HF (µg)	-2.10 ± 1.4	10.6 ± 17	-0.287 ± 0.5	9.97 ± 0.5	-0.0675 ± 0.5	29.6 ± 0.5
Na in HF (µg)	0.715 ± 1.6	23.5 ± 15	-6.27 ± 0.5	60.7 ± 0.5	1.03 ± 0.5	94.9 ± 0.5
S in HF (µg)	5.72 ± 4.8	16.5 ± 16	0.280 ± 0.5	14.4 ± 0.5	0.671 ± 0.5	21.8 ± 0.5
Si in HF (µg)	473 ± 120	2960 ± 970	316 ± 0.5	3020 ± 0.5	645 ± 0.5	3530 ± 0.5
Total B (µg)	-2.96 ± 2.9	13.5 ± 22	7.25 ± 0.5	12.2 ± 0.5	-0.311 ± 0.5	49.6 ± 0.5
Total Na (µg)	669 ± 230	1230 ± 320	574 ± 0.5	817 ± 0.5	290 ± 0.5	311 ± 0.5
Total S (µg)	1430 ± 1300	1240 ± 780	379 ± 0.5	743 ± 0.5	174 ± 0.5	594 ± 0.5
Total Si (µg)	507 ± 150	3100 ± 1100	378 ± 0.5	3110 ± 0.5	651 ± 0.5	3600 ± 0.5
Normalized B (µg/cm ²)	-1.85 ± 1.8	9.09 ± 15	4.54 ± 0.5	7.56 ± 0.5	-0.195 ± 0.5	30.6 ± 0.5
Normalized Na (µg/cm ²)	419 ± 140	803 ± 200	360 ± 0.5	514 ± 0.5	182 ± 0.5	192 ± 0.5
Normalized S (µg/cm ²)	897 ± 810	823 ± 530	249 ± 0.5	463 ± 0.5	109 ± 0.5	366 ± 0.5
Normalized Si (µg/cm ²)	318 ± 96	2020 ± 660	237 ± 0.5	1970 ± 0.5	408 ± 0.5	2220 ± 0.5
Mean Pit Depth (µm)	0.204 ± 0	9.57 ± 0	1.08 ± 0.5	2.74 ± 0.5	2.26 ± 0.5	7.16 ± 0.5
Pit Density (µg/cm ²)	31.9 ± 0	33.1 ± 0	279 ± 0.5	40.3 ± 0.5	203 ± 0.5	46.4 ± 0.5
Mean Pit Diameter (µm)	7.03 ± 0	19.9 ± 0	15.0 ± 0.5	9.71 ± 0.5	16.9 ± 0.5	20.8 ± 0.5
Max Pit Depth (µm)	5.05 ± 0	57.2 ± 0	19.9 ± 0.5	48.1 ± 0.5	14.6 ± 0.5	32.4 ± 0.5

Appendix C Microscopy of CMC Coupons

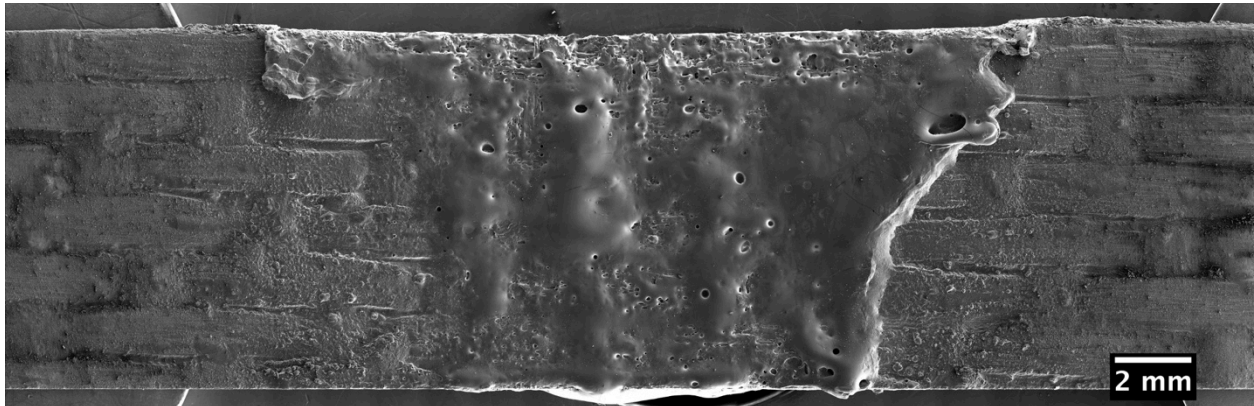


Figure C-1 – SEM Micrograph of the face of MI-BR-24 after exposure in the burner rig, leading edge on top, impingement site in center of coupon.

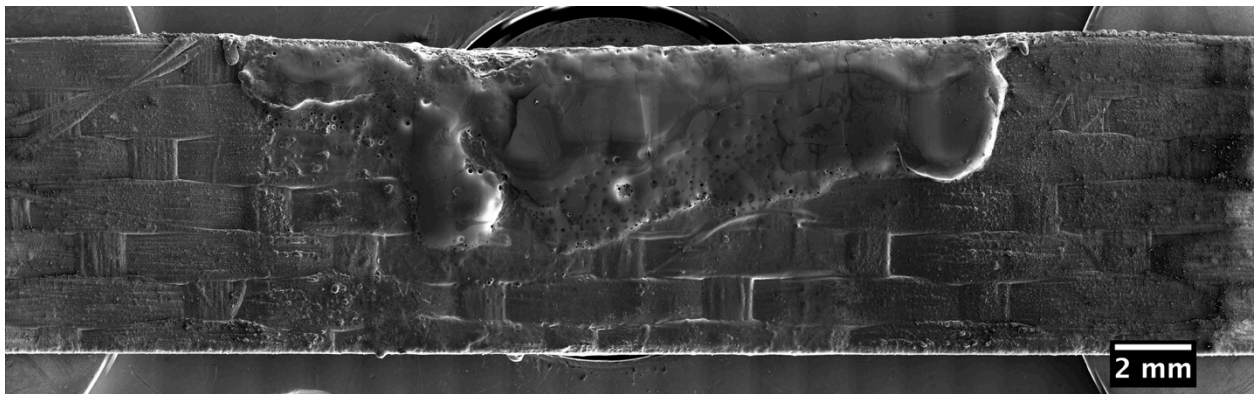
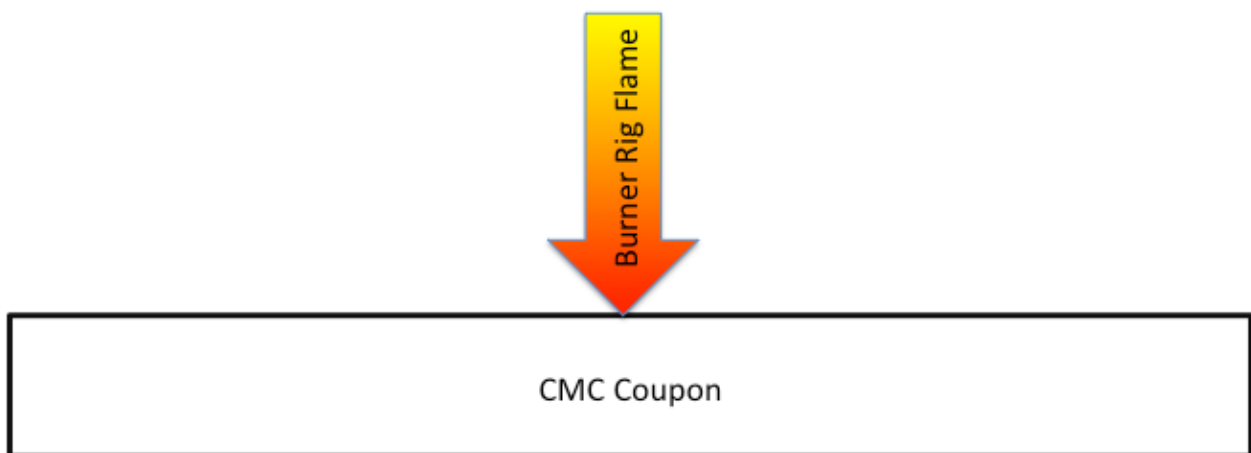


Figure C-2 – SEM Micrograph of the face of CVI-BR-24 after exposure in the burner rig, leading edge on top, impingement site in center of coupon.



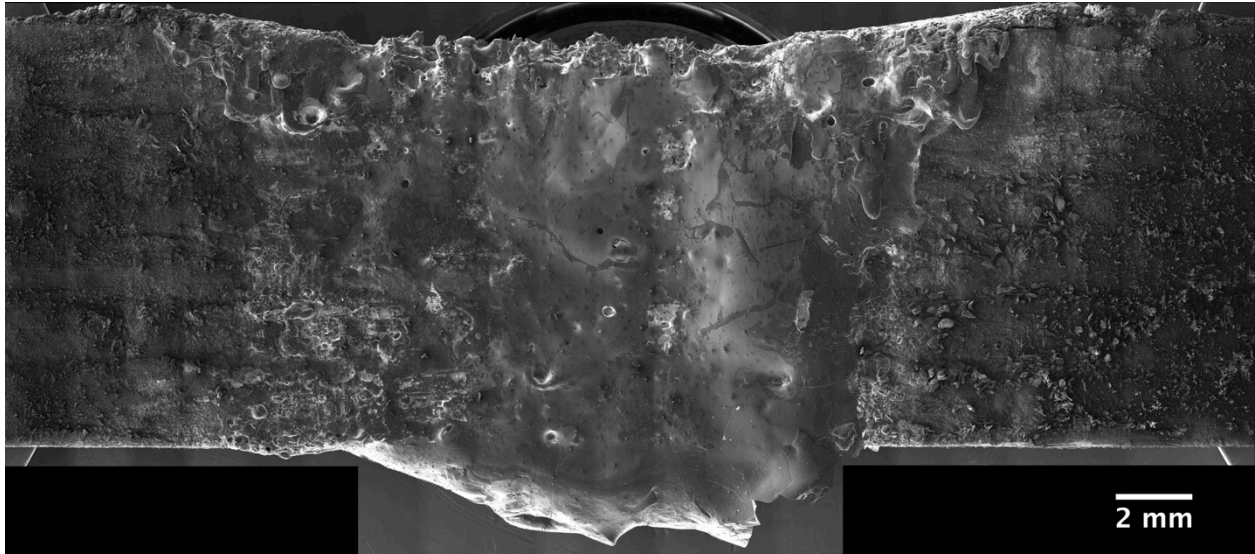


Figure C-3 – SEM Micrograph of the face of MI-BR-45 after exposure in the burner rig, leading edge on top, impingement site in center of coupon.

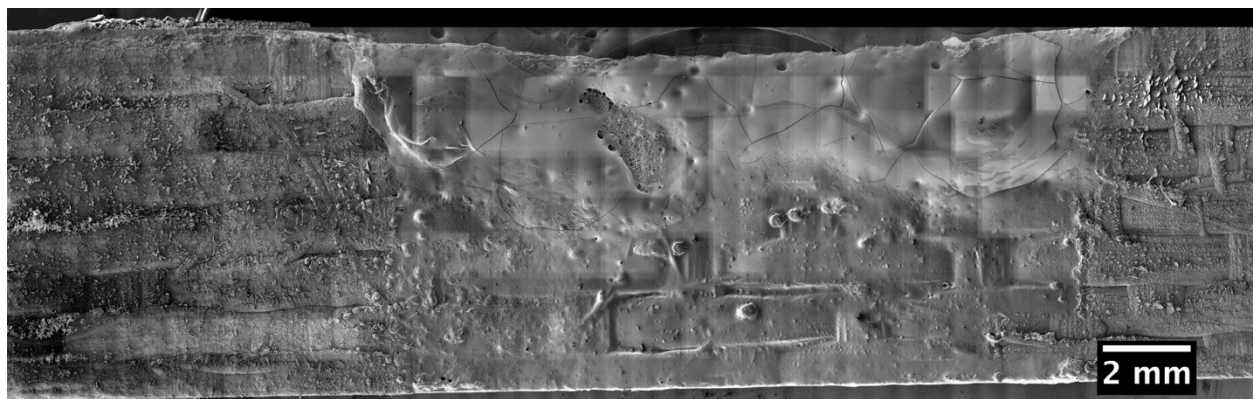
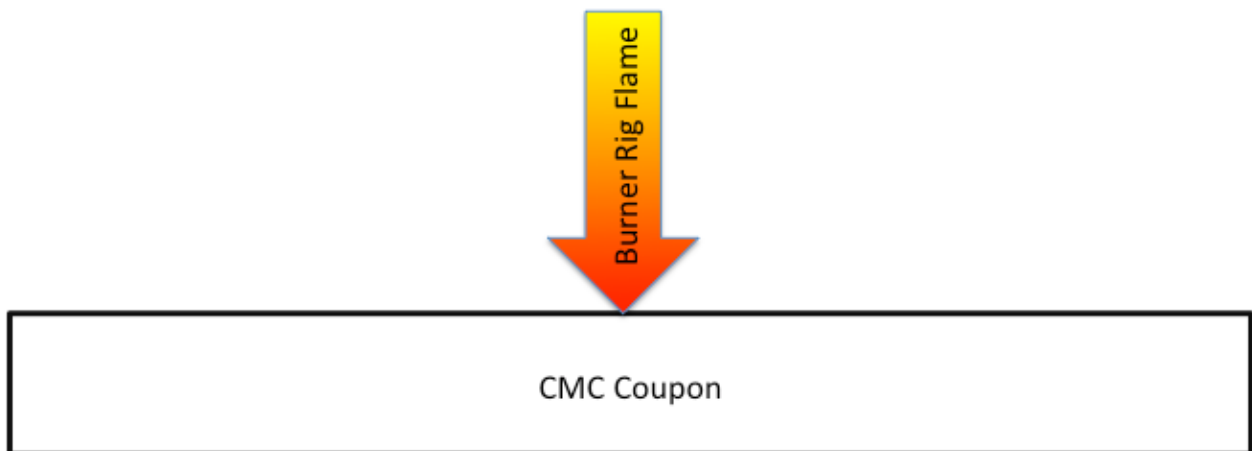


Figure C-4 – SEM Micrograph of the face of CVI-BR-45 after exposure in the burner rig, leading edge on top, impingement site in center of coupon.



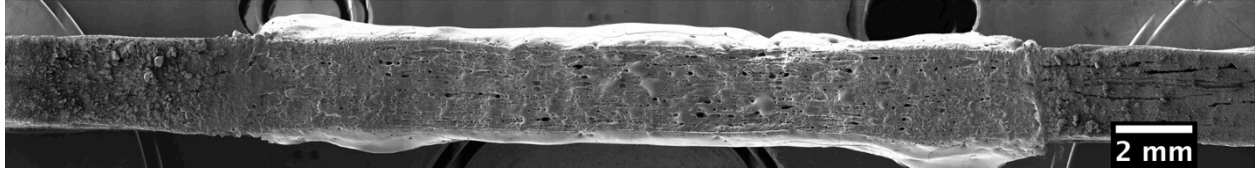


Figure C-5 – SEM Micrograph of the leading edge of MI-BR-24 after exposure in the burner rig, impingement site in center of coupon.

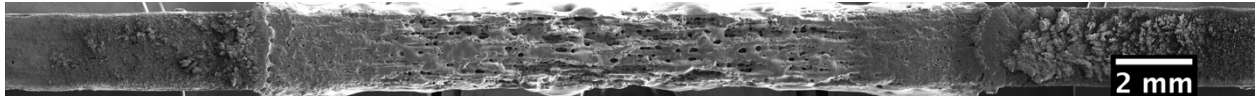


Figure C-6 – SEM Micrograph of the leading edge of CVI-BR-24 after exposure in the burner rig, impingement site in center of coupon.

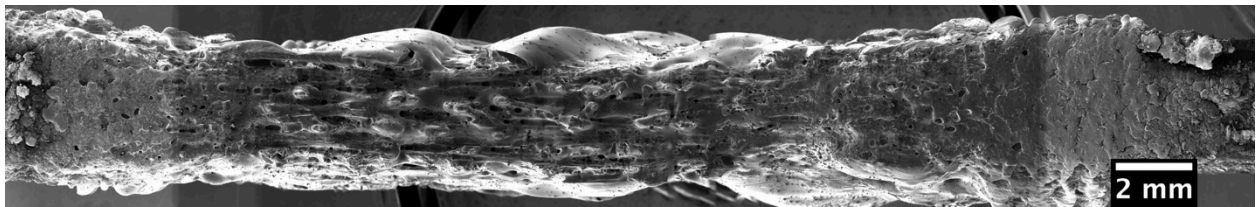


Figure C-7 – SEM Micrograph of the leading edge of MI-BR-45 after exposure in the burner rig, impingement site in center of coupon.

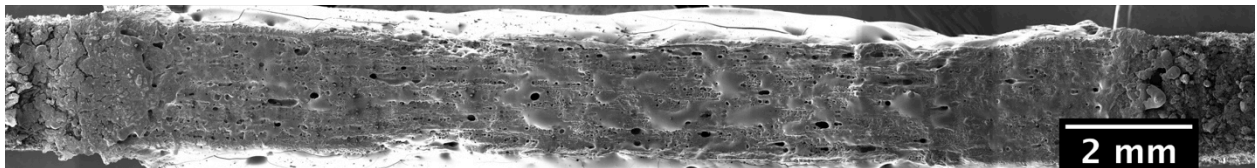
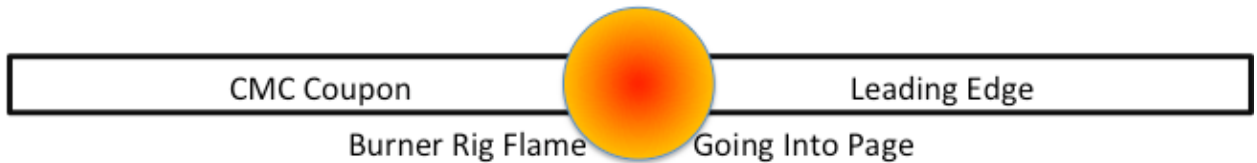


Figure C-8 – SEM Micrograph of the leading edge of CVI-BR-45 after exposure in the burner rig, impingement site in center of coupon.



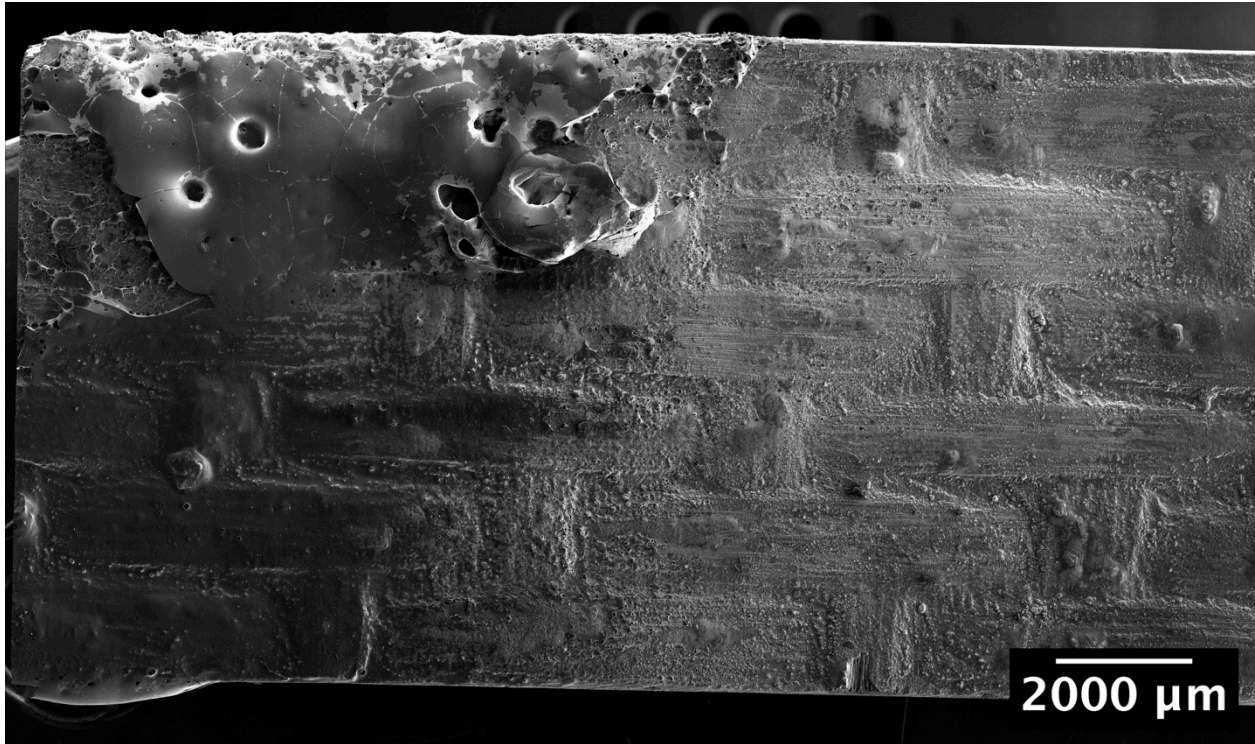
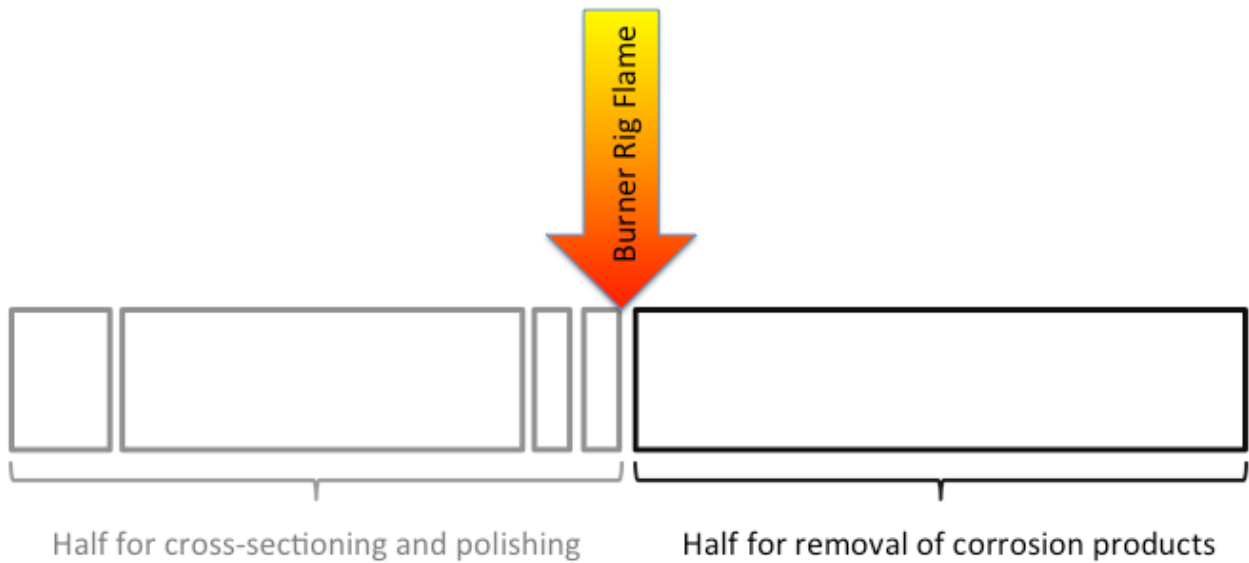


Figure C-9 – SEM Micrograph of the face of MI-BR-24 after sectioning and water digestion, leading edge on top, cut edge (formerly the center of the impingement site) on the left.



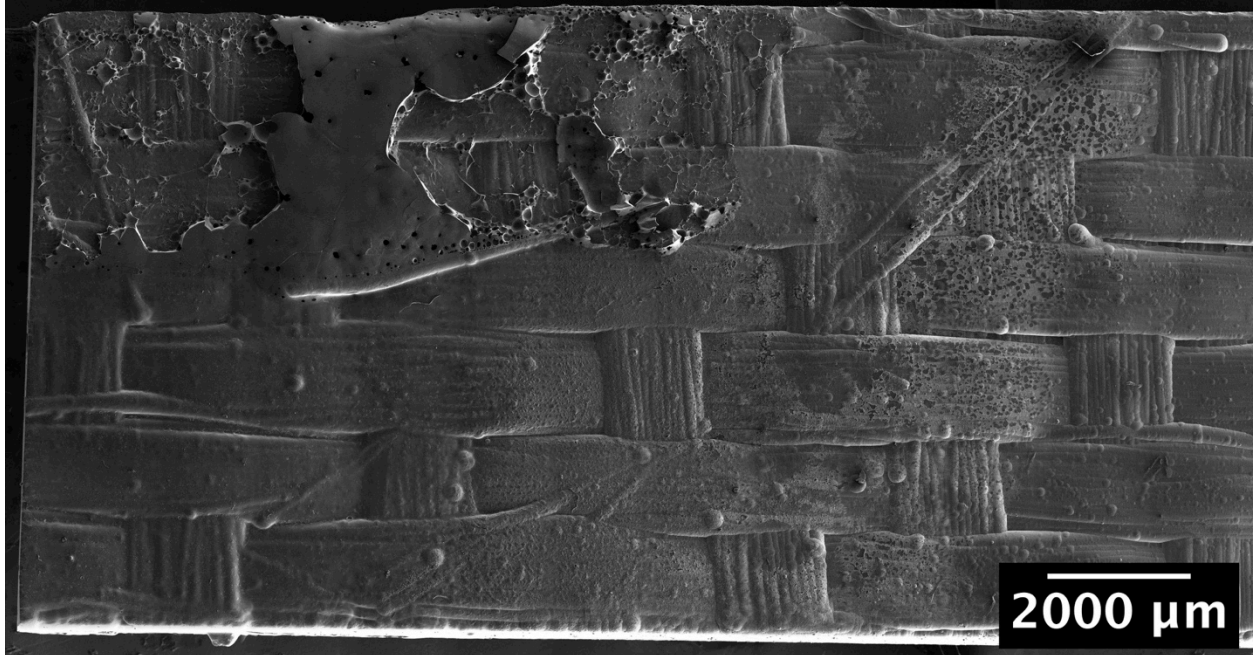
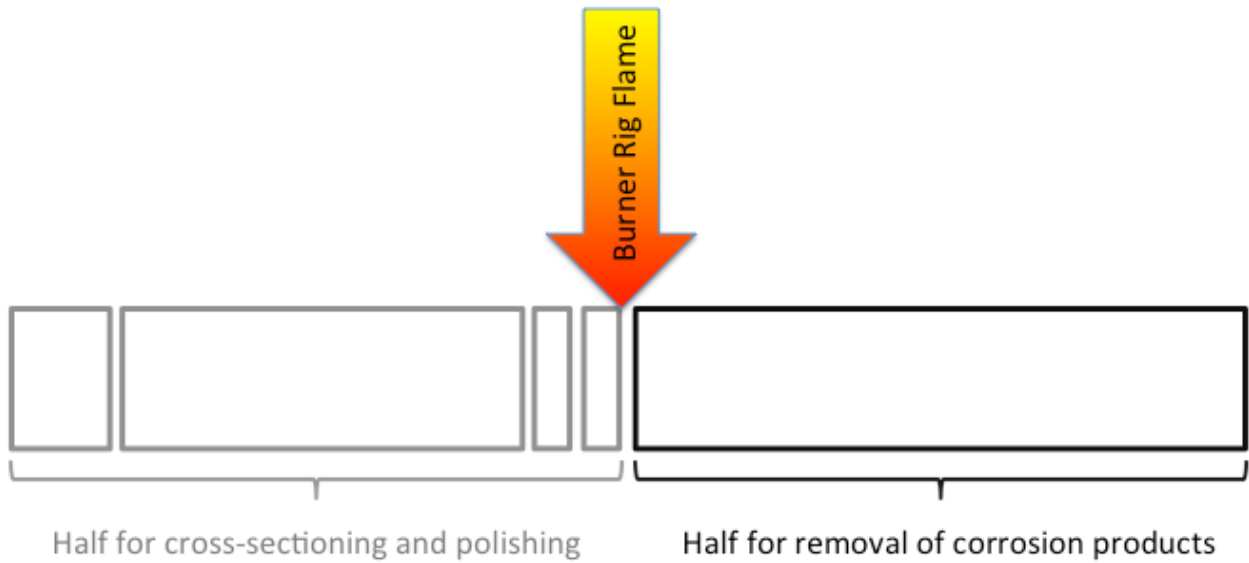


Figure C-10 – SEM Micrograph of the face of CVI-BR-24 after sectioning and water digestion, leading edge on top, cut edge (formerly the center of the impingement site) on the left.



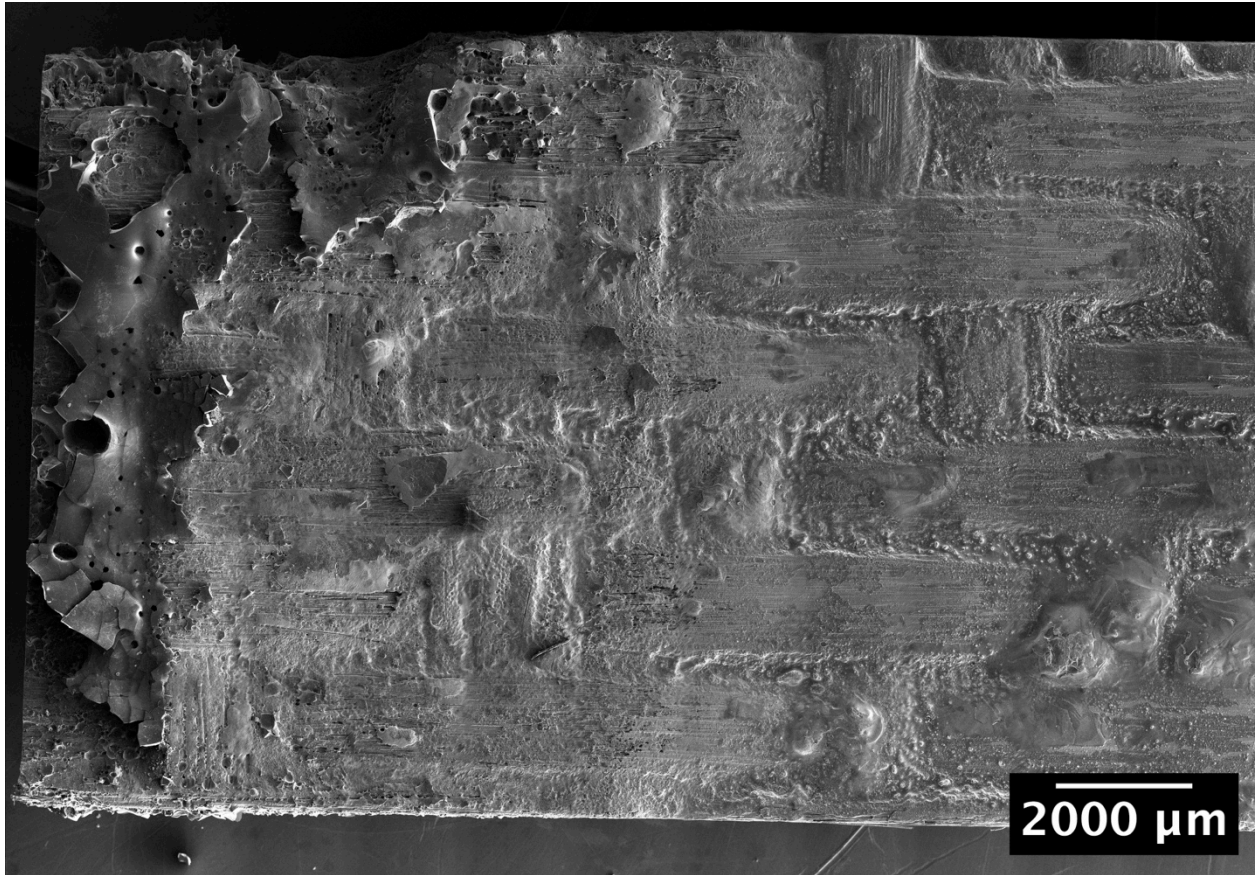
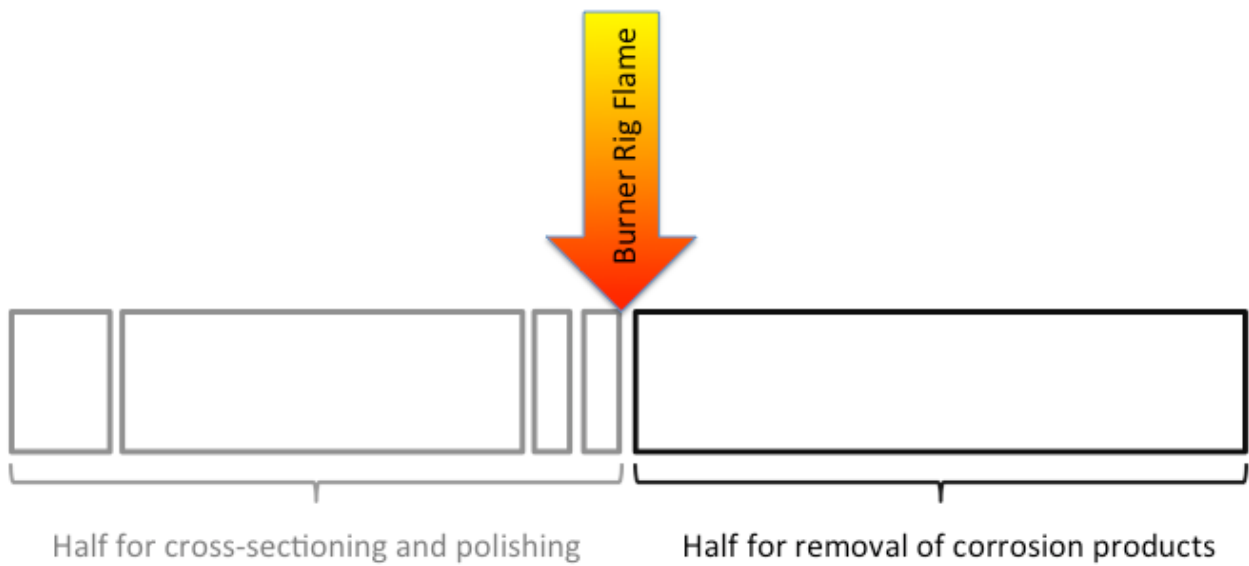


Figure C-11 - SEM Micrograph of the face of MI-BR-45 after sectioning and water digestion, leading edge on top, cut edge (formerly the center of the impingement site) on the left.



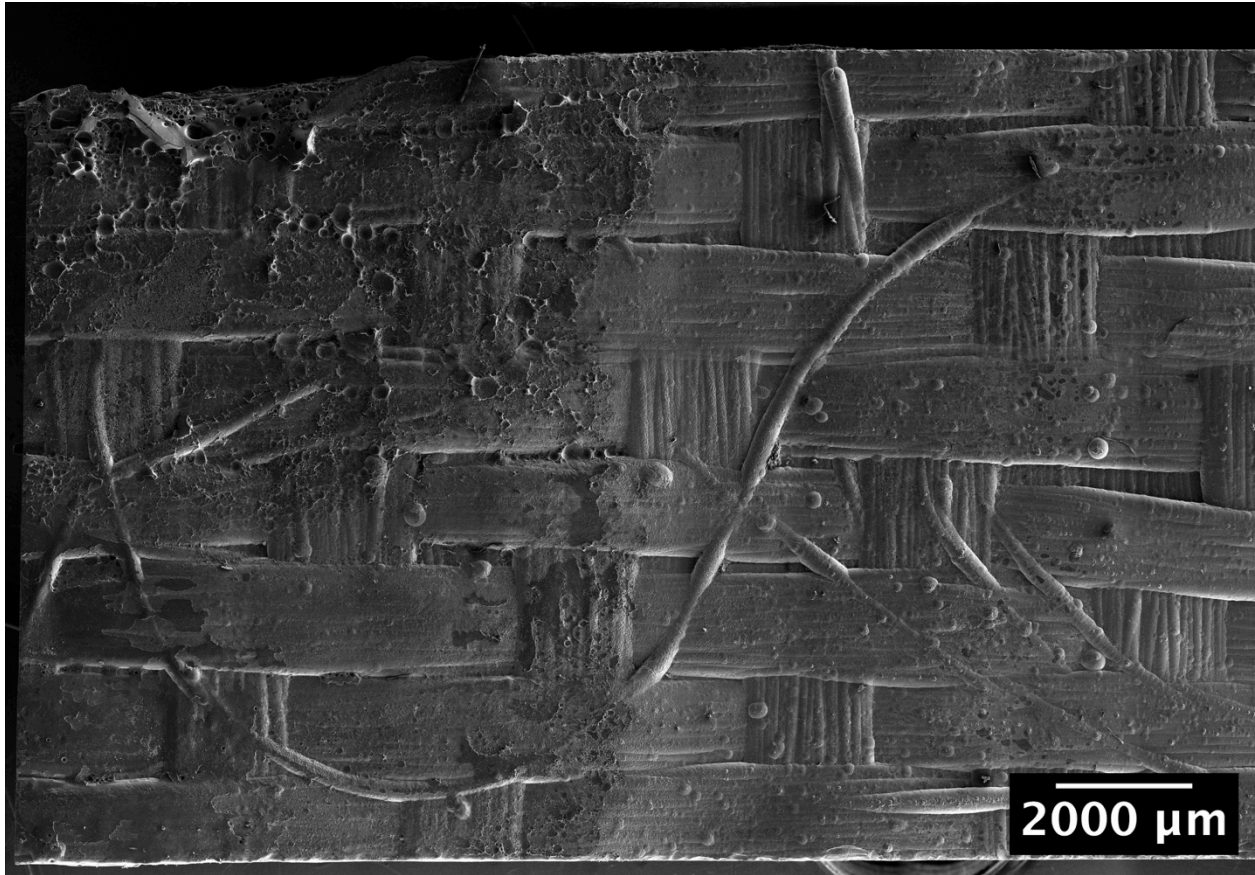
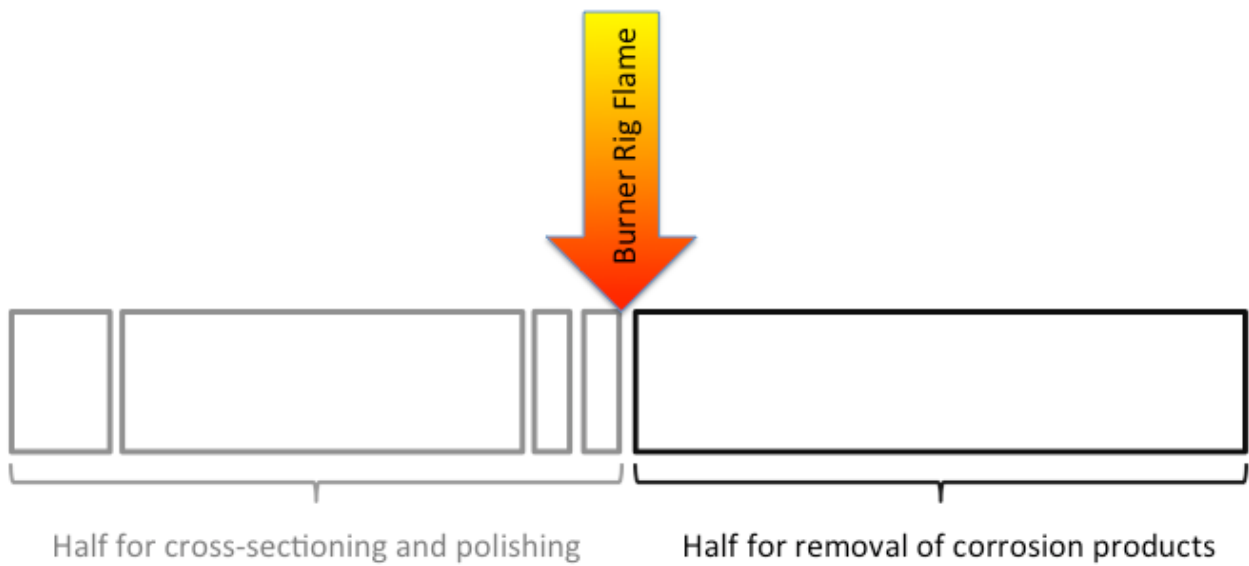


Figure C-12 – SEM Micrograph of the face of CVI-BR-45 after sectioning and water digestion, leading edge on top, cut edge (formerly the center of the impingement site) on the left.



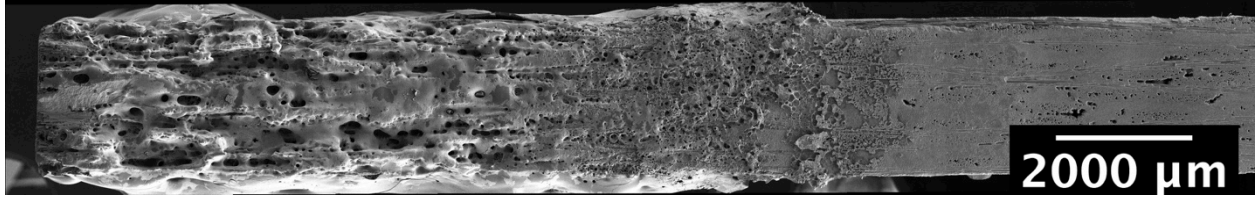


Figure C-13 – SEM Micrograph of the leading edge of MI-BR-24 after sectioning and water digestion, cut edge (formerly the center of the impingement site) on the left.

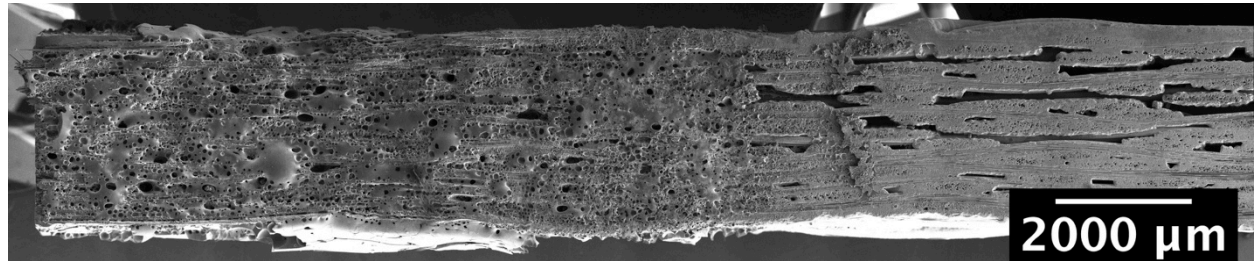


Figure C-14 – SEM Micrograph of the leading edge of CVI-BR-24 after sectioning and water digestion, cut edge (formerly the center of the impingement site) on the left.

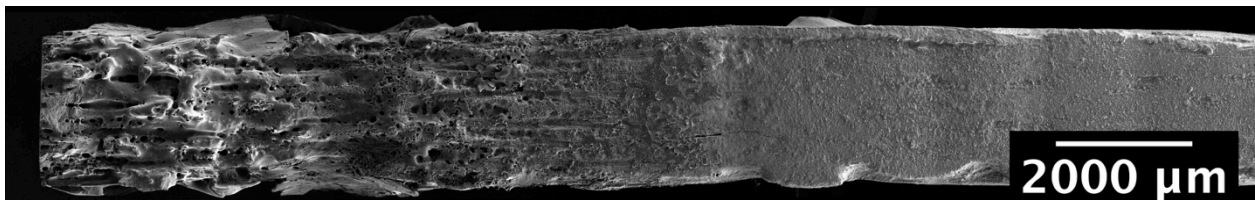


Figure C-15 – SEM Micrograph of the leading edge of MI-BR-45 after sectioning and water digestion, cut edge (formerly the center of the impingement site) on the left.

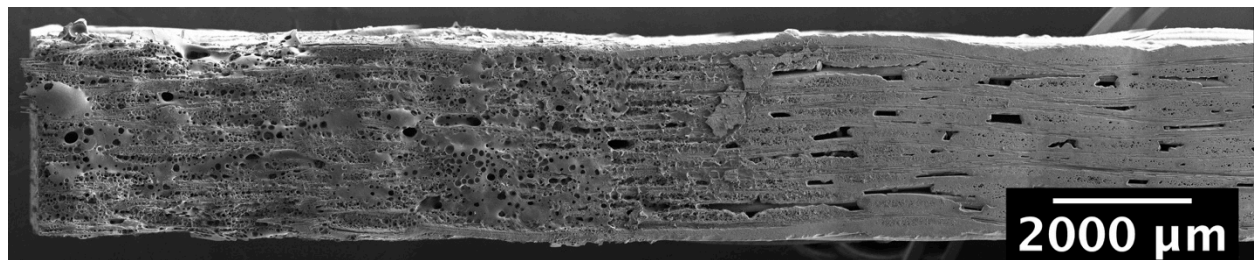
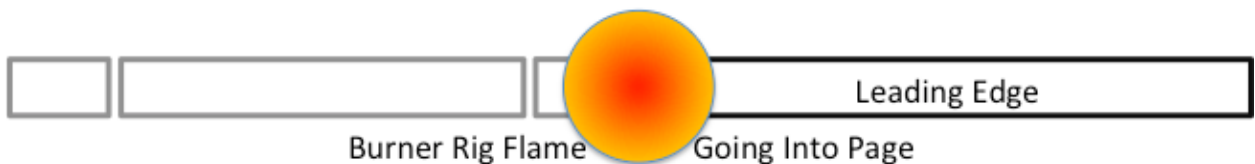


Figure C-16 – SEM Micrograph of the leading edge of CVI-BR-45 after sectioning and water digestion, cut edge (formerly the center of the impingement site) on the left.



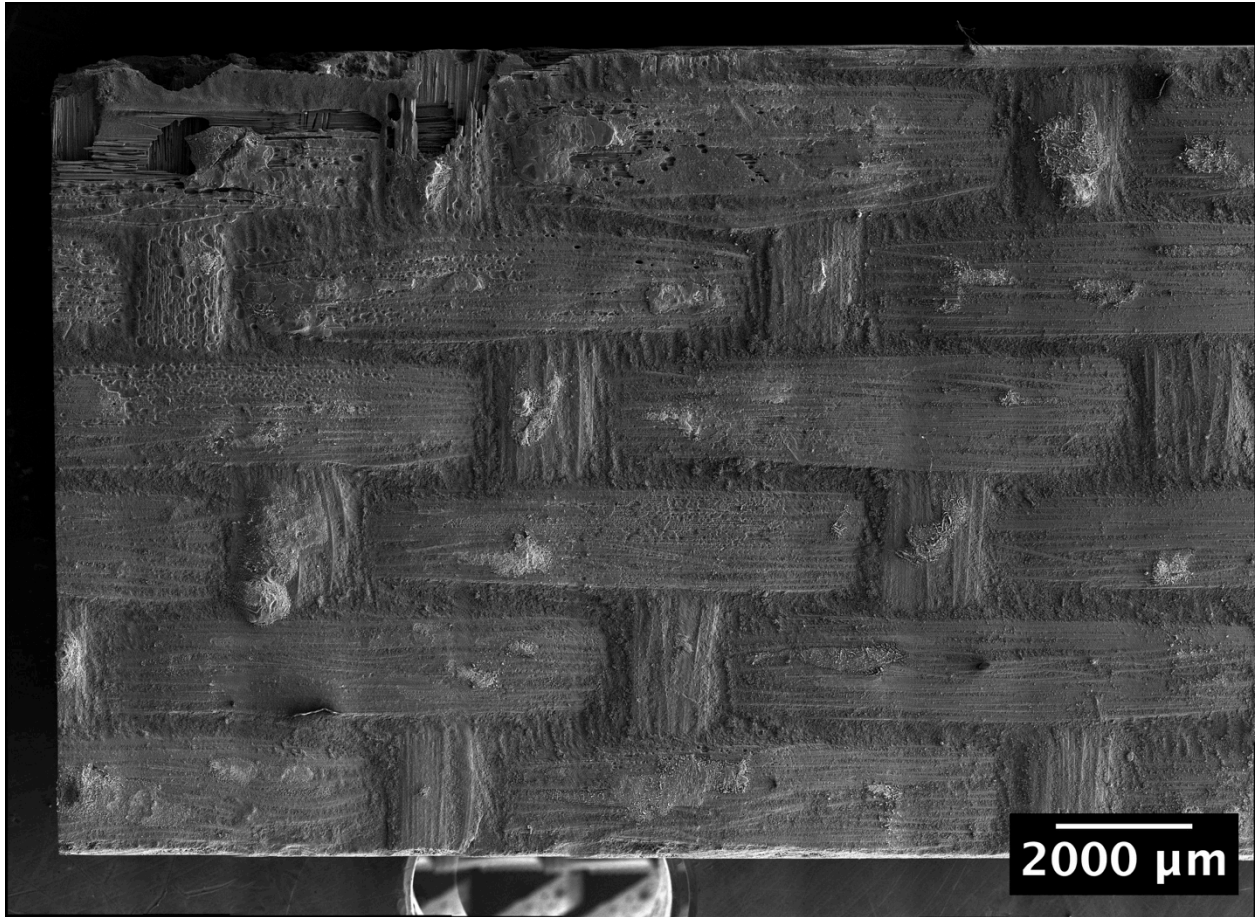
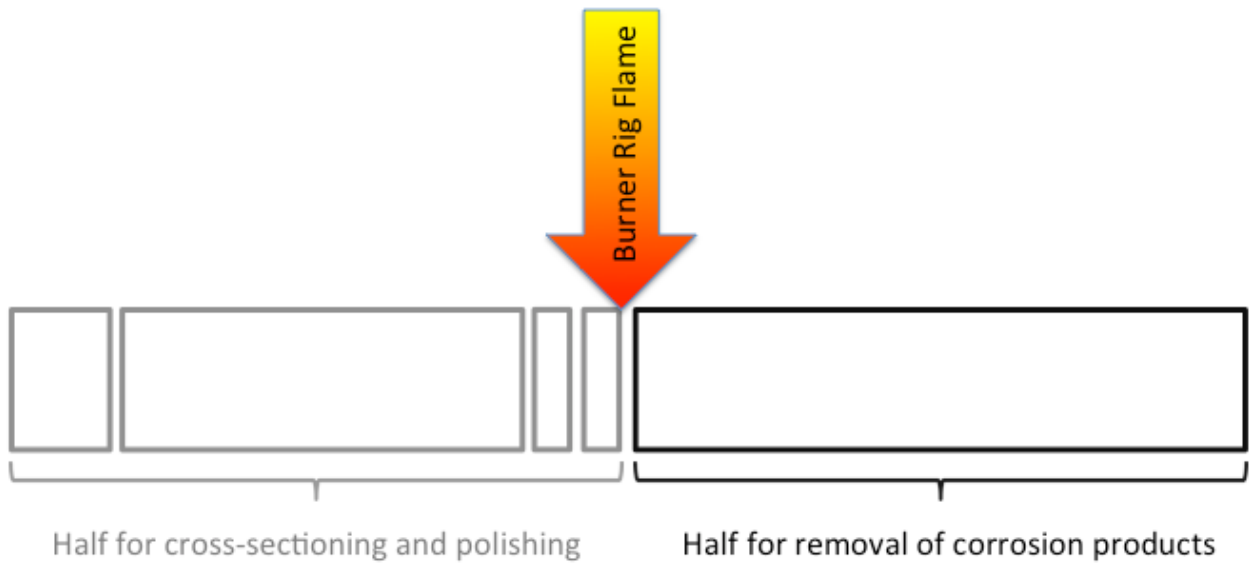


Figure C-17 – SEM Micrograph of the face of MI-BR-24 after sectioning and HF digestion, leading edge on top, cut edge (formerly the center of the impingement site) on the left.



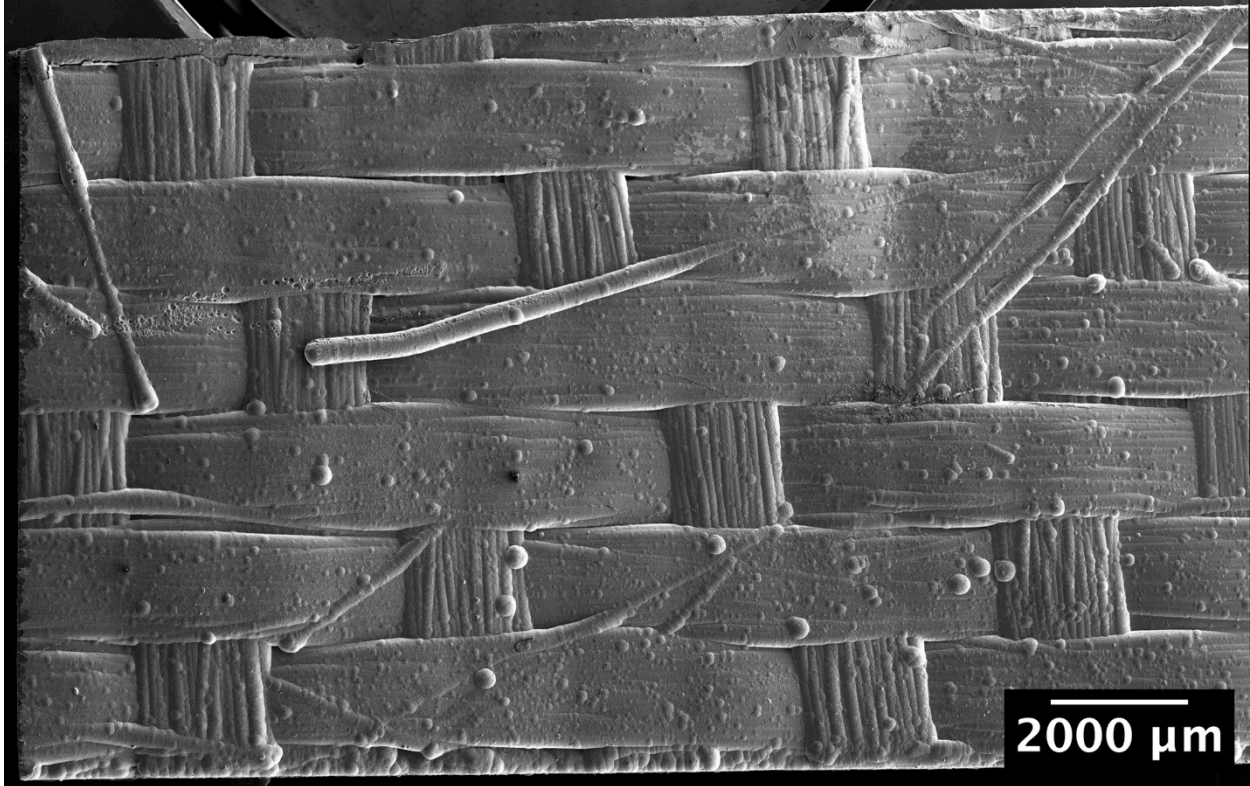
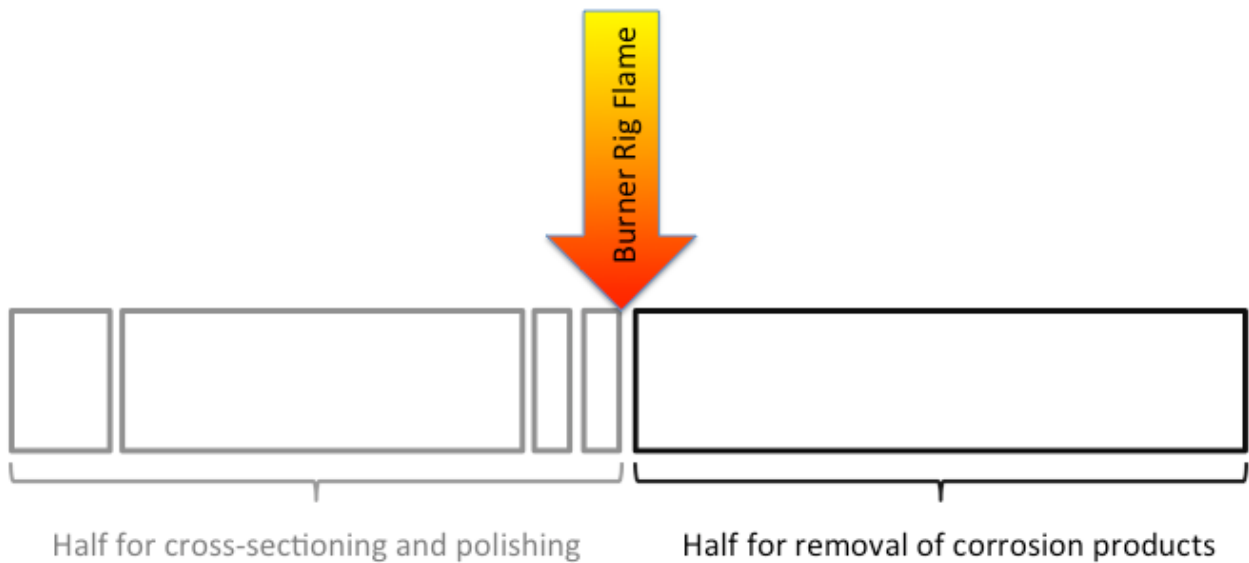


Figure C-18 – SEM Micrograph of the face of CVI-BR-24 after sectioning and HF digestion, leading edge on top, cut edge (formerly the center of the impingement site) on the left.



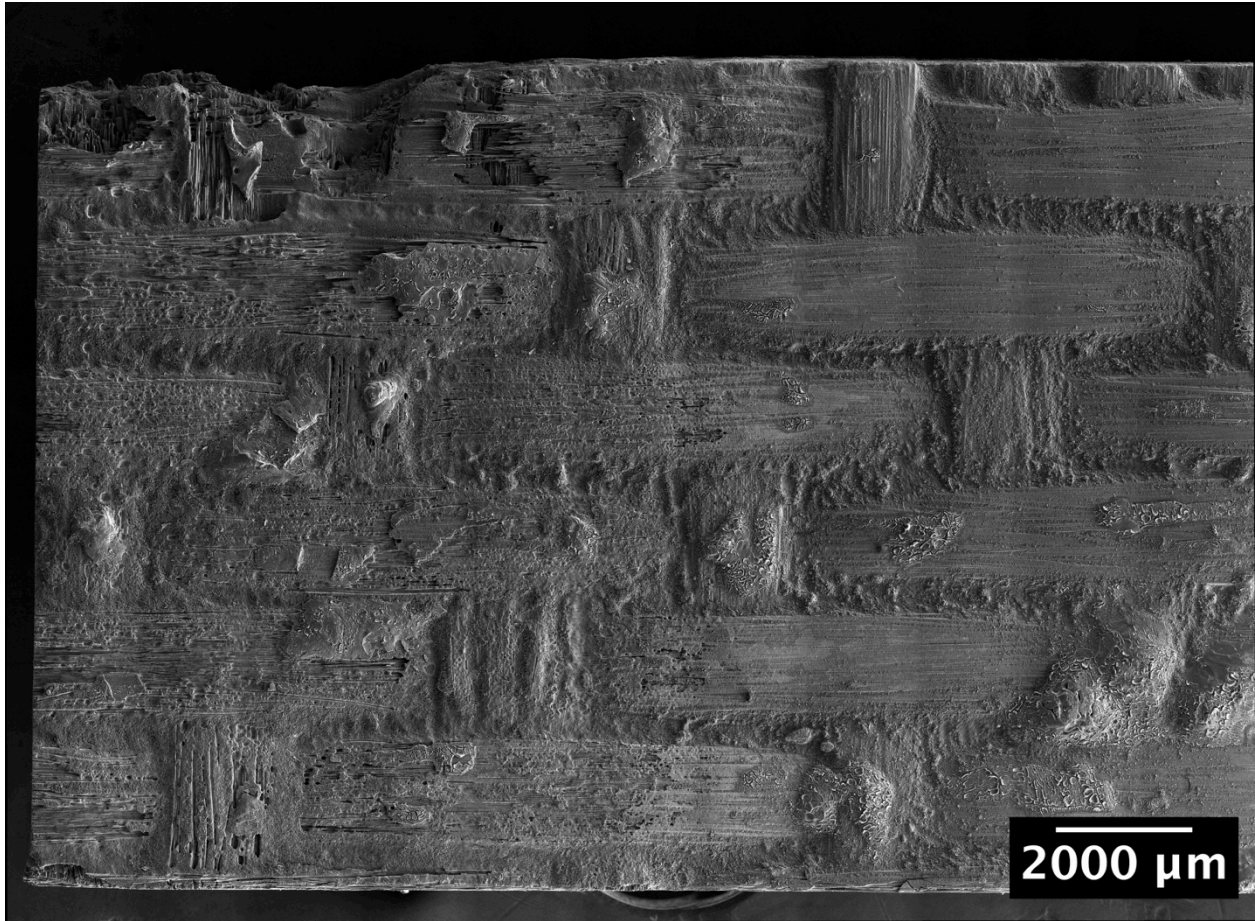
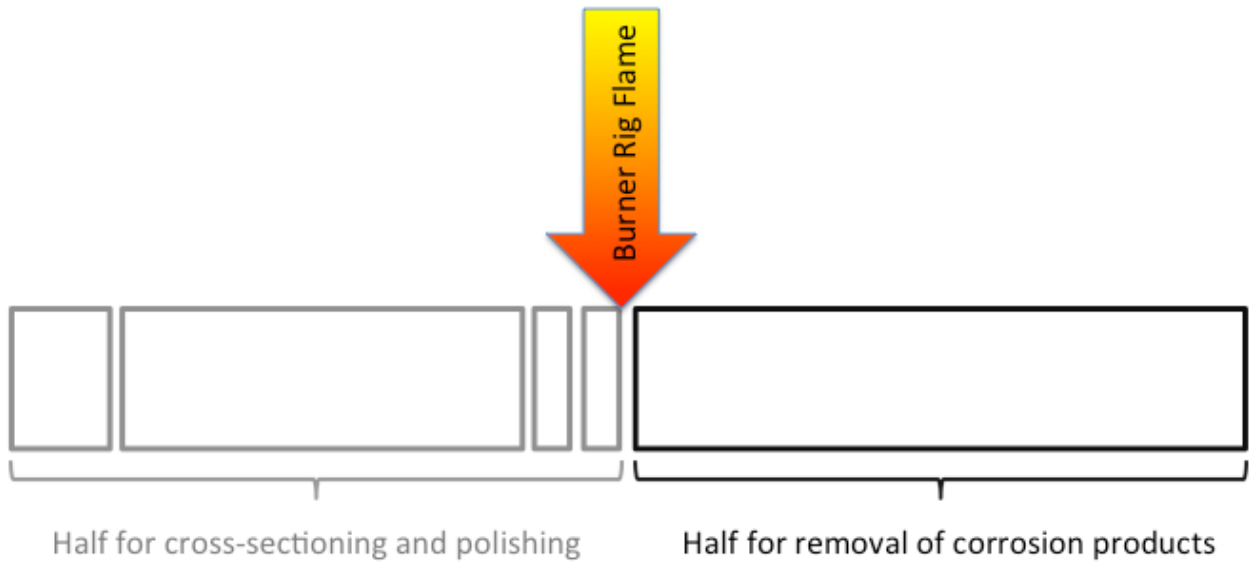


Figure C-19 – SEM Micrograph of the face of MI-BR-45 after sectioning and HF digestion, leading edge on top, cut edge (formerly the center of the impingement site) on the left.



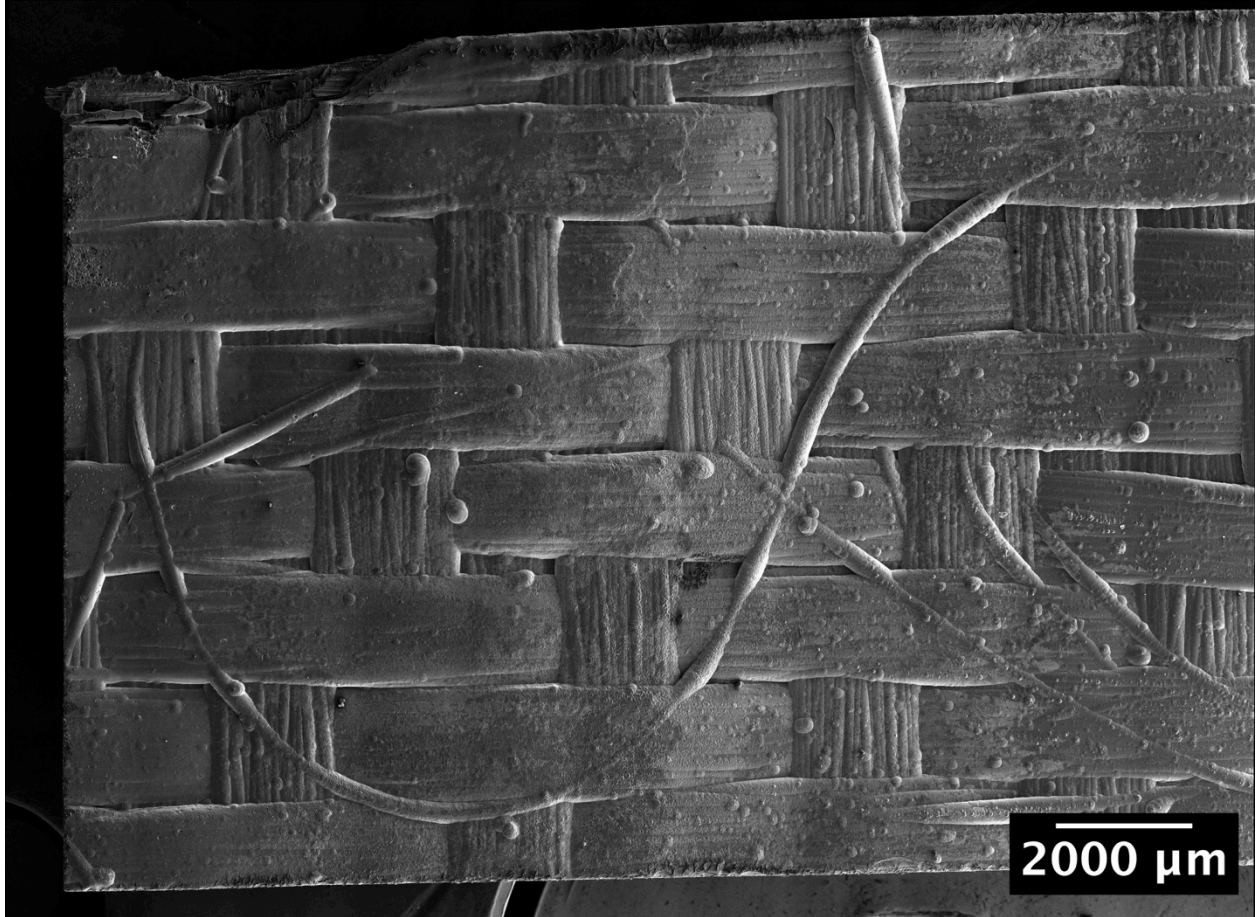
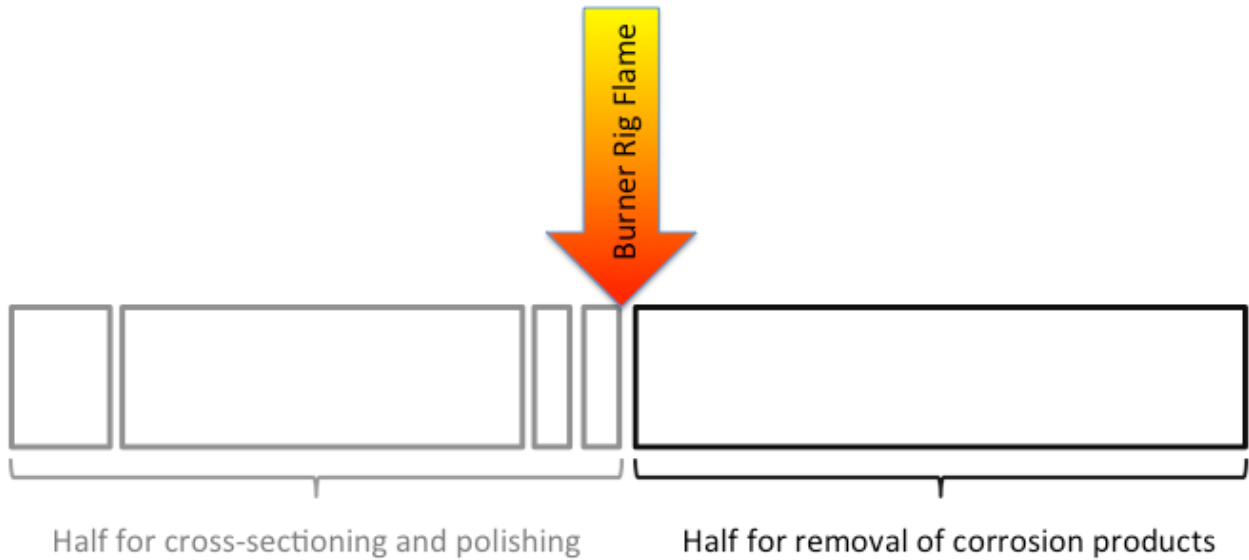


Figure C-20 – SEM Micrograph of the face of CVI-BR-45 after sectioning and HF digestion, leading edge on top, cut edge (formerly the center of the impingement site) on the left.



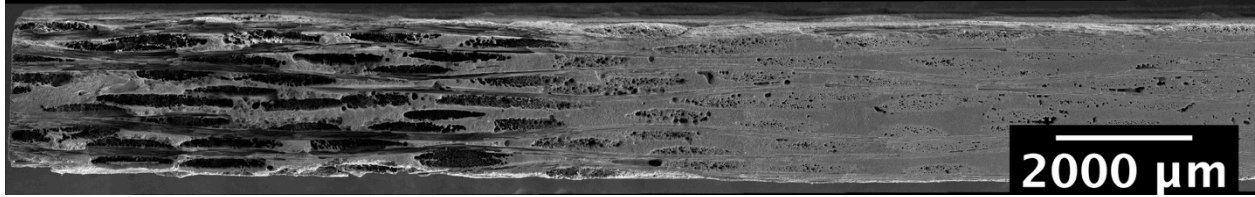


Figure C-21 – SEM Micrograph of the leading edge of MI-BR-24 after sectioning and HF digestion, cut edge (formerly the center of the impingement site) on the left.

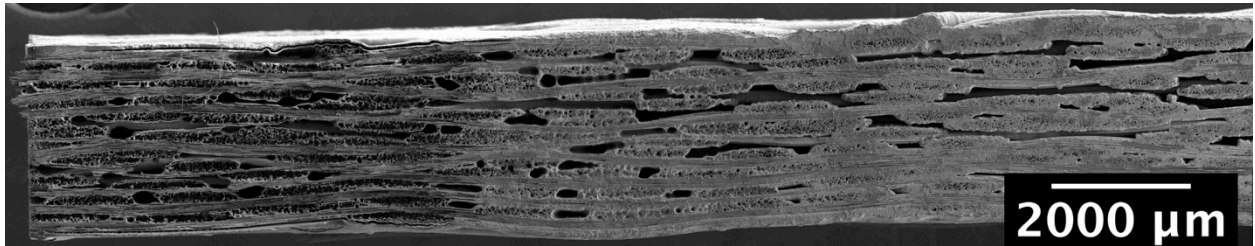


Figure C-22 – SEM Micrograph of the leading edge of CVI-BR-24 after sectioning and HF digestion, cut edge (formerly the center of the impingement site) on the left.

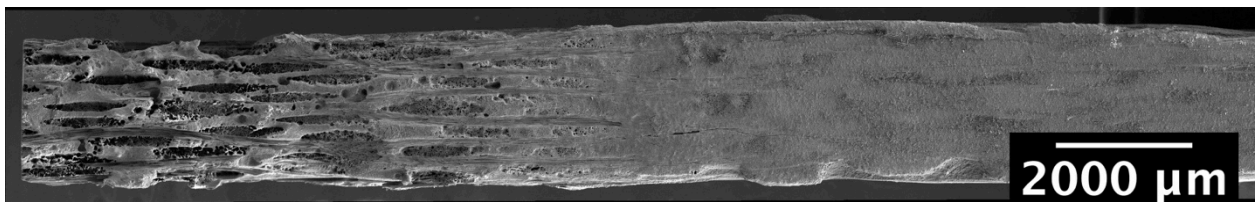


Figure C-23 – SEM Micrograph of the leading edge of MI-BR-45 after sectioning and HF digestion, cut edge (formerly the center of the impingement site) on the left.

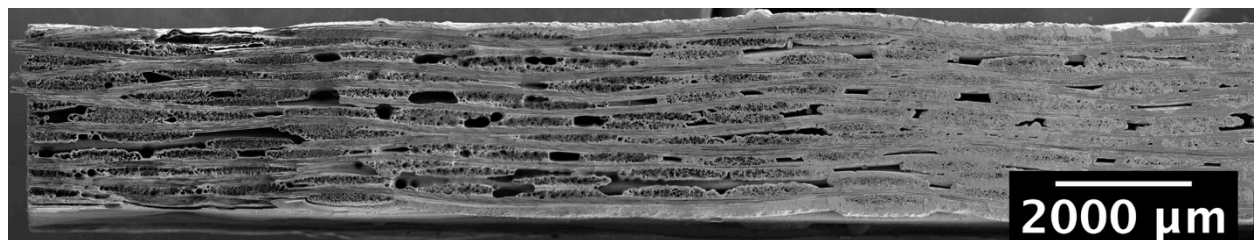
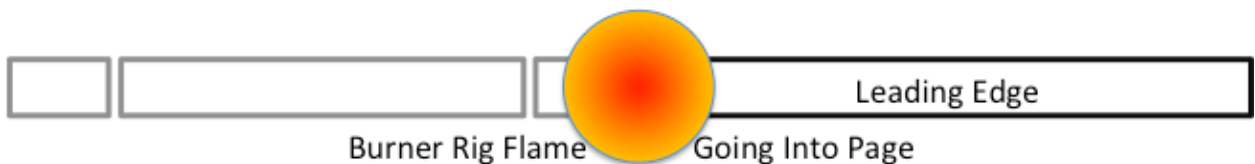


Figure C-24 – SEM Micrograph of the leading edge of CVI-BR-45 after sectioning and HF digestion, cut edge (formerly the center of the impingement site) on the left.



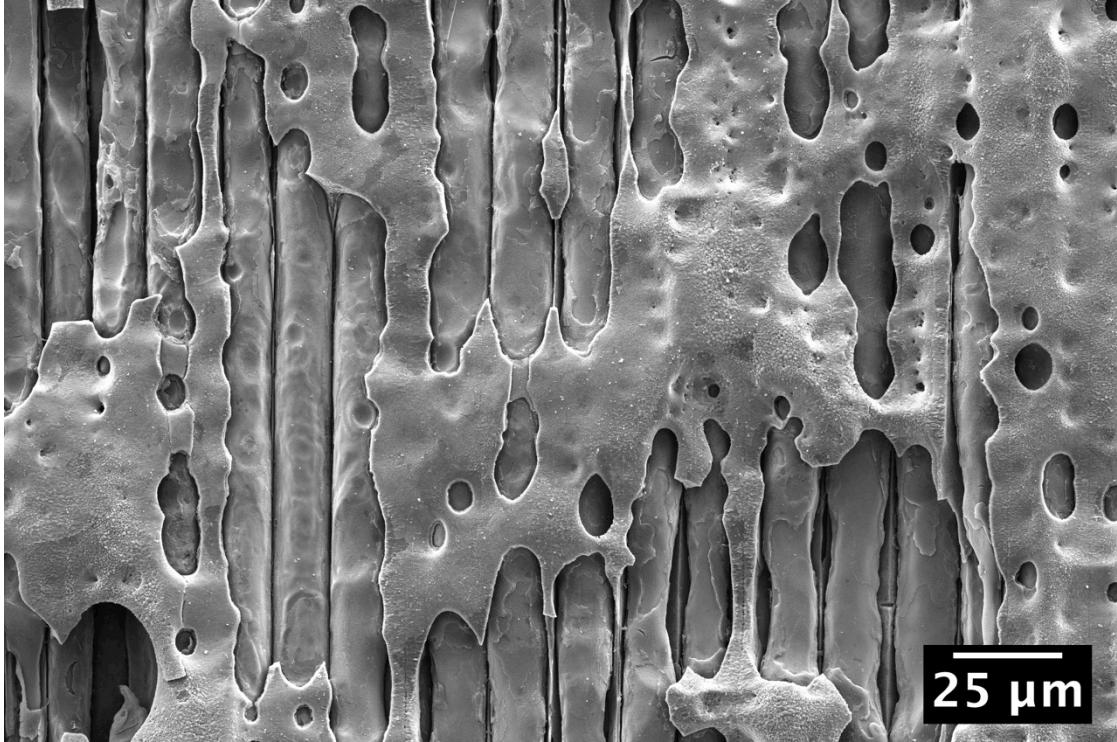


Figure C-25 - SEM micrograph of the face of MI-BR-45 after HF digestion showing pitting and attack of the Hi-Nicalon fibers and dense CVI SiC layer.

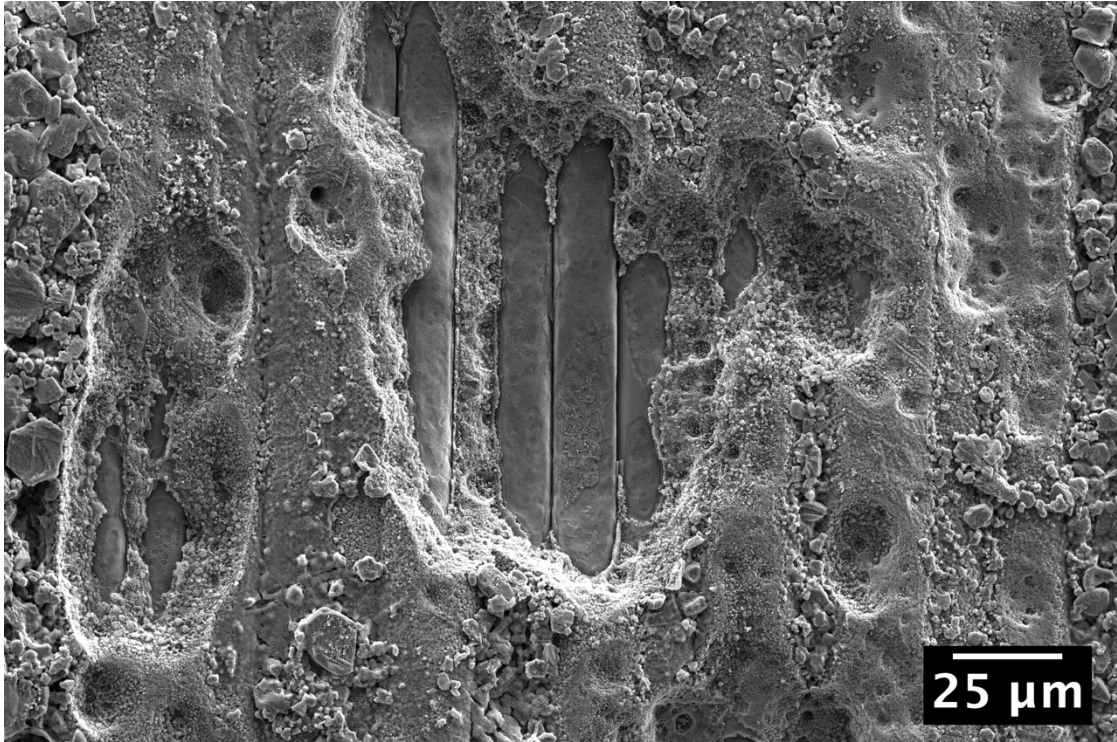


Figure C-26 - SEM micrograph of the face of MI-BR-24 after HF digestion showing pitting and attack of the Hi-Nicalon fibers and dense CVI SiC layer. Also visible is some of the remaining SiC particulates from the MI process.

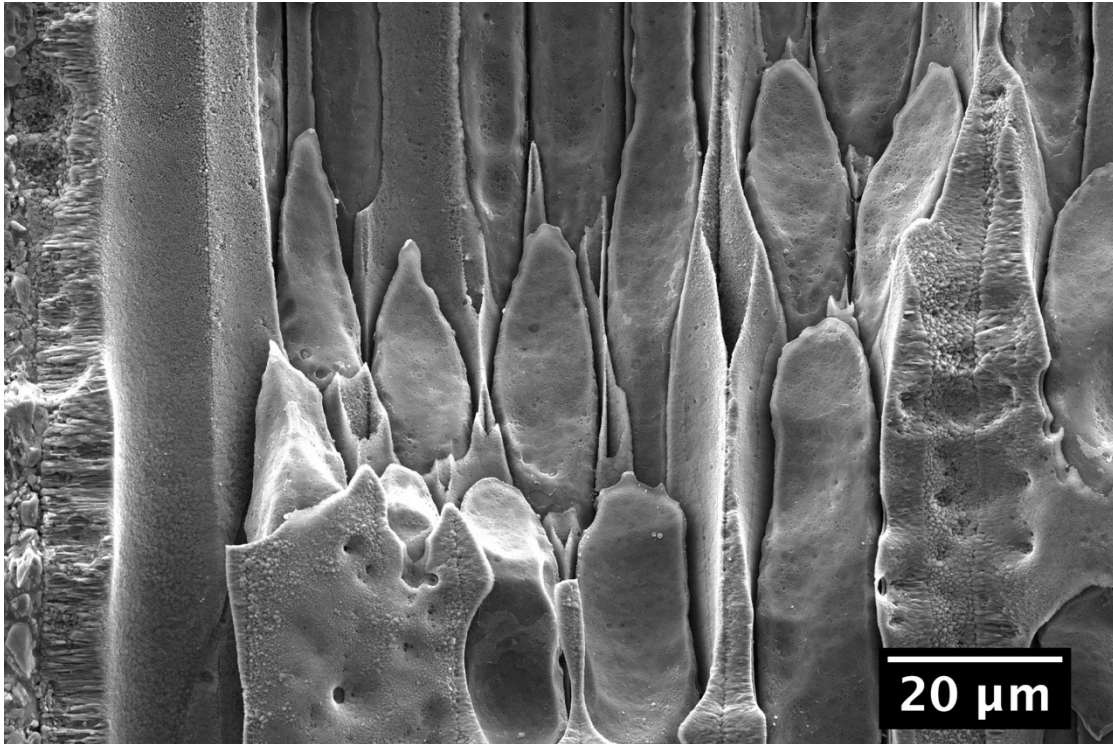


Figure C-27 – SEM micrograph of the face of MI-BR-24 after HF digestion showing attack of the Hi-Nicalon fibers and dense CVI SiC layer.

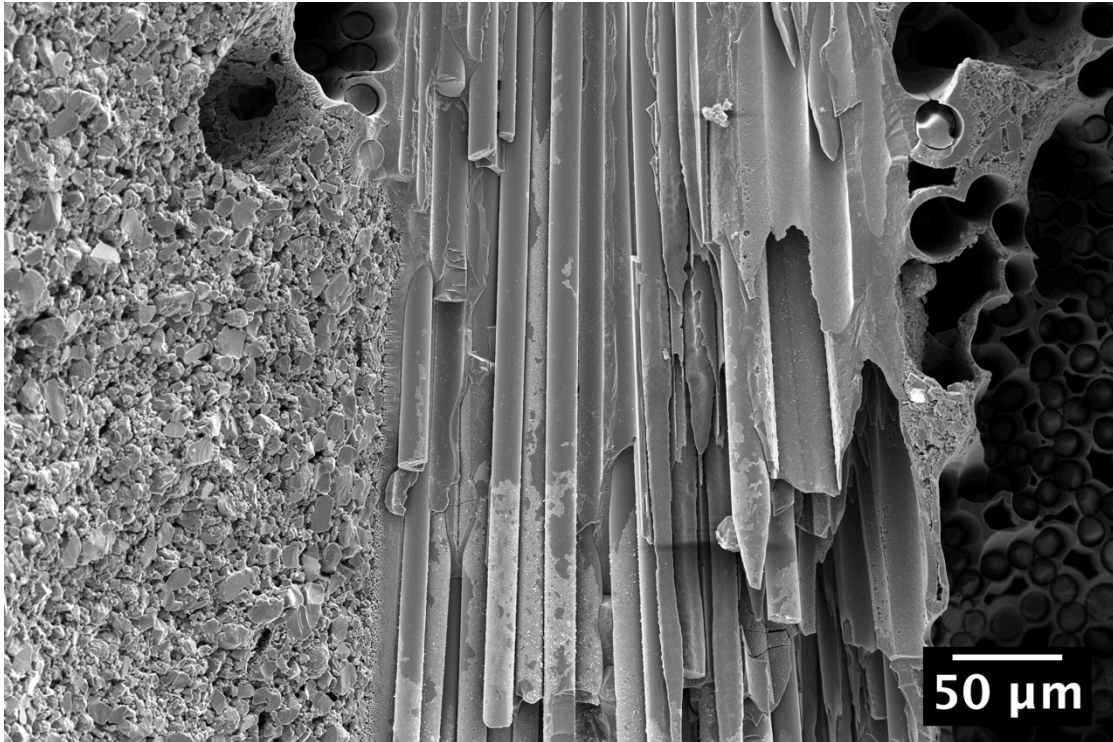


Figure C-28 – SEM micrograph of the leading edge of MI-BR-24 after HF digestion. The fiber tows exposed end-on show the greatest recession, followed by the fiber tows exposed lengthwise, and the matrix shows the least recession.

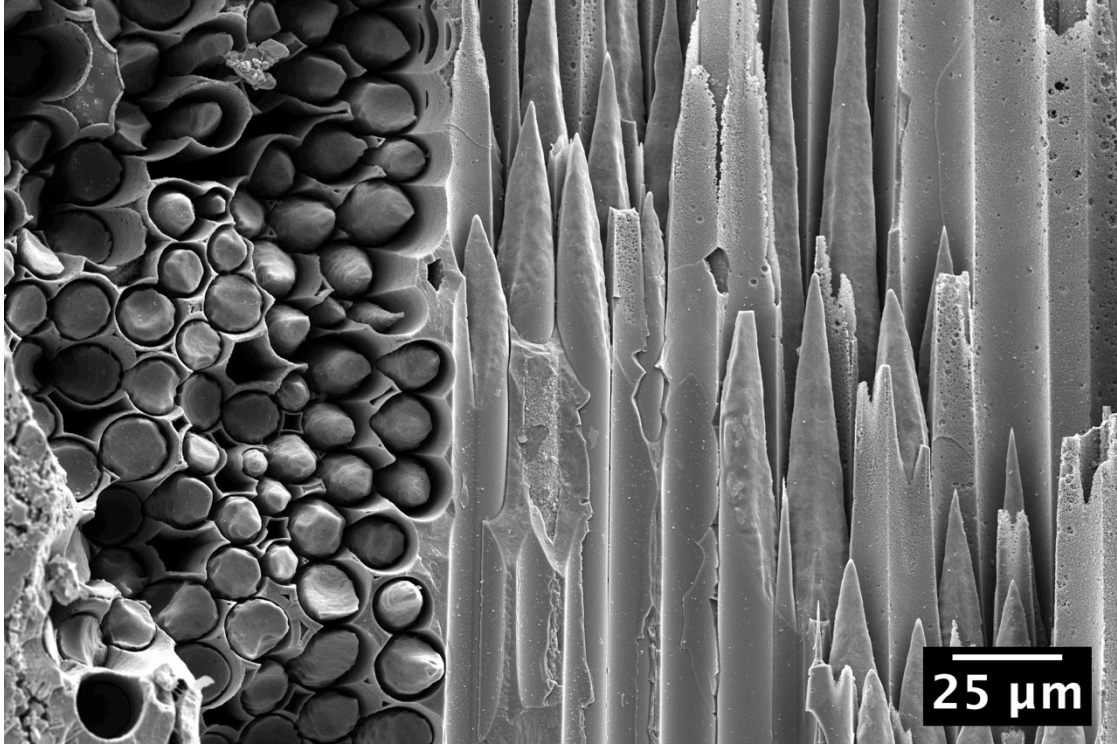


Figure C-29 – SEM micrograph of the leading edge of MI-BR-24 after HF digestion. The fibers oriented in both directions show evidence of consumption down the fiber length resulting in the pointed shape.

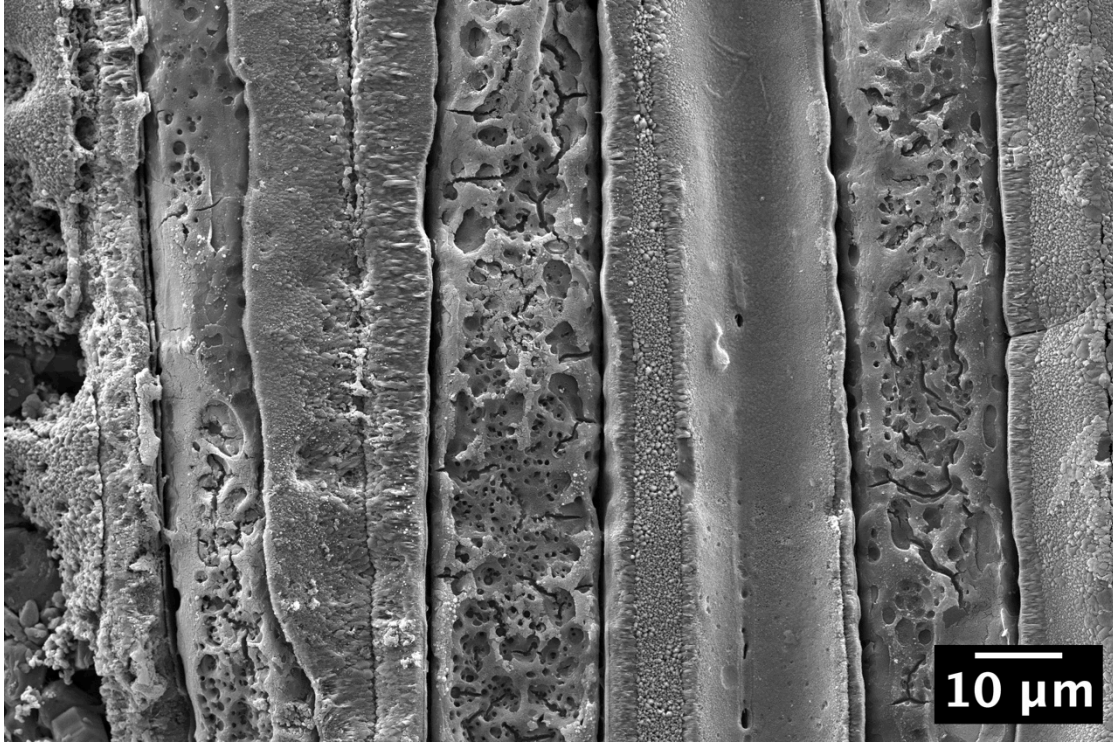


Figure C-30 – SEM micrograph of the face of MI-BR-45 after HF digestion showing pitting and attack of the Hi-Nicalon fibers. The dense CVI SiC layer appears fairly resistant to hot corrosion attack.

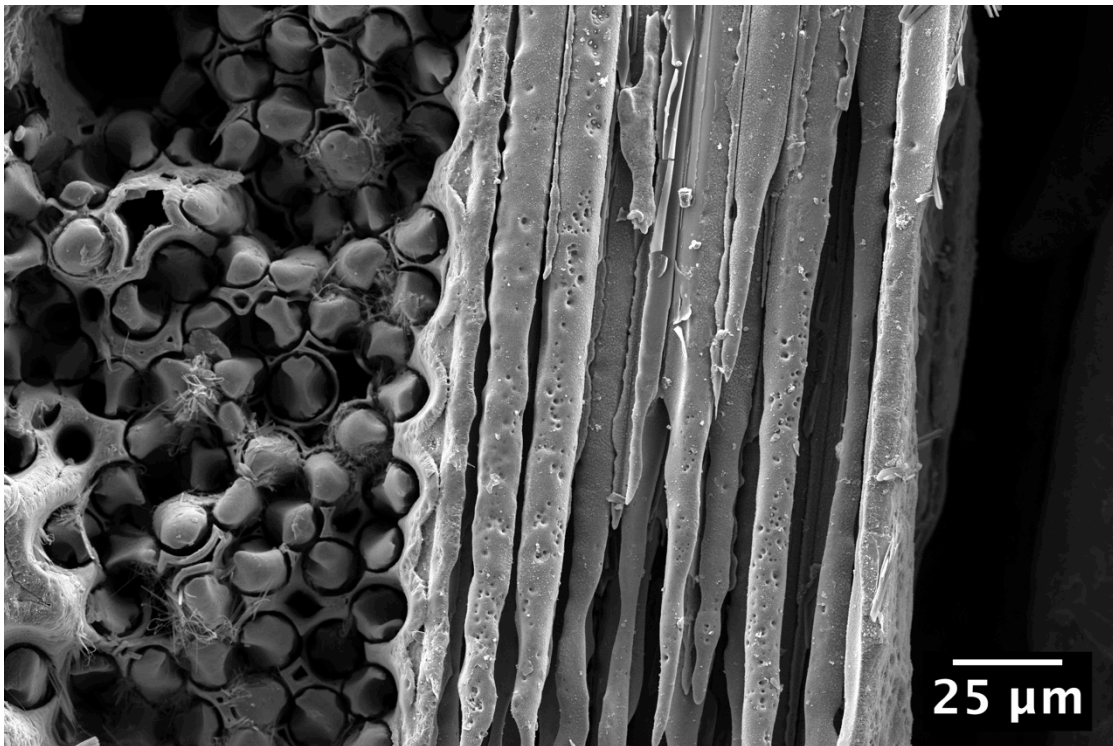


Figure C-31 – SEM micrograph of the leading edge of CVI-BR-24 after HF digestion showing pitting and attack of the Hi-Nicalon-S fibers.

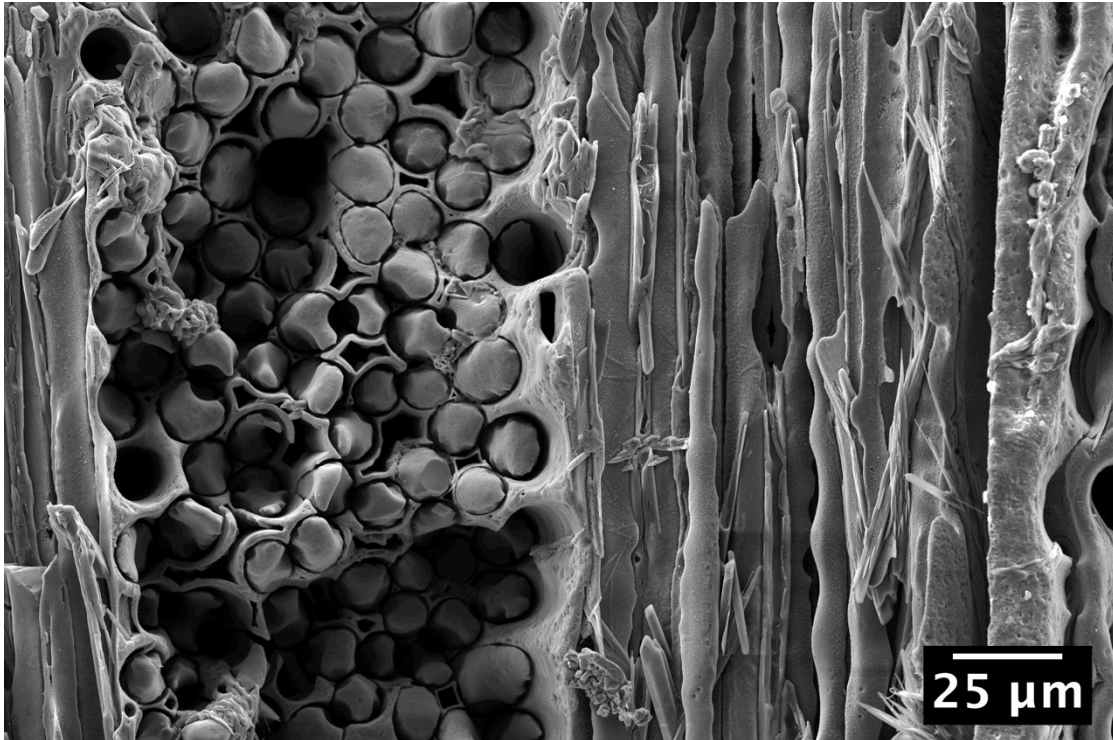


Figure C-32 – SEM micrograph of the leading edge of CVI-BR-24 after HF digestion showing uniform attack of fiber tows in both orientations.

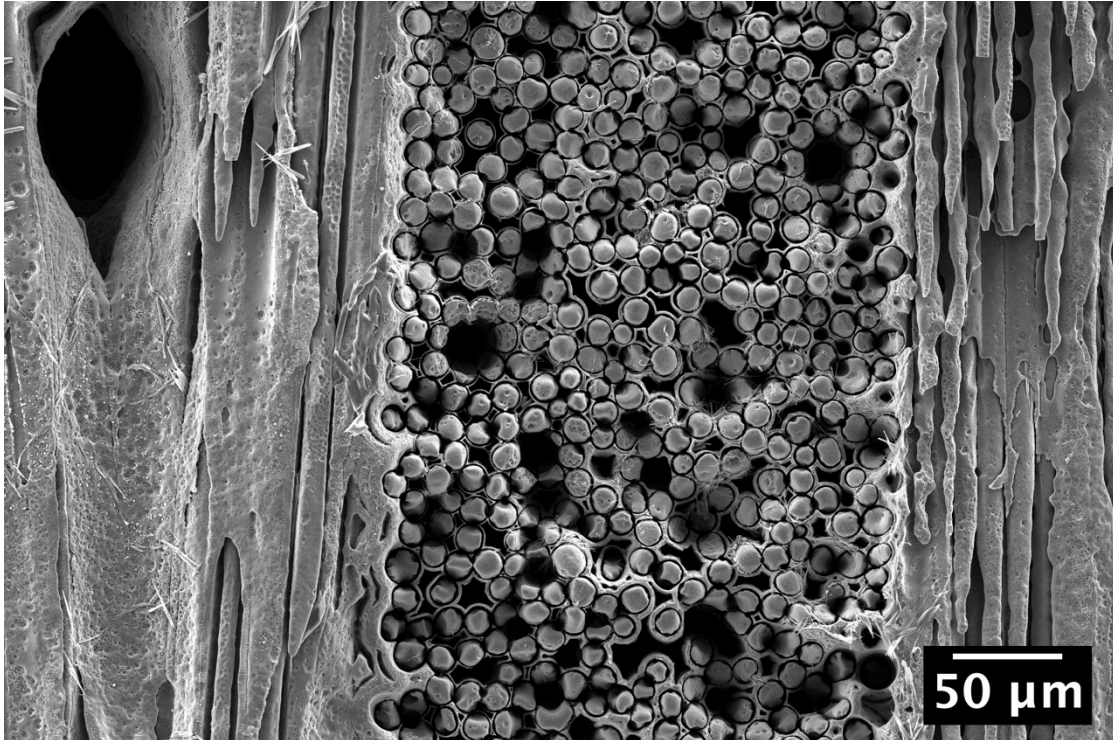


Figure C-33 – SEM micrograph of the leading edge of CVI-BR-45 after HF digestion showing uniform attack of the fiber tows and the matrix.

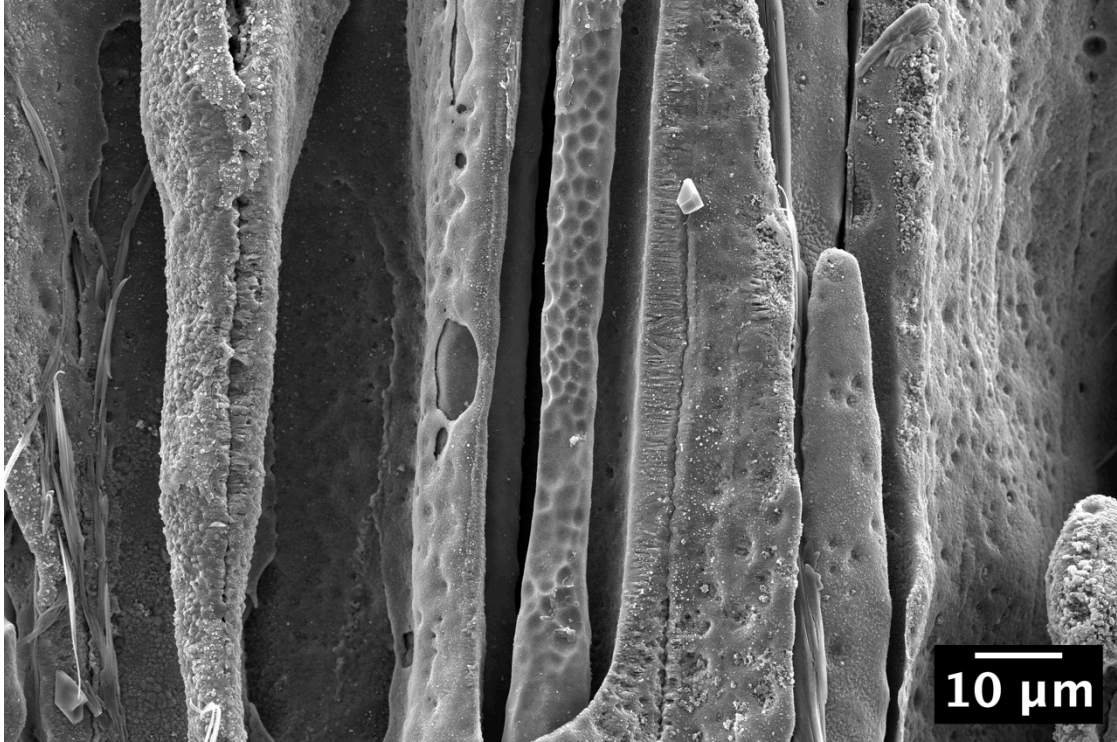


Figure C-34 – SEM micrograph of the leading edge of CVI-BR-45 after HF digestion. The Hi-Nicalon-S fiber is pitted and attacked and has been consumed radially resulting in a narrowing of the fiber.

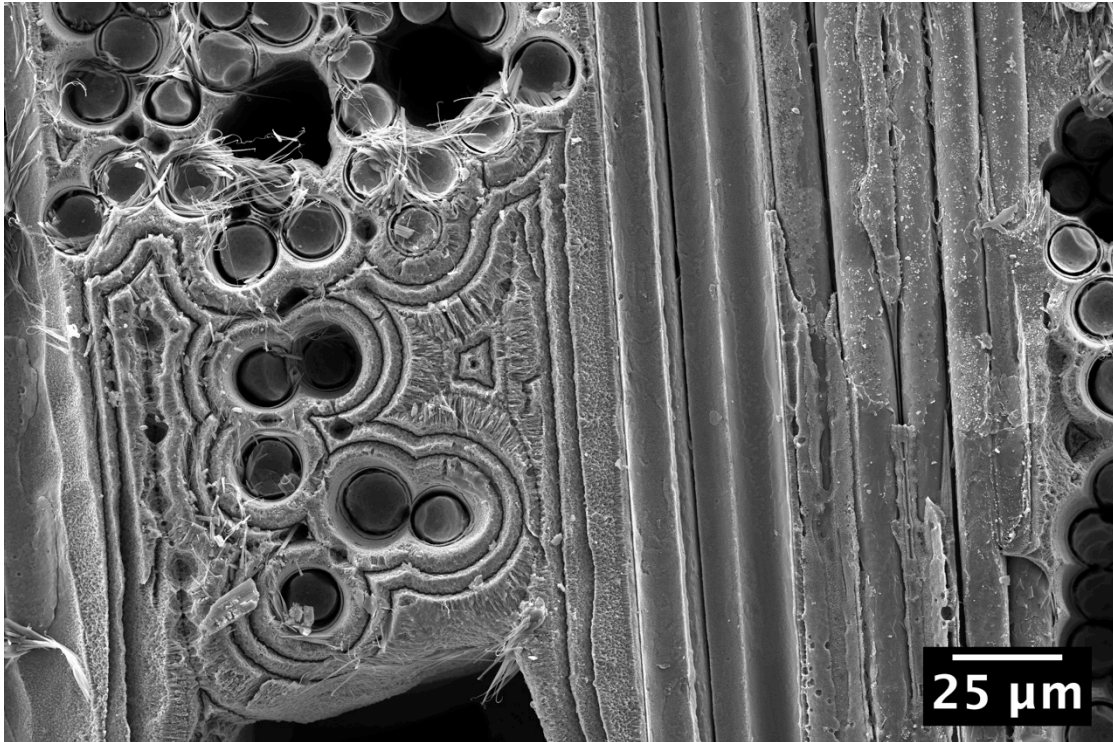


Figure C-35 – SEM micrograph of the leading edge of CVI-BR-45 after HF digestion showing uniform attack of the fiber tows and the matrix. The CVI matrix shows evidence of increased attack at interfaces between CVI coating layers.

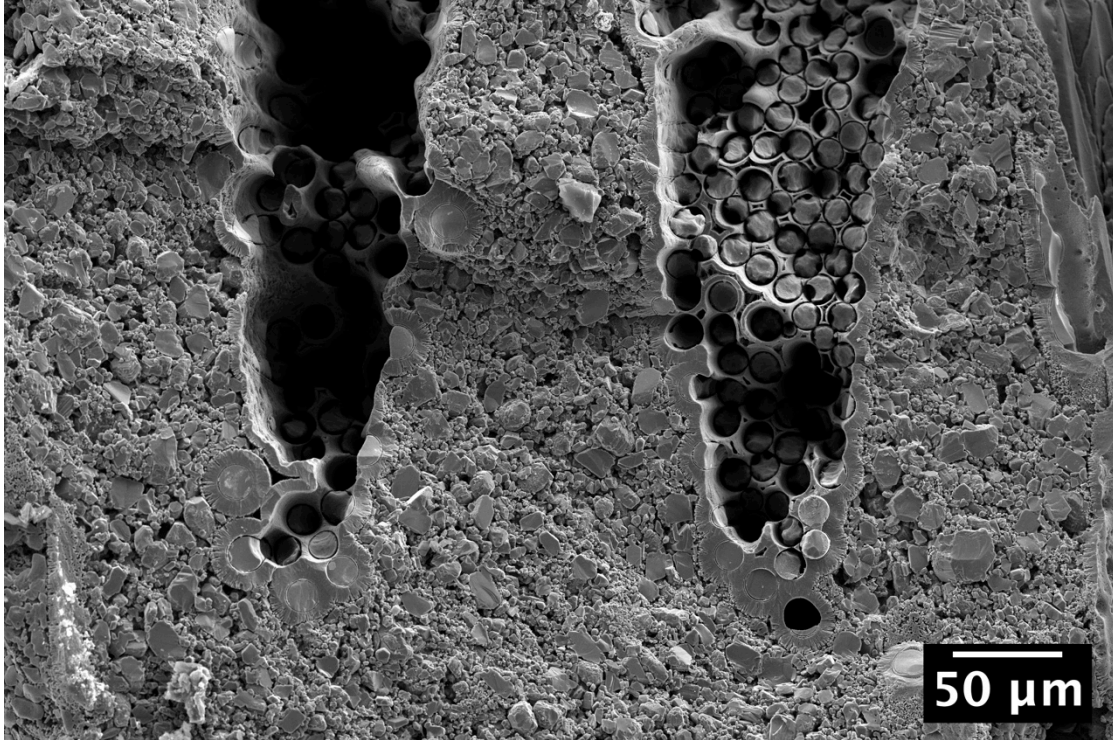


Figure C-36 – SEM micrograph of the leading edge of MI-BR-45 after HF digestion. The fiber tows exposed end-on are attacked more severely than the matrix, and the SiC particulates from the MI process remain in the matrix.

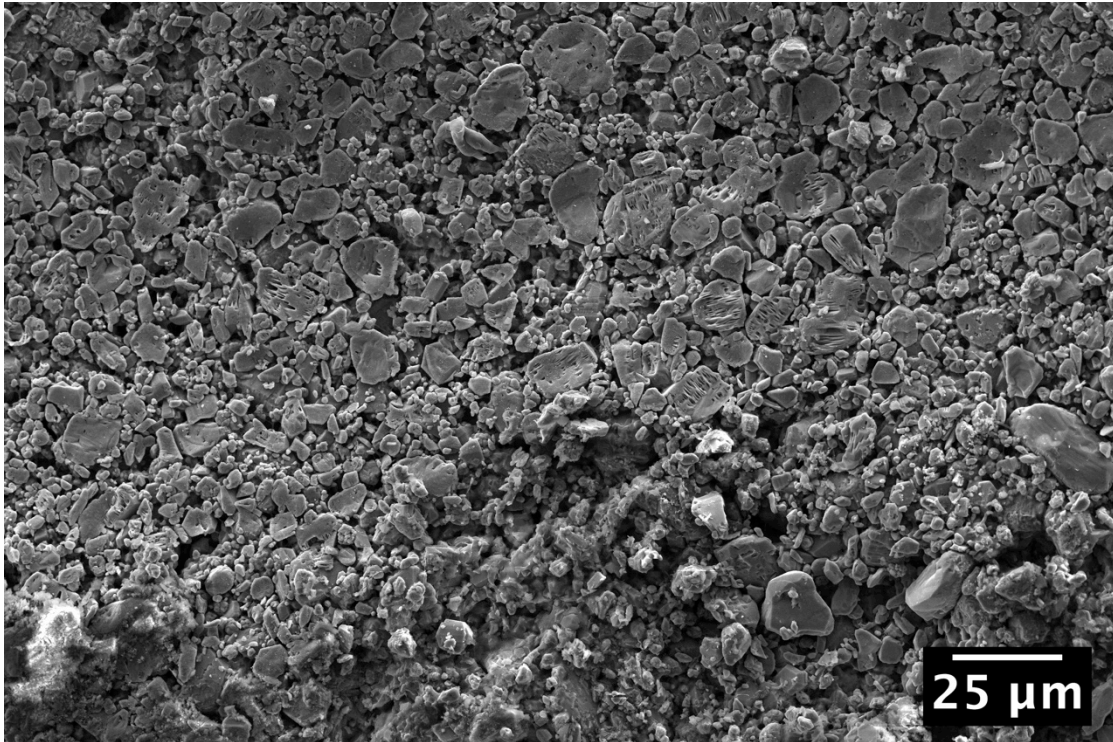


Figure C-37 – SEM micrograph of the face of MI-BR-24 after HF digestion showing the SiC particulates remaining from the MI process.

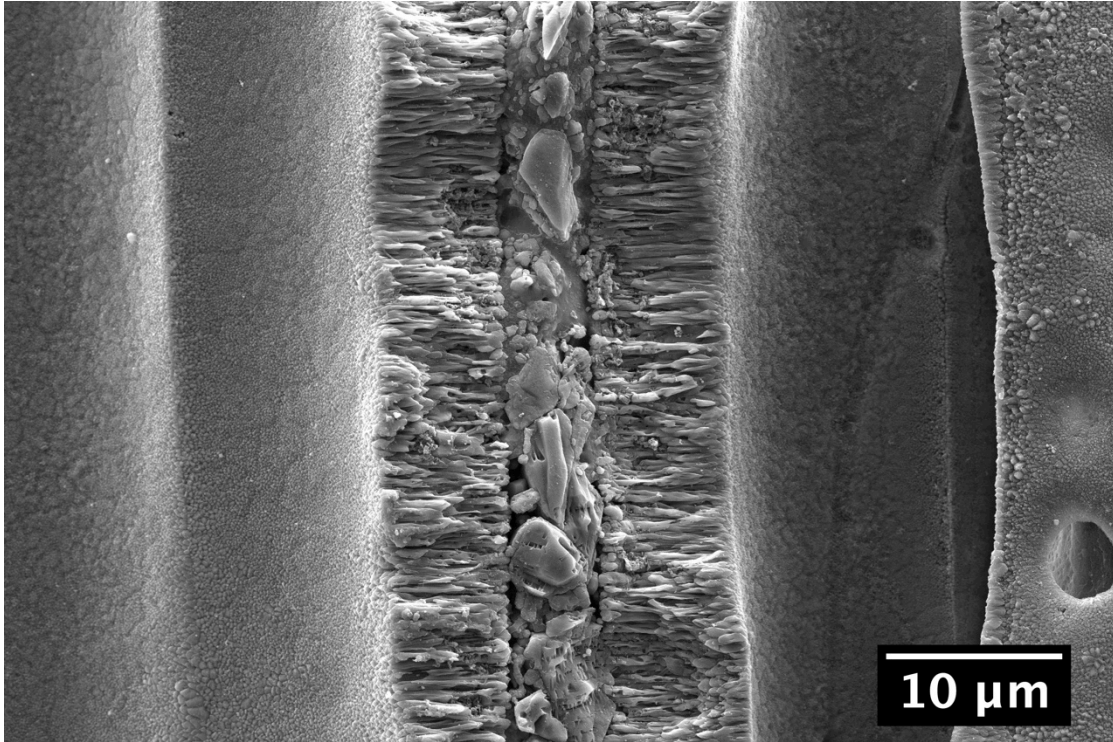


Figure C-38 – SEM micrograph of the face of MI-BR-24 after HF digestion showing the dense CVI SiC layer with relatively little attack.

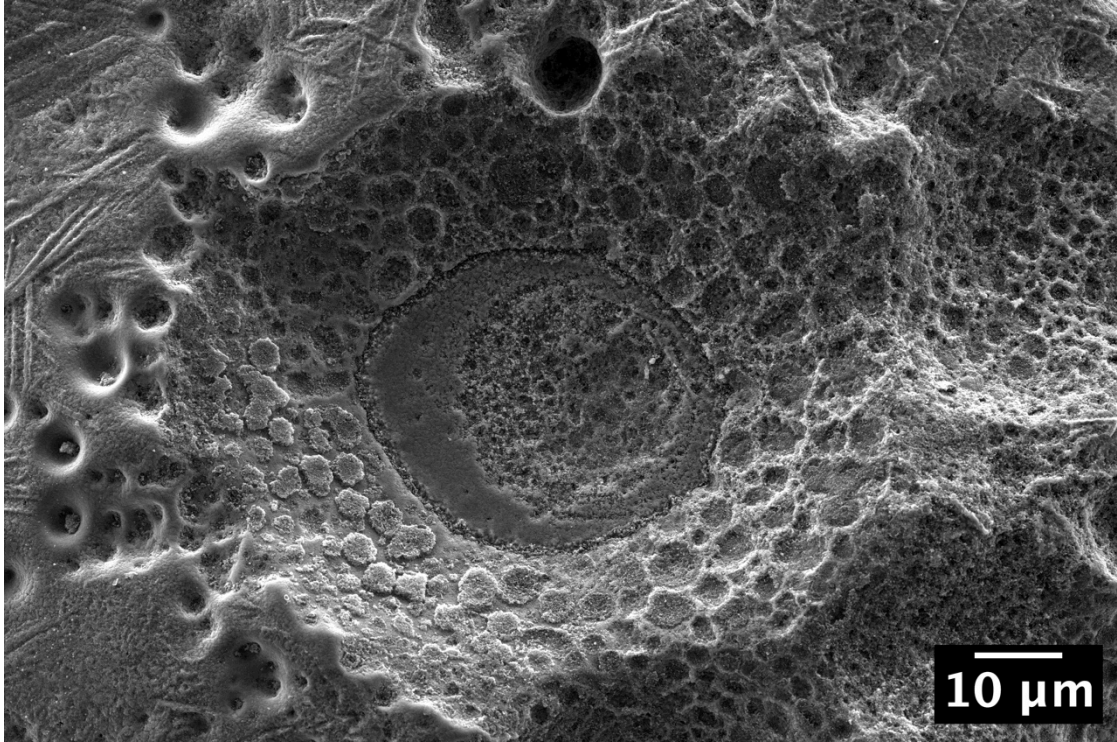


Figure C-39 – SEM micrograph of the face of CVI-BR-24 after HF digestion showing slight pitting of SiC seal coat.

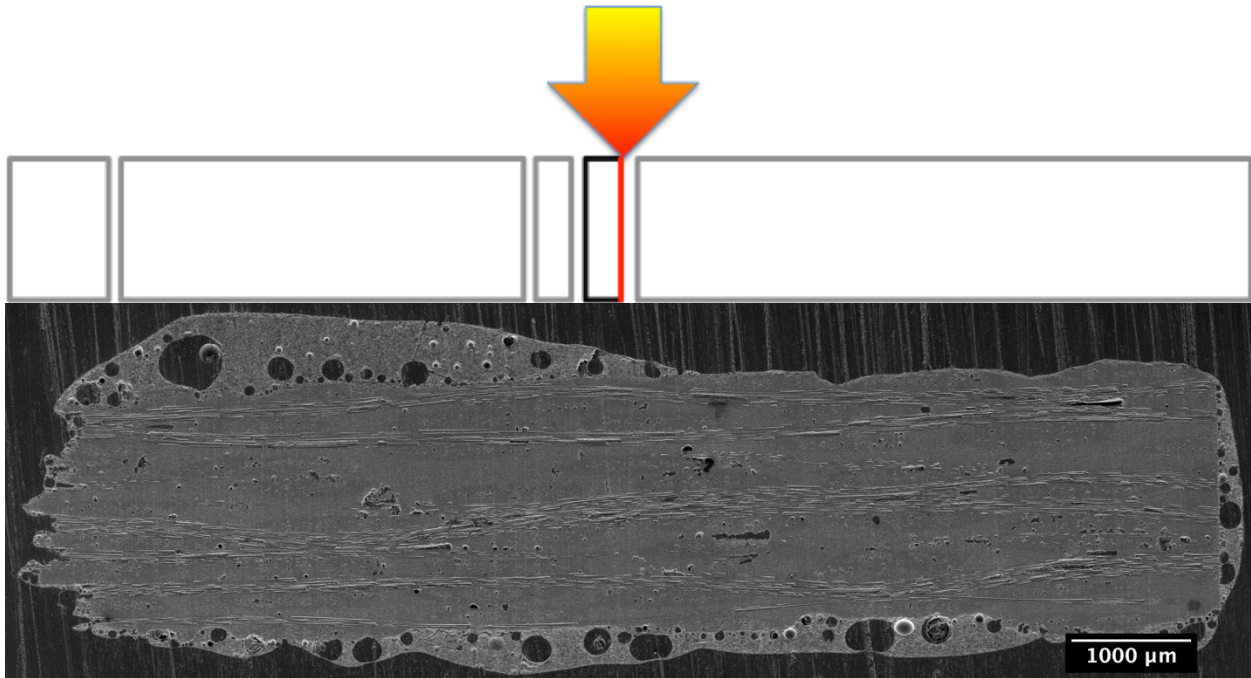


Figure C-40 – SEM Micrograph of the first cross-section of MI-BR-24 after exposure in the burner rig, leading edge on the left.

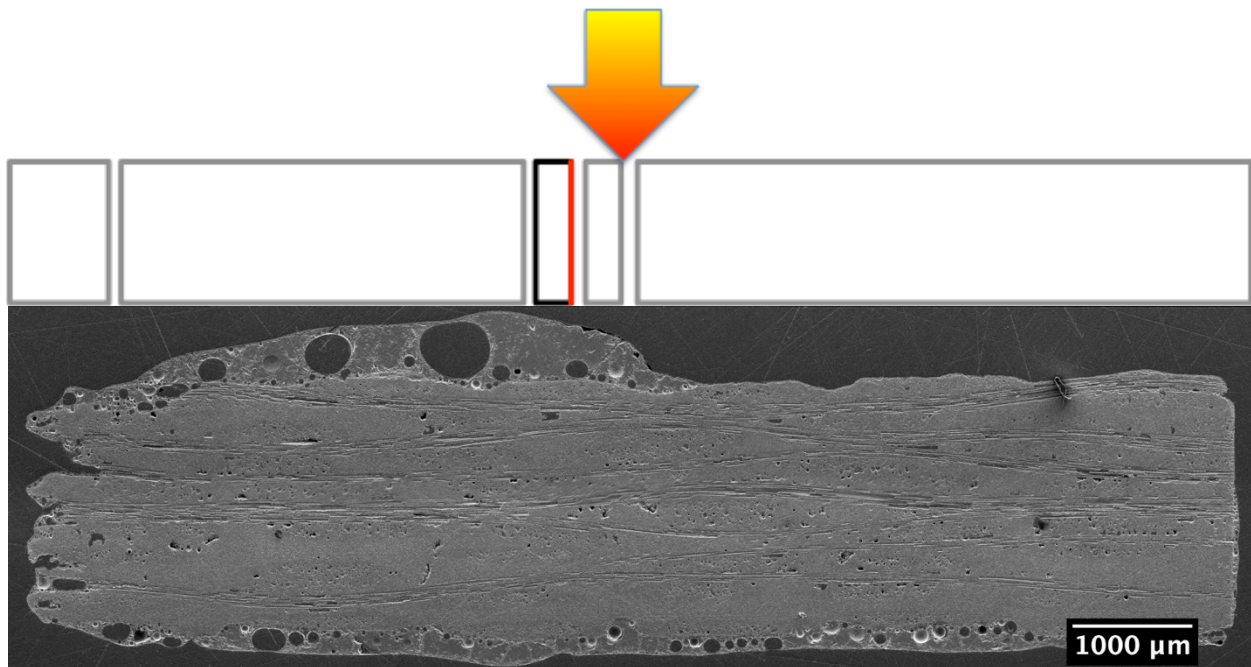


Figure C-41 – SEM Micrograph of the second cross-section of MI-BR-24 after exposure in the burner rig, leading edge on the left.

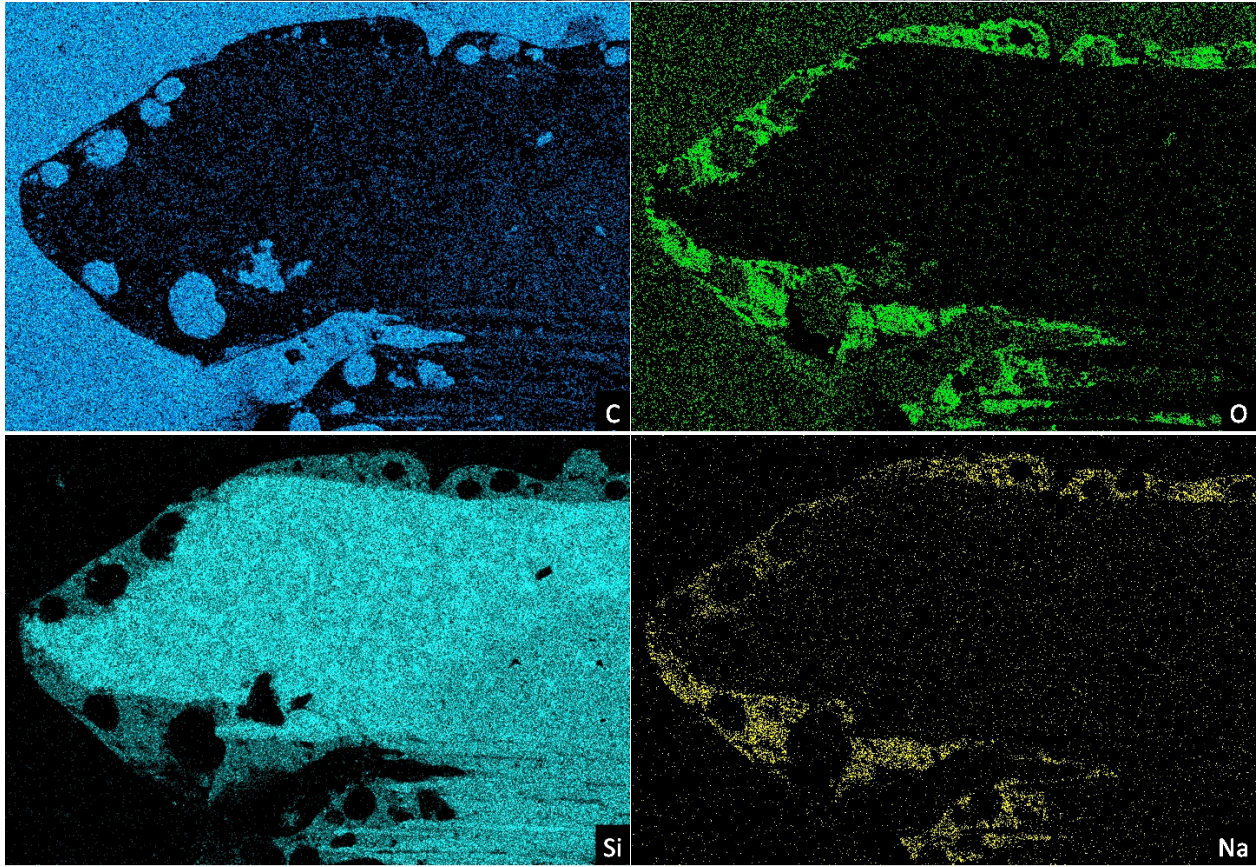
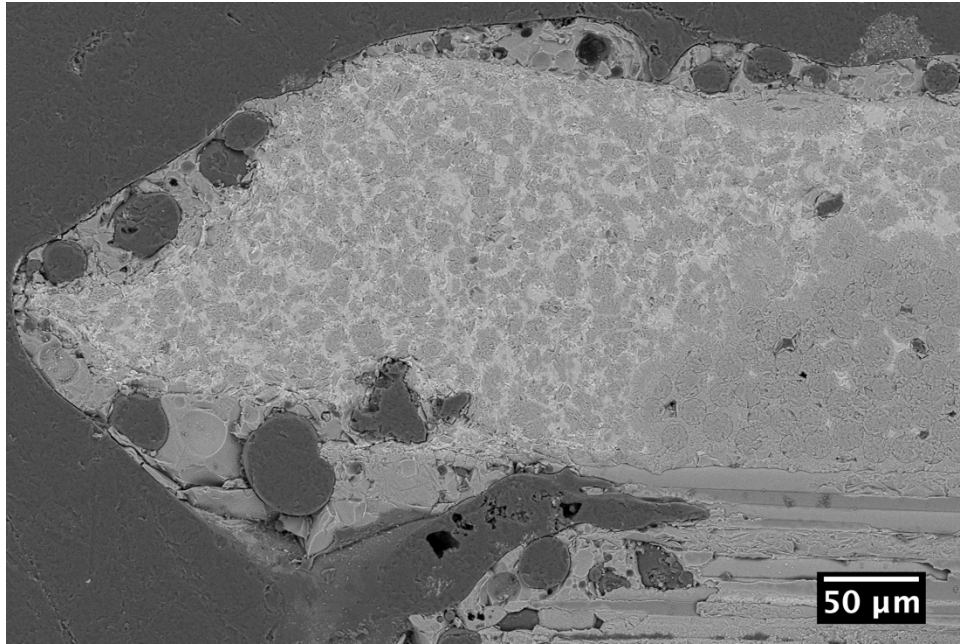


Figure C-42 – Top: An SEM micrograph of the second cross-section of MI-BR-24. Middle: EDS maps for C (left) and O (right). Bottom: EDS maps for Si (left) and Na (right). The fiber tows exposed end-on are attacked most aggressively, and the matrix is fairly resistant to hot corrosion attack.

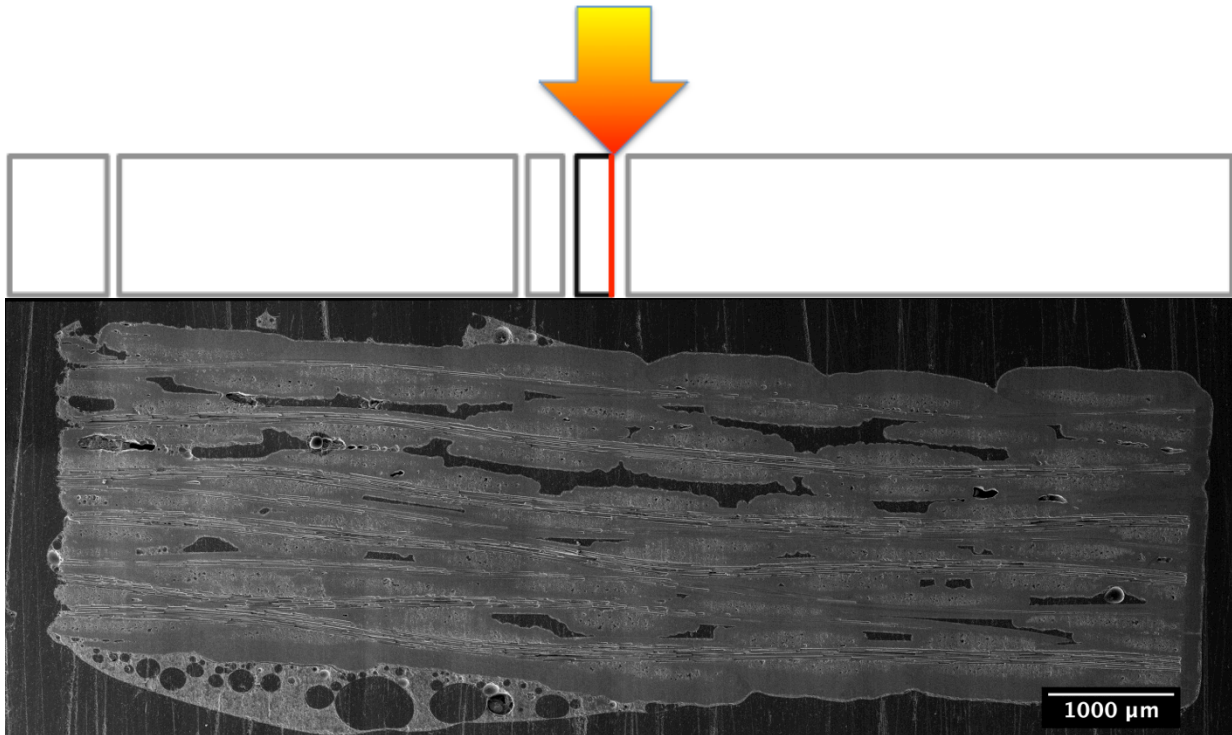


Figure C-43 – SEM Micrograph of the first cross-section of CVI-BR-24 after exposure in the burner rig, leading edge on the left.

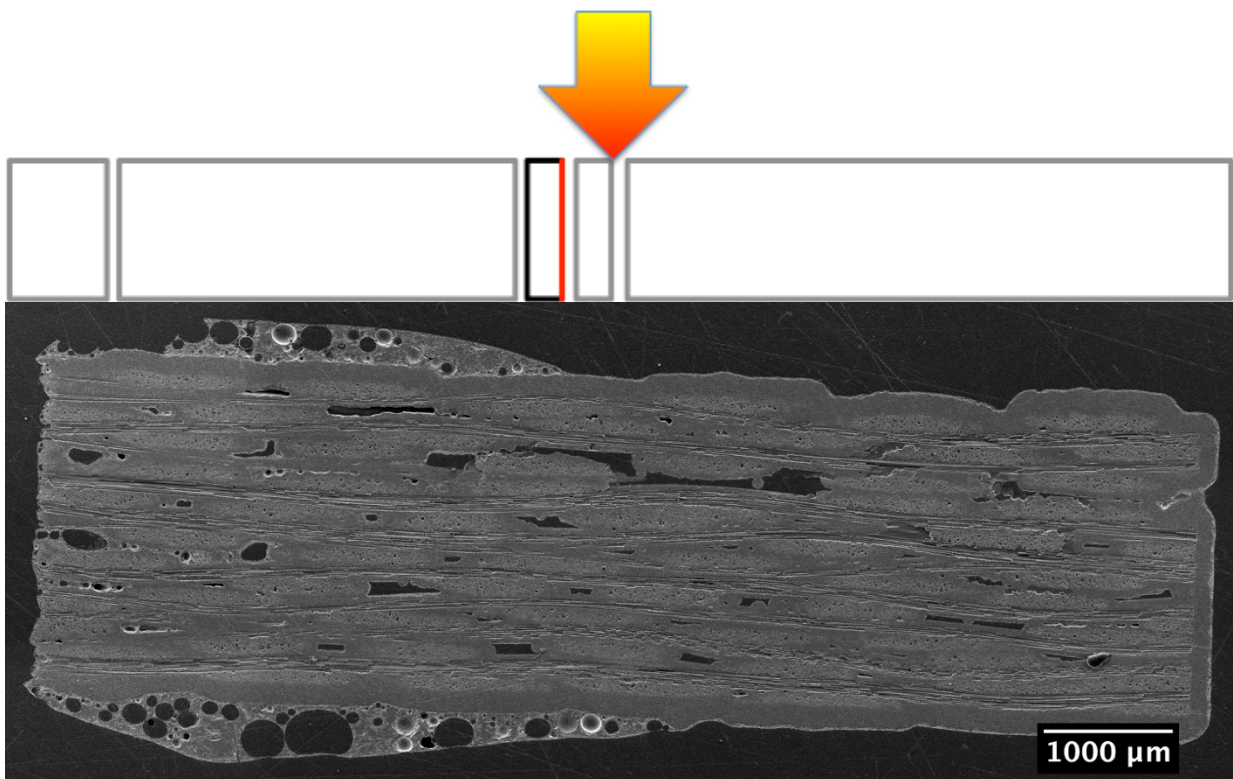


Figure C-44 – SEM Micrograph of the second cross-section of CVI-BR-24 after exposure in the burner rig, leading edge on the left.

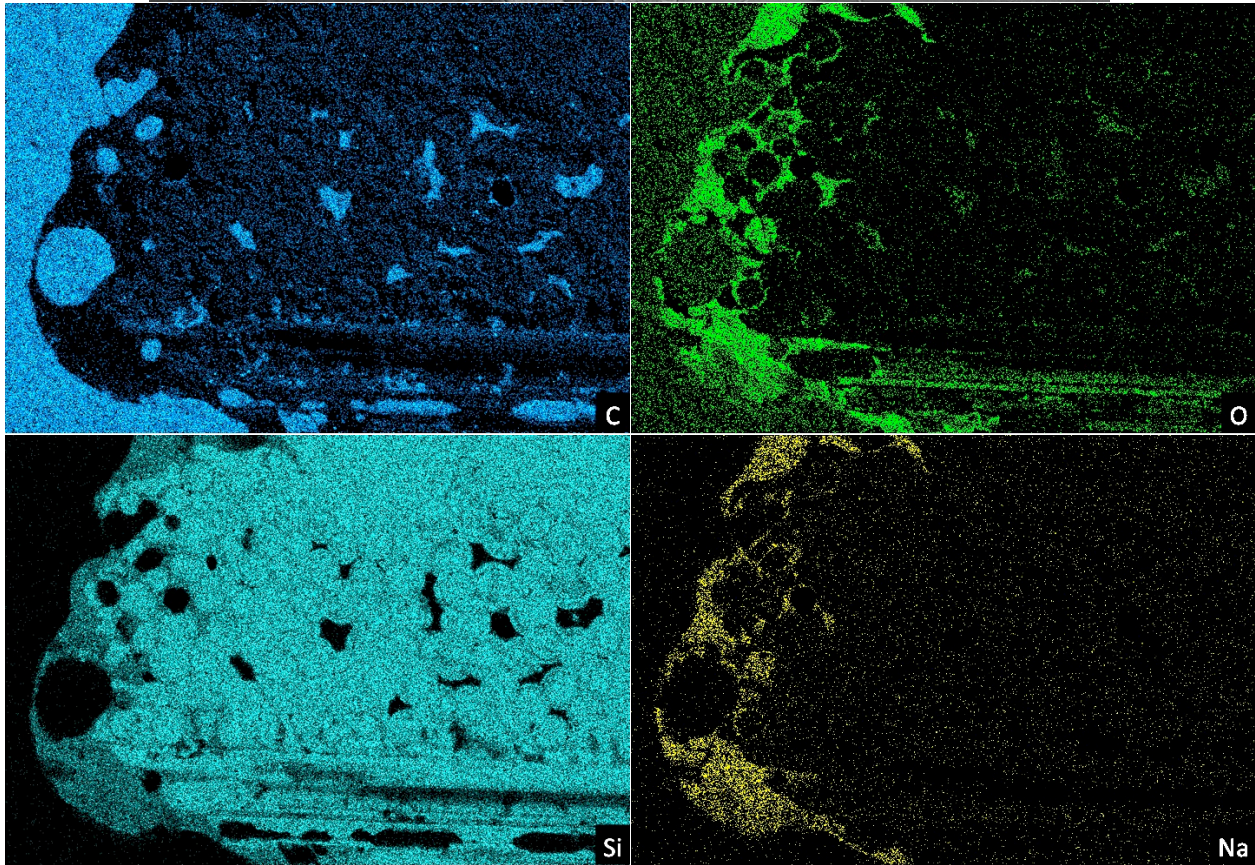
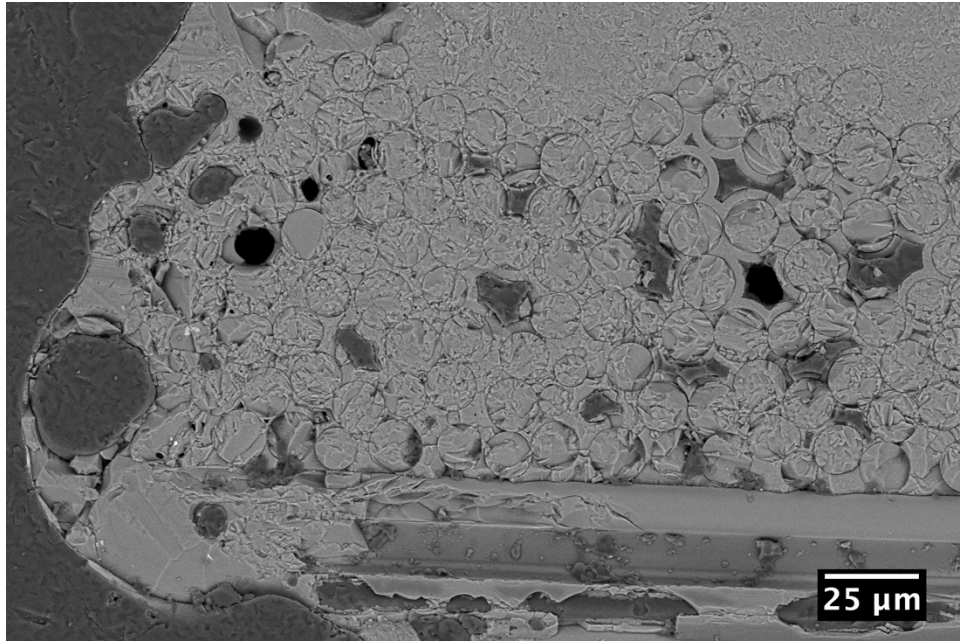


Figure C-45 - Top: An SEM micrograph of the second cross-section of CVI-BR-24. Middle: EDS maps for C (left) and O (right). Bottom: EDS maps for Si (left) and Na (right). Attack is fairly uniform, but corrosion proceeds down the fiber lengths and in between individual fibers.

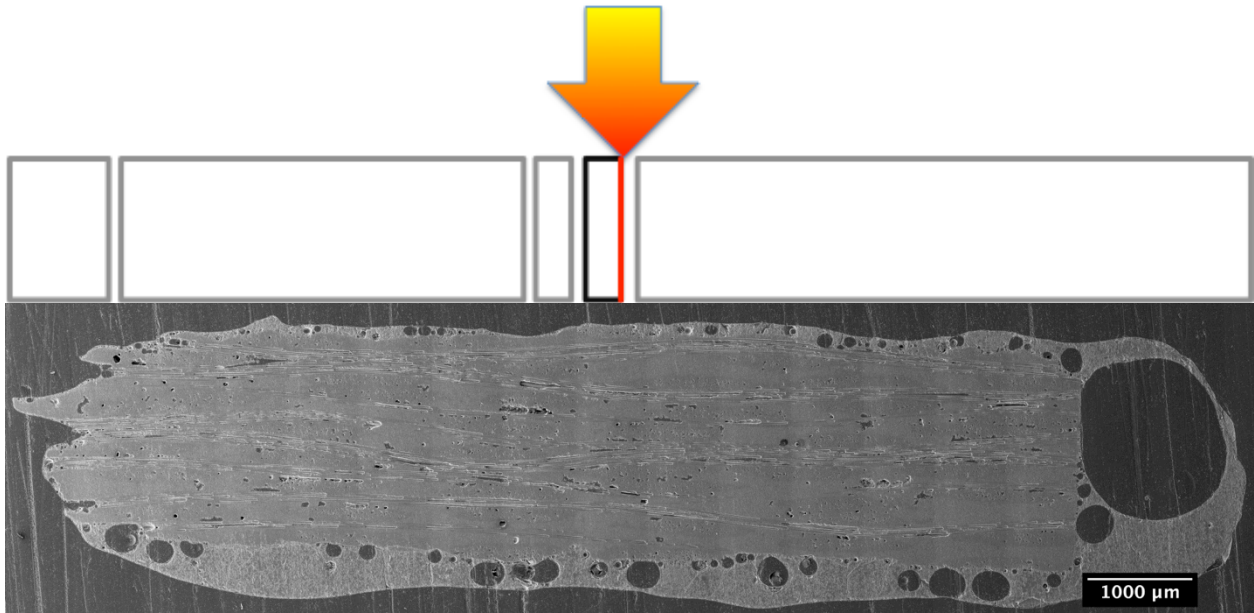


Figure C-46 – SEM Micrograph of the first cross-section of MI-BR-45 after exposure in the burner rig, leading edge on the left.

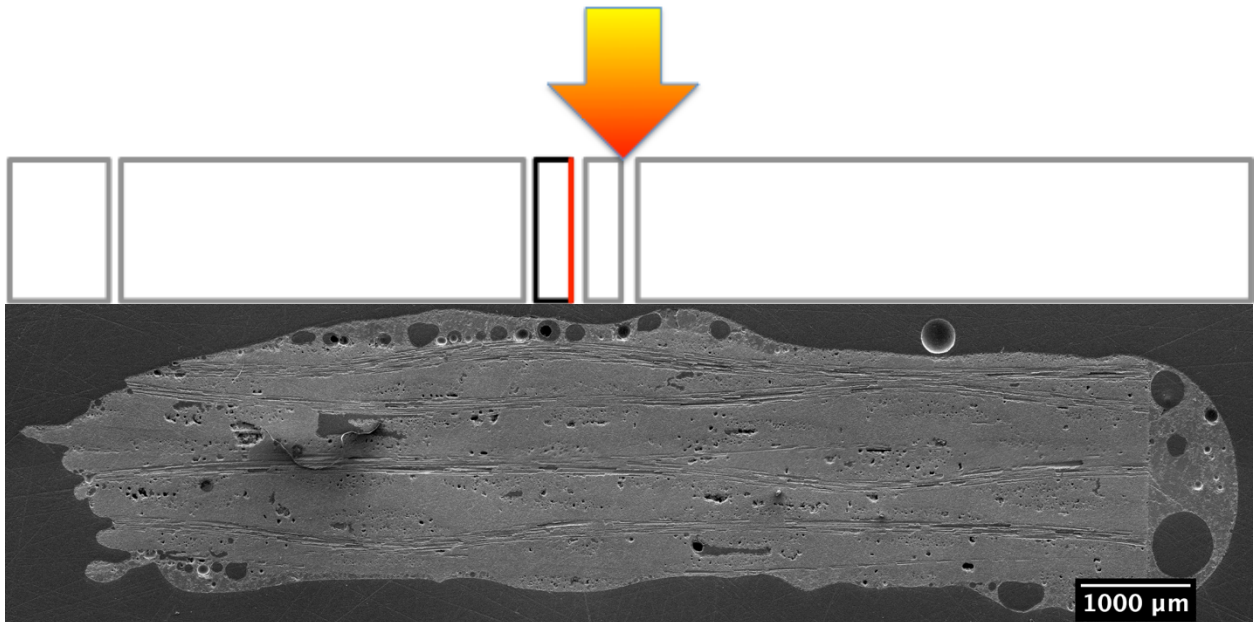


Figure C-47 – SEM Micrograph of the second cross-section of MI-BR-45 after exposure in the burner rig, leading edge on the left.

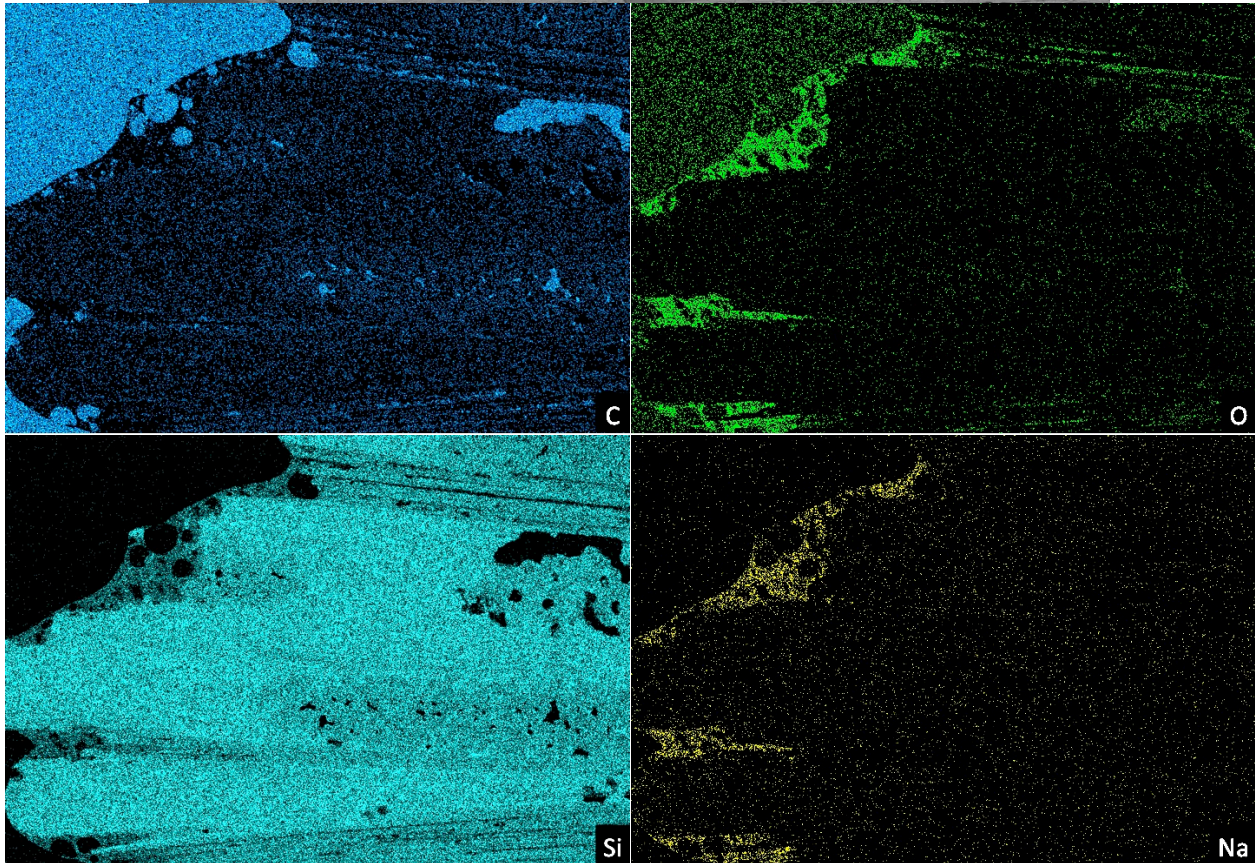
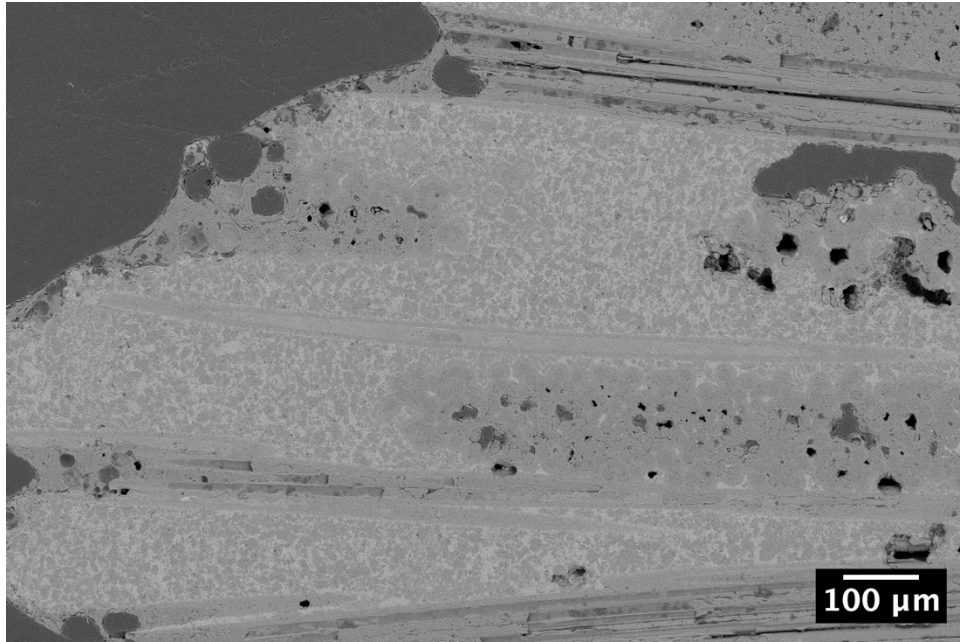


Figure C-48 – Top: An SEM micrograph of the second cross-section of MI-BR-45. Middle: EDS maps for C (left) and O (right). Bottom: EDS maps for Si (left) and Na (right). The fiber tows exposed end-on are attacked most aggressively, and the matrix is fairly resistant to hot corrosion attack.

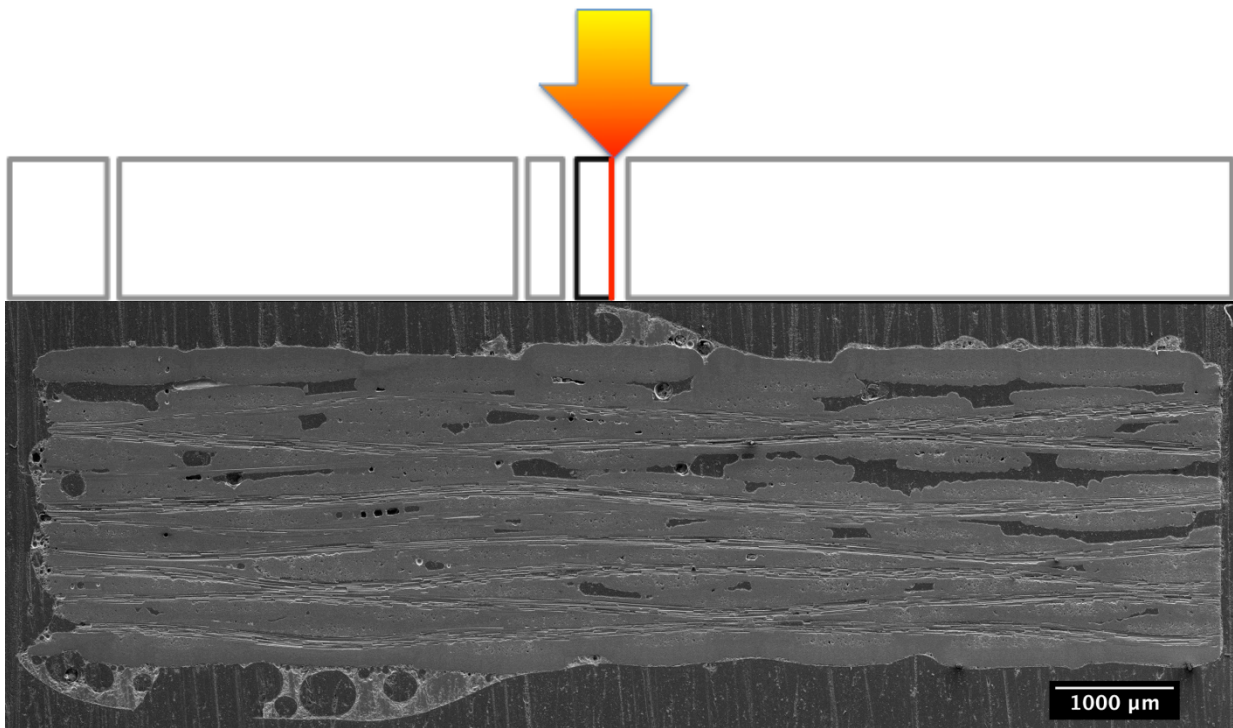


Figure C-49 – SEM Micrograph of the first cross-section of CVI-BR-45 after exposure in the burner rig, leading edge on the left.

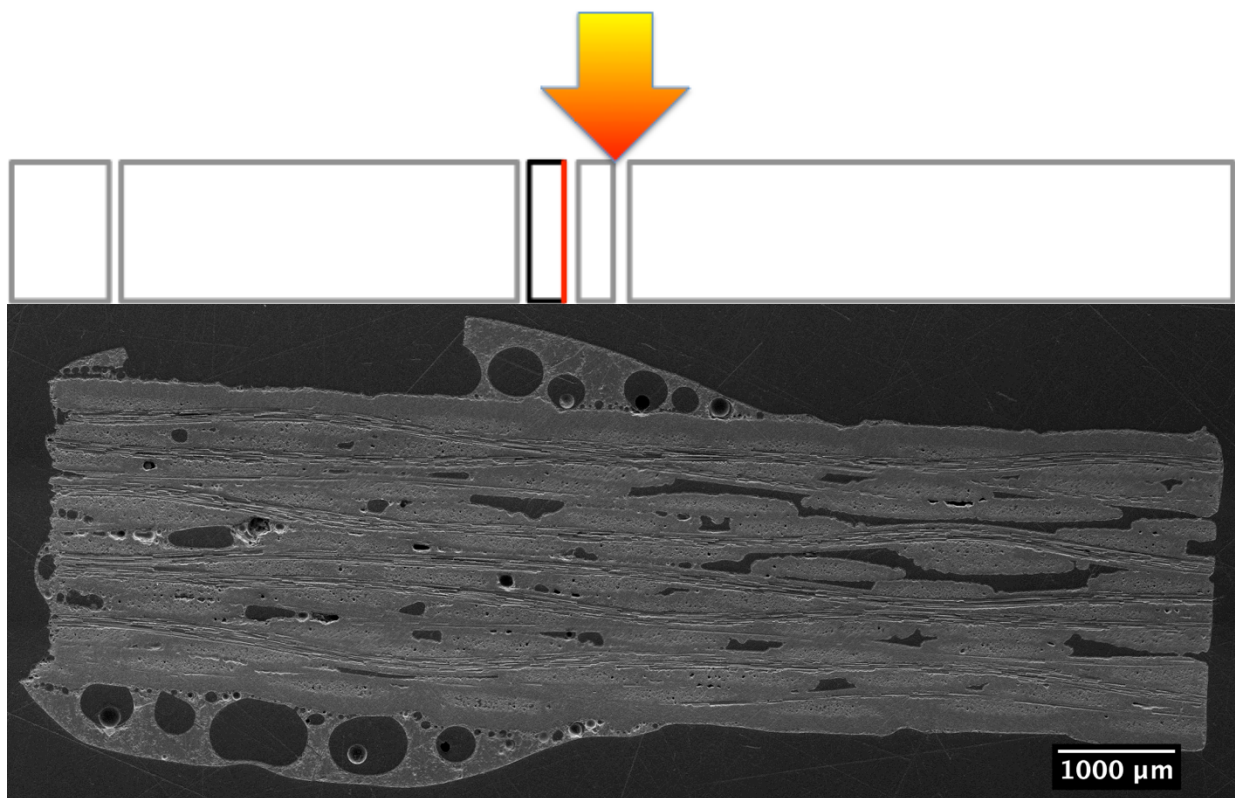


Figure C-50 – SEM Micrograph of the second cross-section of CVI-BR-45 after exposure in the burner rig, leading edge on the left.

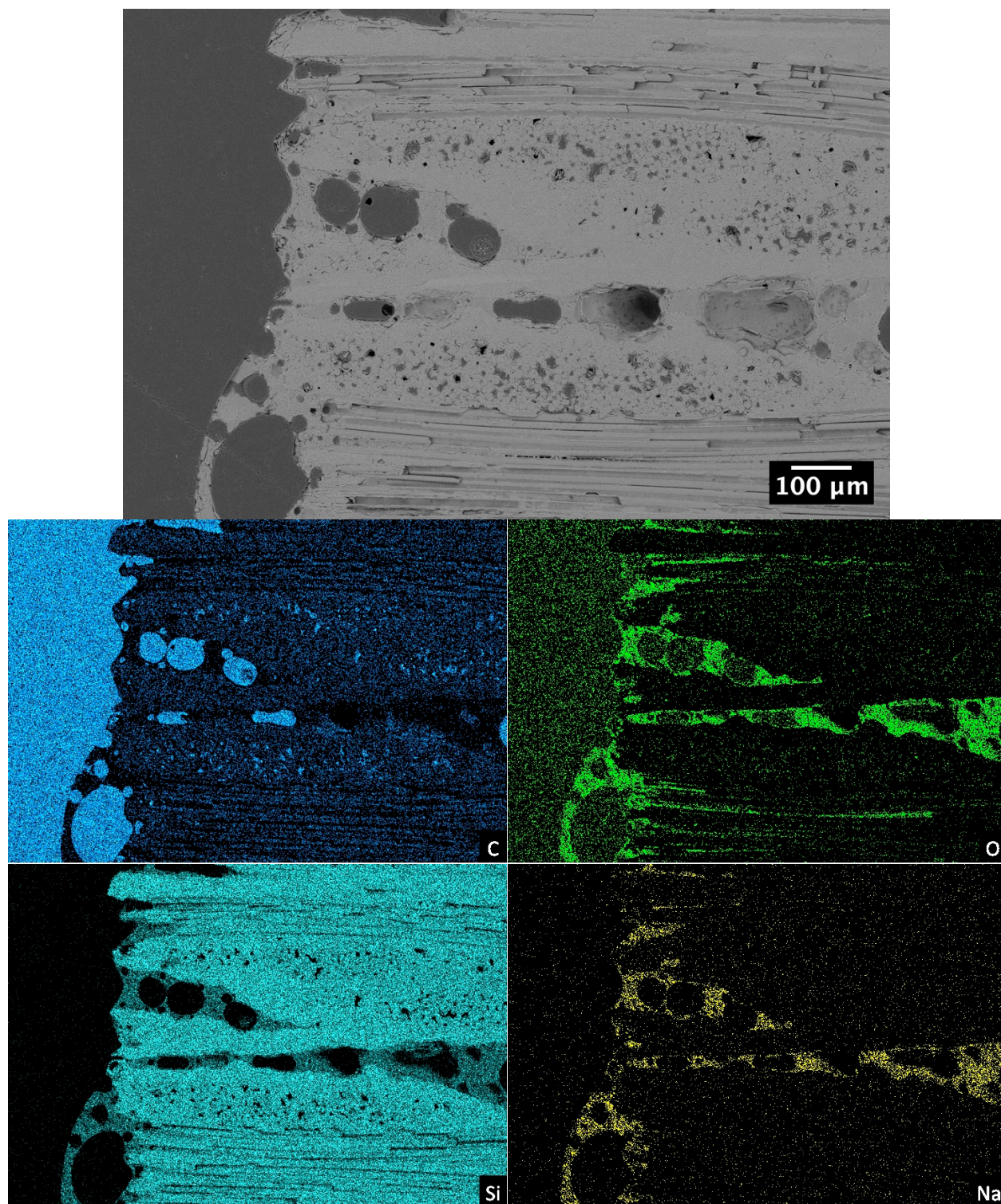


Figure C-51 - Top: An SEM micrograph of the second cross-section of CVI-BR-45. Middle: EDS maps for C (left) and O (right). Bottom: EDS maps for Si (left) and Na (right). The large voids in the CVI matrix allow for easy ingress of corrosion products.

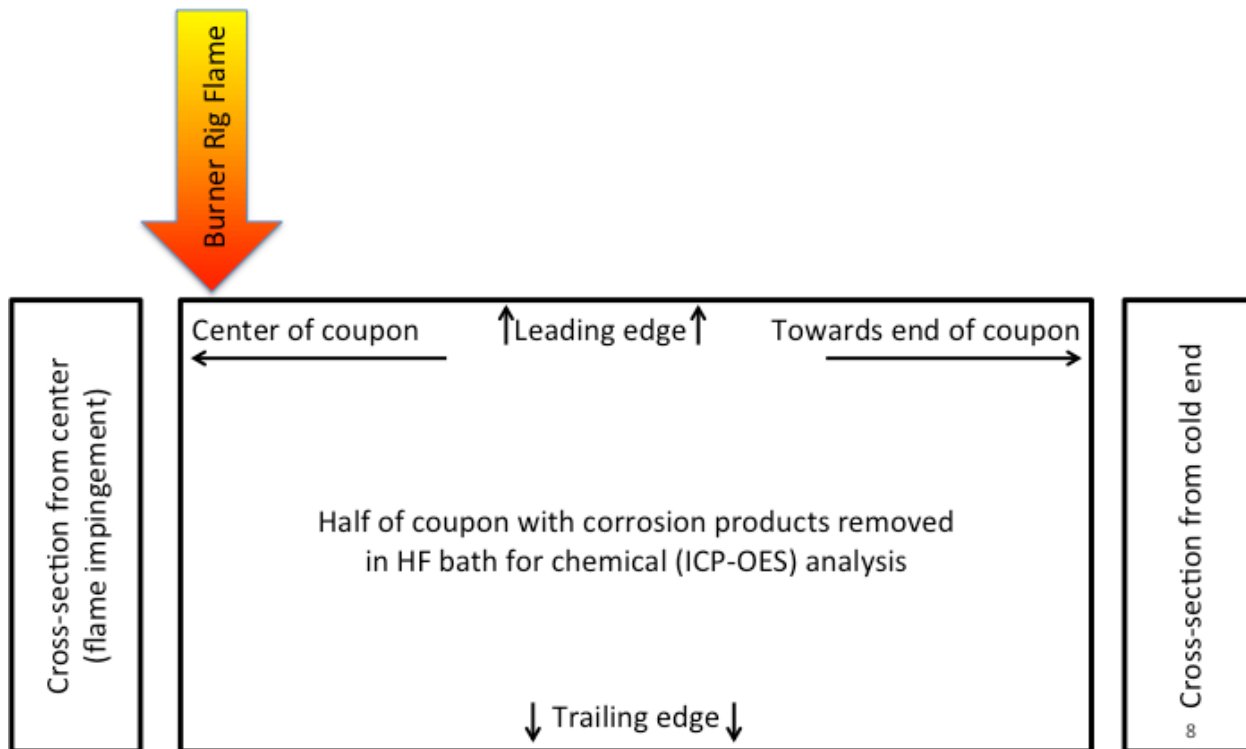


Figure C-52 – Schematic diagram of the arrangement of micrographs for determining recession in the burner rig coupons.

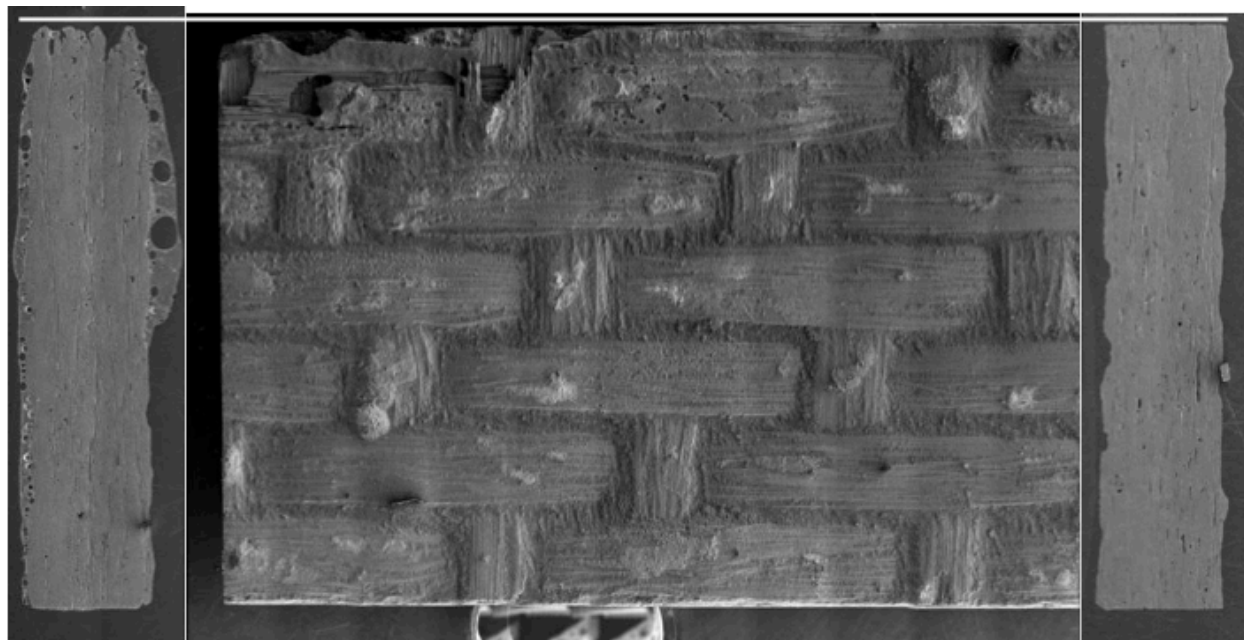


Figure C-53 – Recession for the MI-BR-24 coupon was approximately 1mm.

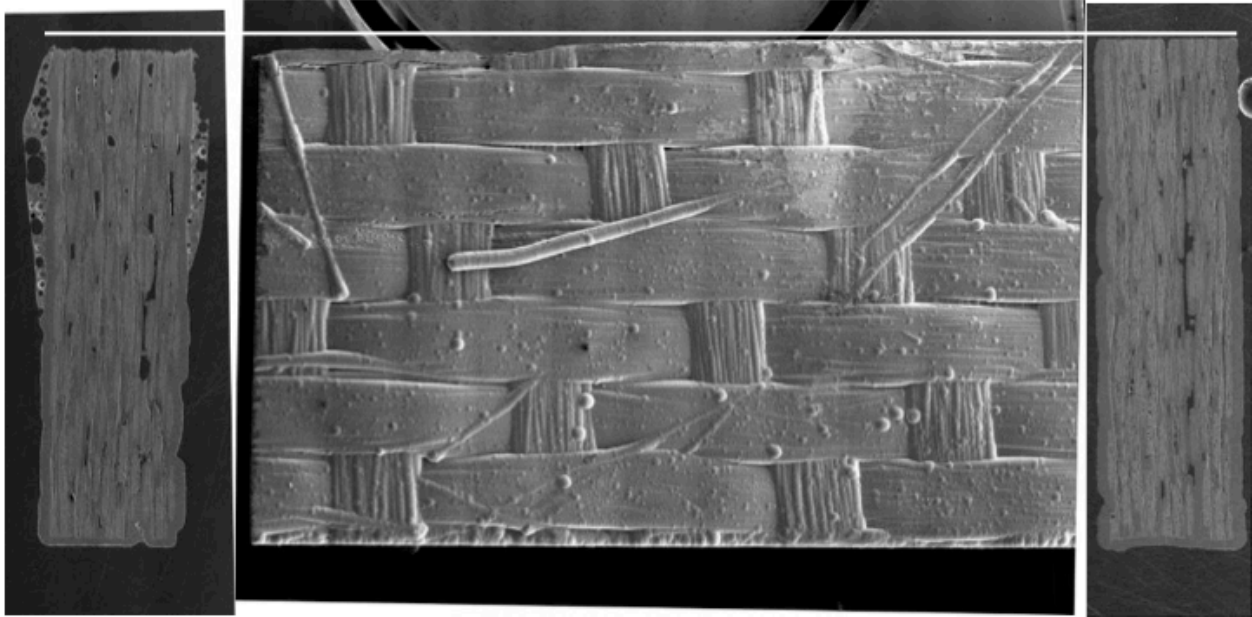


Figure C-54 – Recession for the CVI-BR-24 coupon was approximately 2mm.

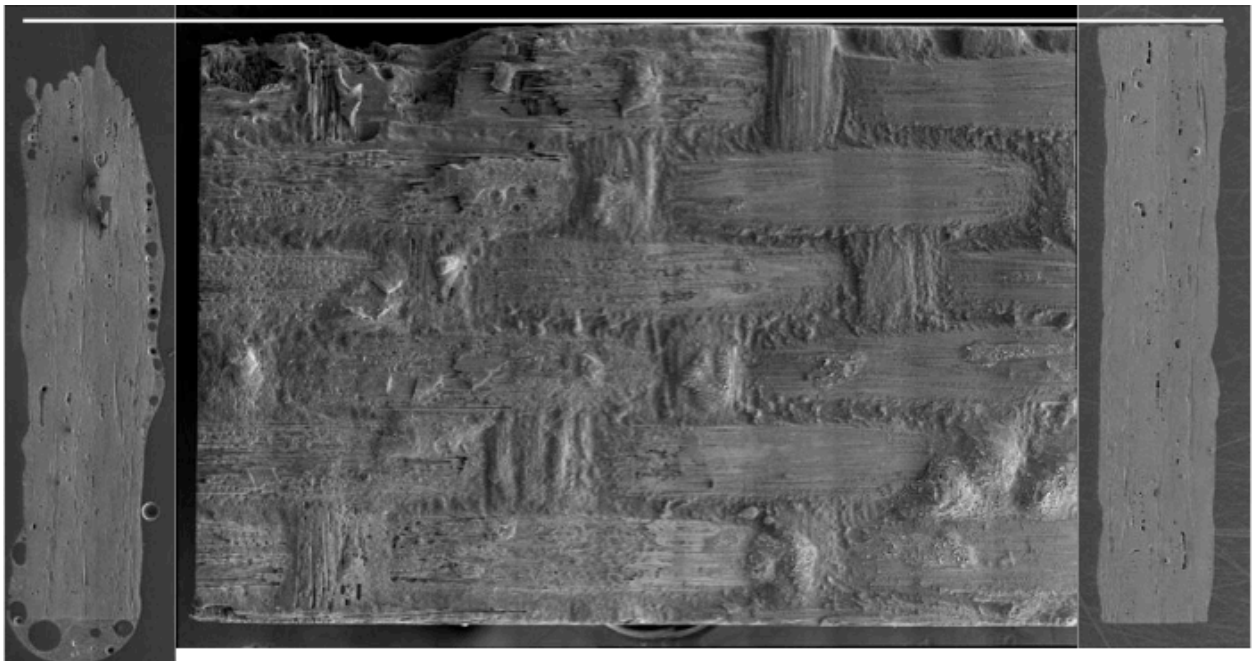


Figure C-55 – Recession for the MI-BR-45 coupon was approximately 8mm.

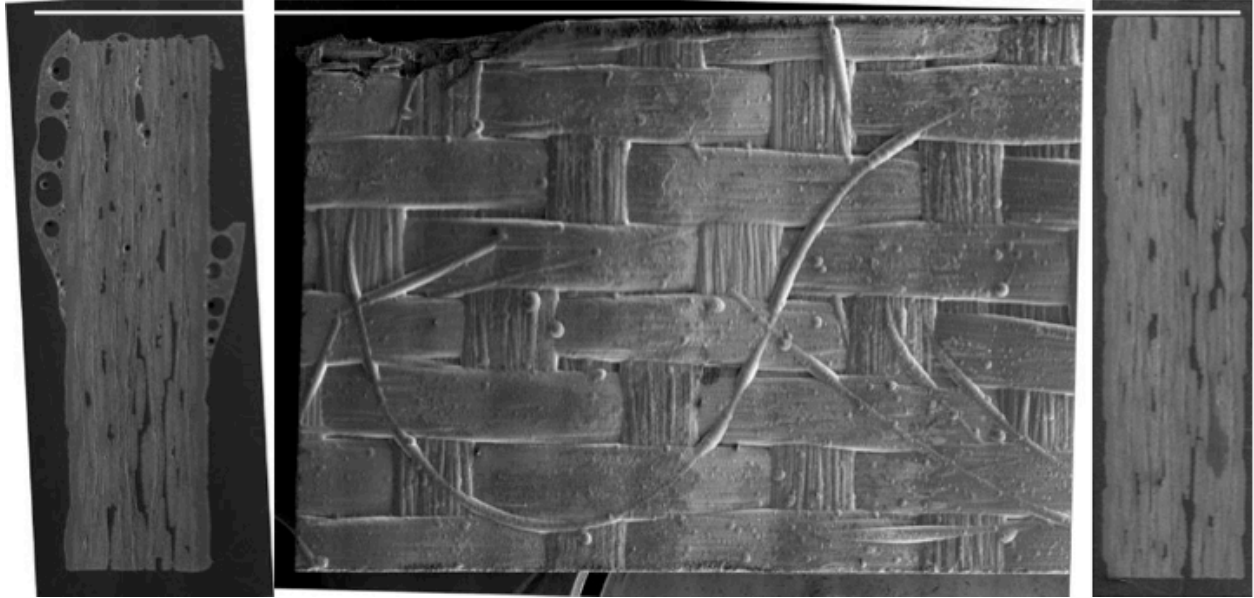


Figure C-56 – Recession for the CVI-BR-45 coupon was approximately 5mm.

Appendix D Electrochemical Measurement Data

Table D-1 – Predicted Na₂O activities for each sample, measured potentials, and corresponding Na₂O activities in the Na₂SO₄ melt.

Sample ID	Oxide Species	Gas (ppm SO ₂)	Na ₂ O ₂ Added	Predicted -log(<i>a</i> Na ₂ O)	Measured Potential [mV]	Experimental -log(<i>a</i> Na ₂ O)
EC-1	NiO	1000		13.6	-126.9	13.75
EC-2	NiO	1000		13.6	-123.4	13.72
EC-3	NiO	1000		13.6	-131.7	13.79
EC-4	NiO	2.5		11.0	46.8	12.26
EC-5	NiO	2.5		11.0	56.5	12.17
EC-6	NiO	2.5		11.0	124.0	11.59
EC-7	NiO	2.5		11.0	124.5	11.59
EC-8	NiO	25		12.0	34.5	12.36
EC-9	NiO	25		12.0	29.0	12.41
EC-10	NiO	25		12.0	48.0	12.25
EC-11	NiO	25		12.0	40.4	12.31
EC-12	NiO	25		12.0	24.4	12.45
EC-13	SiO ₂	25		12.0	57.0	12.17
EC-14	SiO ₂	25		12.0	56.0	12.18
EC-15	SiO ₂	25		12.0	57.5	12.17
EC-16	SiO ₂	25		12.0	56.5	12.17
EC-17	SiO ₂	25		12.0	56.2	12.18
EC-18	SiO ₂	25		12.0	55.5	12.18
EC-19	SiO ₂	100		12.6	-3.0	12.69
EC-20	SiO ₂	100		12.6	-3.6	12.69
EC-21	SiO ₂	100		12.6	-1.9	12.68
EC-22	SiO ₂	100		12.6	-1.5	12.67
EC-23	SiO ₂	100		12.6	-1.2	12.67
EC-24	SiO ₂	100		12.6	-1.4	12.67
EC-25	NiO	2.5	Y	11.0	364.7	9.53
EC-26	NiO	2.5	Y	11.0	355.8	9.6
EC-27	NiO	2.5	Y	11.0	302.2	10.06
EC-28	NiO	2.5	Y	11.0	299.5	10.09
EC-29	NiO	2.5	Y	11.0	246.4	10.54
EC-30	NiO	2.5	Y	11.0	243.3	10.57
EC-31	SiO ₂	1	Y	10.6	230.0	10.68
EC-32	SiO ₂	1	Y	10.6	244.9	10.56
EC-33	SiO ₂	Ar	Y	<10.6	250.0	10.51
EC-34	SiO ₂	Ar	Y	<10.6	254.7	10.47
EC-35	NiO	1000		13.6	-180.0	14.205
EC-36	NiO	1000		13.6	-189.0	14.283
EC-37	NiO	1000		13.6	-189.0	14.283
EC-38	NiO	1000		13.6	-165.0	14.076
EC-39	NiO	1000		13.6	-170.0	14.119
EC-40	NiO	1000		13.6	-190.0	14.291
EC-41	SiO ₂	1		10.6	94.0	11.852
EC-42	SiO ₂	1	Y	10.6	260.0	10.426
EC-43	SiO ₂	1	Y	10.6	255.6	10.463
EC-44	SiO ₂	1	Y	10.6	240.0	10.597
EC-45	SiO ₂	1	Y	10.6	271.0	10.331
EC-46	SiO ₂	1	Y	10.6	246.0	10.546
EC-47	B ₂ O ₃	100		12.6	-300.0	15.236

Sample ID	Oxide Species	Gas (ppm SO ₂)	Na ₂ O ₂ Added	Predicted $-\log(aNa_2O)$	Measured Potential [mV]	Experimental $-\log(aNa_2O)$
EC-48	B ₂ O ₃	1		10.6	-143.8	13.894
EC-49	B ₂ O ₃	1		10.6	-138.6	13.85
EC-50	B ₂ O ₃	1		10.6	-174.5	14.156
EC-51	B ₂ O ₃	1		10.6	-174.3	14.158
EC-52	B ₂ O ₃	1		10.6	-188.4	14.278
EC-53	B ₂ O ₃	1		10.6	-187.7	14.271
EC-54	B ₂ O ₃	1000		13.6	-152.4	13.968
EC-55	B ₂ O ₃	1000		13.6	-148.5	13.935
EC-56	B ₂ O ₃	10,000		14.6	-230.0	14.635
EC-57	B ₂ O ₃	10,000		14.6	-231.0	14.643
EC-58	B ₂ O ₃	10,000		14.6	-234.5	14.674
EC-59	B ₂ O ₃	1	Y	10.6	-54.2	13.125
EC-60	B ₂ O ₃	1	Y	10.6	-42.0	13.02
EC-61	B ₂ O ₃	1	Y	10.6	-29.0	12.908

10 Works Cited

- 1 N.S. Jacobson, "Kinetics and mechanism of corrosion of SiC by molten salts," *J. Am. Ceram. Soc.*, **69** [1] 74–82 (1986).
- 2 N.S. Jacobson and J.L. Smialek, "Corrosion pitting of SiC by molten salts," *J. Electrochem. Soc.*, **133** [12] 2615–2621 (1986).
- 3 N.S. Jacobson, "Corrosion of Silicon-Based Ceramics in Combustion Environments," *J. Am. Ceram. Soc.*, **76** [1] 3–28 (1993).
- 4 J. Kim, "Hot corrosion of hot-pressed silicon carbide," *J. Mater. Sci. Lett.*, **15** 6–9 (1996).
- 5 D.W. Mckee and D. Chatterji, "Corrosion of Silicon Carbide in Gases and Alkaline Melts," *J. Am. Ceram. Soc.*, **1975** [51] 7–10 (1976).
- 6 D. Shi and R.A. Rapp, "The Solubility of SiO₂ in Fused Na₂SO₄ at 900°C," *Isothermal Hydrog. Annealing*, **133** [4] 849–850 (1986).
- 7 Committee on Advanced Fibers for High-Temperature Ceramic Composites, "Ceramic Fibers and Coatings: Advanced Materials for the Twenty-First Century," in *Publ. NMAB-494*. National Academy of Sciences - National Materials Advisory Board, Washington, DC, 1998.
- 8 R. Naslain, O. Dugne, and A. Guette, "Boron Nitride Interphase in Ceramic-Matrix Composites," *J. Am. Ceram. Soc.*, **88** [i] 2482–2488 (1991).
- 9 R. Naslain, A. Guette, F. Rebillat, R. Paillet, F. Langlais, and X. Bourrat, "Boron-bearing species in ceramic matrix composites for long-term aerospace applications," *J. Solid State Chem.*, **177** [2] 449–456 (2004).
- 10 G.N. Morscher, H.M. Yun, J.A. DiCarlo, and L. Thomas-Ogbuji, "Effect of a boron nitride interphase that debonds between the interphase and the matrix in SiC/SiC composites," *J. Am. Ceram. Soc.*, **12** 104–112 (2004).
- 11 N.S. Jacobson, J.L. Smialek, and D.S. Fox, "Molten Salt Corrosion of SiC and Si₃N₄"; pp. 99–136 in *Handb. Ceram. Compos. Vol. 1 Synth. Prop.* Edited by N.P. Cheremisinoff. Marcel Dekker, Inc, New York, 1990.
- 12 H. Flood and T. Förland, "The Acidic and Basic Properties of Oxides," *Acta Chem. Scand.*, 592–604 (1947).

- 13 E. Opila and R. Hann, "Paralinear oxidation of CVD SiC in water vapor," *J. Am. Ceram. Soc.*, **80** [1] 197–205 (1997).
- 14 N.S. Jacobson, E.J. Opila, and K.N. Lee, "Oxidation and corrosion of ceramics and ceramic matrix composites," *Curr. Opin. Solid State Mater. Sci.*, **5** 301–309 (2001).
- 15 N. Jacobson, D. Myers, E. Opila, and E. Copland, "Interactions of water vapor with oxides at elevated temperatures," *J. Phys. Chem. Solids*, **66** [2-4] 471–478 (2005).
- 16 N.S. Jacobson and J.L. Smialek, "The hot corrosion of sintered α -SiC at 1000°C," *J. Am. Ceram. Soc.*, **68** [8] 432–439 (1985).
- 17 S. Wu, L. Cheng, L. Zhang, Y. Xu, X. Luan, and H. Mei, "Corrosion of SiC/SiC composite in Na₂SO₄ vapor environments from 1000 to 1500°C," *Compos. Part A Appl. Sci. Manuf.*, **37** [9] 1396–1401 (2006).
- 18 L. Cheng, Y. Xu, L. Zhang, and X. Luan, "Corrosion of a 3D-C / SiC composite in salt vapor environments," *Carbon N. Y.*, **40** [May 2001] 877–882 (2002).
- 19 V. Pareek and D. Shores, "Oxidation of silicon carbide in environments containing potassium salt vapor," *J. Am. Ceram. Soc.*, **63** [3] 556–563 (1991).
- 20 M.J. McNallan, S.Y. Lee, and P.P. Hsu, "Oxidation of silicon based ceramics in the presence of alkali halides," *Corros. Adv. Ceram.*, **267** 189–202 (1994).
- 21 M.A. Lamkin, F.L. Riley, and R.J. Fordham, "Oxygen mobility in silicon dioxide and silicate glasses: a review," *J. Eur. Ceram. Soc.*, **10** [5] 347–367 (1992).
- 22 J. Horbach, W. Kob, and K. Binder, "Structural and dynamical properties of sodium silicate melts: an investigation by molecular dynamics computer simulation," *Chem. Geol.*, **174** [1-3] 87–101 (2001).
- 23 R.A. Rapp, "Hot corrosion of materials: a fluxing mechanism?," *Corros. Sci.*, **44** 209–221 (2002).
- 24 R.A. Rapp, "Chemistry and electrochemistry of hot corrosion of metals," *Mater. Sci. Eng.*, **87** 319–327 (1987).
- 25 N.S. Jacobson, "Sodium sulfate: Deposition and dissolution of silica," *Oxid. Met.*, **31** [1-2] 91–103 (1989).
- 26 L. Filipuzzi and R. Naslain, "Oxidation Mechanisms and Kinetics of 1D-SiC/C/SiC Composite Materials: II, Modeling," *J. Am. Ceram. Soc.*, **77** [2] 467–480 (1994).

- 27 L. Filipuzzi, G. Camus, and R. Naslain, "Oxidation Mechanisms and Kinetics of 1D-SiC/C/SiC Composite Materials: I, An Experimental Approach," *J. Am. Ceram. Soc.*, **77** [2] 459–66 (1994).
- 28 S. Wu, L. Cheng, and L. Zhang, "Oxidation behavior of 3D Hi-Nicalon/SiC composite exposed in wet and simulated air environments," *Corros. Sci.*, **66** 111–117 (2013).
- 29 N.S. Jacobson, G.N. Morscher, D.R. Bryant, and R.E. Tressler, "High-Temperature Oxidation of Boron Nitride: II, Boron Nitride Layers in Composites," *J. Am. Ceram. Soc.*, **82** [6] 1473–1482 (2004).
- 30 B.W. Sheldon, E.Y. Sun, S.R. Nutt, and J.J. Brennan, "Oxidation of BN-Coated SiC Fibers in Ceramic Matrix Composites," *J. Am. Ceram. Soc.*, **79** [2] 539–543 (1996).
- 31 T. Rockett and W. Foster, "Phase Relations in the System Boron Oxide–Silica," *J. Am. Ceram. Soc.*, **48** [2] 75–80 (1965).
- 32 J. Schlichting, "Oxygen transport through glass layers formed by a gel process," *J. Non. Cryst. Solids*, **63** 173–181 (1984).
- 33 F. Kracek, "The System Sodium Oxide-Silica," *J. Phys. Chem.*, **34** [7] 1583–1598 (1930).
- 34 G.W. Morey and H.E. Merwin, "Phase Equilibrium Relationships in the Binary System, Sodium Oxide-Boric Oxide, with Some Measurements of the Optical Properties of the Glasses," *J. Am. Chem. Soc.*, **58** [11] 2248–2254 (1936).
- 35 G.W. Watt, R.E. Andresen, and R.A. Rapp, "A comparison of reference electrodes in molten sodium sulfate," 81–109 (n.d.).
- 36 G. Morscher, "Tensile Stress Rupture of SiC_f/SiC_m Minicomposites with Carbon and Boron Nitride Interphases at Elevated Temperatures in Air," *J. Am. Ceram. Soc.*, **42** 2029–2042 (1997).
- 37 N. Cocera, N.R. De Esparza, I. Ocaña, and J.M. Sanchez, "Oxidation resistance of highly porous CVD-SiC coated Tyranno fiber composites," *J. Eur. Ceram. Soc.*, **31** [6] 1155–1164 (2011).
- 38 E. Klatt, A. Frass, M. Frieß, D. Koch, and H. Voggenreiter, "Mechanical and microstructural characterisation of SiC- and SiBNC-fibre reinforced CMCs manufactured via PIP method before and after exposure to air," *J. Eur. Ceram. Soc.*, **32** [14] 3861–3874 (2012).
- 39 L. Cheng, Y. Xu, L. Zhang, and X. Yin, "Oxidation behavior of three-dimensional SiC/SiC composites in air and combustion environment," *Compos. Part A Appl. Sci. Manuf.*, **31** [9] 1015–1020 (2000).

- 40 S. Wu, L. Cheng, L. Zhang, Y. Xu, and Q. Zhang, "Oxidation behavior of 3D Hi-Nicalon/SiC composite," *Mater. Lett.*, **60** [25-26] 3197–3201 (2006).
- 41 X. Luan, L. Cheng, Y. Xu, and L. Zhang, "Stressed oxidation behaviors of SiC matrix composites in combustion environments," *Mater. Lett.*, **61** [19-20] 4114–4116 (2007).
- 42 A. Eckel, J. Cawley, and T. Parthasarathy, "Oxidation kinetics of a continuous carbon phase in a nonreactive matrix," *J. Am. Ceram. Soc.*, **78** 972–80 (1995).
- 43 C. Bale, P. Chartrand, S. Degterov, G. Eriksson, K. Hack, R. Ben Mahfoud, J. Melançon, A. Pelton, *et al.*, "FactSage thermochemical software and databases," *Calphad*, **26** [2] 189–228 (2002).
- 44 D. Faucett and S. Choi, "Strength Degradation of Oxide/Oxide and SiC/SiC Ceramic Matrix Composites in CMAS and CMAS/Salt Exposures;" pp. 1–8 in *Proceeding ASME Turbo Expo 2011*. 2011.
- 45 R. Lowden and R. James, *High-temperature corrosion of Nicalon (tm)/SiC composites*. 1991.
- 46 H.E. Eaton and G.D. Linsey, "Accelerated oxidation of SiC CMC's by water vapor and protection via environmental barrier coating approach," *J. Eur. Ceram. Soc.*, **22** [14-15] 2741–2747 (2002).
- 47 K.N. Lee, D.S. Fox, and N.P. Bansal, "Rare earth silicate environmental barrier coatings for SiC/SiC composites and Si₃N₄ ceramics," *J. Eur. Ceram. Soc.*, **25** [10] 1705–1715 (2005).
- 48 J.M. Hagan and E.J. Opila, "High-Temperature Na₂SO₄ Deposit-Assisted Corrosion of Silicon Carbide – I: Temperature and Time Dependence," *J. Am. Ceram. Soc.*, **98** [4] 1275–1284 (2015).
- 49 R. Browning, J.L. Smialek, and N.S. Jacobson, "Multielement Mapping of α -SiC by Scanning Auger Microscopy," *Adv. Ceram. Mater.*, (1987).
- 50 K. Nickel, "Corrosion of non-oxide ceramics," *Ceram. Int.*, **23** 127–133 (1997).
- 51 C. Berthold and K. Nickel, "Hot-corrosion behaviour of silica and silica-formers: external versus internal control," *J. Eur. Ceram. Soc.*, **5** [1998] 2365–2372 (1998).
- 52 K. Nickel and S. Merkel, "Mechanisms and kinetics of silica-rich binary Na₂O-SiO₂ glass corrosion in 100°C water at pH=7," *Key Eng. Mater.*, **336-338** 1823–1826 (2007).

- 53 S. Preibisch, S. Saalfeld, and P. Tomancak, "Globally optimal stitching of tiled 3D microscopic image acquisitions," *Bioinformatics*, **25** [11] 1463–1465 (2009).
- 54 J. Schindelin, I. Arganda-Carreras, E. Frise, V. Kaynig, M. Longair, T. Pietzsch, S. Preibisch, C. Rueden, *et al.*, "Fiji: an open-source platform for biological-image analysis," *Nat Meth*, **9** [7] 676–682 (2012).
- 55 O. Flores, R.K. Bordia, D. Nestler, W. Krenkel, and G. Motz, "Ceramic Fibers Based on SiC and SiCN Systems: Current Research, Development, and Commercial Status," *Adv. Eng. Mater.*, **16** 621–636 (2014).
- 56 J.A. Dicarlo and H. Yun, "Non-oxide (Silicon Carbide) Fibers;" pp. 33–52 in *Handb. Ceram. Compos.* Edited by N.P. Bansal. Springer, 2005.
- 57 D.S. Fox, R.A. Miller, D. Zhu, M. Perez, M.D. Cuy, and R.C. Robinson, *Mach 0.3 Burner Rig Facility at the NASA Glenn Materials Research Laboratory*. Cleveland, OH, 2011.
- 58 D. Gupta and R. Rapp, "The Solubilities of NiO, Co₃O₄, and Ternary Oxides in Fused Na₂SO₄ at 1200°K," *J. Electrochem. Soc.*, **127** [10] 2194–2202 (1980).
- 59 G. Janz, F. Dampier, G. Lakshminarayanan, P. Lorenz, and R. Tomkins, *Molten Salts: Volume 1, Electrical Conductance, Density, and Viscosity Data*. 1968.
- 60 P. Gielisse and W. Foster, "The system Al₂O₃-B₂O₃," *Nature*, **195** [4836] 69–70 (1962).
- 61 R. Browning, J.L. Smialek, and N.S. Jacobson, "Multielement Mapping of α -SiC by Scanning Auger Microscopy," *Adv. Ceram. Mater.*, **2** [4] 773–79 (1987).
- 62 R. Naslain, O. Dugne, and A. Guette, "Boron Nitride Interphase in Ceramic-Matrix Composites," *J. Am. Ceram. Soc.*, **74** [i] 2482–2488 (1991).
- 63 G.N. Morscher, D.R. Bryant, and R.E. Tressler, "Environmental Durability of BN-Based Interphases (for SiC_f/SiC_m Composites) in H₂O Containing Atmospheres at Intermediate Temperatures"; in *Proc. 21st Annu. Conf. Compos. Adv. Ceram. Mater. Struct. A Ceram. Eng. Sci. Proc.* Edited by J.P. Singh. John Wiley & Sons, Inc., Hoboken, NJ, USA, 1997.
- 64 C.E. Ramberg, G. Cruciani, K.E. Spear, and R.E. Tressler, "Passive-Oxidation Kinetics of High-Purity Silicon Carbide from 800° to 1100°C," *J. Am. Ceram. Soc.*, **79** [11] 2897–2911 (1996).
- 65 B. Deal and A. Grove, "General relationship for the thermal oxidation of silicon," *J. Appl. Phys.*, **163** [1948] 3770–3778 (1965).
- 66 T. Rockett and W. Foster, "The Thermal Stability of Purified Tridymite," *Am. Mineral.*, **52** 1233–1240 (1967).

- 67 A. Atkinson, "Transport processes during the growth of oxide films at elevated temperature," *Rev. Mod. Phys.*, **57** [2] 437–470 (1985).
- 68 T. Sun, J.J. Brown, and G.R. Pickrell, "High temperature alkali corrosion of SiC and Si₃N₄," *Fuel Process. Technol.*, **44** 213–236 (1995).
- 69 S. Sōmiya, "Hydrothermal corrosion of nitride and carbide of silicon," *Mater. Chem. Phys.*, **67** [1-3] 157–164 (2001).
- 70 K. Ghanbari-Ahari and K.S. Coley, "High-temperature corrosion of a silicon-infiltrated silicon carbide material in combustion atmospheres," *J. Eur. Ceram. Soc.*, **17** [8] 995–1001 (1997).
- 71 D. Baxter, A. Bellosi, and F. Monteverde, "Oxidation and burner rig corrosion of liquid phase sintered SiC," *J. Eur. Ceram. Soc.*, **20** [3] 367–382 (2000).
- 72 T. Akiyama, K. Nakamura, T. Ito, H. Kageshima, and M. Uematsu, "Diffusion of carbon oxides in SiO₂ during SiC oxidation: A first-principles study," *J. Appl. Phys.*, **113** [18] (2013).
- 73 S.K. Dubrovo and Y.A. Shmidt, "Reactions of vitreous silicates and aluminosilicates with aqueous solutions Communication I. Reactions of vitreous sodium silicates with water and with hydrochloric acid solutions," *Bull. Acad. Sci. USSR, Div. Chem. Sci.*, **2** [4] 535–543 (1953).
- 74 J.C. Drake, C. Frondel, and C. Klein, "Mineralogical, petrological, and chemical features of four Apollo 12 lunar microgabbros," *Proc. Second Lunar Sci. Conf.*, **1** 265–284 (1971).
- 75 E. Poerschke and E.J. Opila, "Interactions Between Na₂SO₄, B₂O₃, and SiO₂: Relevance to Hot Corrosion of Ceramic Matrix Composites," *J. Am. Ceram. Soc.*, [In Preparation] (2015).
- 76 J. Lipowitz, J. Rabe, A. Zangvil, and Y. Xu, "Structure and Properties of Sylramic™ Silicon Carbide Fiber - A Polycrystalline, Stoichiometric β-SiC Composition," *Ceram. Eng. Sci. Proc.*, **18** [3] 147–157 (1997).
- 77 E.J. Opila, "Oxidation and Volatilization of Silica Formers in Water Vapor," *J. Am. Ceram. Soc.*, **86** [8] 1238–1248 (2003).
- 78 R.A. Golden and E.J. Opila, "A Method for Assessing the Stability of Oxides in High-Temperature High-Velocity Water Vapor," *J. Am. Ceram. Soc.*, [In Preparation] (2015).
- 79 S.L. Dos Santos E Lucato, O.H. Sudre, and D.B. Marshall, "A Method for Assessing Reactions of Water Vapor with Materials in High-Speed, High-Temperature Flow," *J. Am. Ceram. Soc.*, **94** [SUPPL. 1] 186–195 (2011).

- 80 D.A. Palmer, P. Bénézeth, and D.J. Wesolowski, "Solubility of Nickel Oxide and Hydroxide in Water," *14th Int. Conf. Prop. Water Steam Kyoto*, 264–269 (1980).
- 81 D.A. Palmer, P. Bénézeth, C. Xiao, D.J. Wesolowski, and L.M. Anovitz, "Solubility measurements of crystalline NiO in aqueous solution as a function of temperature and pH," *J. Solution Chem.*, **40** [4] 680–702 (2011).
- 82 P. Jose, D. Gupta, and R. Rapp, "Solubility of α -Al₂O₃ in Fused Na₂SO₄ at 1200 K," *J. Electrochem. Soc.*, **132** [3] 735–737 (1985).
- 83 R. Fournier and J. Rowe, "The solubility of amorphous and high pressures silica in water at high temperatures," *Am. Mineral.*, **62** 1052–1056 (1977).
- 84 M.P. Verma and I.D.I. Electricas, "Revised Quartz Solubility Temperature Dependence Equation Along the Water-Vapor Saturation Curve;" pp. 1927–1932 in *World Geotherm. Conf.* 2000.
- 85 G.W. Morey, R.O. Fournier, and J.J. Rowe, "The solubility of amorphous silica at 25°C," *J. Geophys. Res.*, **69** [10] 1995 (1964).
- 86 Y.S. Zhang and R.A. Rapp, "Solubility of α -Fe₂O₃ in Fused Na₂SO₄ at 1200 K," *J. Electrochem. Soc.*, **327** [March] 734–735 (1985).
- 87 Y.S. Zhang and R.A. Rapp, "Solubility of Cr₂O₃ in Fused Na₂SO₄ at 1200 K," *J. Electrochem. Soc.*, **133** 655–657 (1986).
- 88 S. Gordon and B.J. McBride, *Computer program for calculation of complex chemical equilibrium compositions and applications. Part 1: Analysis*. Cleveland, OH, 1994.
- 89 M.J. Zehe, S. Gordon, and B.J. McBride, *CAP: A Computer Code for Generating Tabular Thermodynamic Functions from NASA Lewis Coefficients*. Cleveland, OH, 2002.
- 90 T. Wakasugi, A. Ohkawa, J. Fukunaga, and R. Ota, "Solubility of Ag₂O into the B₂O₃–Al₂O₃ system," *J. Non. Cryst. Solids*, **255** [1999] 127–131 (1999).
- 91 R. Meyer, "Activity-Coefficient and Vacancy Flow Effects on Tracer Diffusion Coefficients in Silver-Gold Alloys," *Phys. Rev.*, **163** [3] 641–644 (1967).
- 92 D.A. Shores and R.C. John, "A study of the Ag (s) /Ag₂SO₄+Na₂SO₄ (l) 1102 reference electrode," *J. Appl. Electrochem.*, **10** [2] 275–283 (1980).